UNIVERSITY OF CALIFORNIA,
IRVINE

Neural Network Closure Modeling of Longitudinal Combustion Instability in a Liquid-propellant Rocket Engine

DISSERTATION

submitted in partial satisfaction of the requirements
for the degree of

DOCTOR OF PHILOSOPHY

in Mechanical and Aerospace Engineering

by

Zeinab Shadram

Dissertation Committee:
Professor William A. Sirignano, Chair
Professor Athanasios Sideris, Co-chair
Professor Tryphon Georgiou
Professor Feng Liu

2021

DEDICATION

To my parents and my brothers,
for all their encouragement and dedicated support.
&
To my beloved husband,
for all his love and support that gave me the power to continue my journey
with all its ups and downs.

TABLE OF CONTENTS

Page

LIST OF FIGURES **v**

LIST OF TABLES **ix**

ACKNOWLEDGMENTS **x**

VITA **xi**

ABSTRACT OF THE DISSERTATION **xiii**

1 Introduction **1**
1.1 Neural Networks 3
1.2 Motivation 7
1.3 Outline 9

2 Background on Combustion Instability Analysis **10**
2.1 Numerical Scheme 10
2.2 Flamelet Model 12
2.3 Combustion Modeling and Challenges 13
2.3.1 Rayleigh Index as an Instability Criterion 15

3 Neural Networks **16**
3.1 Introduction to Neural Networks 17
3.1.1 Overfitting 18
3.1.2 NN Development Process 19
3.2 The Learning Algorithm 20

4 Neural-Network-based Closure Model For CVRC: Learning From Flamelet Table Data **22**
4.1 NN Development 23
4.1.1 Sample Selection 23
4.1.2 Network Structure 24
4.2 NN Performance Analysis 25
4.2.1 Offline Test 25
4.2.2 Online Test 29
4.2.3 Computational Cost 64

4.3 Concluding Remarks 66

5 Physics-aware NN Design Based on CFD Simulation Data 68
5.1 Neural-Network Based Closure Model For CVRC: Learning From CFD Simulation Data 68
5.1.1 NN Development: Sample Selection 69
5.1.2 NN Development: Algorithm and Structure 72
5.2 NN Performance Analysis 74
5.2.1 Test on Flamelet Table 74
5.2.2 In-Situ Test of NN-based Models in CFD 89
5.3 Concluding Remarks 115

6 Conclusions and Future Work 117

Bibliography 121

Appendix A Numerical Framework for CVRC 129
A.1 Governing Equations 129
A.2 Turbulence Model 130
A.3 Combustion Model 131
A.4 Numerical Scheme 133
A.5 Solution Procedure 134
A.6 Multiblock Domain 135

LIST OF FIGURES

Page

1.1 Top level architecture of CFD code 3

2.1 Schematic of CVRC configuration 11
2.2 Top level architecture of CFD code 11

3.1 Single-output NN structure 17
3.2 Schematic of a neuron as a computing unit in the NN 17

4.1 Offline result comparison for internal energy, flame temperature, and PVRR 27
4.2 Offline result comparison for gas constant, thermal conductivity, ratio of heat capacity, ratio of heat capacity coefficient 28
4.3 14-cm, dynamic equilibrium: distribution of relative error (%) calculated from NN_a-based simulation comparison with the table-based one 32
4.4 14-cm, dynamic equilibrium: distribution of fluctuation correlation between pressure signals calculated from NN_a-based and table-based simulations . . . 33
4.5 14-cm, dynamic equilibrium: the distribution of the pressure fluctuation rms calculated from NN_a-based (4.5b) to the one calculated from table-based (4.5a) simulations 34
4.6 14-cm, dynamic equilibrium: comparison of pressure signals and FFTs at two different points on the top wall between the NN_a-based and the table-based simulations 35
4.7 14-cm, dynamic equilibrium: comparison of pressure signals at different points on centerline between the NN_a-based and the table-based simulations 36
4.8 14-cm, dynamic equilibrium: comparison of pressure mean, the first, the second, and the third mode shapes between NN_a-based and table-based simulations 37
4.9 14-cm, dynamic equilibrium: comparison of radial-averaged mRI and RI between the NN_a-based and the table-based simulations 38
4.10 14-cm, dynamic equilibrium: comparison of mRI from the NN_a- and the table-based simulations 39
4.11 14-cm, dynamic equilibrium: comparison of RI from the NN_a- and the table-based simulations 39
4.12 14-cm, dynamic equilibrium: time-averaged values of progress variable from the NN_a-based and the table-based simulations 40
4.13 14-cm, dynamic equilibrium: time-averaged values of mixture fraction from the NN_a-based and the table-based simulations 40

4.14 14-cm, dynamic equilibrium: time-averaged values of PVRR from the NN_a-based and the table-based simulations 41
4.15 14-cm, dynamic equilibrium: time-averaged values of temperature from the NN_a-based and the table-based simulations 41
4.16 14-cm, dynamic equilibrium: time-averaged values of axial velocity from the NN_a-based and the table-based simulations 42
4.17 14-cm, dynamic equilibrium: time-averaged values of vorticity from the NN_a-based and the table-based simulations 42
4.18 14-cm, transient: distribution of relative error (%) between pressure signals from the NN_b-based and the table-based simulations 43
4.19 14-cm, transient: distribution of pressure fluctuation correlation between the NN_b-based and the table-based simulations 44
4.20 14-cm, transient: the distribution of the pressure fluctuation rms ratio calculated from the NN_b-based simulation (4.20b) to the table-based (4.20a) one . 45
4.21 14-cm, transient: the NN_b-based and the table-based simulations comparison of pressure signal at two different points on the top wall 46
4.22 14-cm, transient: the NN_b-based and the table-based simulations comparison of pressure signal at two different points in the combustor 47
4.23 14-cm, transient: comparison of pressure mean, the first, and the second mode shapes between NN_b-based and table-based simulations (last 4 ms) 48
4.24 14-cm, transient: comparison of radial-averaged mRI and RI between the NN_a-based and the table-based simulations 49
4.25 14-cm, transient: comparison of RI and mRI between the NN_b-based and the table-based simulations 49
4.26 14-cm, transient: pressure snapshots from the NN_b-based and the table-based simulations 51
4.27 14-cm, transient: axial velocity snapshots from the NN_b-based and the table-based simulations 52
4.28 14-cm, transient: vorticity snapshots from the NN_b-based and the table-based simulations 53
4.29 14-cm, transient: mixture fraction snapshots from the NN_b-based and the table-based simulations 54
4.30 14-cm, transient: progress variable snapshots from the NN_b-based and the table-based simulations 55
4.31 14-cm, transient: PVRR snapshots from the NN_b-based and the table-based simulations 56
4.32 14-cm, transient: temperature snapshots from the NN_b-based and the table-based simulations 57
4.33 9-cm case: distribution of relative error (%) between pressure signals calculated from the NN_b-based and the table-based simulations 58
4.34 9-cm case: pressure fluctuation correlation between calculated from the NN_b-based and the table-based simulations 59
4.35 9-cm case: the distribution of pressure fluctuation rms ratio calculated from NN_b-based (4.35b) to the one calculated from table-based (4.35a) simulations 60

4.36 9-cm case: comparison of pressure signals on the wall, at pressure antinode and near the nozzle, between the NN_b-based and the table-based simulations 61
4.37 9-cm case: comparison of pressure mean and the first and second mode shape between NN_b-based and table-based simulations 62
4.38 9-cm case: comparison ofmRI from the NN_b-based and the table-based simulations 63
4.39 9-cm case: comparison of RI afrom the NN_b-based and the table-based simulations 64

5.1 The NN development process 69
5.2 Coverage of the flamelet table by training set 71
5.3 Comparison of NN-based models and the flamelet table data of internal energy and flame temperature 76
5.4 Comparison of $\widetilde{T_f}$ between NN-based and table-based flamelet models . . . 77
5.5 PVRR NN performance analysis 79
5.6 Comparison of PVRR between NN-based and table-based flamelet models . 80
5.7 Comparison of $\widetilde{e_f}$ between NN-based and table-based flamelet models 82
5.8 Comparison of $\widetilde{\lambda}$ between NN-based and table-based flamelet models 83
5.9 Comparison of $\widetilde{\gamma}$ between NN-based and table-based flamelet models 83
5.10 Comparison of $\widetilde{a}_\gamma$ between NN-based and table-based flamelet models 84
5.11 Comparison of $\widetilde{R}$ between NN-based and table-based flamelet models 84
5.12 $\widetilde{T_f}$: comparison of NN and table between P-NN and PA-NN 86
5.13 $\widetilde{\lambda}$: comparison of NN and table between P-NN and PA-NN 86
5.14 $\widetilde{\gamma}$: comparison of NN and table between P-NN and PA-NN 87
5.15 $\widetilde{a}_\gamma$: comparison of NN and table between P-NN and PA-NN 87
5.16 $\widetilde{e_f}$: comparison of NN and table between P-NN and PA-NN 88
5.17 $\widetilde{R}$: comparison of NN and table between P-NN and PA-NN 88
5.18 TR: comparison of pressure time signals at representative points 89
5.19 DE: distribution of relative error (%) between NN-base and table-based simulations 90
5.20 DE: distribution of pressure signal fluctuation correlation between NN-based and table-based simulations 91
5.21 DE: comparison of pressure time signals at representative points 92
5.22 DE: comparison of pressure mean, the first mode and its phase, and the second mode shapes between NN-based and table-based simulations along the centerline 93
5.23 DE: the rms of pressure signal fluctuations are compared between the simulations based on NN (5.23b) and table(5.23a). 94
5.24 DE: the mRI from the NN-based and the table-based simulations are compared 95
5.25 DE: time-averaged values of flow temperature from the NN-based and the table-based simulations 96
5.26 DE: time-averaged values of density from the NN-based and the table-based simulations 96
5.27 DE: time-averaged values of PVRR from the NN-based and the table-based simulations 97

5.28 DE: time-averaged values of axial velocity from the NN-based and the table-based simulations . . . 97
5.29 TG: distribution of relative error (%) between NN-based and table-based simulations . . . 98
5.30 TG: distribution of pressure signal fluctuation correlation between NN-based and table-based simulations . . . 99
5.31 TG: comparison of pressure time signals at representative points . . . 100
5.32 TG: comparison of pressure mean, the first mode and its phase, and the second mode shapes between NN-based and table-based simulations along the centerline 101
5.33 TG: the rms of pressure signal fluctuations are compared between the simulations based on NN (5.33b) and table(5.33a) . . . 102
5.34 TG: the *mRI* from the NN-based and the table-based simulations are compared 103
5.35 TG: density . . . 104
5.36 TG: axial velocity . . . 105
5.37 TG: temperature . . . 106
5.38 TG: PVRR . . . 107
5.39 TG: mixture ratio . . . 108
5.40 TG: vorticity . . . 109
5.41 9-cm case: distribution of relative error (%) between pressure signals calculated from the NN-based and the table-based simulations . . . 110
5.42 9-cm case: fluctuation correlation between pressure signals calculated from the NN-based and the table-based simulations . . . 111
5.43 9-cm case: the distribution of the ratio of the rms of the pressure signal from NN-based (5.43b) to the one from table-based (5.43a) simulations . . . 112
5.44 9-cm case: comparison of pressure signals at two representative point and their FFT, between the NN-based and the table-based simulations . . . 113
5.45 9-cm case: comparison of pressure mean and the first and second mode shape between NN-based and table-based simulations . . . 114
5.46 9-cm case: comparison of *mRI* from the NN-based and the table-based simulations . . . 115

LIST OF TABLES

Page

4.1 Comparison of relative MSE (%) results for NN_a and NN_b on all data in the flamelet table-based CFD 26
4.2 Error analysis summary for the 14-cm oxidizer post configuration test base for dynamic equilibrium and transient cases 31
4.3 CPU time per time step between two consecutive time samples statistics comparison among table-based, NN_a-based, and NN_b-based simulations for 14-cm dynamic equilibrium case 65

5.1 Selected structure for each NN for the flame variables 73
5.2 Summary of relative error and NN structure of P-NN 85

ACKNOWLEDGMENTS

I would like to express my sincere gratitude toward my advisors, Professor William Sirignano and Professor Athanasios Sideris, who patiently guided me through this journey. Their immense knowledge and experience have always inspired me in my academic research, and their persistent encouragement and generous supports helped me to achieve what I am presenting in this dissertation. I am very thankful to Professor Tryphon Georgiouand Professor Feng Liu for kindly participating on my dissertation committee and for all I learned from them during my years at UCI.

I am very thankful to Dr. Tuan Minh Nguyen, whose mentorship and support as the senior labmate helped me to overcome obstacles in my Ph.D. journey. I would also like to thank my current and former labmates, Dr. Pavel Popov, Dr. Arash Zandian, Dr. Albert Jorda Juanos, and Jordi Poblador-Ibanez.

I am very thankful to my family and friends for all their support and encouragement. I am also very grateful to my husband, Dr. Peyman Nazari, for his love, understanding, and support in every possible way during my pursuit of Ph.D degree.

I would also want to thank the Air Force Office of Scientific Research for their support for this work and Dr. Mitat Birkan as the scientific officer.

VITA

Zeinab Shadram

EDUCATION

Doctor of Philosophy in Mechanical and Aerospace Engineering **2021**
University of California, Irvine *Irvine, CA*

Master of Science in Aerospace Engineering **2014**
Sharif University of Technology *Tehran, Iran*

Bachelor of Science in Aerospace Engineering **2011**
Sharif University of Technology *Tehran, Iran*

RESEARCH EXPERIENCE

Graduate Research Assistant **2015–2021**
University of California, Irvine *Irvine, California*

Student Research Assistant **2009–2014**
Sharif University of Technology *Tehran, Iran*

TEACHING EXPERIENCE

Teaching Assistant **2016–2021**
University of California, Irvine *Irvine, California*

Teaching Assistant **2011–2012**
Sharif University of Technology *Tehran, Iran*

REFEREED JOURNAL PUBLICATIONS

Neural Network Flame Closure for a Turbulent Combustor with Unsteady Pressure **2020**
AIAA Journal

Physics-Aware Neural Network Flame Closure for Combustion Instability Modeling in a Single-Injector Engine **2021**
Submitted to Combustion and Flame

REFEREED CONFERENCE PUBLICATIONS

Neural Network Closure Models for Estimating Flame Variables in a Liquid-propellant Rocket Engine **Jan 2019**
AIAA Scitech 2019 Forum

A Neural Network-Based Flamelet Model for a Liquid Propellant Rocket Engine with Partially Premixed Flame **Mar 2019**
11th National Combustion Meeting

ABSTRACT OF THE DISSERTATION

Neural Network Closure Modeling of Longitudinal Combustion Instability in a Liquid-propellant Rocket Engine

By

Zeinab Shadram

Doctor of Philosophy in Mechanical and Aerospace Engineering

University of California, Irvine, 2021

Professor William A. Sirignano, Chair

In this work, neural network (NN)-based models are generated to replace flamelet tables for sub-grid modeling in large-eddy simulations of a single-injector liquid-propellant rocket engine. The NN training process presents an extraordinary challenge. The multi-dimensional combustion instability problem involves multi-scale lengths and characteristic times in an unsteady flow problem with nonlinear acoustics, addressing both transient and dynamic-equilibrium behaviors, superimposed on a turbulent reacting flow with very narrow, moving flame regions. Accurate interpolation between the points of the training data becomes vital.

Computationally efficient and accurate flamelet models for a turbulent combustor are needed for useful large eddy simulations (LES). Promise is offered through the use of deep learning NN. Here, a well-studied configuration through prior LES and experiment is used but now with NN providing the sub-grid model for the flamelets. It is of special interest to extend the use of NN modeling for unsteady behavior of mean pressure and velocity fields.

Two different approaches for NN design are proposed, based on the source of training data used in the NN development. In the first approach, data in the flamelet libraries are used as a source for training NNs to replace those flamelet libraries in the CFD simulation of a turbulent diffusion flame with unsteady pressure. The models are validated on those libraries

and verified by being implemented into CFD simulations. Both transient and dynamic equilibrium oscillatory conditions are considered by varying initial conditions of the simulations. Two different geometrical configurations are also tested. The NN-based simulations are favorably compared with their table-based counterparts.

The NNs proposed based on the second approach are trained based on data processed from a few CFD simulations of a single-injector liquid-propellant rocket engine with different dynamical configurations to reproduce the information stored in a flamelet table. The training set is also enriched by data from the physical characteristics and considerations of the combustion model. Flame temperature is used as an extra input for other flame variables to improve the NN-based model accuracy and physical consistency. The trained NNs are first tested offline on the flamelet table. These physics-aware NN-based closure models are successfully implemented into CFD simulations and verified by being tested on various dynamical configurations. The results from those tests are in good agreement with their counterpart table-based CFD simulations.

Chapter 1

Introduction

Combustion instability is an acoustical phenomenon caused by the high rate of energy release that increases pressure oscillation amplitude inside a combustion chamber; i.e., combustion excites and sustains an unstable high-amplitude pressure oscillation, which can be destructive. While the pressure in most rockets and jet engines can oscillate, their unstable behaviors can differ. The issue of combustion instabilities became a major topic of study during the 1960s, due to the instabilities found in the Rocketdyne F1 engine, which was a part of the Apollo program [1, 2]. The study and theorization of liquid-propellant rocket engine (LPRE) combustion instabilities have been a major research subject for decades [3, 4, 5, 6]. One key component of these studies is the numerical analysis done through computational fluid dynamics (CFD) simulations, which requires the development of descriptive models that can represent a complicated phenomenon, such as combustion in a turbulent reacting flow with unsteady pressure. A vast amount of research has been conducted to generate such descriptive models [7, 8, 9, 10, 11, 12].

The configuration of interest in this work is a single-injector LPRE. Purdue University's Continuously Variable Resonant Combustor (CVRC) experiment provides a fundamental

test case [13, 14, 15]. CVRC is a combustion chamber with a single-element injector/oxidizer post, in which the oxidizer post length can be varied, resulting in configurations with different stability characteristics. Although it uses gaseous injection, the CVRC is an experiment that is widely accepted as a valid benchmark for computational methods that address combustion instability in liquid-propellant rocket engines.

Current computational capabilities for reacting flows in realistic combustion chambers do not allow for resolution of the smallest scales of importance. Therefore, large eddy simulations (LES) rather than direct numerical simulations (DNS) are common [16, 17, 18, 19]. This requires models for sub-grid phenomena, especially for the combustion process. For gaseous reactants, the flamelet model ([20, 21]) enjoys popularity. The sub-grid model has been employed through a look-up table approach ([22, 23, 24]) that avoids the need for a computational time step determined by the chemical kinetics time scales, which typically are shorter than the ones from the numerically resolved physics. Nguyen et al. developed a hybrid LES/Reynolds-Averaged Navier-Stokes (RANS) code, capturing combustion instabilities in CVRC at a much lower computational cost compared to prior works [22]. The results from [22] were compared favorably with experimental data and numerical simulations of the CVRC experiment developed at Purdue University [25, 14]. Implementing the flamelet model was a key step in reducing the computational cost. The schematic of the developed code by [22], which is used in this work, is provided in Figure 1.1. The block diagram shows how the flamelet model interacts with other sub-blocks of the code.

Flamelet libraries are essentially sets of input/output blocks that can be isolated and replaced by neural network (NN)-based models. Thus, the flamelet model provides a proper stepping stone for exploring the use of machine learning in combustion studies. An ultimate goal of utilizing machine learning in combustion instability studies is to use the data from experiments and detailed computationally expensive CFD simulations to develop lower-cost NN-based descriptive sub-grid models.

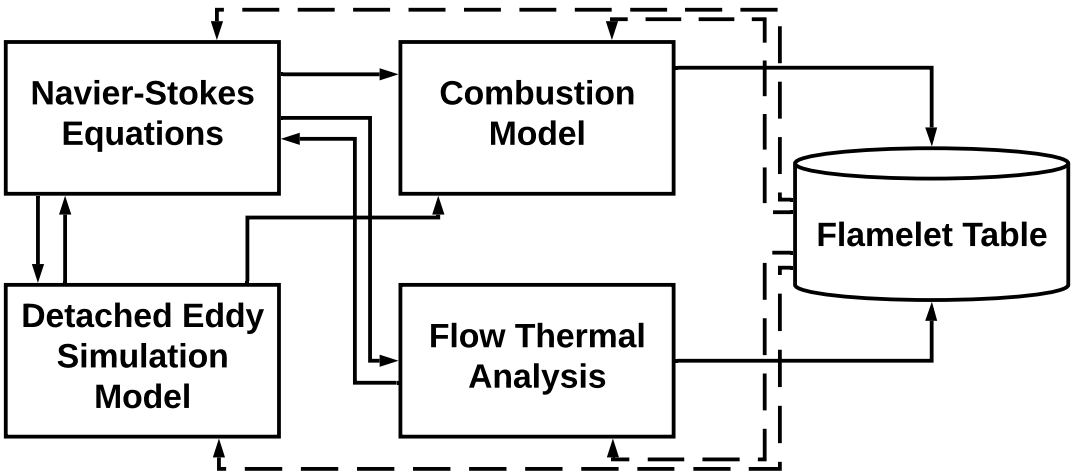

Figure 1.1: Top level architecture of CFD code

1.1 Neural Networks

Neural networks have been introduced to fluid mechanics and combustion for many years now. Machine learning techniques have been used in fluid mechanics for different purposes such as clustering, classification, dimensionality reduction, and regression analysis. Brunton et al. [26] provides a survey of different subfields of machine learning techniques and their application in fluid mechanics. Applications of data-driven methods in modeling turbulence were surveyed in [27].

NNs can be used for dividing a set of data into groups that have similar patterns. If the groups are known in advance, the machine learning classification algorithm is used to assign each data to the proper group. The algorithm learns to do that, following a set of examples that we provide to it at the training stage. Essentially, it assigns any new data to a class with training examples most similar to it. If the groups are not known, the machine learning clustering algorithm assigns a set of data into different clusters by finding similar patterns in that set of data. Machine learning algorithms are also used for dimensionality reduction to transform data from an originally high-dimensional space into a surrogate low-dimensional one such that the new space retains the important properties of the original data. The

application of machine learning that is of interest of this work is regression. Regression can be used for developing closure models for both static (quasi-steady) and dynamic systems. As for the dynamic models, recursive NNs were utilized to predict the unsteady boundary-layer development [28]. The focus of this work is utilizing NNs for developing closure models for the flamelet model as a quasi-steady system. NN closure models have been incorporated for turbulence flow modeling in [29, 30, 31, 32, 33]. In the following, we discuss the main contributions of NNs in turbulent combustion.

Clustering is used mainly in the tabulation of probability density function (pdf)-based turbulent. In [34], it was tried to address the limitations in pdf-based turbulent combustion using machine learning to reduce the required memory for those models. The self-organizing maps (SOM) algorithm [35] was used to cluster the pdf tables into several parts; subsequently [34] generated a NN for each of the clusters as a local function for thermo-chemical quantities. Their algorithm was tested on a turbulent jet diffusion flame in RANS and LES simulations. The pdf-based model in this work takes the combustion state variables and enthalpy as inputs to generate density, temperature, and mass fractions of 20 species. This model is independent of pressure and is not proper for combustion instability analysis. SOM-based clustering has been successfully implemented within the context of combustion modeling and chemistry [36, 37]. Also, [38] used a NN to predict combustion instabilities in a gas turbine engine. Clustering methods are also used in the visualization of flow with turbulent combustion. In [39], a clustering approach was proposed for the segmentation, visualization, and potentially the tracking of regions of interest in large tensor data based on specified parameters such as strain tensor value. In [40], K-means, a clustering algorithm [41], was used to assign thermo-chemical variables (temperature and 11 mass fractions) into different clusters. Then, NNs were used to develop a model for the time evolution of chemistry. The NN in that work has four dense hidden layers, leading to a neural network with 179,851 weights and biases. The method was tested on a non-premixed syngas oxy-flame at a fixed

low pressure ($\approx$ 300 kPa). After the clustering, [40] used the principal component analysis (PCA) algorithm to reduce the dimensionality of each cluster.

Generally, PCA algorithms are used for chemistry reduction. A chemistry dimensionality reduction approach was developed in [42] and applied in the DNS of a turbulent non-premixed syngas oxy-flame interacting with a cooled wall. The reduced chemistry and temperature subsequently were used as inputs of a NN to predict the corresponding chemical sources. PCA approach was also used by [43] for dimensionality reduction as a post-processing step in DNS of an opposed-jet hydrogen/air diffusion flame. Two different PCA-based methods for an unsteady perfectly stirred reactor were developed in [44, 45] based on the use of local and global combustion data in a turbulent reacting flow. They showed the ability of PCA-based combustion models in capturing the behavior from flamelet-like flames to distributed reaction regimes. Similar work on the dimensionality reduction of turbulent combustion was conducted in [46, 47, 48, 49, 50].

The development of closure models is categorized under the regression subfield of machine learning, in which a mapping is learned to transfer a set of inputs to the desired outputs. Earlier, in the 1990s, NNs were successfully used to represent chemical source terms in a turbulent diffusion flame, which was a chemical system of H2/C02/02 mixtures using a three-step reduced chemical mechanism [51]. This relatively simple case was one of the pioneering works in which NN was implemented for combustion modeling. That work was continued upon in [52] with a more comprehensive discussion on the feasibility of using NN in modeling chemical mechanisms. They showed that prediction of the turbulent jet flow field and H2/CO2 diffusion flame characteristics using the neural network approach was in good agreement with those obtained using other methods and the experimental data. In addition, [53] introduced an integrated pdf/neural network approach for the simulation of simple turbulent diffusion flames leading to a significant reduction in computer memory.

They concluded that the performance of the neural network model strongly depends on the selection of the sufficiently representative training set.

More recently, NNs were also used for tabulation of methane/air combustion mechanisms in [36], and the model was implemented into turbulent non-premixed Sydney flame L. Training data was generated by spanning the composition space of a family of non-premixed flames in an artificial set-up, i.e. a set of laminar flamelets with an artificial pilot in mixture fraction space to emulate ignition. Prior to this, [54] used NNs for the representation of a reduced CH4 combustion mechanism, including 13 species, to compute the evolution of mass fractions and another one for density and temperature as functions of the mass fractions. More recently, [55] developed NN models that generate the evolution of mass fractions based on themselves and enthalpy. The model was implemented into Sandia flame D, E, and F. [56] from the same research group, implemented an NN-based tabulation into Sandia flame L simulation.

Moreover, convolutional NNs have been developed to estimate unfiltered variables from filtered ones from LES simulation with turbulent combustion [57]. Convolutional NNs have also been used to estimate the sub-grid reaction scale rates [58]. Filtered progress variable source term was modeled through deep NN using data from a DNS of a low Mach number swirl burner configuration of a fuel lean methane/air premixed flame at a fixed pressure, and the model was implemented successfully into LES analysis [59]. The modeling of sub-grid quantities such as scalar dissipation rate and mixture fraction for spray flame were also discussed in [60, 61]. A DNS simulation was used as the source of training, and mixing quantities were modeled as a mapping of turbulent flow variables with a dense NN consisting of 4 hidden layers with 500 neurons in each layer. To model flamelet in LES framework for a spray flame, [62] developed a deep set of neural networks. They classified the species into different groups based on their correlation to one another and designed a NN for each class to replace the look-up flamelet table.

Menon and co-workers ([63, 64]) used NN for the coupling of the linear eddy mixing (LEM) sub-grid model with the LES. Furthermore, [65, 66, 67] developed NN-based models utilizing the data from flamelet tables and validated their results by comparing CFD simulations based on the flamelet table and the ones based on the NN representation of the flamelet model. In particular, the NN-based flamelet model in [67] has been developed to be used in the Sandia flame D simulation. NNs have been used in [65] for representing a flamelet model in a stably burning flame in Sydney bluff-body swirl-stabilized flame. Among the findings in [65] are that: (1) using NNs requires much less memory than a look-up flamelet table, (2) NNs can obtain a smoother flow field solution, and (3) NNs require higher computational cost than the flamelet table, yet the computational cost of using NNs is still significantly lower than solving the flame equations.

The literature discusses a wide variety of utilization of machine learning in turbulent combustion. However, it has been mainly focused on developing NN-based models for jet flames at a low range fixed pressure, and the coupling of acoustics with the turbulent flame was not discussed. The work presented here focuses on the application of deep learning in turbulent flow with high range unsteady pressure. In this work, we propose NN-based models that are successfully implemented in the CFD simulation of an unstable single-element combustor, in which a highly nonlinear and multidimensional behavior caused by the coupling of acoustics, turbulent internal flow, and combustion is captured.

1.2 Motivation

In today's research world, the massive availability of data has one eminent benefit, which allows the utilization of machine learning to generate data-driven models. Recently there is growing attention toward the coalition of machine learning and turbulent combustion. By means of machine learning and exploitation of this data, it is possible to explore potentially

more descriptive models that help us achieve a better understanding of any phenomena. Particularly, in the study of combustion instability, computationally efficient and accurate flame models are needed for the LES of a turbulent combustor. We envision that future versions of the flamelet model might best be introduced through the use of NNs, allowing nonlinear interpolation that is not easily obtained with the table, which now uses linear interpolation. NN can also allow both experimental and theoretical data to be used.

This work discusses two main approaches. In a nutshell, for the first approach, we used the flamelet table as the training source, while in the second approach, the data from CFD is the source for training of NNs. In the following, each of the two approaches is explained in more detail.

Approach 1: we use the data from the look-up table for training the NNs. In attempting to study the capability of the NNs not only to reproduce combustion behavior but also its integration into CFD calculation. Here, we show that it is possible to design and train neural networks based on stand-alone combustion models and implement them inside different CFD configurations.

Approach 2: data from CFD simulation is used for training the NN-based closure models. Training a NN on CFD data has been suggested as future research in our previous work [68, 69], where only offline tests were analyzed both with single output and multiple outputs NNs. The challenge here comes from the fact that in a CFD simulation of a single configuration, only a small portion (a manifold) of the flamelet space is used; thus, reconstructing the whole flamelet space may be accomplished by training NNs based on data from multiple simulations. Here, we train the NNs on CFD data, which only observes parts of the flamelet space, and verify our model by testing the NNs on a number of different simulations. The designed NNs are also tested on the whole flamelet table library, which includes the unobserved parts as well as the training data.

A key quality in a model used in the combustion instability studies is its capability to capture the coupled relation between pressure and energy-related flame variables such as the progress variable reaction rate (PVRR). Pressure and thus the flame variables change drastically when the instability occurs. The NN training process presents an extraordinary challenge due to the multi-scale lengths and characteristic times in an unsteady flow problem with nonlinear acoustics. The NN models here are successfully implemented in both transient and dynamic-equilibrium behaviors, superimposed on a turbulent reacting flow with very narrow, moving flame regions.

1.3 Outline

A summary on the flamelet model and on our computational testbed is provided in Chapter 2, where different aspects of our computational analysis of the CVRC experiment is discussed. Then, the flamelet model and the challenges in combustion modeling in a system with combustion instability are discussed. A general discussion on the fundamentals of neural network algorithm development is provided in Chapter 3.

The first approach, which is using data from the flamelet table for training the NN-based closure model, is discussed in Chapter 4. The second approach, which is using data from CFD simulation for training NN-based closure model, is discussed in Chapter 5. In both of these chapters, the various facets of the NN development process are provided, and the outputs of the flamelet table with their counterparts in our NN-based models are compared. The functionality of our models are verified by being implemented in different stability and geometry configurations of CVRC CFD simulation. We conclude this work and provide suggestions for future work in Chapter 6.

Chapter 2

Background on Combustion Instability Analysis

This work is developed in pursuit of designing NN-based closure model that are suitable for being used as flame closure model in combustion instability studies.

2.1 Numerical Scheme

The CVRC experiment is a single-injector co-axial dump combustor [70]. A schematic of the CVRC experiment is shown in Figure 2.1. It is an unstable configuration with a variable-length oxidizer post length and a 38-cm combustion chamber. In this configuration, methane is injected through the outer concentric tube at 300 K. The oxidizer, composed of 58% H_2O and 42% O_2, is injected through the inner tube at 1030 K. The equivalence ratio in this globally fuel-lean flow is 0.8, which results from the constant mass flow rate of fuel and oxidizer at 0.027 $\mathrm{kg\,s^{-1}}$ and 0.32 $\mathrm{kg\,s^{-1}}$, respectively. Although the CRVC experiment uses gaseous injection, it is accepted as a valid benchmark for computational methods that

address combustion instability in LPREs. Here, an unstable configuration with a 14-cm oxidizer post length is the main test case; see Figure 2.1. To extend our verification process, a stable configuration is also discussed with a 9-cm oxidizer post length.

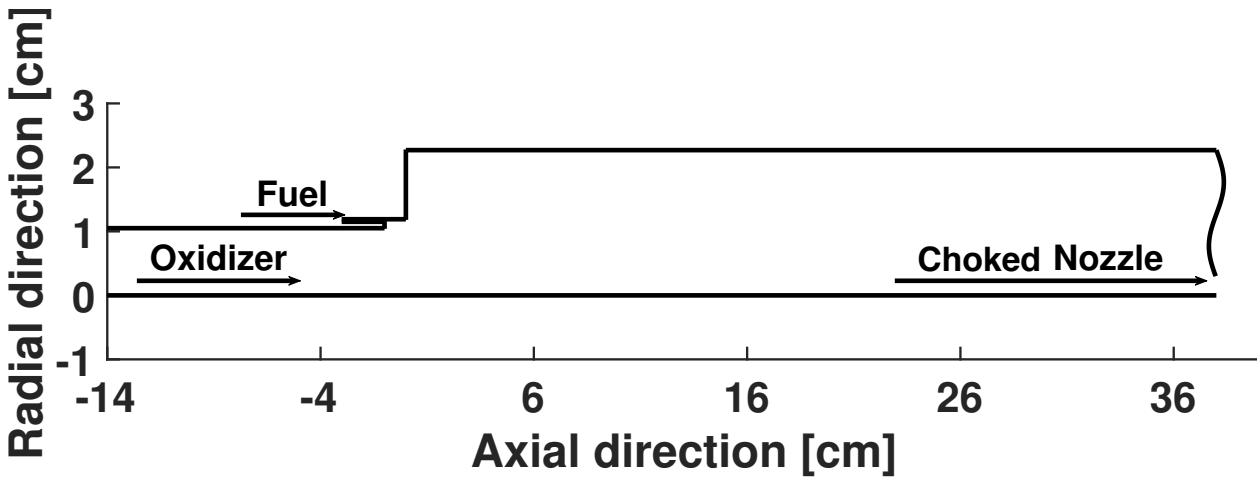

Figure 2.1: Schematic of CVRC configuration

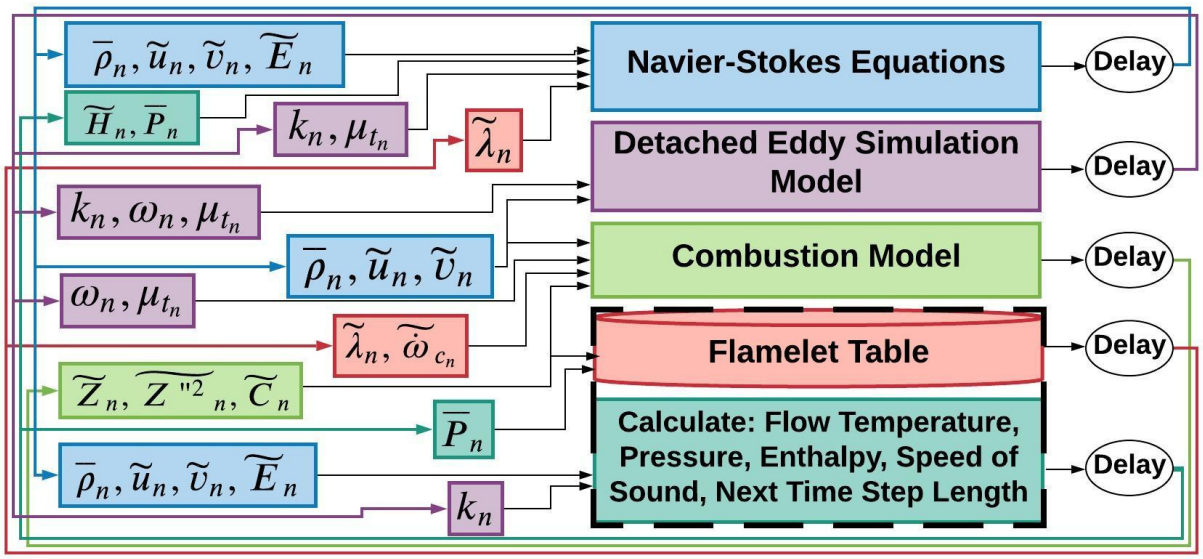

Figure 2.2: Top level architecture of CFD code

Our code [22], which is capable of shock-capturing in the longitudinal mode, is a multi-block, see Figure 2.2, structured finite-difference solver with axisymmetric cylindrical coordinates without imposed swirl. The mesh structure is based on the mesh used in the 3D calculations in [12] and consists of 137,494 grid points. The smallest radial and axial grid sizes are 0.05

mm and 0.2 mm, respectively, which are located around the mixing shear layer or near any walls, and upstream/downstream of the back step, axially. To ensure a high-quality mesh, the maximum grid stretching factor along any direction is 1.05. The entrance-to-throat area ratio is 5. The overall accuracies in time and space are fourth-order and second-order, respectively. At both reactant inlets, a constant mass flow rate boundary condition is implemented using the Navier-Stokes characteristic boundary conditions [71]. Instead of an actual convergent-divergent nozzle computational domain, a computationally efficient short-choked-nozzle [72] outlet boundary condition is used, which leads to a good computational efficiency; this promotes a high amplitude pressure oscillation. The walls are assumed impermeable with the no-slip boundary condition. For the thermal aspect, two different boundary conditions are analyzed; in one case leading to spontaneous instability, the walls are assumed to be adiabatic. The second case assumes an isothermal wall temperature, which leads to triggering instability behavior [23]. A more detailed and discussion on the computational framework is provided in appendix A.

2.2 Flamelet Model

[20] introduced the flamelet concept for turbulent combustion modeling. The flamelet model for turbulent combustion, based on the non-premixed flame physics, has been developed further by [21] for the integration of a sub-grid model with LES. The flamelet model is a sub-grid model, and its raison d'etre is that one cannot afford the grid resolution needed to incorporate combustion details in a DNS that resolves all length and time scales. With the required resolution, the sub-grid model would not be needed. The flamelet model is based on the assumption that time scales for heat and mass diffusion, advection, and strain are larger than the chemical times; thereby, quasi-steadiness for chemistry is used. However, the chemistry is localized in narrow regions, and the stronger assumption of chemical equi-

librium throughout the flow is not employed; i.e., there are narrow flame regions. While using flamelet models results in computational efficiency, they are the product of simplifying assumptions, and they have certain limitations. There are uncertainties associated with presumed sub-grid PDF distributions as well as the progress variable definition. Flamelet theory assumes an axisymmetric strain field, while three-dimensional behavior is commonly found in practice. A single diffusion flamelet occurs with fuel only on one side of the flame and oxygen only on the other side. Experience indicates that combustible mixtures can exist on one or both sides; premixed flames, diffusion flames, and multi-branched flames (e.g., triple flames) can occur. New flamelet models addressing these issues are in development ([73, 74, 75, 76]).

2.3 Combustion Modeling and Challenges

The flamelet approach models the turbulent flame as a collection of laminar flamelets, where the chemical time scales are shorter than the turbulent time scales. Accordingly, the chemistry-related calculation occurs prior to the main flow simulation through a quasi-steady flamelet table for a diffusion flame under normal compressive strain [22, 20, 21]. Decoupling flamelet solution and the resolved LES flow simulation allows the prediction of the complex mechanism at a much lower computational cost, which is the advantage of flamelet modeling ([23]). As shown in Figure 1.1, the inputs to the flamelet model are the flame state variables ($\widetilde{C}$, $\widetilde{Z}$, and $\widetilde{Z''^2}$), and $\overline{P}$. $\widetilde{Z}$ indicates the mixture character at each point. $\widetilde{Z''^2}$ defines the deviation from the mean of $\widetilde{Z}$ and is important for turbulent combustion. Essentially, in turbulent non-premixed modeling, laminar flamelet solutions are convoluted by a subgrid beta probability density function (pdf) of Z to model turbulence-chemistry interaction. The beta pdf parameters are functions of $\widetilde{Z}$ and $\widetilde{Z''^2}$. $\widetilde{C}$ determines how much of the combustion process has been conducted at each time and point in space. A Dirac delta pdf is assumed

to relate C to $\widetilde{C}$ according to the discussions in [21]. The inputs of the flamelet model are collected in $\Psi = [\widetilde{Z}, B, \widetilde{C}, \overline{P}]$, where $B = \frac{\widetilde{Z''^2} - \widetilde{Z}^2}{\widetilde{Z} - \widetilde{Z}^2}$ is a surrogate variable that replaces $\widetilde{Z''^2}$. In the input set, $\overline{P}$ varies between 1 atm and 30 atm, B and $\widetilde{Z}$ range between 0 and 1, and $\widetilde{C}$ varies from 0 to 0.261. The table includes 30 grid points for $\overline{P}$, 85 grid points for $\widetilde{Z}$, 26 grid points for $\widetilde{Z''^2}$, and 156 grid points for $\widetilde{C}$. The output set for this flamelet model is defined as $\Phi = [\widetilde{\dot{\omega}}_C, \widetilde{T}_f, \widetilde{e}_f, \widetilde{R}, \widetilde{\lambda}, \widetilde{\gamma}, \widetilde{a}_\gamma]$. The proposed NN-based models in this work take exactly the same inputs and outputs as the inputs and outputs of the flamelet model stored in Ψ and Φ, respectively. In the CFD structure, flow internal energy along with the above quantities are used to calculate flow temperature and enthalpy. Pressure is calculated based on the ideal gas law after extracting data from the flamelet table in the CFD.

The main difficulty with the flamelet model is that the heat release rate (HRR) becomes a one-dimensional quantity, although embedded in a three-dimensional flow field. Furthermore, in the case of combustion instability, the HRR interactions with turbulence and acoustical phenomena result in extremely nonlinear behaviors. Implementing the flamelet model helps to preserve the multi-scale and highly nonlinear behavior of HRR in the CFD simulation. In the flamelet-based simulation, HRR is not playing a direct role in the governing equation; instead, the PVRR is the variable that affects the governing equations as the source term in the $\widetilde{C}$ transport equation. The flamelet solutions use a complex chemical mechanism (72 reactions with 27 species). HRR relates to the products of all the species PVRRs and their corresponding enthalpies; in contrast, the progress variable, defined as the summation of CO2 and H2, only represents the major global chemical reactions. HRR accounts for more detailed (including less significant) reactions than the PVRR, which indicates the progress of the global methane reaction, using only simple global oxidation chemistry. However, it still has similar multi-dimensional, multi-scale, and highly nonlinear behavior, yet less severe and less costly to model than HRR.

2.3.1 Rayleigh Index as an Instability Criterion

The most important cause of the high-frequency instability is the coupling between the HRR and the acoustic pressure wave. The Rayleigh Index (RI) measures this coupling based on the HRR and pressure fluctuation correlation determining if the HRR drives or damps the pressure wave. The time-averaged local Rayleigh Index is defined over a time period (τ), typically few cycles, starting from an initial time t_o as:

$$RI = \frac{1}{\tau}\int_{t_o}^{t_o+\tau} \frac{\widetilde{\gamma}+1}{\widetilde{\gamma}} \times \frac{p'}{\widehat{P}} \times \frac{HRR'}{\widehat{HRR}} dt \tag{2.1}$$

where p' and HRR' are the local fluctuations in $\overline{P}$ and HRR, respectively [22]. Also, $\widehat{P}$ and $\widehat{HRR}$ are the global time averages of $\overline{P}$ and HRR. A positive (negative) value of RI conveys that the pressure oscillation is driven (damped) by HRR. The importance of RI led us to discuss a similar measure for PVRR oscillations by replacing HRR with $\widetilde{\dot{\omega}}_C$ in Eq. (2.1) to get a modified Rayleigh Index (mRI).

Our analysis in [66] showed that the mRI resembles the same behavior as RI. The time-averaged local mRI is defined in Eq. (2.2) over a time period (τ) which is typically few cycles; where p', and $\dot{\omega}'_C$ are the local fluctuations in $\overline{P}$ and PVRR, respectively. Also, $\widehat{\dot{\omega}}_C$ is the global time average of PVRR.

$$mRI = \frac{1}{\tau}\int_{t_o}^{t_o+\tau} \frac{\widetilde{\gamma}+1}{\widetilde{\gamma}} \times \frac{p'}{\widehat{P}} \times \frac{\dot{\omega}'_C}{\widehat{\dot{\omega}}_C} dt \tag{2.2}$$

Chapter 3

Neural Networks

Artificial Neural networks (NN) are powerful computational systems, which are a subset of the machine learning field. Machine learning includes all the computer algorithms that use data to generate a model or conduct a task. Machine learning algorithms are divided into two major categories of supervised and unsupervised learning. If the algorithm learns from a set of data (training examples) that have an input-output nature, the algorithm is categorized under the supervised learning approaches. There, the algorithm needs to generate an output when an input is provided to it, following what it had learned from those examples. For the unsupervised approach, the training examples are only inputs, i.e. no specified output set is provided for the system. The machine learning algorithm is developed to find a pattern or structure in the input set. Although it is very useful to find patterns among sets of data, the interest of this work is on the supervised learning approaches. The algorithm learns a function that maps an input set to an output set. The supervised learning approaches are great for developing models for complicated physical phenomena that we could not have before based on our knowledge-based approaches. Deep NNs are one of the most widely used machine learning structures with supervised learning approaches. In this work, we use deep

NN to develop flame closure models for the modeling of combustion instabilities in LPREs. Next, we introduce the NNs and explain their development process.

3.1 Introduction to Neural Networks

The structure of a general feed-forward deep NN with a single output is shown in Figure 3.1 and Figure 3.2.

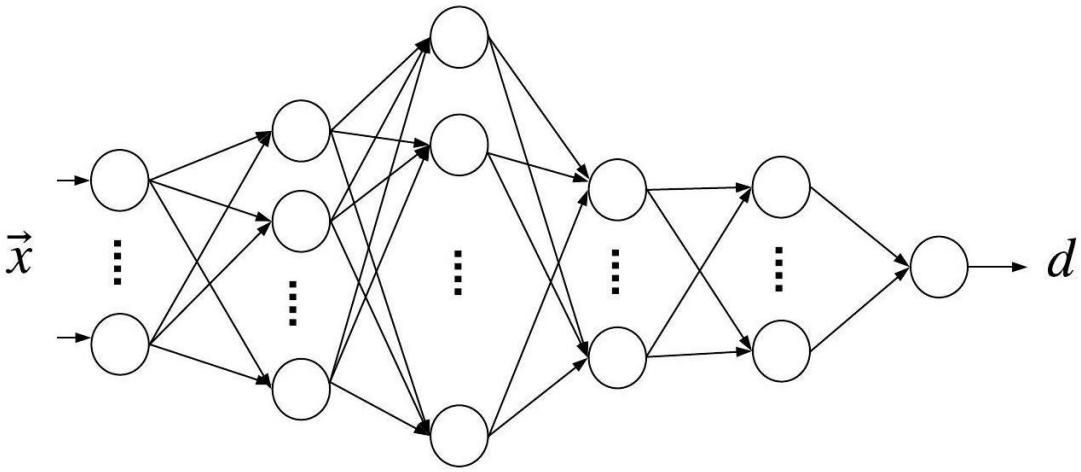

Figure 3.1: Single-output NN structure

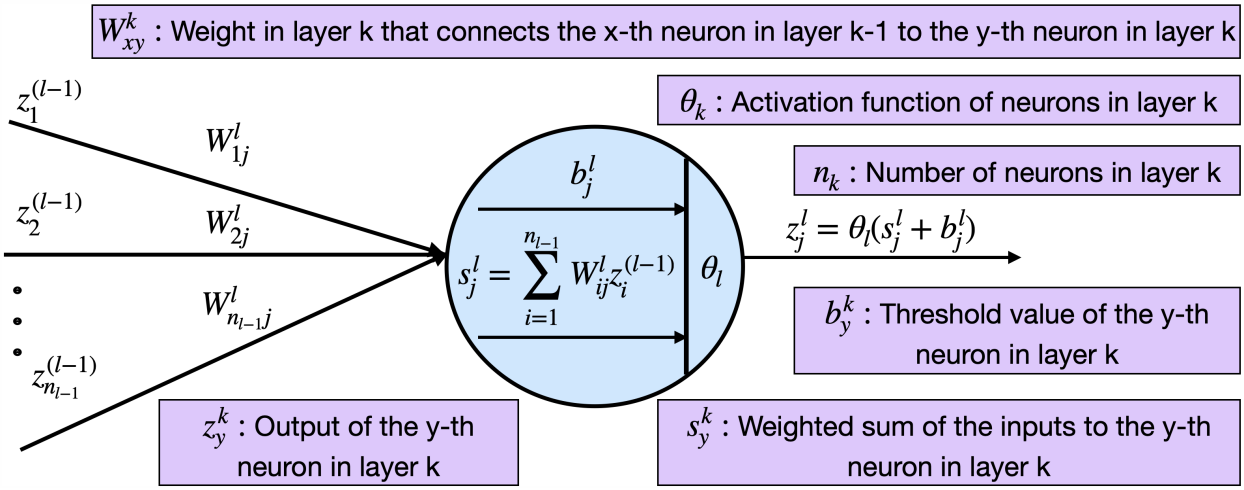

Figure 3.2: Schematic of a neuron as a computing unit in the NN

A NN is a computational unit that replaces an input/output block in a system implementing its original task. After training, the NN learns to perform a task based on input-output examples without knowing the function that maps the inputs to the outputs of the example set. A deep NN contains a series of layers, each of which has several nodes (neurons). Each neuron gets a linear combination of the outputs from neurons in the previous layer as its input, and provides an output, i.e., a specific nonlinear function (activation) of its input used for the next-layer calculations.

The objective of the training process is to find the coefficients of those linear combinations, i.e., the weights, by minimizing a cost function that is defined based on the application of the NN. The NNs that are used for mapping approximation fall under the regression application. They also can be used for clustering and classification. The focus of this work is on the regression type NNs. The commonly used cost function for this application is the least squared error. During the training process, an iterative optimization problem is solved, in which the mean squared of the absolute error between NN outputs and the originally provided examples, i.e. the training data, is minimized over the parameters (weights) of the NN.

3.1.1 Overfitting

If the training process is overextended, typically, the NN performance is only good for the training set; this phenomenon is called overfitting. There are different approaches that can be used to avoid this [77]:

- **Cross-validation:** A validation error is computed on an independent set of samples and used to monitor overfitting and stop training accordingly.

- **Regularization:** A hyperparameter is used to add a penalty to the cost function, this is a common method for solving ill-posed problems and preventing overfitting.

Therefore, providing an appropriate validation set besides the training set is a key step in the NN development process. Also, tuning for the right hyperparameter contributes to having a NN model. The optimal NN weights are obtained as those minimizing the error on the validation set with good generalization properties.

3.1.2 NN Development Process

The NN design and development occur with a sequence of different tasks. First, one should design the structure of the NN by deciding the number of layers and the number of neurons in each layer in the NN. The number of neurons in the first and last layers are selected based on the dimension of input and output vectors, respectively. The layers between the input and output layers are called hidden layers. Typically, the number of hidden layers and their neurons are selected based on experience and the previously successful NN developed for a similar problem.

Another task is to select a proper set of data to serve as the training and validation sets. This data should be rich enough to present the dynamic of the system that is being modeled. A too-large example set makes the training process computationally expensive. However, if the training set is not representative, the NN would not work properly in the general case. The inputs and outputs are standardized before applied to the NN by being centered around their mean and normalized by their standard deviation to improve training performance [77].

The training process is conducted through an iterative algorithm which is called Backpropagation. This algorithm propagates the gradient of the loss function to the weights of the layers prior to the output layer. The Backpropagation algorithm and its attributes are dis-

cussed in Sec. 3.2. Tuning the parameters that control the learning process through this algorithm is another step in the NN development process.

After the NN development, it is crucial that the NN be tested on various cases to measure the performance and robustness of the proposed NN-based model.

3.2 The Learning Algorithm

As discussed above, developing the NN is finalized by finding the weights that connect the neurons of each two consecutive layers. The weights are calculated by minimizing the mean least square difference between the output samples and the outputs of the NN models. The optimization problem is solved through the iterative Backpropagation algorithm [78, 79]. The cost function of the regression NN is defined as:

$$R = \frac{1}{N}\sum_{i=1}^{N}(d_i - y_i)^2 \tag{3.1}$$

where d_i are the sample outputs associated to an input x_i, and y_i the associated output calculated by the NN that is being trained. Here, the cost function is denoted as R, and N is the number of samples in the training set. Following the first-order necessary condition of optimization, to find the right weight in each layer

$$\frac{\partial R}{\partial W_l} = 0 \Rightarrow \frac{1}{2N}\sum_{i=1}^{N}(d_i - y_i)\frac{\partial y_i}{\partial W_l} = 0 \tag{3.2}$$

for W_l which is the weight matrix of layer l. The Backpropagation algorithm propagates the $\frac{\partial y_i}{\partial W_l}$ in Eq. (3.2) between layers in a feedback path, going from the last layer L to layer 1,

which are the output through input layers. This iterative algorithm starts from assigning a random initialization to the weights, calculating the cost function, and in each iteration reducing the cost in the direction of its gradients, i.e. $\frac{\partial R}{\partial W_l}$, with a step size that is called learning rate.

$$W_l(k+1) = W_l(k) + \alpha \frac{\partial R(W_1, W_2, ..., W_L)}{\partial W_l} \tag{3.3}$$

The Eq. (3.3) is a classic iterative optimization method which is called stochastic gradient descent (SGD) [80]. In deep NN design, the SGD algorithm can be improved by using adaptive learning rates. A large learning rate causes the algorithm to diverge, and a small one increases the computational cost by slowing down the process. A comprehensive discussion on SGD algorithms can be found in [81].

RMSProp [82], which is abbreviated from root mean square propagation, is a well-known adaptive update rule, in which the learning rate for a weight is divided in each iteration by a running average of the magnitudes of recent gradients for that weight. This method is shown to be successful in different applications, such as our published work [66]. Adaptive moment estimation (Adam) is an updated version of the RMSProp method, in which in addition to the running average of the first gradient, the second moment of the gradients are used. Great accuracy can be achieved with the Adam update rule, and it is implemented in our work which is discussed in Sec. 5.

The initialization of the weights can be done through different methods. However, [83] showed that using the Xavier algorithm can contribute to designing a NN with better performance. The Xavier initialization picks the weights such that the variances of the activation functions are the same across every layer to prevent the gradient from becoming ill-conditioned.

Chapter 4

Neural-Network-based Closure Model For CVRC: Learning From Flamelet Table Data

The objective of our work is to develop NN-based closure models suitable for studying combustion instability. [1] The key factor in such a model is the capability of capturing the coupled relation between pressure and flame variables, specifically PVRR and HRR. Combustion instability leads to a considerably huge change in pressure, which affects the flame behavior. Thus, it requires the flamelet table to cover a large range of pressure; in fact, [22] needed to generate a flamelet table that takes pressure as an input. As an example, the maximum amount of HRR at 30 atm is 650.5% of the maximum HRR in 8 atm; 8 atm and 30 atm determine the pressure range for the CFD simulation of the CVRC model with a 14-cm oxidizer post after reaching a dynamic equilibrium state. A goal is to develop NNs for calculating flame variables based on a pressure-dependent flamelet model. In this chapter, the approach is to study the data inside the flamelet table directly and develop NNs that

[1] This chapter is adapted from [66], previously published by AIAA Journal

focus on the flamelet model outputs; therefore, the NNs are trained on the flamelet table data that was used in [22]. Several different NN structures are developed. In the most accurate case, separate NNs for each of the flame variables are designed and tested by comparing their output with the output of the similar variable in the table.

4.1 NN Development

The training is performed with the back-propagation method using the RMSProp update rule [77, 84]. We used the Leaky Rectified Linear ($LReLU(x) = max(x, 0.001x)$) activation function in the hidden layers, and linear activation function at the output layer [79]. The NN weights are given the random Xavier initialization [83].

4.1.1 Sample Selection

Enough samples must be provided to capture the problem complexity, while limiting the computational cost of the training. The flame-variable modeling is challenging because it is multi-scale; e.g., PVRR varies from $-284\ \mathrm{kg\,m^{-3}\,s^{-1}}$ to $1.28e5\ \mathrm{kg\,m^{-3}\,s^{-1}}$. Combustion instability occurs from the coupling of high HRR and pressure; thus, the NN must accurately predict points with high HRR. However, the population of these points is relatively smaller than other points, requiring a nonuniform sample selection approach. The samples should be selected to provide a rich data set from high HRR points, with enough samples that should be selected from low HRR points to avoid biasing the NN towards uniformly high HRR values. Based on the designed table resolution, there exist around 10 million cells in the table, which are used for selecting training and validation data sets. Initially, a data set is selected uniformly from the available data in the table, then enriched with more points from higher energy release zones. At this stage, around 500,000 data points are selected

for training, and around 200,000 data points are selected for validation representing 5% and 2% of the available points, respectively. After several iterations, when the learning progress starts to slow down, the partially trained NN is tested on additional data from the table. Then, points with errors higher than a specified bound (e.g., 5%) are added to the training set, and points with errors higher than a lower bound (e.g., 2%) are added to the validation set. Here, different NNs are trained for each output of the table; so, after this step, the training and validation sets are different among outputs. A maximum limit of 1.5 million points (less than 15% of the table data) per set was established after the modification steps.

4.1.2 Network Structure

A general feed-forward NN comprises of layers of different numbers of neurons, which communicate through the weighted links. The focus of this work is to explore the effectiveness of NNs as closure models in turbulent combustion; optimizing the NN structure was beyond the scope of the work. We arrived at the proposed structures in a trial-and-error fashion by increasing the number of neurons in each layer and the number of layers to a point that good accuracy on the training and validation sets is achieved. Our observation is that increasing the number of NN layers leads to better accuracy than increasing the number of neurons in a single layer. Hence, NNs with more layers and fewer neurons on each layer are selected. In particular, two NN structures are introduced here. In the first NN, based on the physical behavior of the flamelet data, the outputs are grouped as G_1: $\widetilde{\dot{\omega}}_C$, G_2: $\widetilde{e}_f$, $\widetilde{R}$, G_3: $\widetilde{T_f}$, $\widetilde{\lambda}$, G_4: $\widetilde{\gamma}$ and G_5: $\widetilde{a}_\gamma$. (G_i denotes a group), and five different NNs (6-layer) are designed, one for each of these sets of outputs, each having 5 hidden layers with 15, 20, 25, 20, and 15 neurons, respectively. The input layer has 4, and the output layer has 1 or 2 neurons depending on the output group. A single output NN with the above structure requires 1771 floating point operations (flop) for data retrieval, while a double-output NN requires 1787 flop. This NN model, referred to as NN_a, requires 8887 flop for overall flame modeling.

Another set of NNs, referred to as NN_b, improves the accuracy by increasing the number of layers and using 7 single-output NNs (8-layer), each with 7 hidden layers with 15, 20, 25, 30, 25, 20, and 15 neurons, respectively. Data retrieval in this NN requires 3326 flop for a single variable and 23,282 flop for all variables. While the structure proposed in NN_b increases the computational cost of retrieving flame data by 162% over NN_a, it gives an approximately 40% reduction in the reconstruction Mean Square Error (MSE).

4.2 NN Performance Analysis

The closure model for flame variables must be implemented inside the CFD. Both the single-output and the multi-output NNs discussed in Sec. 4.1 are implemented to replace the flamelet table. The designed NNs are tested in a stand-alone phase and an in-situ phase. In the stand-alone phase (offline), the NN is tested on all the available table data regardless of whether they are used or not for the training and validation, giving error bounds for each NN output compared to the corresponding table output. The second (online) phase tests whether the NN model can satisfactorily model combustion instability in the single injector LPRE case. Particularly, the highly coupled dynamics governing the LPREs make combustion modeling very sensitive and complicated. Through the online test, NNs are successfully implemented within the CFD, and they are compared with the table-based simulations. In the following, the offline and online test results for NN_a and NN_b are provided.

4.2.1 Offline Test

The NNs are tested on all table data, while at most 15% of the data is used for the training process. Table 4.1 presents the relative MSE for each variable calculated from Eq. (4.1); where x_i is an element from the n elements in the flamelet table, and y_i is the NN-estimated

value for that element.

$$e(\%) = 100 \times \frac{\sqrt{\sum_i^n (y_i - x_i)^2}}{\sqrt{\sum_i^n x_i^2}} \tag{4.1}$$

Table 4.1: Comparison of relative MSE (%) results for NN_a and NN_b on all data in the flamelet table-based CFD

Model	$\widetilde{R}$	$\widetilde{e}_f$	$\widetilde{T_f}$	$\widetilde{\dot{\omega}}_C$	$\widetilde{\lambda}$	$\widetilde{\gamma}$	$\widetilde{a}_\gamma$
NN_a	0.0889	0.14	0.99	5.96	1.04	0.14	1.58
NN_b	0.0506	0.0852	0.63	3.59	0.68	0.0778	0.86

Table 4.1 shows better performance for NN_b than NN_a by 36% to 44%. Having more layers and neurons, besides separate NNs for each variable in NN_b provides more degrees of freedom for the model while, on the downside, it increases the computational cost relative to NN_a by around 2.4 times. The flamelet data calculated through NN_a is compared with the table data for different variables in the left column, and the flamelet data calculated through NN_b is compared with the table data in the right column of Figure 4.1 and Figure 4.2.

In the graphs, the x-axis shows the value of an output variable in the table, and the y-axis shows the value of the same variable estimated from NNs. Perfect estimation implies that all points lie on the $y = x$ line in each graph. On the graphs the lines $y = (1 \pm 1\%)x$, $y = (1 \pm 2\%)x$, $y = (1 \pm 5\%)x$, and $y = (1 \pm 10\%)x$ are provided as guidelines for evaluating the NN performance in estimating the value of each point. Variable $\widetilde{R}$ was estimated with the lowest error (less than 1%).

Table 4.1 shows that the performance of similar NN structures in estimating distinct variables is different. Some variables are estimated much better than others. One of the factors in determining NN performance is the variable range relative to its average value. $\widetilde{R}$ and $\widetilde{\gamma}$ have relatively short ranges, and they are estimated with the lowest errors. PVRR, on the other hand, varies by five orders of magnitudes; thus, it is estimated with the worst error.

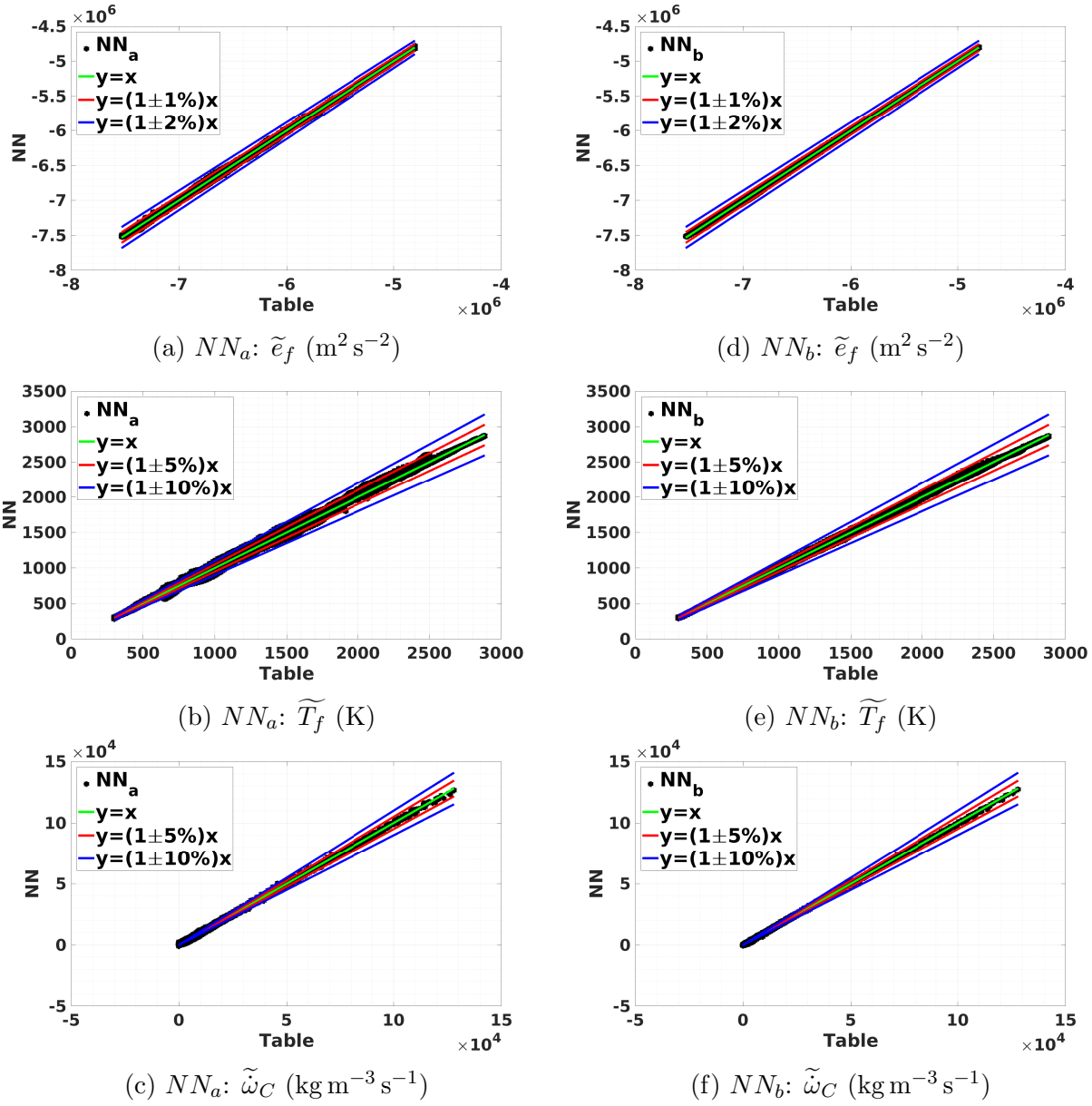

(a) NN_a: $\widetilde{e}_f$ ($\mathrm{m^2\,s^{-2}}$)

(d) NN_b: $\widetilde{e}_f$ ($\mathrm{m^2\,s^{-2}}$)

(b) NN_a: $\widetilde{T_f}$ (K)

(e) NN_b: $\widetilde{T_f}$ (K)

(c) NN_a: $\widetilde{\dot{\omega}}_C$ ($\mathrm{kg\,m^{-3}\,s^{-1}}$)

(f) NN_b: $\widetilde{\dot{\omega}}_C$ ($\mathrm{kg\,m^{-3}\,s^{-1}}$)

Figure 4.1: Offline result comparison for internal energy, flame temperature, and PVRR

Figure 4.1f shows that the worst relative accuracy in PVRR estimation occurs for low values since higher values dominate the training.

Although each variable is estimated with different errors, our studies showed that required levels of accuracy are different for each variable for successfully implementing the model in CFD. Those studies involved a sensitivity analysis of CFD to perturbations in the outputs of the flamelet table. Different simulations were conducted, and in each of them, one of

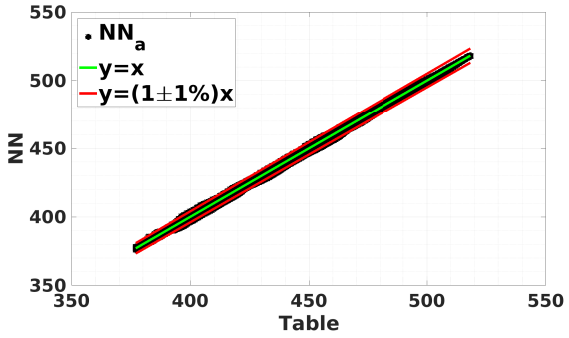

(a) NN_a: $\widetilde{e}_f$ ($\mathrm{m^2\,s^{-2}}$)

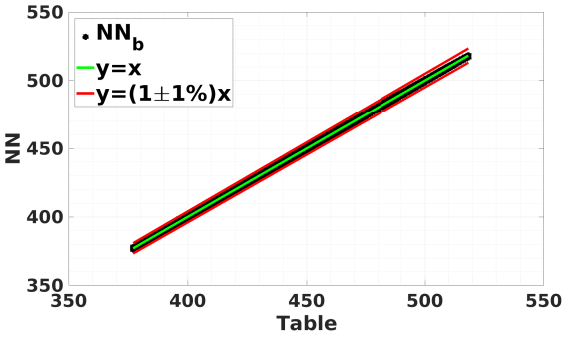

(e) NN_b: $\widetilde{e}_f$ ($\mathrm{m^2\,s^{-2}}$)

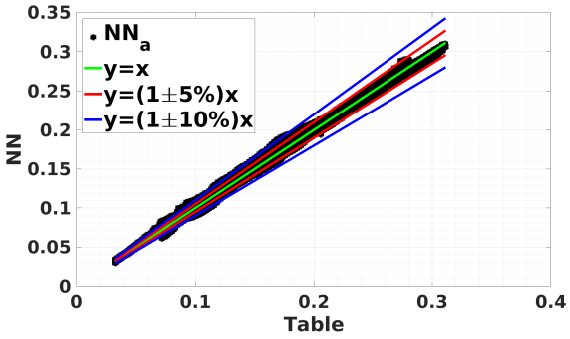

(b) NN_a: $\widetilde{\lambda}$ ($\mathrm{W\,m^{-1}\,K^{-1}}$)

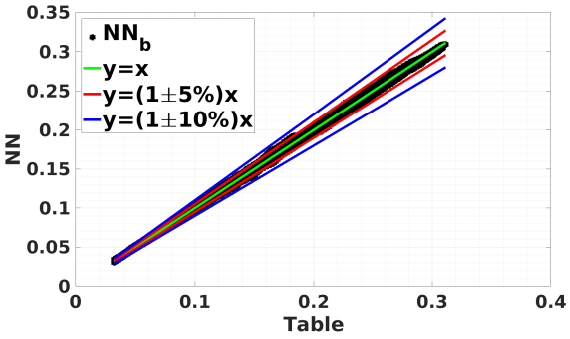

(f) NN_b: $\widetilde{\lambda}$ ($\mathrm{W\,m^{-1}\,K^{-1}}$)

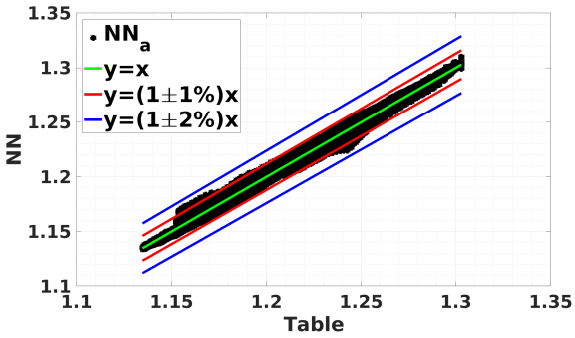

(c) NN_a: $\widetilde{\gamma}$

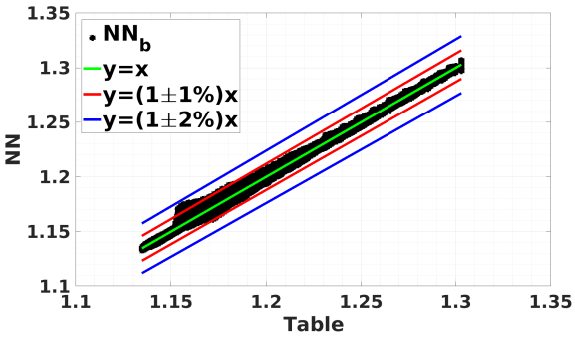

(g) NN_b: $\widetilde{\gamma}$

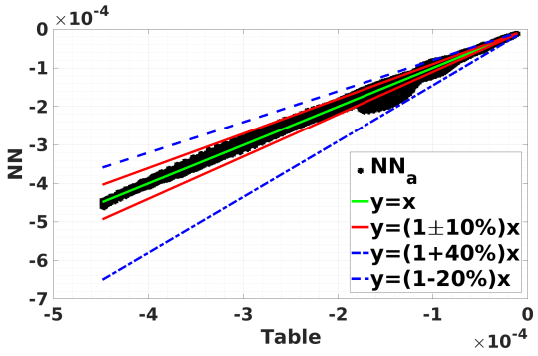

(d) NN_a: $\widetilde{a}_\gamma$ ($\mathrm{K^{-1}}$)

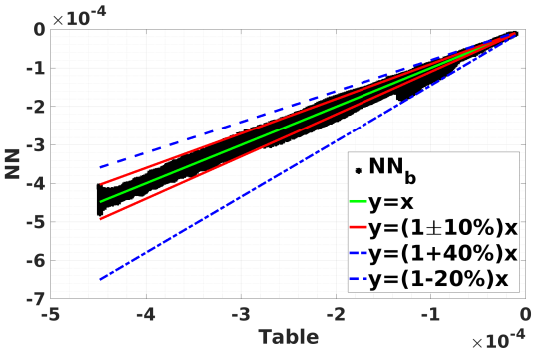

(h) NN_b: $\widetilde{a}_\gamma$ ($\mathrm{K^{-1}}$)

Figure 4.2: Offline result comparison for gas constant, thermal conductivity, ratio of heat capacity, ratio of heat capacity coefficient

the outputs of the flamelet table was perturbed with random Gaussian noise with bounded amplitudes. Then, we measured how that affects the pressure signal. For instance, our modeling error sensitivity analysis in CFD showed that estimating $\widetilde{e}_f$ accurately is more important than others.

4.2.2 Online Test

Next, NN_a and NN_b are introduced in the CFD simulations for replacing the flamelet table. According to [22], the 14-cm oxidizer post is a CVRC configuration with a very high level of instability. In the 14-cm oxidizer post, for each of the NN sets, two different simulations have been conducted starting from two distinct initial conditions. The two initial conditions are selected at a time before the emerging instability and at a time after the instability has been fully developed. The first is called the "transient case," and the second is called the "dynamic equilibrium case." The pressure signals represent the time waveform of pressure at each spatial grid point over the combustor geometry. To validate the NN-based flame models, the results from each simulation is evaluated by investigating the similarity between pressure signals from NN-based and table-based CFD simulations.

To this end, first, we looked at the overall relative error between pressure signals calculated from each CFD. Assume $\boldsymbol{x}$ is the pressure signal from table-based CFD, and $\boldsymbol{y}$ is the pressure signal from the NN-based CFDs. The relative error of signal $\boldsymbol{y}$ with respect to $\boldsymbol{x}$ is calculated based on Eq. (4.1), where the index i runs over the time signals. n is the number of time snapshots, and x_i and y_i are the values of the signals at the i-th time sample. This gives an overall measure of the distance between the two signals relative to the magnitude of the target signal. As shown later in Table 4.2, the third column, the pressure signals in the dynamic equilibrium case are estimated on average with 7.18% and 6.23% error by the NN_a-based and the NN_b-based simulations, respectively. For the transient case, the average

error resulted from both simulations is 5.02%. This close results from both NN-based models raise the question of whether the relative error is a comprehensive measure for the purpose of modeling combustion instability. Equation (4.1) normalizes the distance of two signals by the magnitude of the reference. For oscillating signals with high mean values, such a measure ignores the fluctuations errors. In the combustion instability study, it is of high significance for a model to capture the phase and amplitude of the pressure fluctuation. In that regard, the root mean square (rms) of the pressure signals and their correlations are compared.

The similarity between the phases of two signals ($\boldsymbol{x}$ and $\boldsymbol{y}$) can be measured through their correlation (Pearson's linear correlation coefficient), calculated as:

$$\kappa(\boldsymbol{x}, \boldsymbol{y}) = \frac{\sum_{i=1}^{n}(x_i - \bar{x}_i)(y_i - \bar{y}_i)}{\sqrt{\sum_{i=1}^{n}(x_i - \bar{x}_i)^2 \sum_{i=1}^{n}(y_i - \bar{y}_i)^2}} \tag{4.2}$$

where $\bar{x}$ and $\bar{y}$ are their empirical mean values. The similarity between the two signal's fluctuation amplitudes is measured by comparing their rms. The rms ratio of the fluctuations of $\boldsymbol{y}$ with respect to $\boldsymbol{x}$, is defined as:

$$\eta(\boldsymbol{x}, \boldsymbol{y}) = \frac{rms(\boldsymbol{y})}{rms(\boldsymbol{x})} = \frac{\sqrt{\frac{1}{n}\sum_{i=1}^{n}(y_i - \bar{y}_i)^2}}{\sqrt{\frac{1}{n}\sum_{i=1}^{n}(x_i - \bar{x}_i)^2}} \tag{4.3}$$

In Eq. (4.2) and Eq. (4.3), the time averages of the signals are subtracted from the main signal to calculate the fluctuation signals. Hence, the similarity between their mean values is also measured. The relative error of signal's mean values (e_m) are calculated through Eq. (4.1) by replacing x and y by $\bar{x}$ and $\bar{y}$. When signal amplitude is not constant over time (transient signal), the $\bar{x}_i$ and $\bar{y}_i$ are smoothed versions of the actual signals. Otherwise, the actual means $\bar{x}_i$ and $\bar{y}_i$ are equal for all indexes (dynamic equilibrium).

Table 4.2 summarizes the values of the above criteria for each of the simulations for dynamic equilibrium and transient cases. Each criterion is measured at each grid points on the CVRC geometry. The mean and standard deviation of all the measurements for each criterion is presented in Table 4.2. The first and second columns identify the case and NN model used in each case. The third main column presents the overall error statistics by their mean and standard deviation in the sub-columns. Similarly, the fourth, fifth, and sixth columns present the correlation, rms ratio, and error in mean values. Note that the desired value for correlation and the rms ratio is 100%.

Table 4.2: Error analysis summary for the 14-cm oxidizer post configuration test base for dynamic equilibrium and transient cases

14-cm **oxidizer-post case**		**Dynamic Eq.**		**Transient**	
		NN_a	NN_b	NN_a	NN_b
e **(%):** Eq. (4.1)	**mean**	7.18	6.23	5.02	5.02
	std	2.47	2.34	1.32	1.4
κ **(%):** Eq. (4.2)	**mean**	78.5	82.1	76.66	79.61
	std	12.69	13.71	18.7	14.89
η**(%):** Eq. (4.3)	**mean**	93.71	93.91	75.84	103.63
	std	4.58	2.85	2.35	2.89
e_m**(%):** Eq. (4.1)	**mean**	1.41	0.64	1.27	1.16
	std	0.31	0.19	0.26	0.22

In the dynamic equilibrium case, NN_b has a slightly better performance in all criteria. However, NN_a is selected to represent the flamelet model considering its computational cost, which is around 40% of the NN_b-based simulation computational cost. In the transient case, both NN-based models perform similarly with respect to the overall error, mean, and correlation criteria. However, for the pressure fluctuation, the rms ratio captured by the NN_b-based and the NN_a-based simulations are 103.63% and 75.84%, respectively. Therefore, NN_b is selected for representing the flamelet model. NN_b, which shows higher capability in capturing flame dynamics, is also implemented in the 9-cm oxidizer post configuration, which, according to [22] is recognized as a stable configuration.

Dynamic Equilibrium Case

In combustion instability studies, the accuracy in simulating pressure is perhaps the most significant for validating the model. The relative error between pressure signals from the NN_a-based and the table-based simulations, calculated by Eq. (4.1), is provided as spatial distribution in Figure 4.3a, in Figure 4.3b as the numerical distribution, respectively. The highest error happens near the centerline. In the axisymmetric configuration, the centerline ($r = 0$) can be considered as a singularity and is prone to numerical errors. Accordingly, near the centerline, the signals are noisier and can be modeled with less quality.

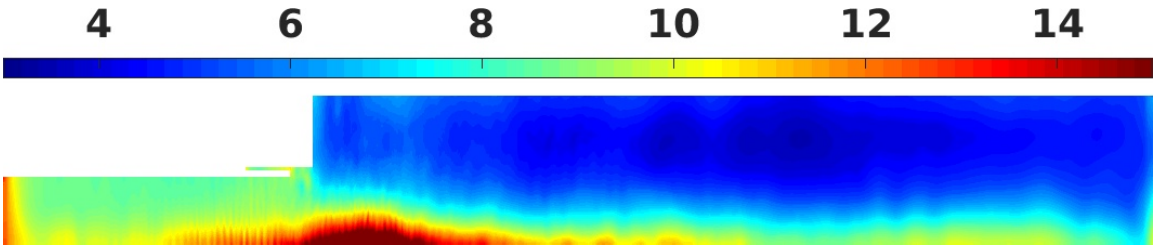

(a) Overall relative error (%)

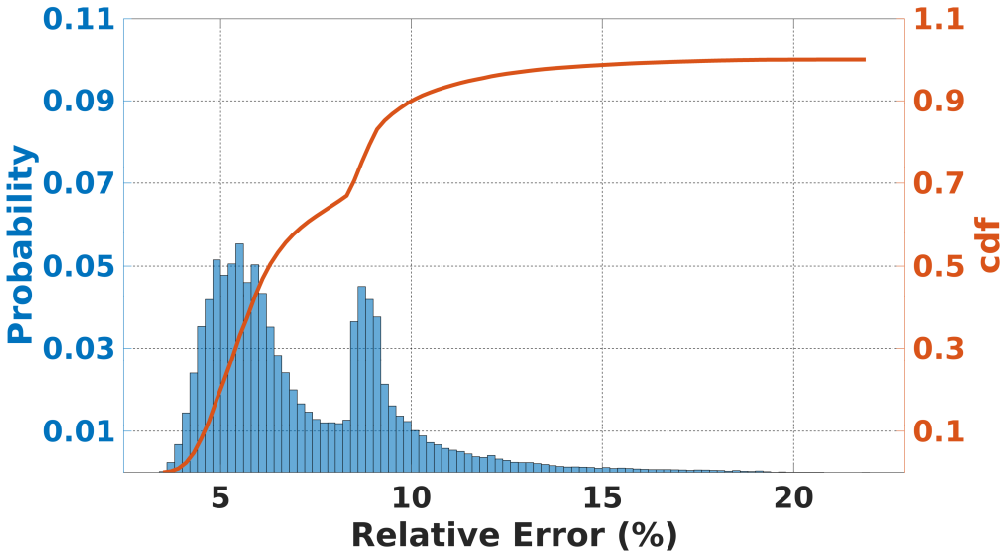

(b) Overall relative error (%) distribution

Figure 4.3: 14-cm, dynamic equilibrium: distribution of relative error (%) calculated from NN_a-based simulation comparison with the table-based one

The correlation of the fluctuation of the pressure signal at each grid point with the pressure signal at the same point from the original table-based simulation is provided in Figure 4.4a

and Figure 4.4b showing the spatial and numerical distribution of the correlations, respectively. The points with lower than 80% correlation are located in the pressure node, where the amplitudes of pressure harmonics are almost equal and smaller relative to other locations (see Figure 4.8b); therefore, the fluctuation signals there can be considered as noise.

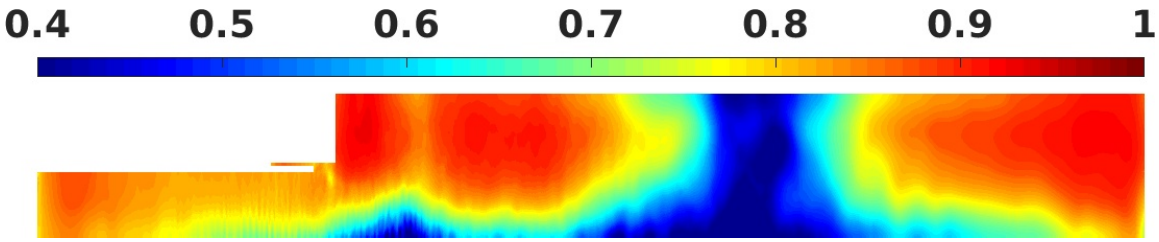

(a) Fluctuation correlation

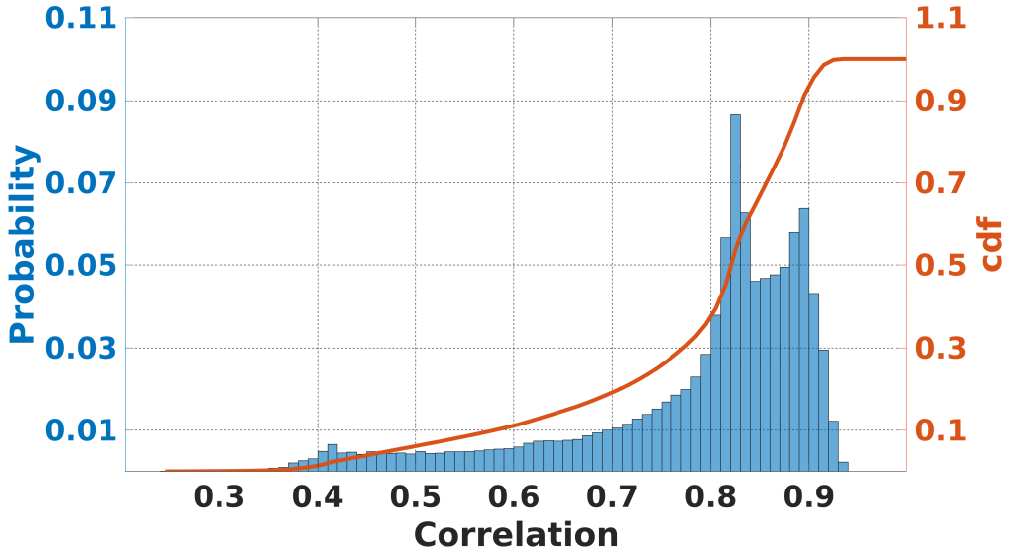

(b) Fluctuation correlation distribution

Figure 4.4: 14-cm, dynamic equilibrium: distribution of fluctuation correlation between pressure signals calculated from NN_a-based and table-based simulations

Moreover, Figure 4.5, compares the ratio of pressure fluctuation rms calculated from the NN_a-based simulation to the rms calculated from the table-based simulation; the rms of fluctuations of the two simulations are shown in Figure 4.5b and Figure 4.5a, respectively. The parts of the combustor in which the rms of pressure fluctuations is lower is consistent with the regions where correlation is lower. As shown in Figure 4.5c, around 90% of the points in the NN-based simulation capture more than 90% of the rms of the points in the table-based simulation.

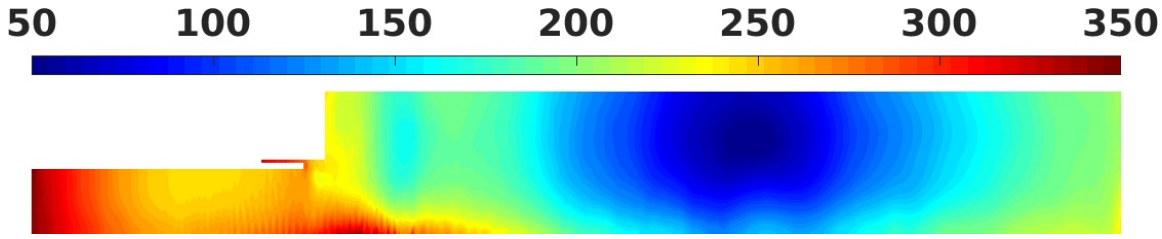

(a) Table-based

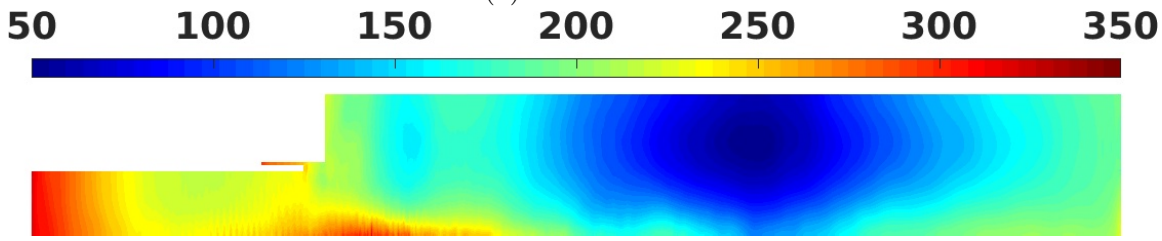

(b) NN_a-based

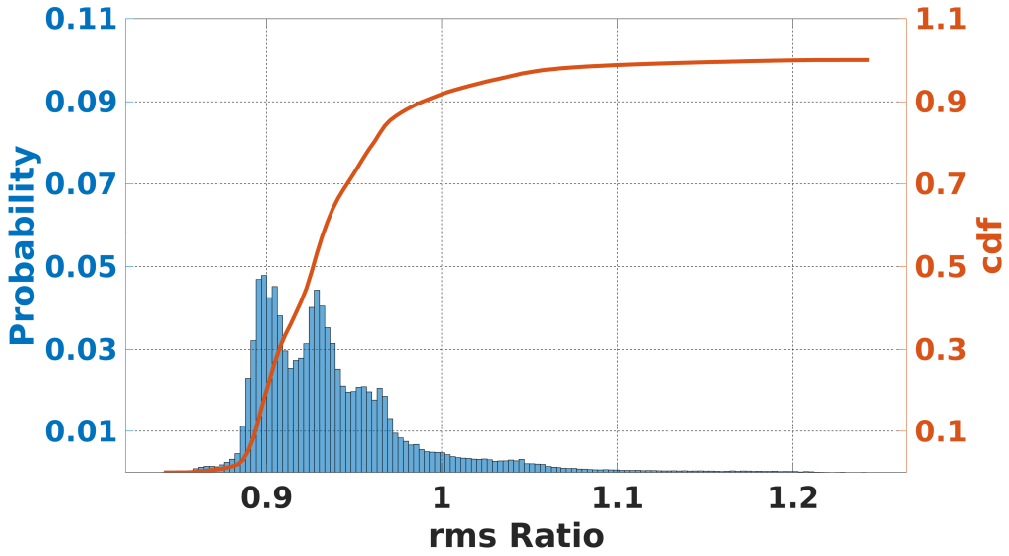

(c) rms ratio distribution

Figure 4.5: 14-cm, dynamic equilibrium: the distribution of the pressure fluctuation rms calculated from NN_a-based (4.5b) to the one calculated from table-based (4.5a) simulations

The errors that are calculated from Eq.(4.1) to Eq.(4.3) are demonstrated by comparing pressure signals calculated from the table-based and the NN-based simulations at few points in the following. Figure 4.6a and Figure 4.6c compare the pressure signals at the antinode (10 cm), and near the nozzle at the pressure tab (37 cm) on the top wall. At the antinode, the correlation is 87.73%, and near the nozzle, the correlation is 91.21%. At these points, the overall relative errors are 4.91% and 4.98%, respectively. The rms ratio is 95%, and the mean value is estimated with a 1.4% error at $x = 10$ cm.

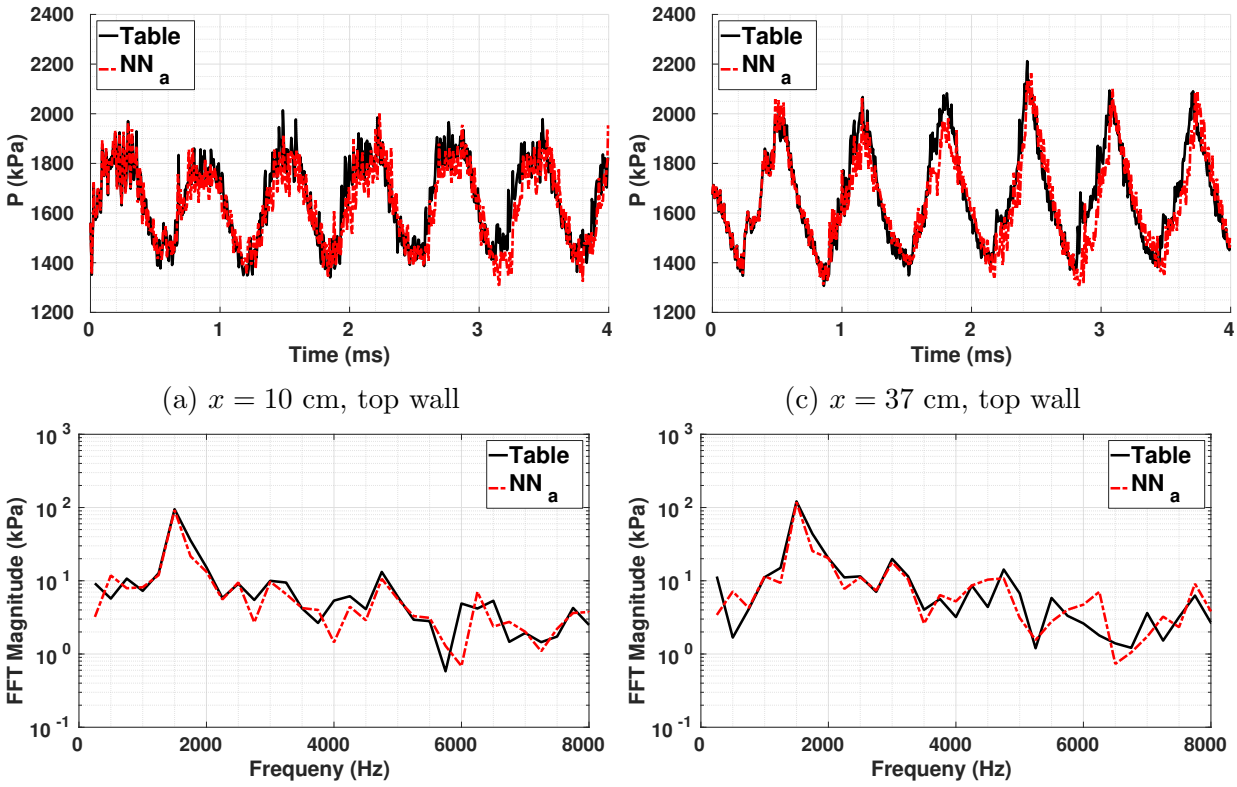

(a) $x = 10$ cm, top wall

(c) $x = 37$ cm, top wall

(b) Pressure FFT at $x = 10$ cm

(d) Pressure FFT at $x = 37$ cm

Figure 4.6: 14-cm, dynamic equilibrium: comparison of pressure signals and FFTs at two different points on the top wall between the NN_a-based and the table-based simulations

At $x = 37$ cm, the rms ratio is 94.74%, and the mean value is estimated with a 1.14% error. The first and second modes of oscillations are captured with high accuracy in these signals. The antinode and pressure tab are the common points that are investigated for each test because of their geometrical importance and to provide reference points among different cases. As shown in Figure 4.6b and Figure 4.6d, the frequency content, i.e. the fast Fourier transform (FFT), of pressure signals at both of these points that are calculated from the NN-based simulation are in great agreement with the table-based one.

Figure 4.7a and Figure 4.7c compare pressure signals at points with lower correlations and higher error values. One of the points with a lower correlation is located on the centerline at 21.8 cm, i.e., the pressure node vicinity. Figure 4.7a compares the pressure signal at this point between the NN-based and the table-based simulations. The correlation at this point

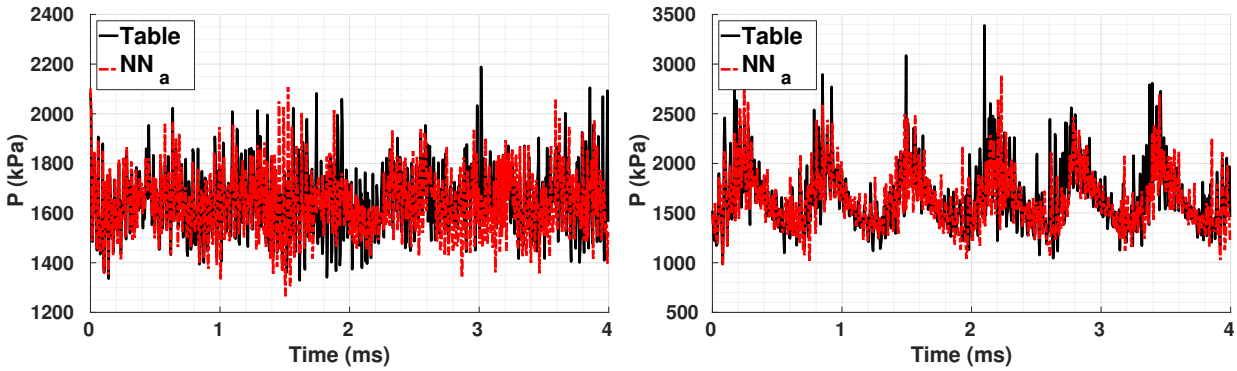

(a) $x = 21.8$ cm, centerline

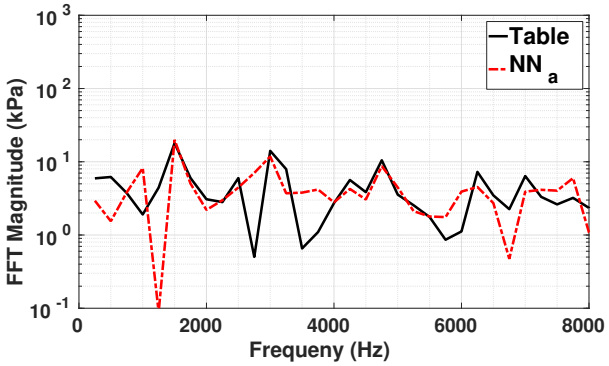

(b) Pressure FFT at $x = 21.8$ cm

(c) $x = 1.14$ cm, centerline

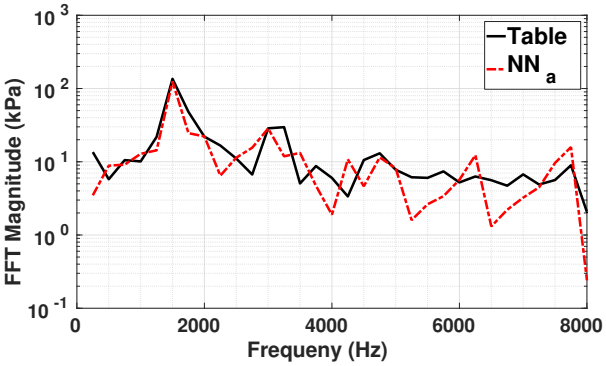

(d) Pressure FFT at $x = 1.14$ cm

Figure 4.7: 14-cm, dynamic equilibrium: comparison of pressure signals at different points on centerline between the NN_a-based and the table-based simulations

is 40.07%. The overall error at this point is 9%, the rms ratio is 96.72%, and the mean value error is 0.9%. At 21.8 cm, looking at the pressure signal in the frequency domain, the power of the signal is distributed almost evenly among different modes, and the first mode is weaker relative to other locations. Essentially the higher frequencies are more significant at this point; see Figure 4.7b.

The other point is located on the centerline at 1.14 cm, which is right after the dump plane near the mixing layer. Figure 4.7c and Figure 4.7d compares the pressure signal and its FFT at this point with 53.64% correlation. The overall error at this point is 17.72%, the rms ratio is 89.03%, and the mean value error is 2.15%. This point is located near the oxidizer post and combustor interface, at $r = 0$; a singular point with a very high density mesh. The spikes are associated with quantitative excursions of pressure at and beyond the limits used

for the construction of the table (30 atm). Spikes do occur in close-neighboring physical locations with the NN as well. The spikes, fortunately, occur only in regions where little reaction occurs, near the centerline and near the entrance for the propellant flow into the main chamber. Thereby, with no reaction locally, these spikes have no consequence on the Rayleigh Index and the stability of the combustion chamber. Note that the physical behavior is chaotic, and therefore each realization can differ in detail. Spikes cannot be expected to occur always at the same location when the small quantitative differences (i.e., numerical errors) in constraints can appear between NN and the table.

Also, to compare the frequency content of pressure signals, the longitudinal mode shapes of the signals over the centerline are compared. In Figure 4.8, pressure mode shapes are

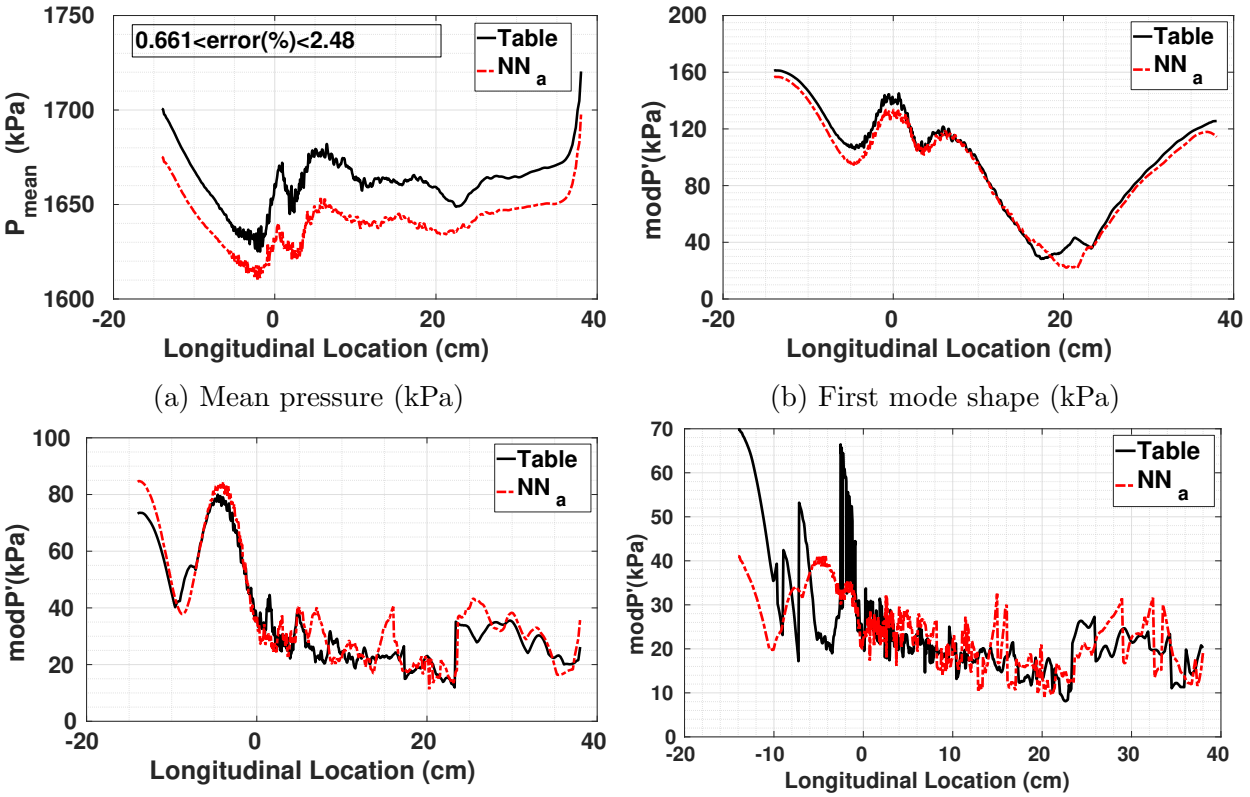

(a) Mean pressure (kPa)

(b) First mode shape (kPa)

(c) Second mode shape (kPa)

(d) Third mode shape (kPa)

Figure 4.8: 14-cm, dynamic equilibrium: comparison of pressure mean, the first, the second, and the third mode shapes between NN_a-based and table-based simulations

demonstrated by plotting the modulus of the Fourier spectrum peaks at each grid point

along the centerline. First, the time-average of the signals, which are plotted in Figure 4.8a, are subtracted from it. Then, the Fourier spectrum is calculated for each of the centered signals. The first and the second modes are plotted in Figure 4.8b and Figure 4.8c. The NN_a-based simulation gives a good estimate of the mean, the first and the second longitudinal modes; it starts to deviate as for the third mode; however, the effect of the third mode in the overall results is considered negligible.

As discussed before, it is important for a model to provide a good estimation of RI to be useful in combustion instability research. The local mRI and RI are compared for

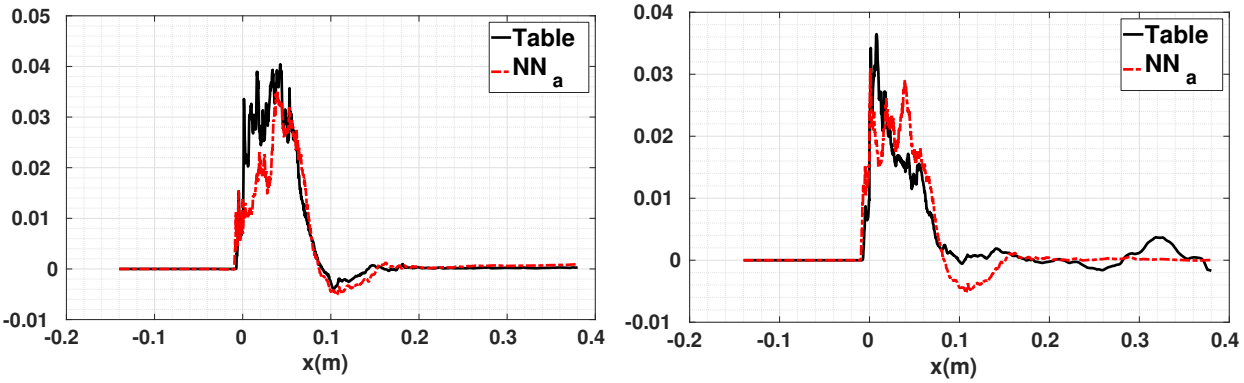

(a) Radial-averaged mRI

(b) Radial-averaged RI

Figure 4.9: 14-cm, dynamic equilibrium: comparison of radial-averaged mRI and RI between the NN_a-based and the table-based simulations

the NN-based and the table-based simulations in Figure 4.9a and Figure 4.9b in a radially averaged 1D manner, and in Figure 4.10 and Figure 4.11 in a 2D manner, respectively. This comparison shows that the NN_a-based simulation captures the location of the flame that drives instability, yet underestimates the flame near the corner. Particularly, the NN_a-based simulation underestimates mRI from the table-based simulation near the corner and dump plane. HRR is calculated after the CFD simulation was conducted, only for the purpose of calculating RI. For RI, there exists a good correlation in the flame zone, but discrepancies downstream. The slight underestimation of RI and mRI are consistent with the slight underestimation of the rms value of the limit cycle with the NN-based simulation.

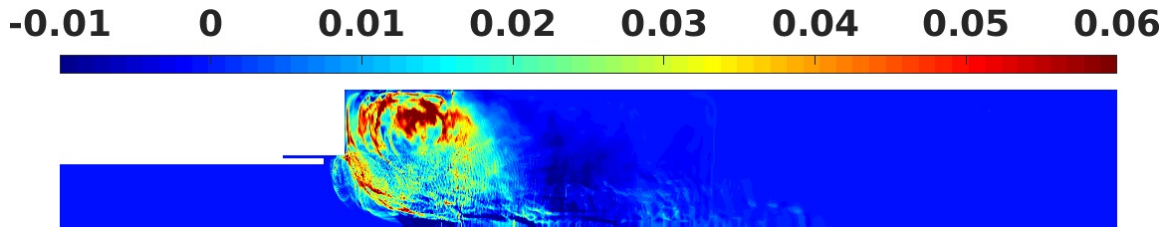

(a) Table-based CFD: mRI

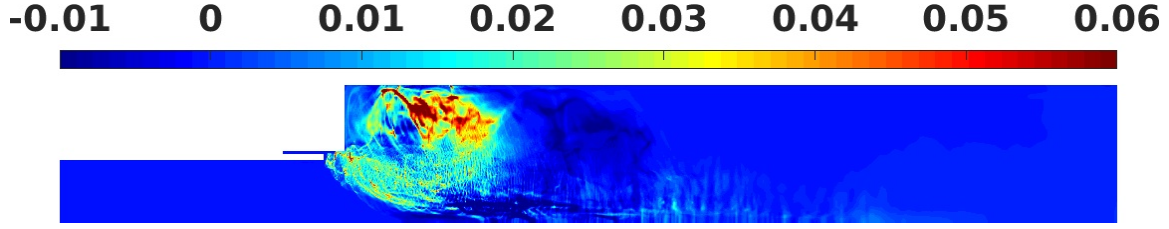

(b) NN_a-based CFD: mRI

Figure 4.10: 14-cm, dynamic equilibrium: comparison of mRI from the NN_a- and the table-based simulations

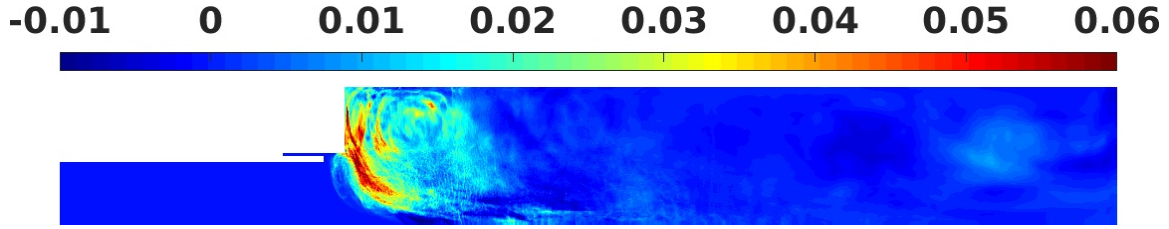

(a) Table-based CFD: RI

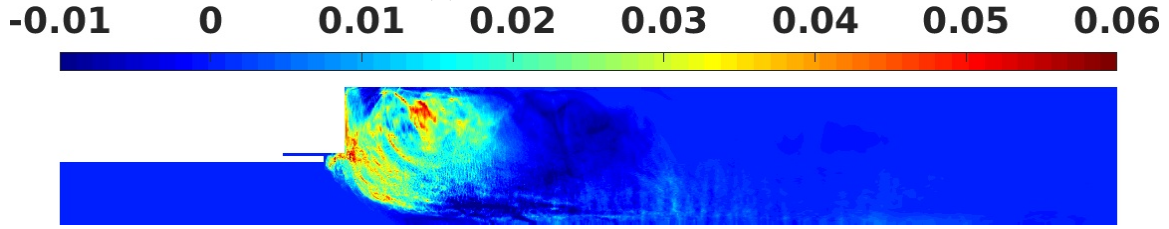

(b) NN_a-based CFD: RI

Figure 4.11: 14-cm, dynamic equilibrium: comparison of RI from the NN_a- and the table-based simulations

In the following, other significant variables are briefly compared between the NN_a-based and table-based simulations by demonstrating their time-averaged behavior. Figure 4.12a and Figure 4.12b compare the contour plots of time-averaged progress variable. In addition, the time-averaged mixture fraction (Figure 4.13a and Figure 4.13b), time-averaged of PVRR (Figure 4.14a and Figure 4.14b), time-averaged temperature (Figure 4.15a and Figure 4.15b), time-averaged axial velocity (Figure 4.16a and Figure 4.16b), and time-averaged vorticity

(Figure 4.17a and Figure 4.17b) are provided and compared. Although there are differences in the detailed behavior, the overall shapes are very similar between the two simulations.

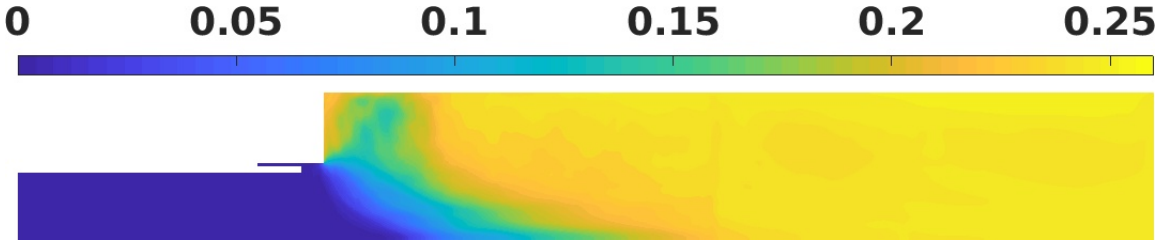

(a) $\widehat{C}$, table

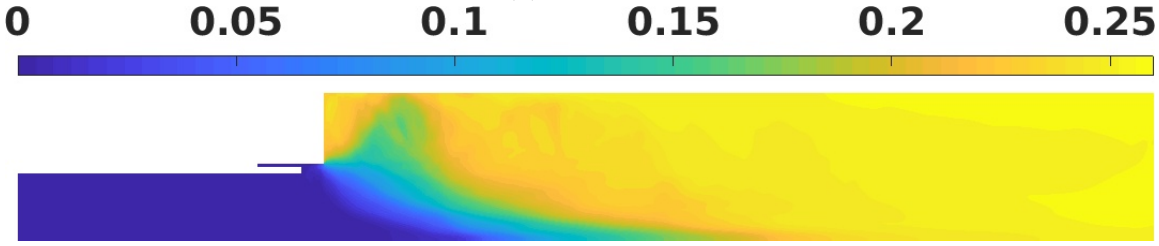

(b) $\widehat{C}$, NN_a

Figure 4.12: 14-cm, dynamic equilibrium: time-averaged values of progress variable from the NN_a-based and the table-based simulations

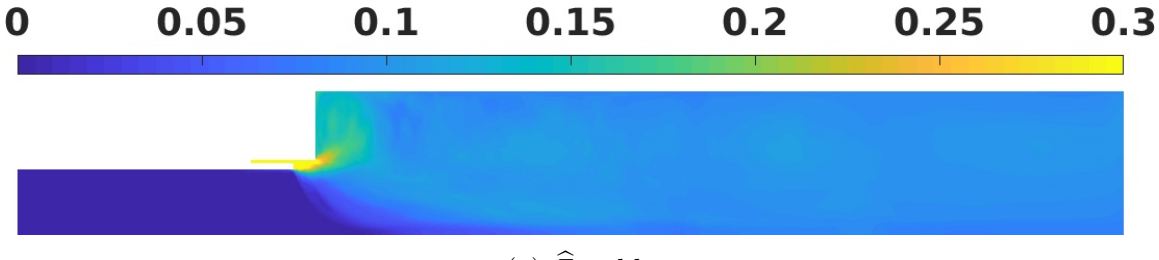

(a) $\widehat{Z}$, table

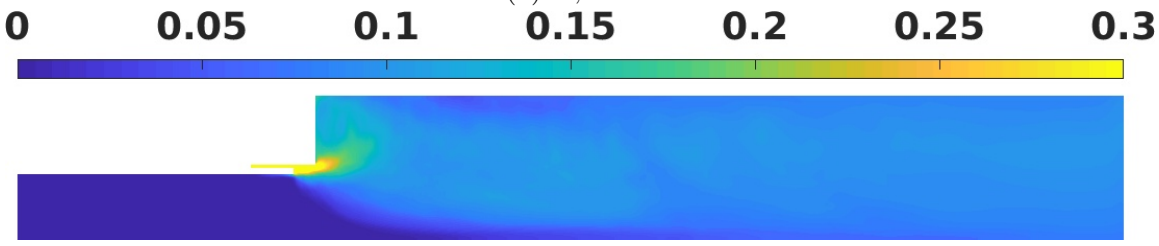

(b) $\widehat{Z}$, NN_a

Figure 4.13: 14-cm, dynamic equilibrium: time-averaged values of mixture fraction from the NN_a-based and the table-based simulations

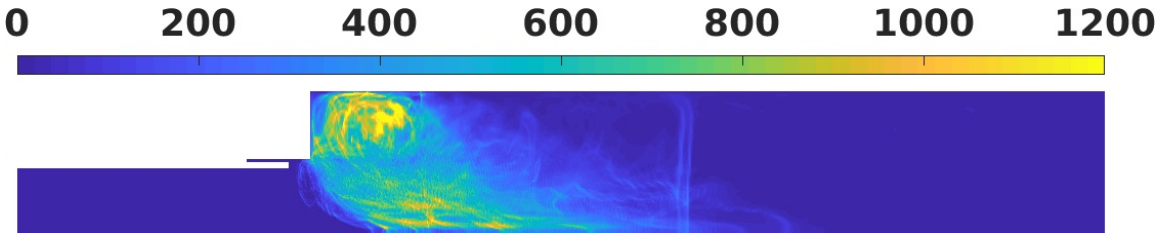

(a) $\widehat{\dot{\omega}}_C$ ($\mathrm{kg\,m^{-3}\,s^{-1}}$), table

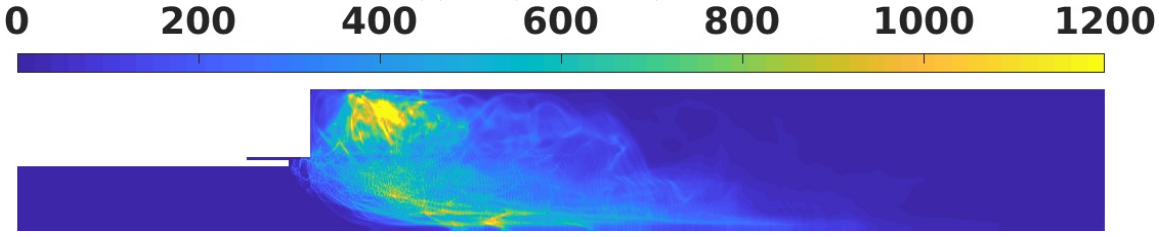

(b) $\widehat{\dot{\omega}}_C$ ($\mathrm{kg\,m^{-3}\,s^{-1}}$), NN_a

Figure 4.14: 14-cm, dynamic equilibrium: time-averaged values of PVRR from the NN_a-based and the table-based simulations

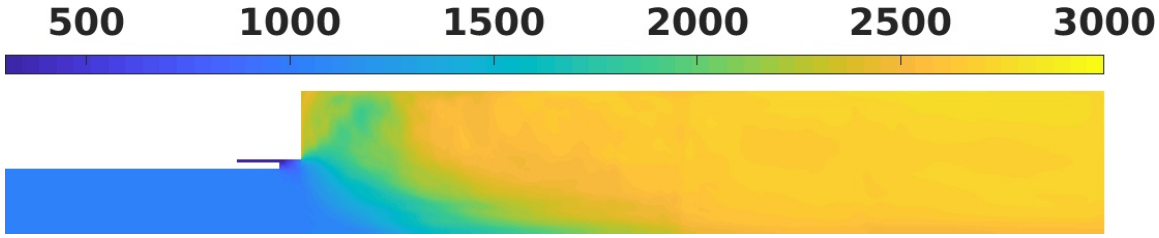

(a) $\widehat{T}$ (K), table

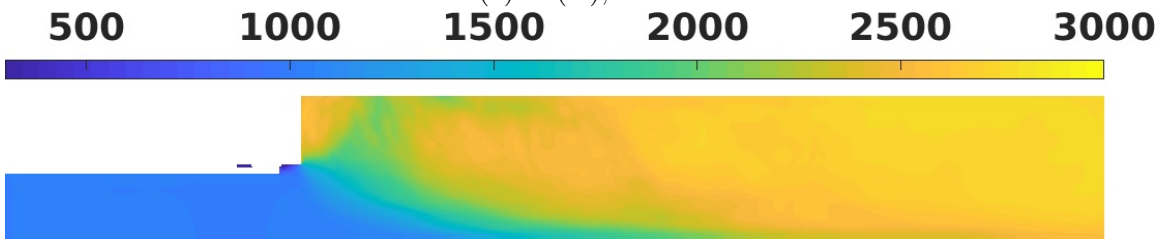

(b) $\widehat{T}$ (K), NN_a

Figure 4.15: 14-cm, dynamic equilibrium: time-averaged values of temperature from the NN_a-based and the table-based simulations

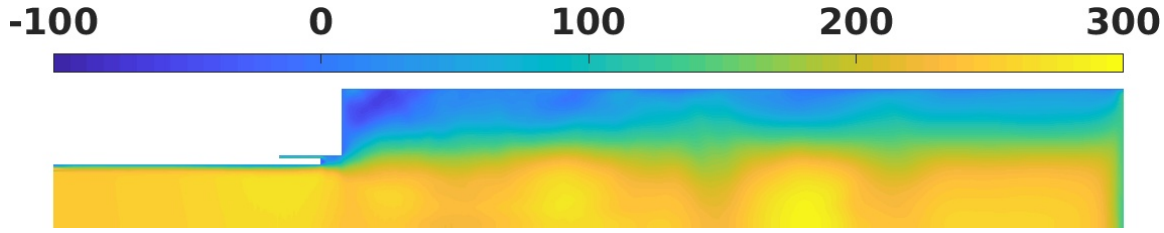

(a) $\widehat{U}$ $(\mathrm{m\,s^{-2}})$, table

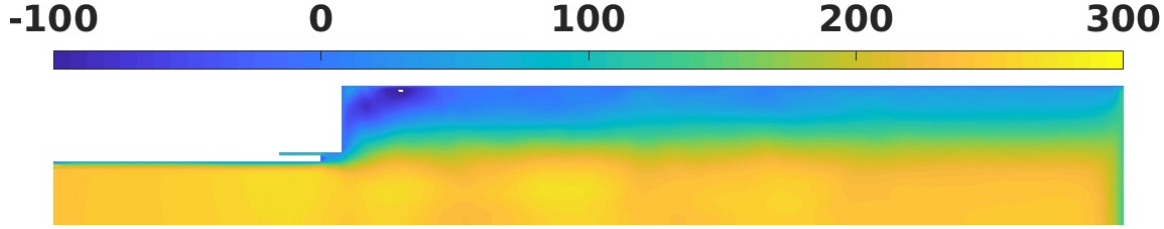

(b) $\widehat{U}$ $(\mathrm{m\,s^{-2}})$, NN_a

Figure 4.16: 14-cm, dynamic equilibrium: time-averaged values of axial velocity from the NN_a-based and the table-based simulations

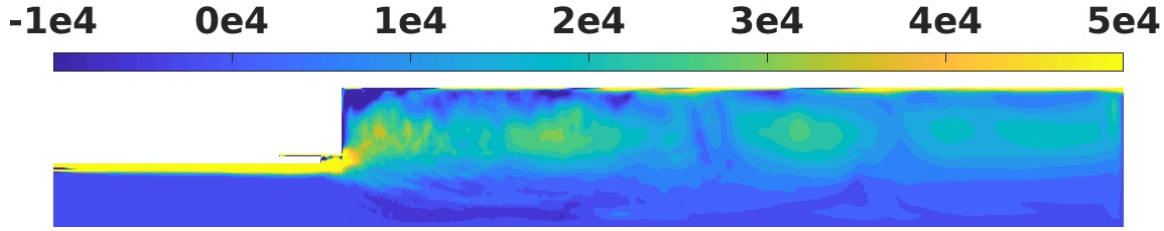

(a) $\widehat{\Omega}$ $(\mathrm{s^{-1}})$, table

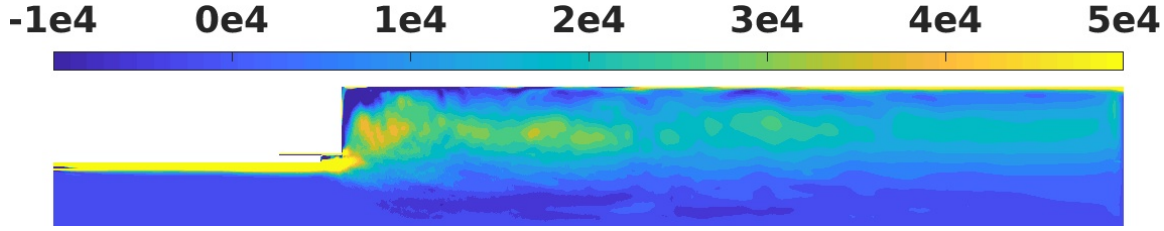

(b) $\widehat{\Omega}$ $(\mathrm{s^{-1}})$, NN_a

Figure 4.17: 14-cm, dynamic equilibrium: time-averaged values of vorticity from the NN_a-based and the table-based simulations

Transient Case

As discussed before, the NN_a-based simulation underestimates the rms value of pressure fluctuation in the transient case, while the NN_b-based simulation has a similar rms with the table-based one. Accordingly, NN_b is selected as the flame model for the transient simulation. The relative error between the NN_b-based and the table-based simulations is provided as spatial distribution in Figure 4.18a, and as numerical distribution in Figure 4.18b. Similar to the dynamic equilibrium case, in the axisymmetric configuration, the centerline ($r = 0$) can be considered as a singularity and prone to numerical error and noisier signals.

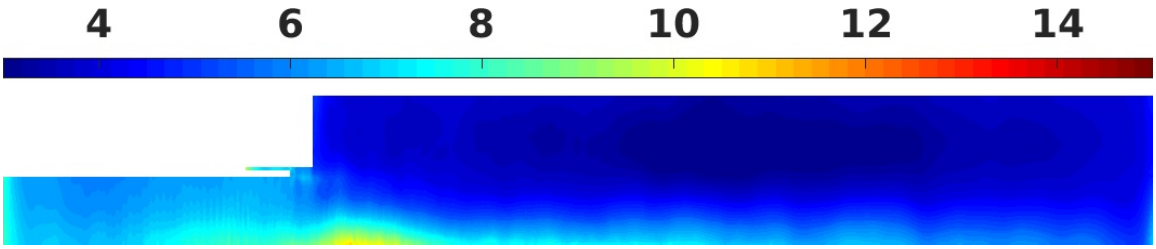

(a) Overall relative error (%)

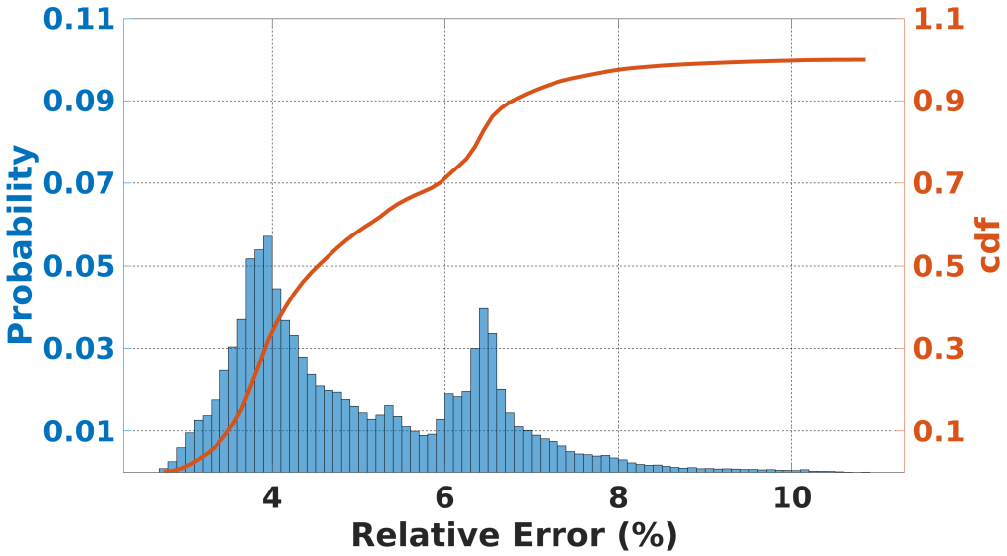

(b) Overall relative error (%) distribution

Figure 4.18: 14-cm, transient: distribution of relative error (%) between pressure signals from the NN_b-based and the table-based simulations

Correlation measures how two signals are similar after their mean values have been subtracted. In the transient case, using a global mean value will distort the ability of correlation

in measuring the performance of a model. To calculate the local mean value, the signals are smoothened using local quadratic regression [85]. The mean values are subtracted from each signal at each spatial point to get the fluctuation signals. The correlation of the fluctuation of the pressure signal at each grid point from the NN_b-based and the original table-based simulations are shown in the contour plot in Figure 4.19a and as numerical distribution in Figure 4.19b. The fluctuations at around 50% of the points are correlated more than 85% between the two simulations.

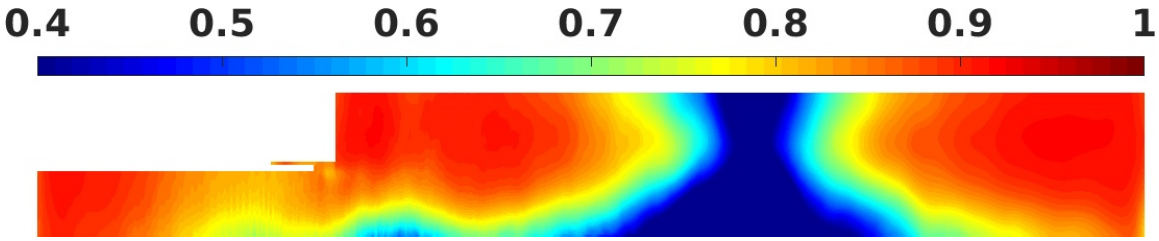

(a) Fluctuation correlation

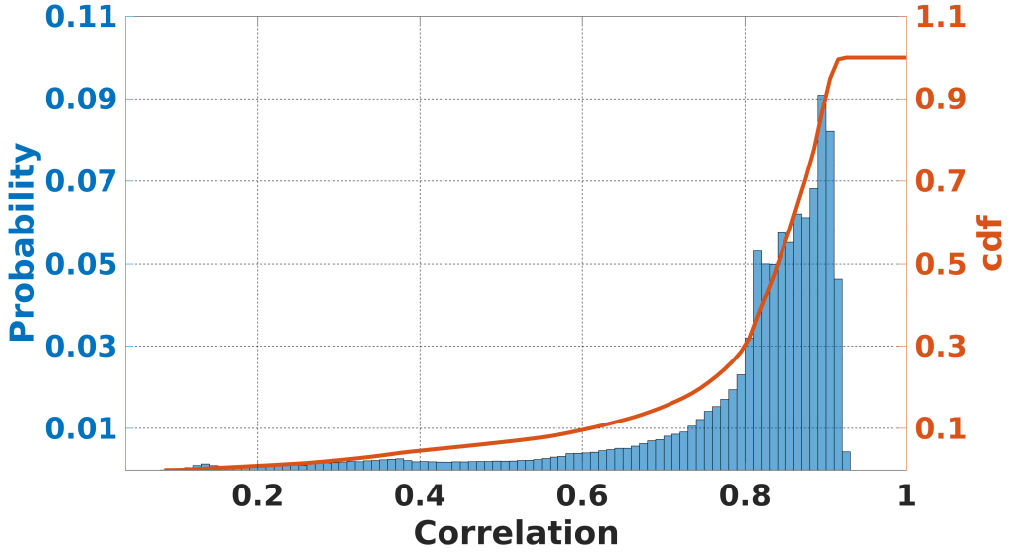

(b) Fluctuation correlation distribution

Figure 4.19: 14-cm, transient: distribution of pressure fluctuation correlation between the NN_b-based and the table-based simulations

In addition, the pressure fluctuation rms values calculated from the NN_b-based simulation (Figure 4.20b) are compared to those calculated from the table-based simulation (Figure 4.20a) through their ratio at each grid point. Around 80% of the points are overestimated less than 5%, as shown in Figure 4.20c.

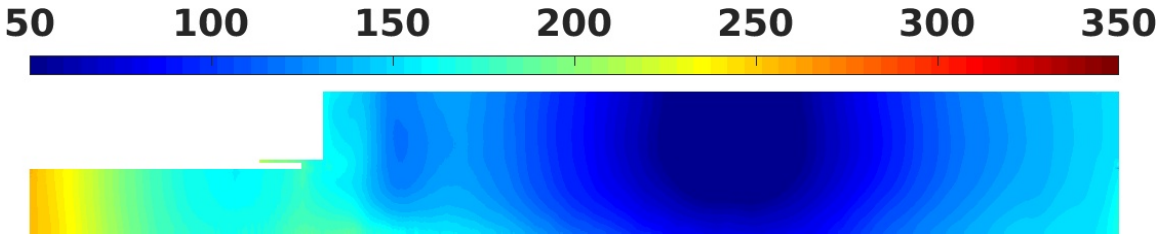

(a) Table-based pressure signal rms (kPa)

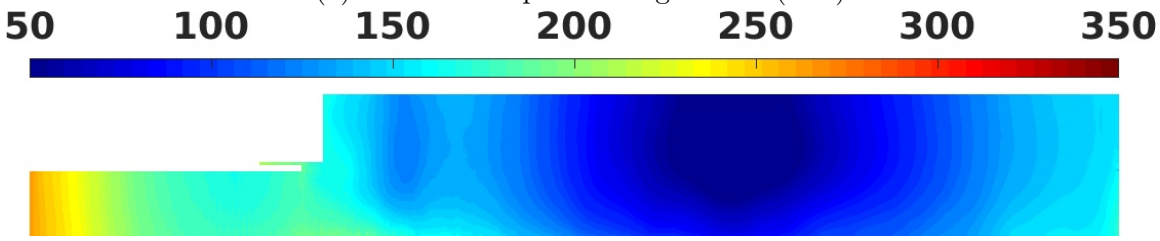

(b) NN_b-based pressure signal rms (kPa)

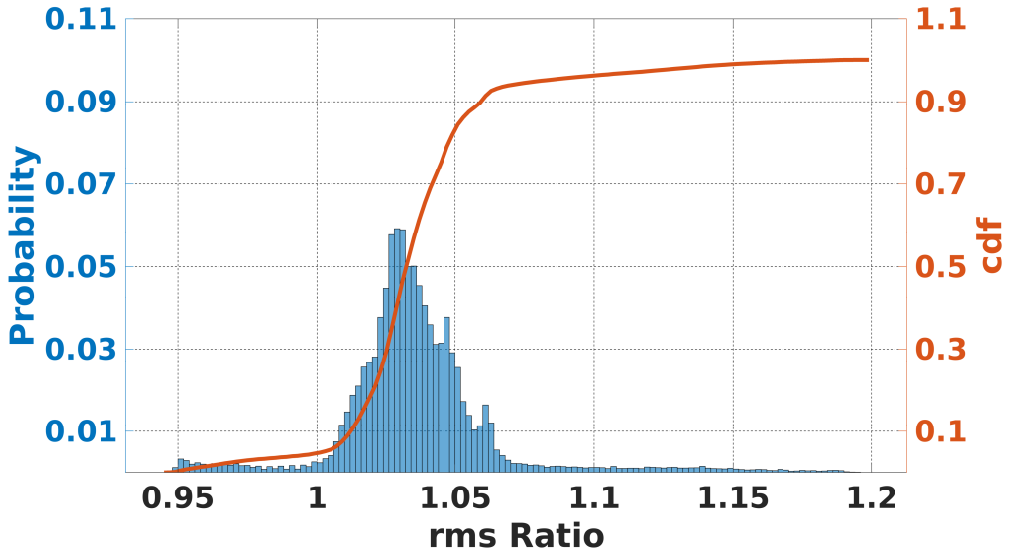

(c) rms ratio distribution

Figure 4.20: 14-cm, transient: the distribution of the pressure fluctuation rms ratio calculated from the NN_b-based simulation (4.20b) to the table-based (4.20a) one

Figure 4.21a and Figure 4.21c compare the pressure signals at the antinode (10 cm) and near the nozzle (37 cm) on the top wall for the transient case. At the antinode, the correlation is 87.65%, and near the nozzle, the correlation is 91.46%. At these points, the overall relative errors are 3.65% and 4.02%, respectively. The rms ratio is 104.41%, and the mean value is estimated with 0.95% error at $x = 10$ cm. At $x = 37$ cm, the rms ratio is 100.42%, and the mean value is estimated with a 1.43% error.

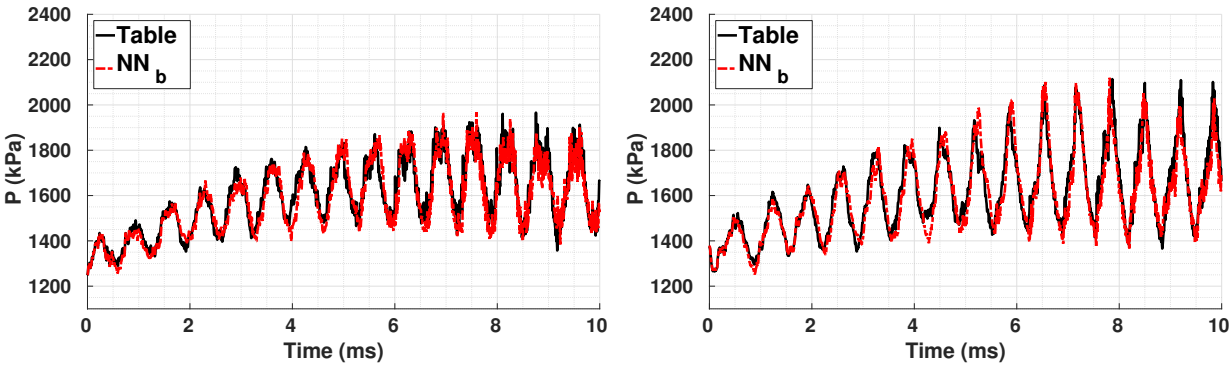

(a) $x = 10$ cm, top wall

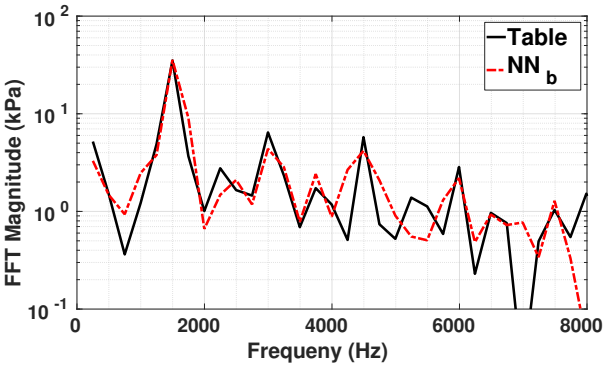

(b) Pressure FFT at $x = 10$ cm

(c) $x = 37$ cm, top wall

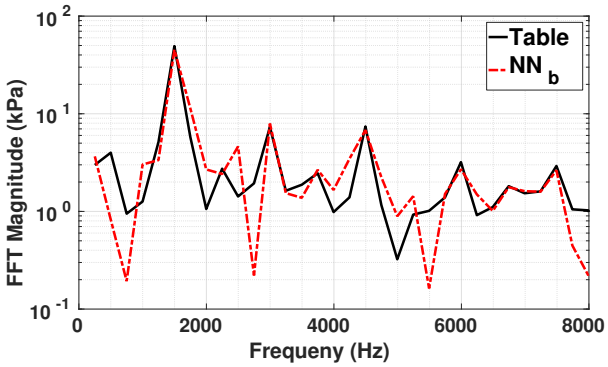

(d) Pressure FFT at $x = 37$ cm

Figure 4.21: 14-cm, transient: the NN_b-based and the table-based simulations comparison of pressure signal at two different points on the top wall

The FFT of these signals after reaching a quasi-steady state are compared. As shown in Figure 4.21b and Figure 4.21d, the frequency content of pressure signals at both of these points that are calculated from the NN-based simulation are in great agreement with the table-based one.

Figure 4.22a and Figure 4.22b compare the pressure signal and it FFT located on the centerline near the pressure node (17.1 cm) between the NN-based simulation and the original one, where the correlation is 12.48%. The overall error at this point is 7.33%, the rms ratio is 112.02%, and the mean value error is 1.08%. Another point with low correlation is located above the centerline at 2.58 cm, which is right after the dump plane near the centerline. Figure 4.22c and Figure 4.22d compare the pressure signal and its FFT at this point with a correlation of 71.36%. The overall error at this point is 7.42%, the rms ratio is 105.79%,

and the mean value error is 1.15%. These points are selected to demonstrate the need for different criteria to measure error. In Figure 4.21, the overall errors are similar, yet the correlations are drastically different. The frequency content of both signals are captured to a great extent for the first three modes.

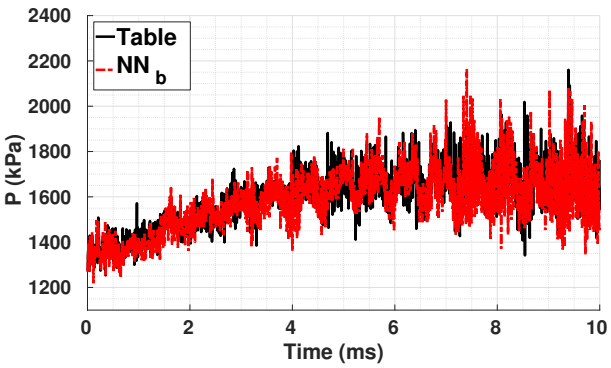

(a) $x = 17.11$ cm, centerline

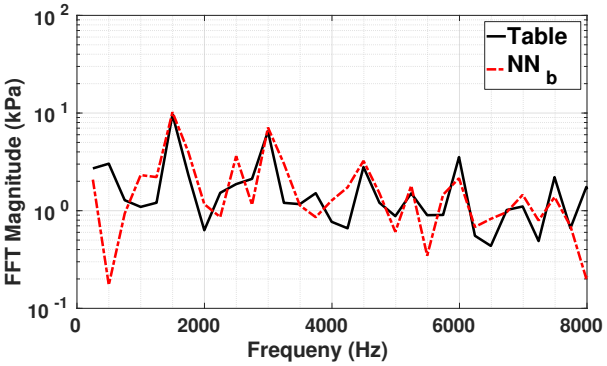

(b) Pressure FFT at $r = 0$ at $x = 17.11$ cm

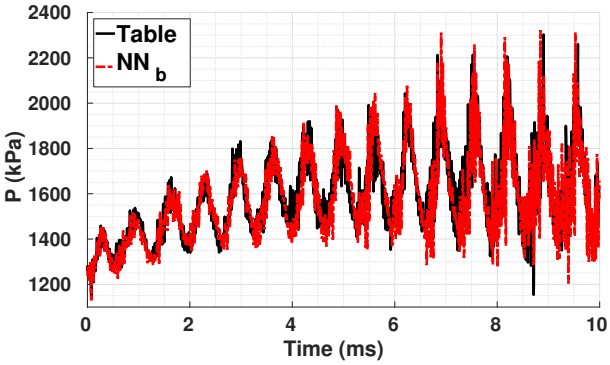

(c) $x = 2.58$ cm, $r = 0.37$ cm

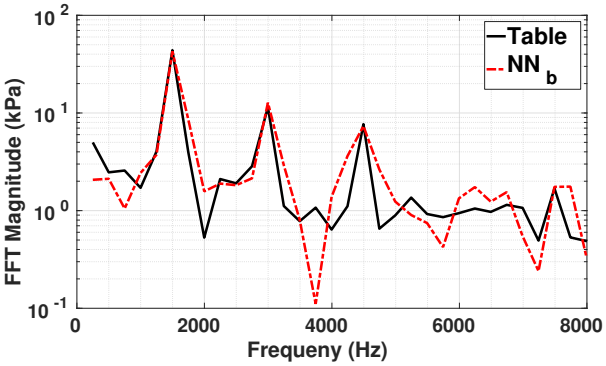

(d) Pressure FFT at $r = 0.37$ cm and $x = 2.58$ cm

Figure 4.22: 14-cm, transient: the NN_b-based and the table-based simulations comparison of pressure signal at two different points in the combustor

The frequency content of pressure signals are compared through the mode shapes over the centerline. In the analysis here, only the steady-state parts of the simulations are considered. The time-average of each of the signals is plotted in Figure 4.23a. The value of the Fourier spectrum for the first and the second modes are plotted in Figure 4.23b and Figure 4.23c. The NN-based simulation presents a good estimate of the mean, the first and second modes. The discrepancies between the two NN-based and table-based simulations start to grow from the third mode.

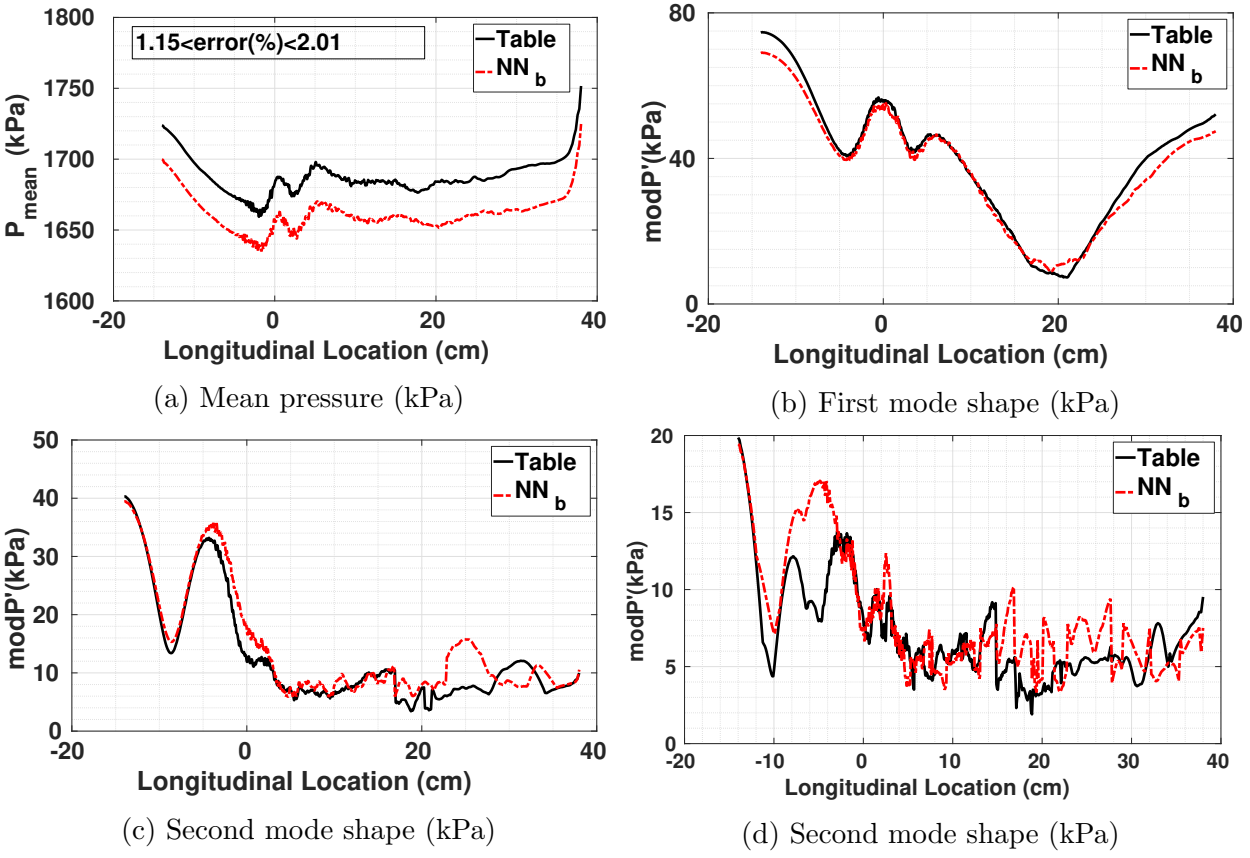

(a) Mean pressure (kPa)

(b) First mode shape (kPa)

(c) Second mode shape (kPa)

(d) Second mode shape (kPa)

Figure 4.23: 14-cm, transient: comparison of pressure mean, the first, and the second mode shapes between NN_b-based and table-based simulations (last 4 ms)

Similar to the dynamic equilibrium case, the radially averaged 1D comparison of the local RI and mRI are provided in Figure 4.24b and Figure 4.24a, respectively. Two-dimensional contours of the local RI and mRI are compared for the NN-based simulation in Figure 4.25. Comparing Figure 4.25b with Figure 4.25a, and comparing Figure 4.25d with Figure 4.25c, show a great similarity in the correlation of pressure with HRR and PVRR between the two simulations.

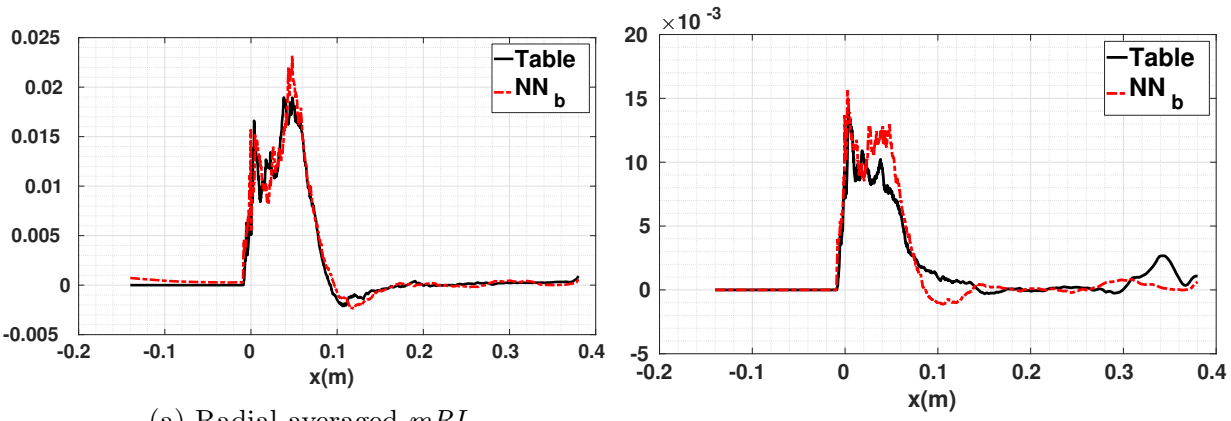

(a) Radial-averaged mRI

(b) Radial-averaged RI

Figure 4.24: 14-cm, transient: comparison of radial-averaged mRI and RI between the NN_a-based and the table-based simulations

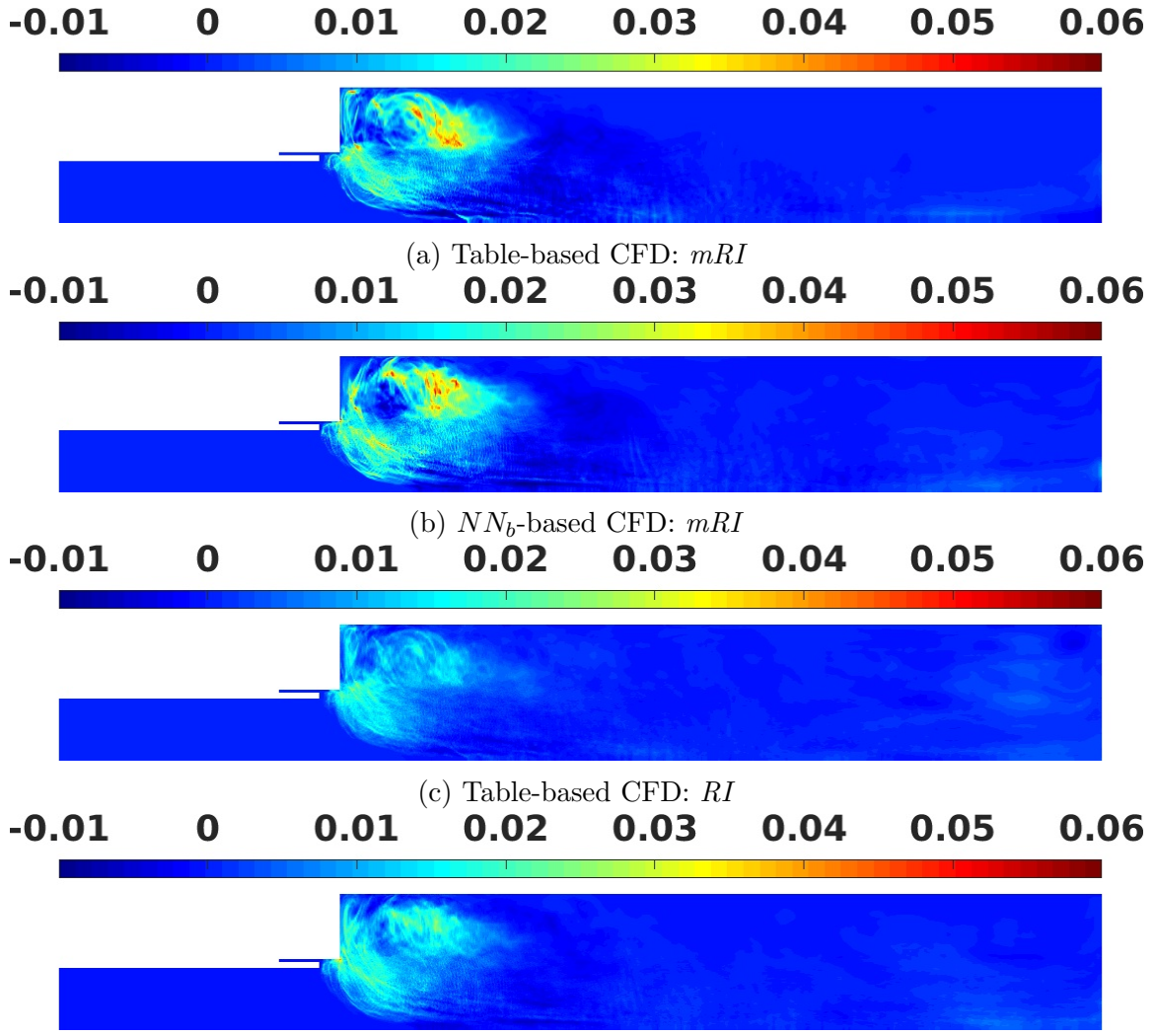

(a) Table-based CFD: mRI

(b) NN_b-based CFD: mRI

(c) Table-based CFD: RI

(d) NN_b-based CFD: RI

Figure 4.25: 14-cm, transient: comparison of RI and mRI between the NN_b-based and the table-based simulations

At three time points from the transient simulation, the snapshots of pressure, axial velocity, vorticity, mixture fraction, progress variable, PVRR, and temperature (Figure 4.26 to Figure 4.32) are compared between the NN_b-based and the table-based simulations. The time snapshots are selected at $t_1 = 0.5$ ms, $t_2 = 3.5$ ms, and $t_3 = 6.5$ ms, where the last time point is associated with the time that signals have reached to the limit cycle, while the other two time points are associated with the growing parts of the pressure signal. In the progress variable graphs, the flame front shape is predicted with great accordance, Figure 4.31. The flame front is the curve (thin flame) that separates the low and high temperature zones. These quantities are governed by both turbulence and acoustic behavior. The turbulent combustion causes the system to become chaotic, while the acoustic phenomena cause the system to resemble waveforms and modal behavior. Accordingly, for variables that are dominantly affected by turbulence, the performance of the NN-based model can be assessed by the statistical characteristics and consequences of those variables, while for variables where the acoustic phenomena are the significant driver, the NN-based model can be compared in a point-wise manner. One major statistical consequence for a variable such as PVRR is the modified RI that was shown in Figure 4.25b and Figure 4.25a for the NN-based and table-based simulations, respectively. The mRI calculated from NN-based simulation shows highly consistent behavior to the mRI calculated from table-based Simulation, despite the differences that can be spotted in the detailed behavior of PVRR in the time snapshots (e.g., Figure 4.31f vs. Figure 4.31e).

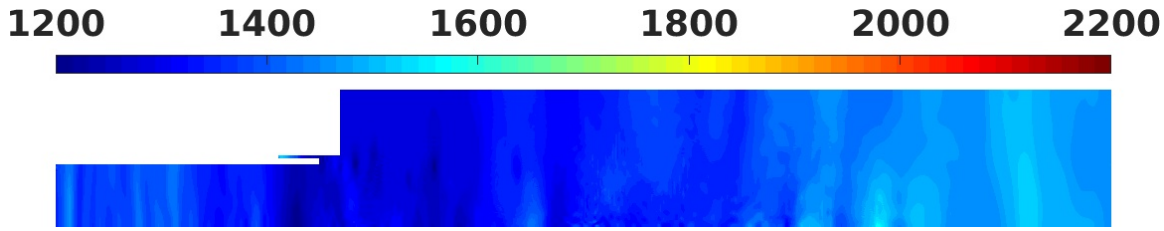

(a) $\overline{P}$ (kPa), t_1, table

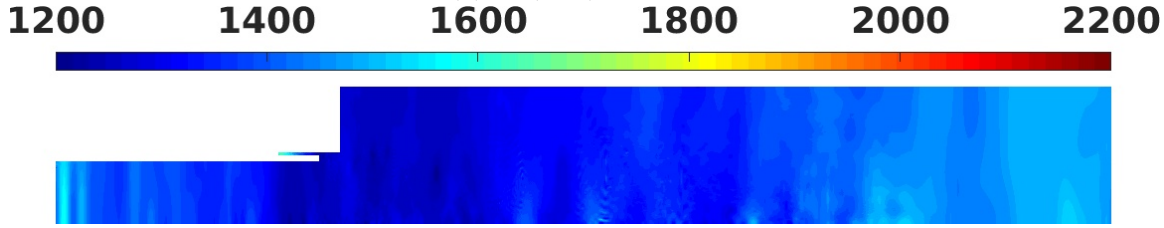

(b) $\overline{P}$ (kPa), t_1, NN_b

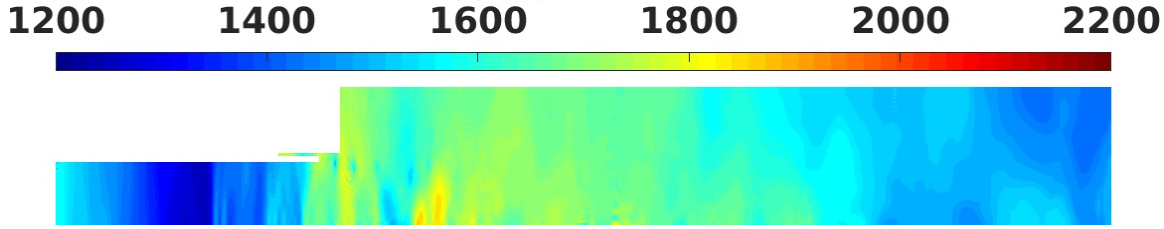

(c) $\overline{P}$ (kPa), t_2, table

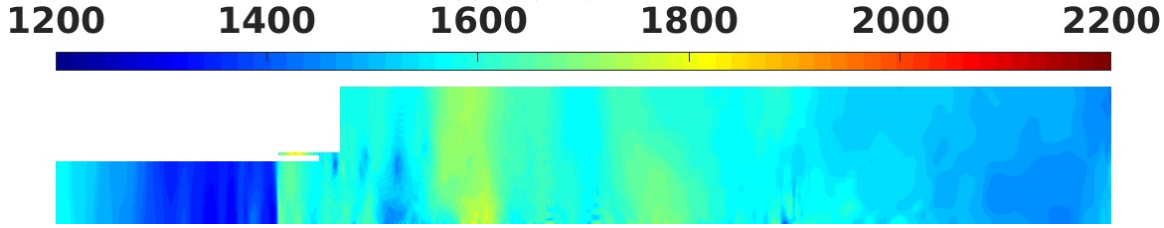

(d) $\overline{P}$ (kPa), t_2, NN_b

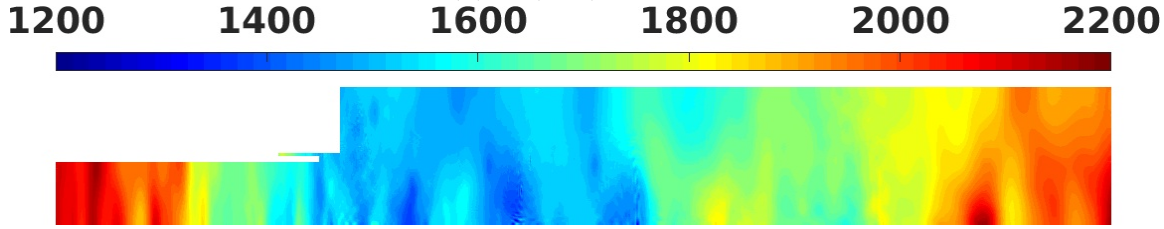

(e) $\overline{P}$ (kPa), t_3, table

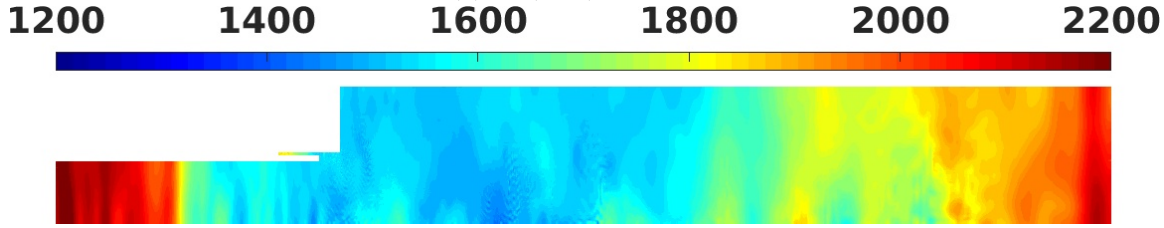

(f) $\overline{P}$ (kPa), t_3, NN_b

Figure 4.26: 14-cm, transient: pressure snapshots from the NN_b-based and the table-based simulations

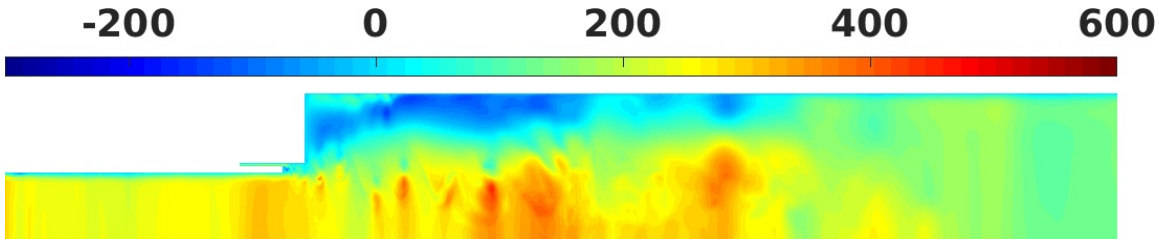

(a) $\widetilde{U}$ ($\mathrm{m\,s^{-1}}$), t_1, table

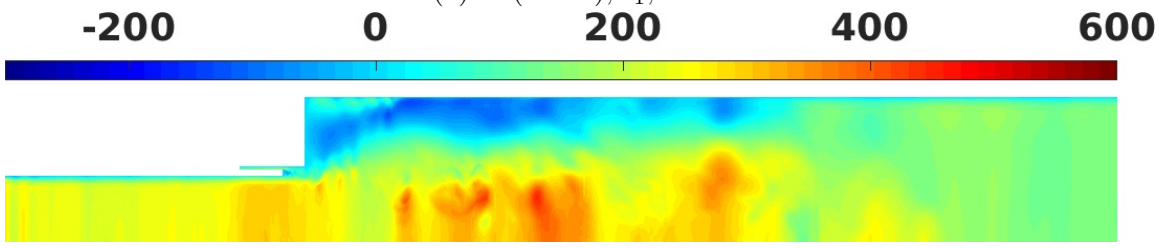

(b) $\widetilde{U}$ ($\mathrm{m\,s^{-1}}$), t_1, NN_b

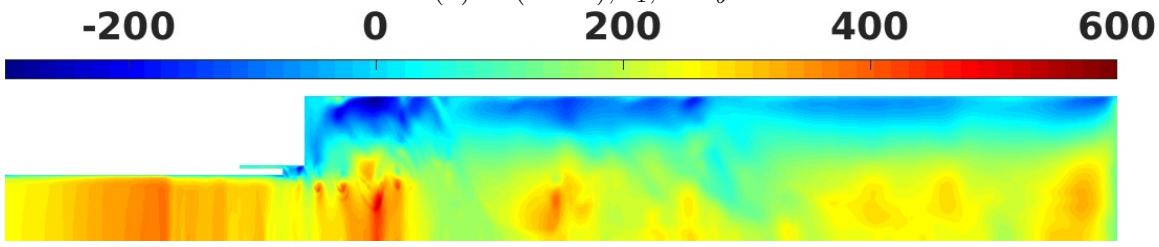

(c) $\widetilde{U}$ ($\mathrm{m\,s^{-1}}$), t_2, table

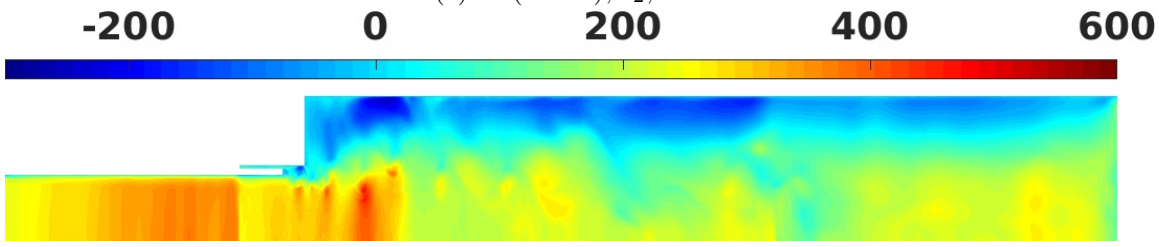

(d) $\widetilde{U}$ ($\mathrm{m\,s^{-1}}$), t_2, NN_b

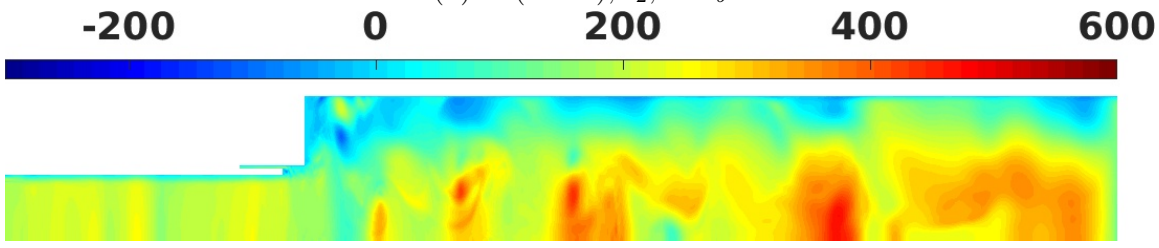

(e) $\widetilde{U}$ ($\mathrm{m\,s^{-1}}$), t_3, table

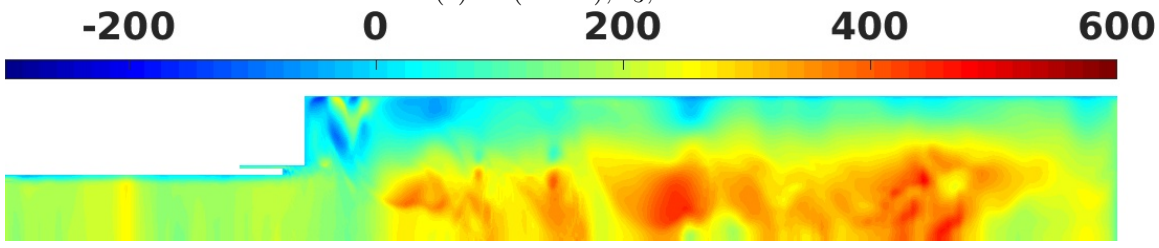

(f) $\widetilde{U}$ ($\mathrm{m\,s^{-1}}$), t_3, NN_b

Figure 4.27: 14-cm, transient: axial velocity snapshots from the NN_b-based and the table-based simulations

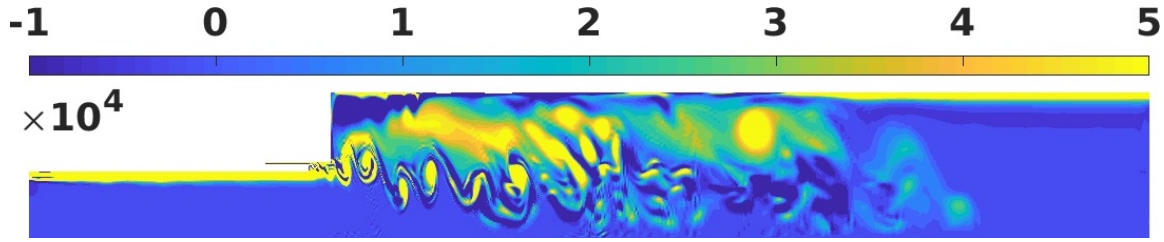

(a) $\widetilde{\Omega}$ (s^{-1}), t_1, table

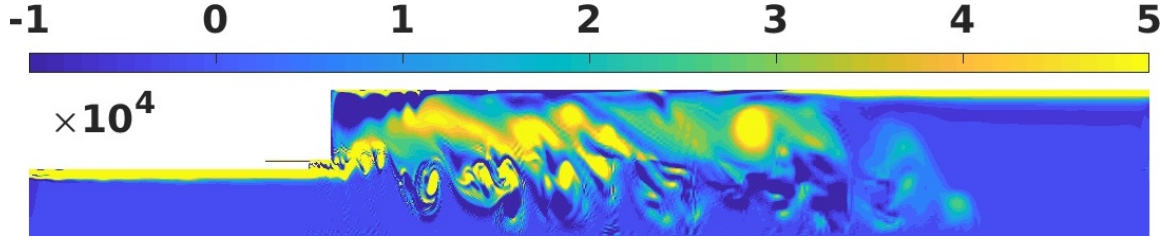

(b) $\widetilde{\Omega}$ (s^{-1}), t_1, NN_b

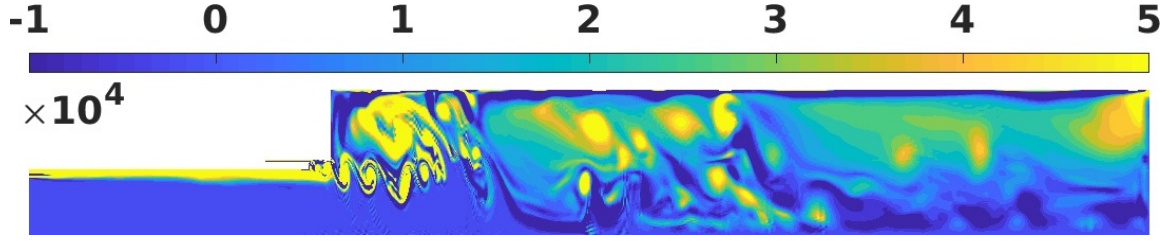

(c) $\widetilde{\Omega}$ (s^{-1}), t_2, table

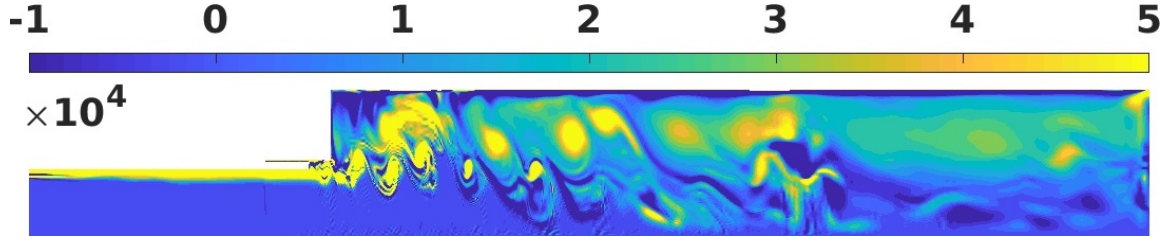

(d) $\widetilde{\Omega}$ (s^{-1}), t_2, NN_b

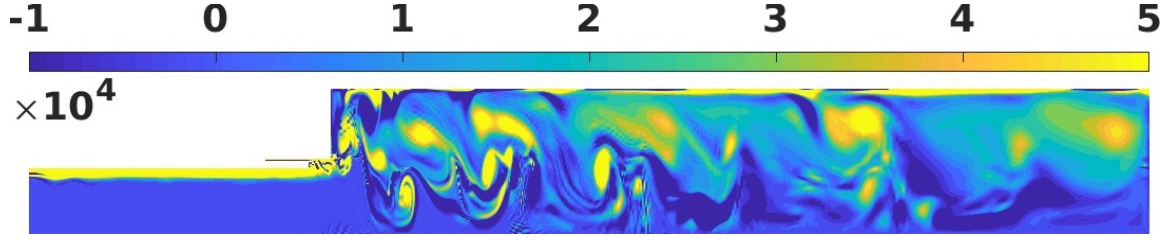

(e) $\widetilde{\Omega}$ (s^{-1}), t_3, table

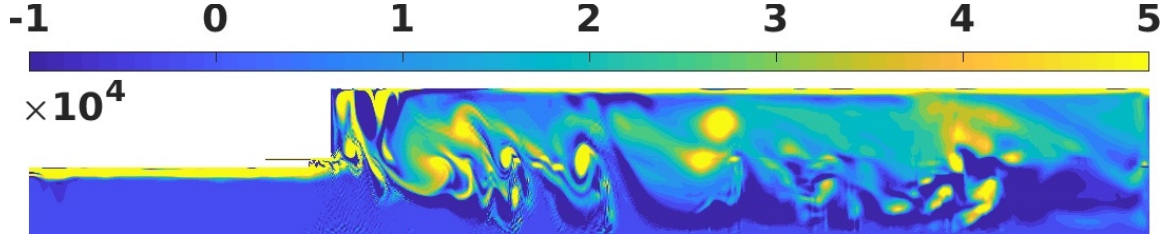

(f) $\widetilde{\Omega}$ (s^{-1}), t_3, NN_b

Figure 4.28: 14-cm, transient: vorticity snapshots from the NN_b-based and the table-based simulations

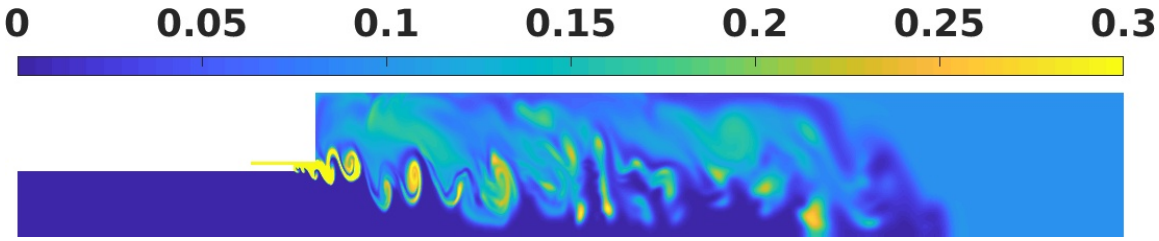

(a) $\widetilde{Z}$, t_1, table

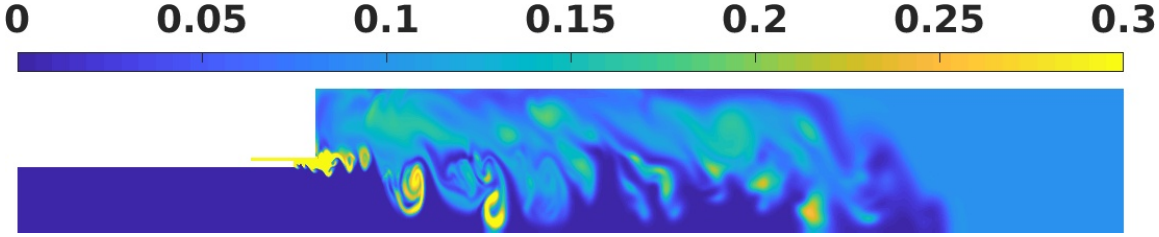

(b) $\widetilde{Z}$, t_1, NN_b

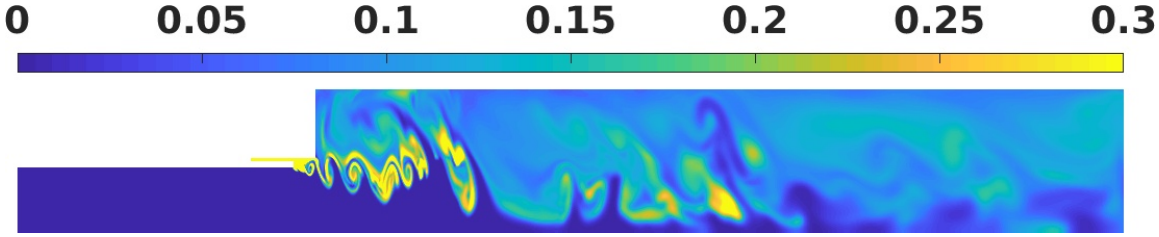

(c) $\widetilde{Z}$, t_2, table

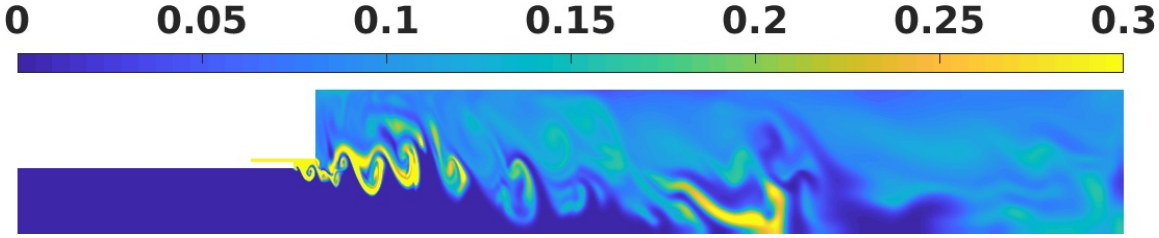

(d) $\widetilde{Z}$, t_2, NN_b

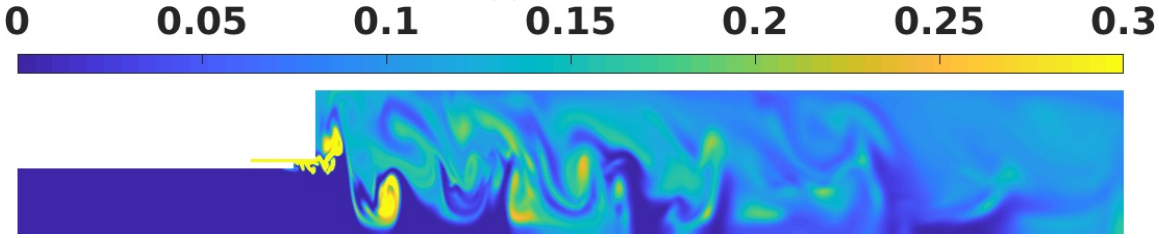

(e) $\widetilde{Z}$, t_3, table

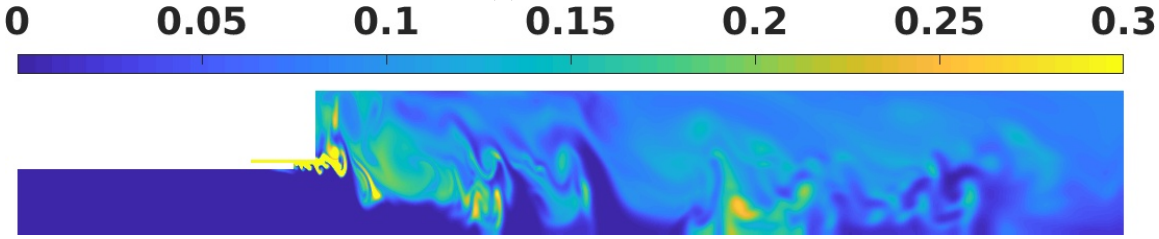

(f) $\widetilde{Z}$, t_3, NN_b

Figure 4.29: 14-cm, transient: mixture fraction snapshots from the NN_b-based and the table-based simulations

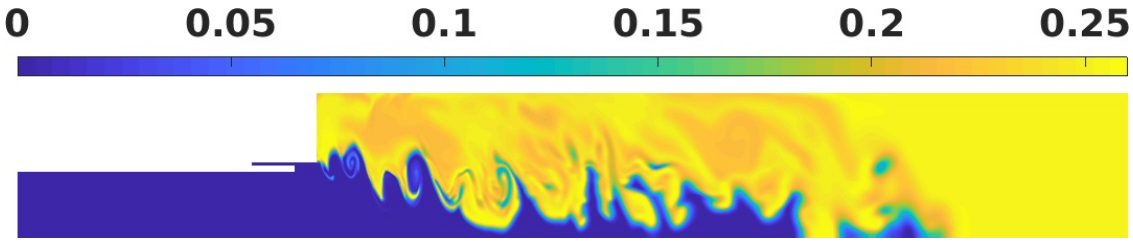

(a) $\widetilde{C}$, t_1, table

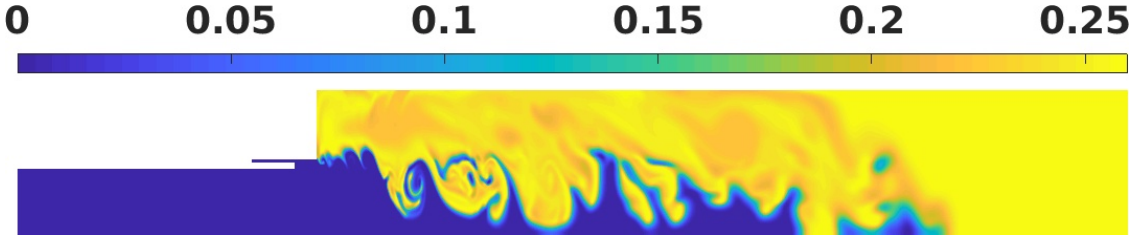

(b) $\widetilde{C}$, t_1, NN_b

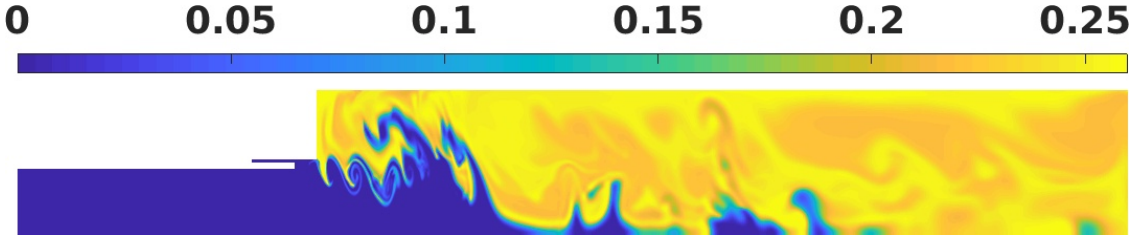

(c) $\widetilde{C}$, t_2, table

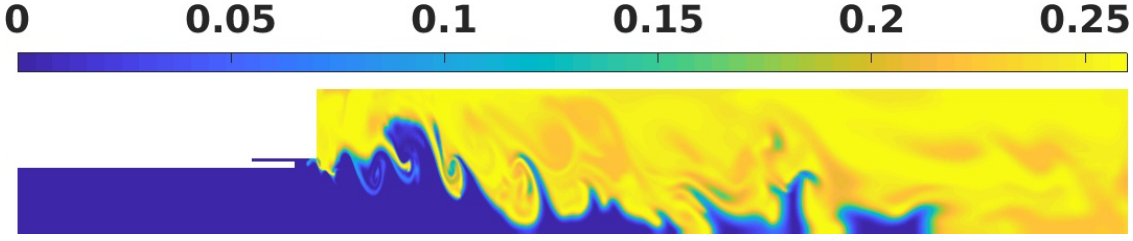

(d) $\widetilde{C}$, t_2, NN_b

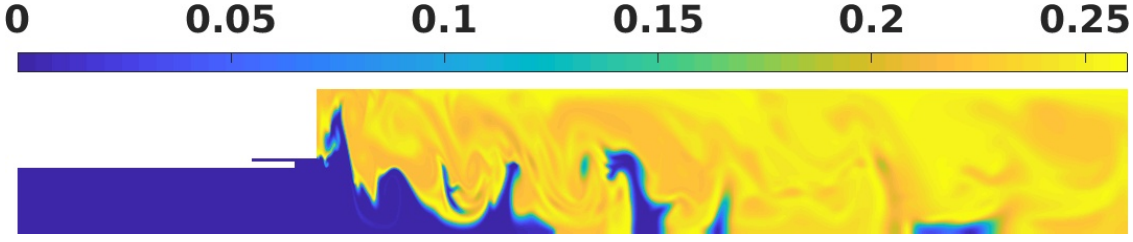

(e) $\widetilde{C}$, t_3, table

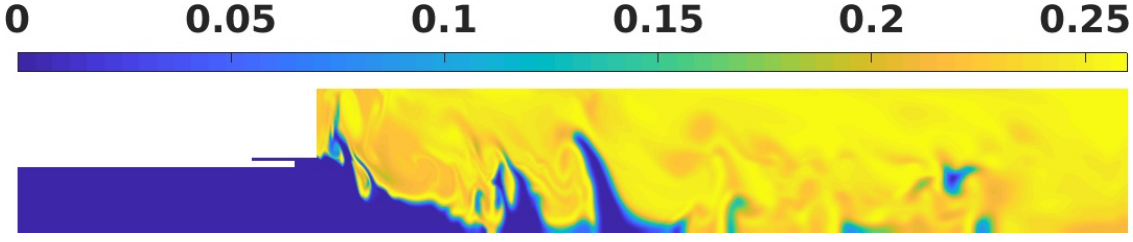

(f) $\widetilde{C}$, t_3, NN_b

Figure 4.30: 14-cm, transient: progress variable snapshots from the NN_b-based and the table-based simulations

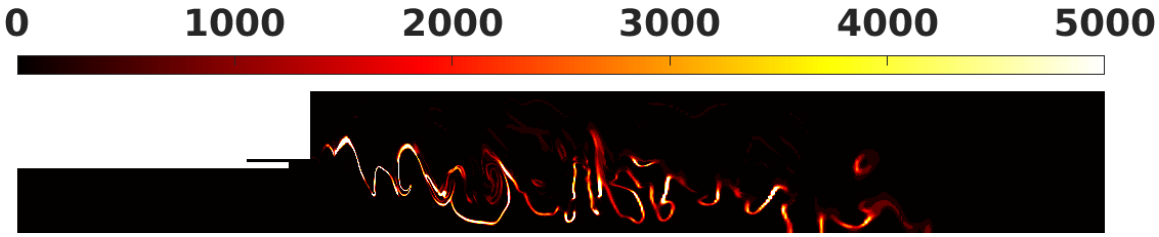

(a) $\widetilde{\dot{\omega}}_C$ ($\mathrm{kg\,m^{-3}\,s^{-1}}$), t_1, table

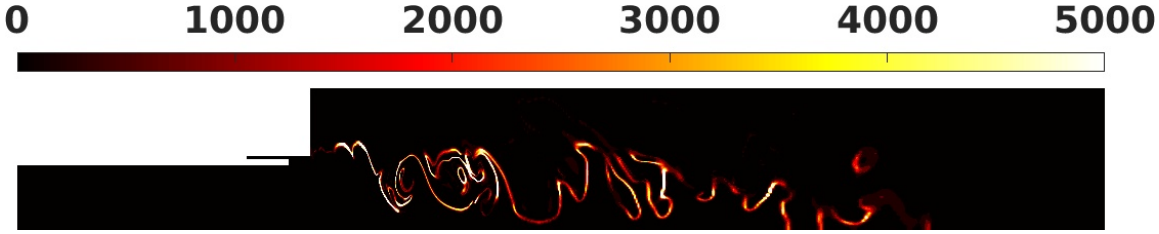

(b) $\widetilde{\dot{\omega}}_C$ ($\mathrm{kg\,m^{-3}\,s^{-1}}$), t_1, NN_b

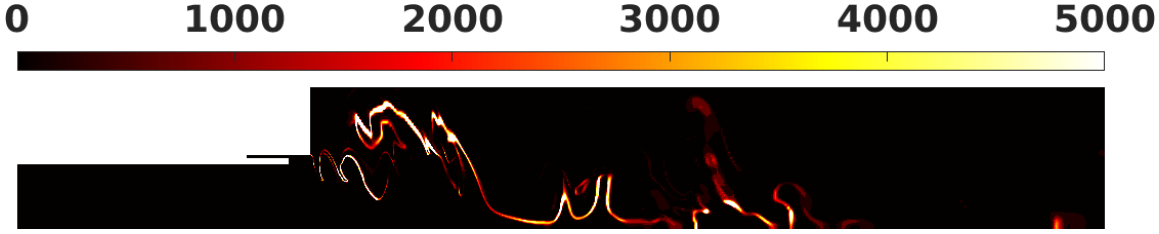

(c) $\widetilde{\dot{\omega}}_C$ ($\mathrm{kg\,m^{-3}\,s^{-1}}$), t_2, table

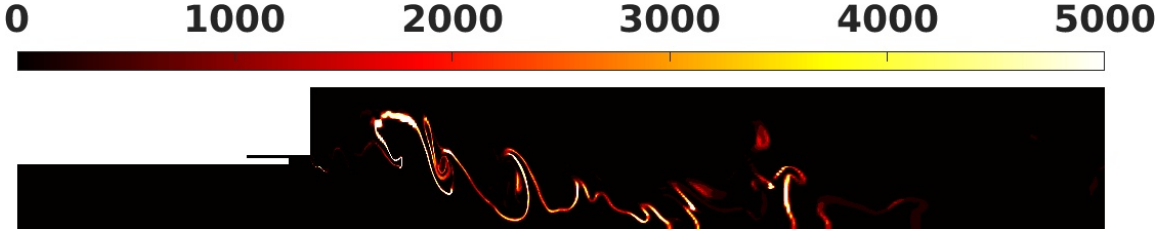

(d) $\widetilde{\dot{\omega}}_C$ ($\mathrm{kg\,m^{-3}\,s^{-1}}$), t_2, NN_b

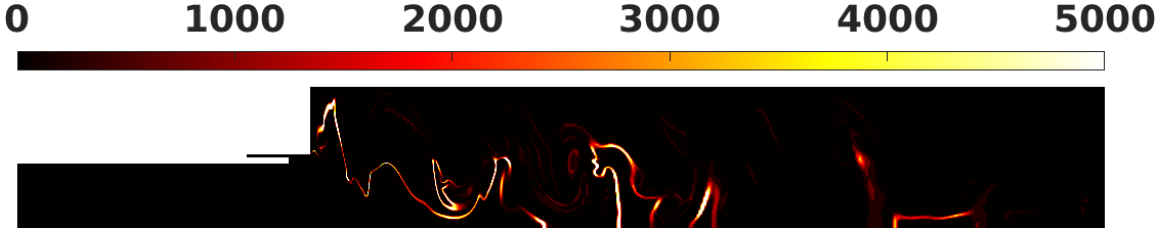

(e) $\widetilde{\dot{\omega}}_C$ ($\mathrm{kg\,m^{-3}\,s^{-1}}$), t_3, table

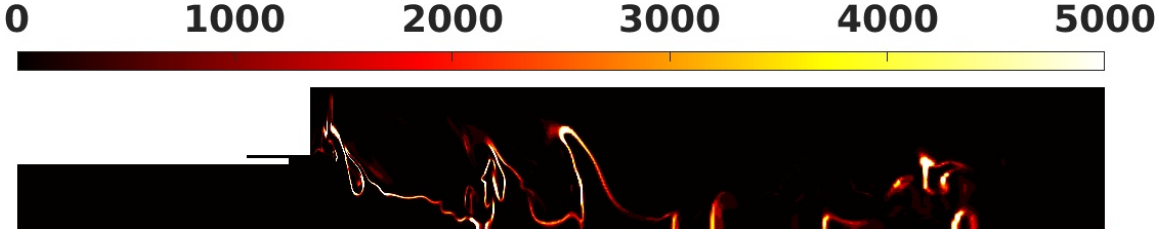

(f) $\widetilde{\dot{\omega}}_C$ ($\mathrm{kg\,m^{-3}\,s^{-1}}$), t_3, NN_b

Figure 4.31: 14-cm, transient: PVRR snapshots from the NN_b-based and the table-based simulations

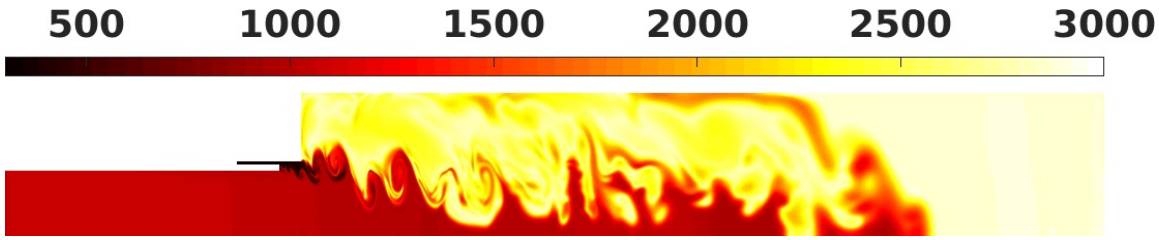

(a) $\widetilde{T}$ (K), t_1, table

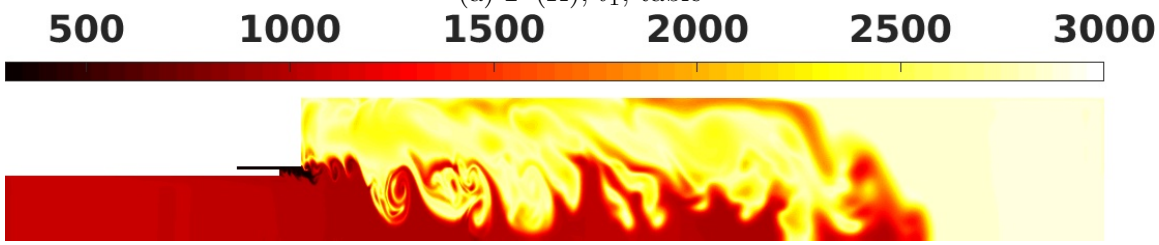

(b) $\widetilde{T}$ (K), t_1, NN_b

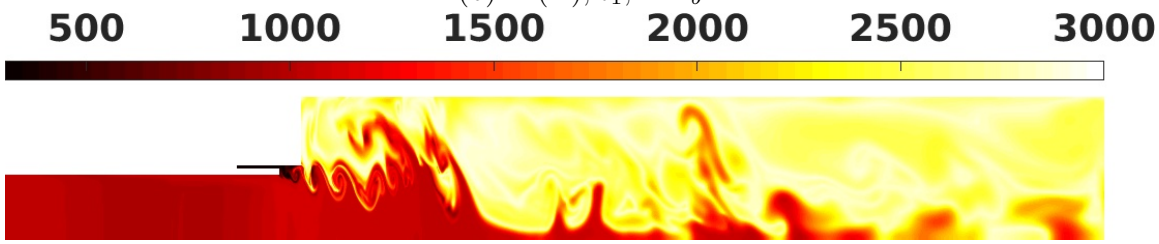

(c) $\widetilde{T}$ (K), t_2, table

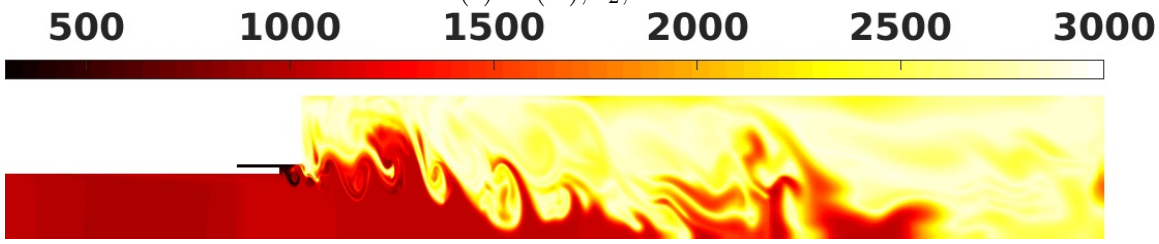

(d) $\widetilde{T}$ (K), t_2, NN_b

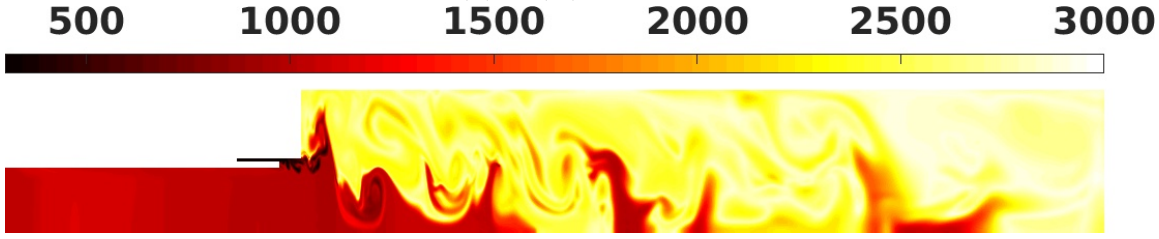

(e) $\widetilde{T}$ (K), t_3, table

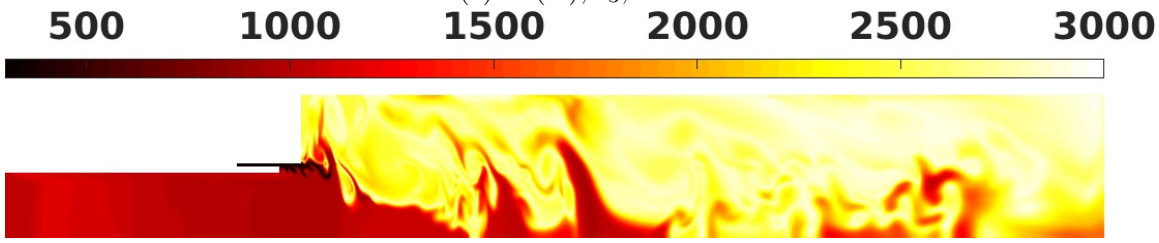

(f) $\widetilde{T}$ (K), t_3, NN_b

Figure 4.32: 14-cm, transient: temperature snapshots from the NN_b-based and the table-based simulations

9-cm Case

NN training was designed mostly for the purpose of reproducing the CFD simulation results of the CVRC experiment under unstable pressure oscillation conditions. This happens when the oxidizer post length is 14 cm. If the length is 9 cm, the pressure oscillations grow to a limit cycle, which is much smaller than in the 14-cm case. So the 9-cm is considered to be stable. Next, to validate its generality, the NN_b model, which was successfully implemented in the 14-cm transient case, is also implemented in the 9-cm case. The relative error between the NN-based and the table-based simulations is shown as spatial distribution in Figure 4.33a, and as numerical distribution in Figure 4.33b.

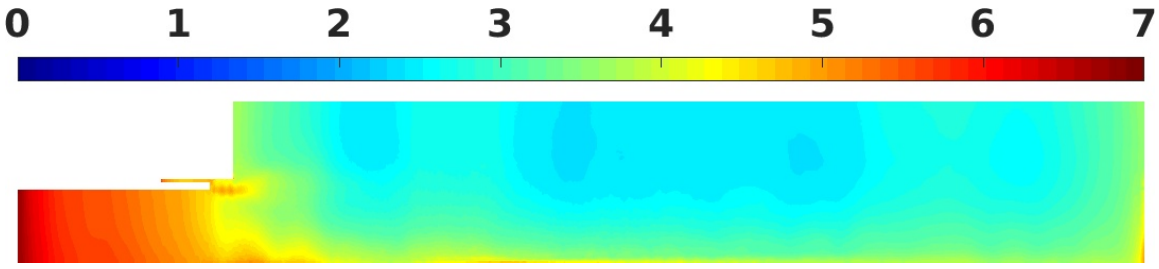

(a) Overall relative error (%)

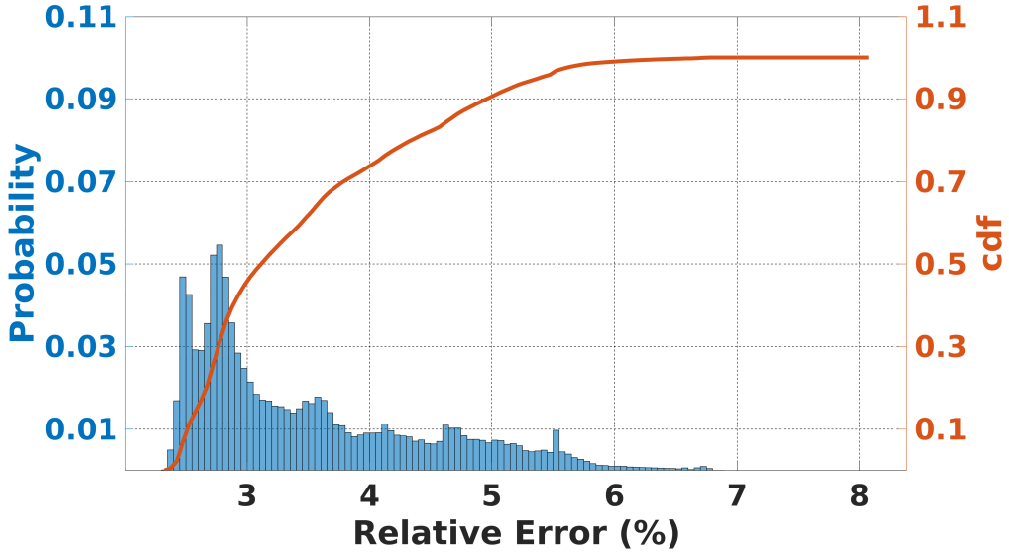

(b) Overall relative error (%) distribution

Figure 4.33: 9-cm case: distribution of relative error (%) between pressure signals calculated from the NN_b-based and the table-based simulations

The highest error occurs in the oxidizer post, as the NN is not forced to have certain values there, whereas, the table values are enforced at the non-reacting zones.

The correlation of the fluctuations of the pressure signals from their mean value from the NN_b-based and table-based simulations is shown Figure 4.34a, and Figure 4.34b providing the spatial and numerical distribution of the correlations, respectively. The oscillations are not well correlated. The reason is that the oscillation amplitude (roughly about 50 kPa) is very small relative to the mean value (roughly about 1600 kPa). Essentially, the maximum oscillation amplitude is around 3% of the mean value, and it can be considered as noise.

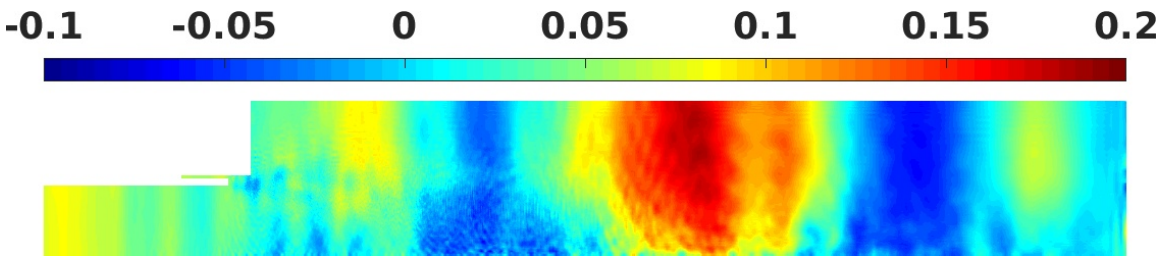

(a) Fluctuation correlations

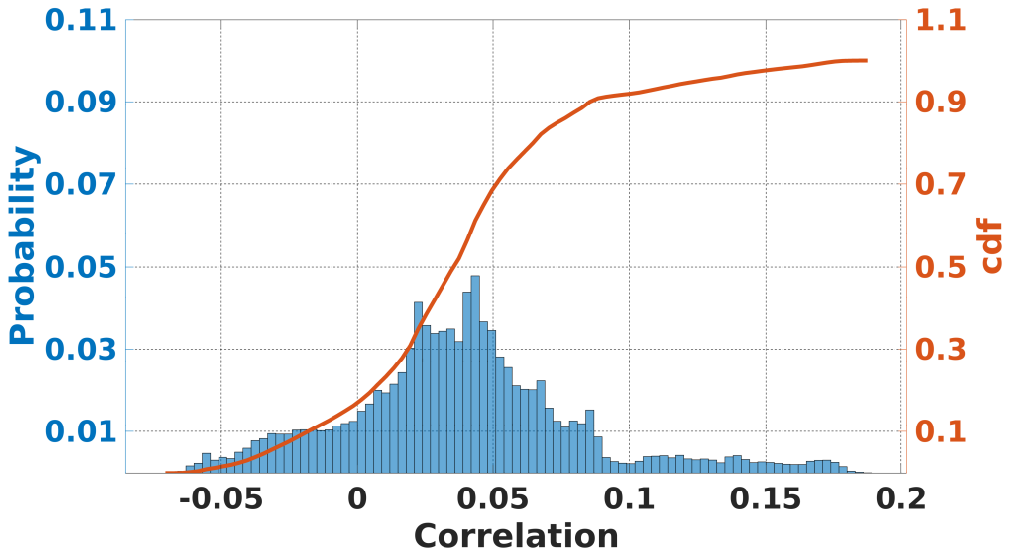

(b) Fluctuation correlation distribution

Figure 4.34: 9-cm case: pressure fluctuation correlation between calculated from the NN_b-based and the table-based simulations

The distribution ratio of pressure fluctuation rms in the NN_b-based simulation (Figure 4.35b) to that in the table-based simulation (Figure 4.35a) is shown in Figure 4.35c. Most of the

points have a similar rms value. Here again, the NN_b-based simulation overestimated the rms values. Both the rms values and their spatial gradients in the 9-cm case are lower than the ones in the 14-cm unstable case. The pressure rms values are higher at the inlet, and they become smaller throughout the combustor.

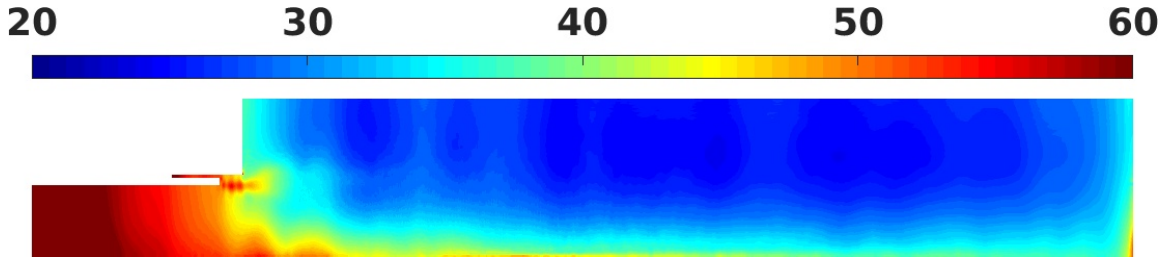

(a) Table-based pressure signal rms (kPa)

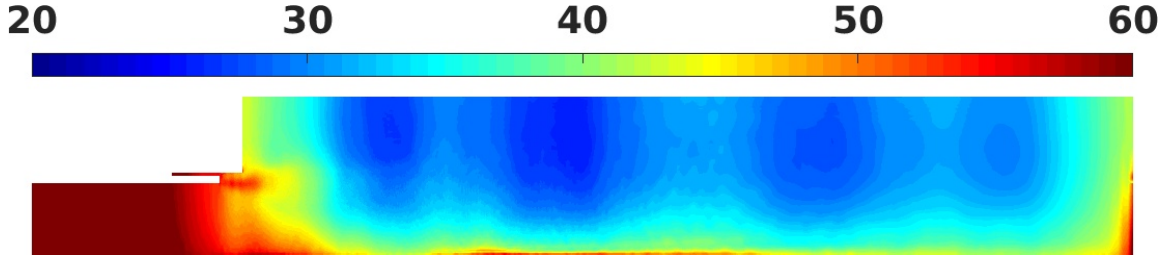

(b) NN_b-based pressure signal rms (kPa)

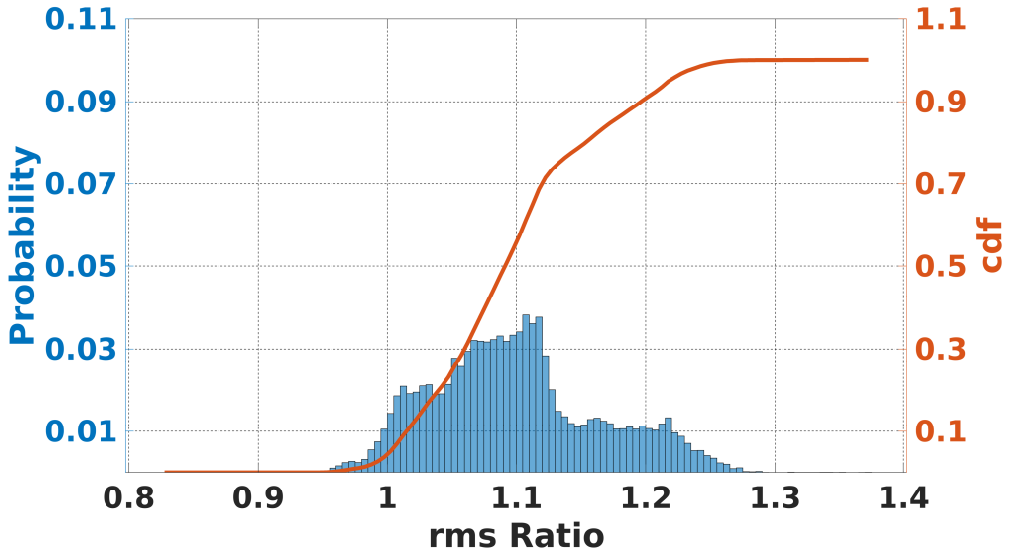

(c) rms ratio distribution

Figure 4.35: 9-cm case: the distribution of pressure fluctuation rms ratio calculated from NN_b-based (4.35b) to the one calculated from table-based (4.35a) simulations

Figure 4.36 compares the pressure signal at the antinode (10 cm) and near the nozzle (37 cm) on the top wall, calculated from the NN_b-based simulation with that from the table-based simulation.

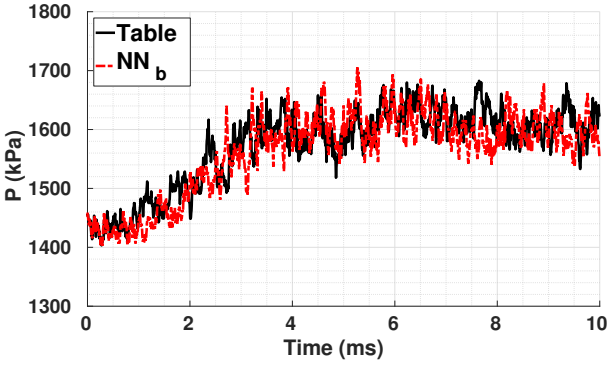

(a) Pressure signal at $x = 10$ cm

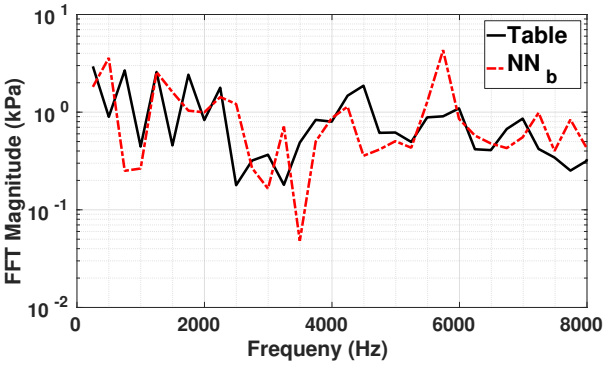

(b) Pressure FFT at $x = 10$ cm

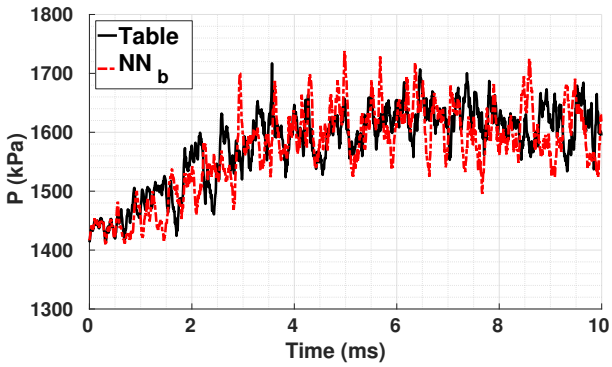

(c) Pressure signal at $x = 37$ cm

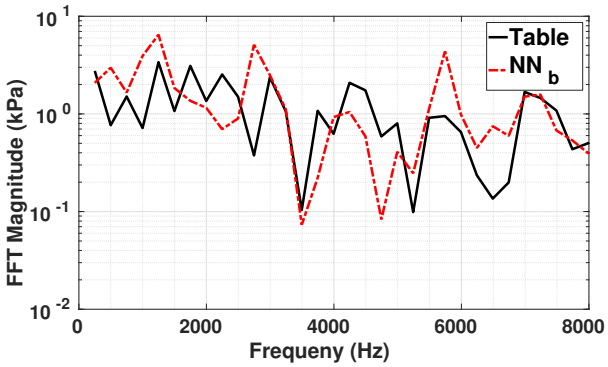

Figure 4.36: 9-cm case: comparison of pressure signals on the wall, at pressure antinode and near the nozzle, between the NN_b-based and the table-based simulations

At the antinode, the correlation is -3.68%, and near the nozzle, the correlation is 0.32%. At these points, overall relative errors are 2.71% and 3.25%, respectively. The rms ratio is 108.32%, and the mean value is estimated with 0.8% error at $x = 10$ cm. At $x = 37$ cm, the rms ratio is 125.11%, and the mean value is estimated with 0.8% error. The low correlations between the fluctuations of signals are because of the noisy nature of the pressure waveform in this configuration. Here, we are not interested in capturing noise, and we did not pursue refining the NN for a better performance. However, although it is harder to generate a fully correlated signal, the modal frequencies and signal trends are similar between the NN-based and table-based simulations. As shown in Figure 4.36b and Figure 4.36c, the frequency

contents of pressure signals at both of these points resemble noisy behavior, as the amplitude of higher frequencies is in the same order as the lower ones. This behavior is captured in both simulations.

The pressure mode shape shows similar behavior in Figure 4.37 for the mean value and the first and the second mode shapes, where the modes are not predicted as well as the mean. The first and the second modes in the 9-cm case have relatively small magnitudes; also, the magnitude of the modes are approximately equally distributed. In the combustion zone, the first mode is approximately 0.31% of the mean in the NN-based simulation and 0.22% in the table-based simulation. Similarly, the second mode is approximately 0.25% of the mean in the NN-based simulation and 0.19% in the table-based simulation in the combustion zone.

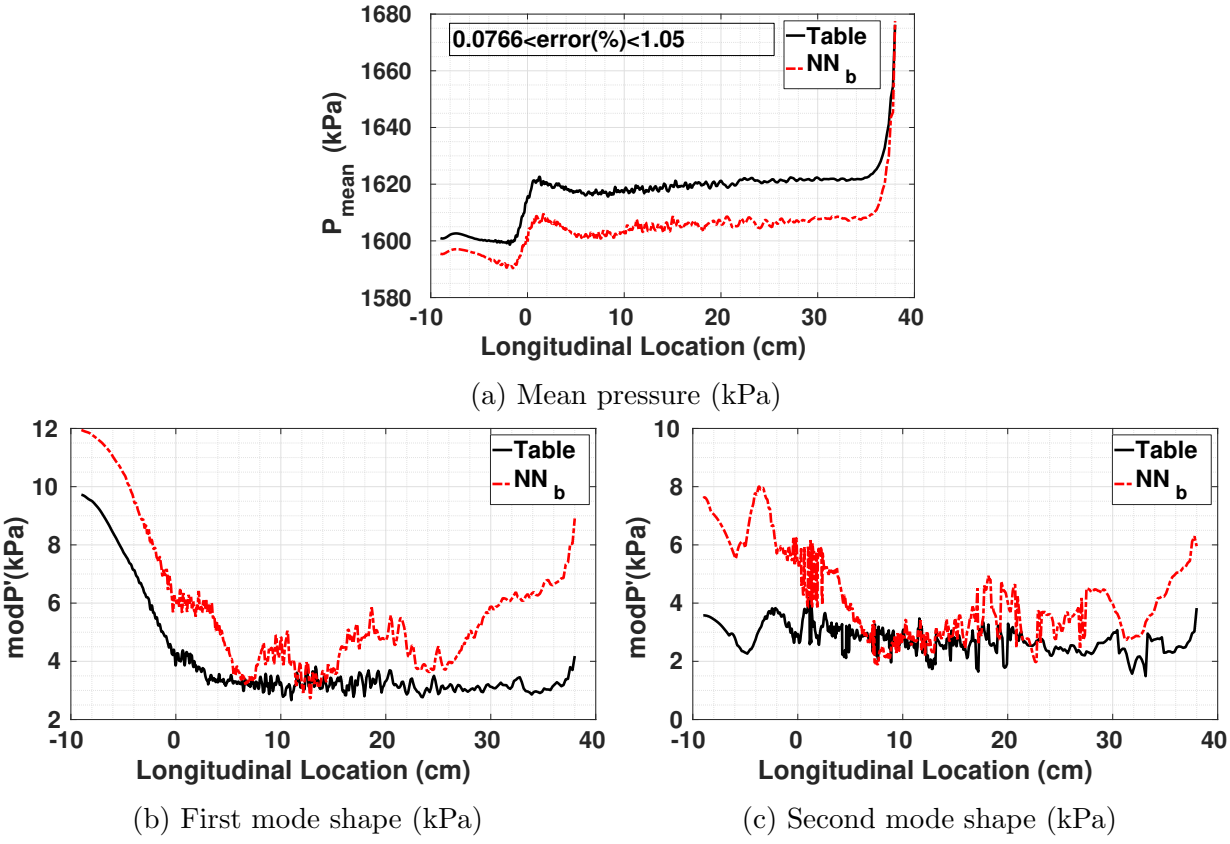

(a) Mean pressure (kPa)

(b) First mode shape (kPa)

(c) Second mode shape (kPa)

Figure 4.37: 9-cm case: comparison of pressure mean and the first and second mode shape between NN_b-based and table-based simulations

Since the 9-cm oxidizer post configuration leads to a stable configuration, the observed pressure fluctuations resemble relatively small amplitude. Essentially, the dynamic of the system is governed significantly by turbulent combustion rather than acoustic behavior. The turbulence leads to chaotic behavior in fluctuations for different quantities. Therefore, it is expected from a model to regenerate similar statistical behavior, such as Rayleigh Index, rather than regenerating exactly the same solution as the reference model.

ThemRI and RI are compared for the two simulations in Figure 4.38 and Figure 4.39, respectively. Comparing Figure 4.38a with Figure 4.38b and comparing Figure 4.39a with Figure 4.39b show that the NN_b-based simulation is very similar to the table-based one in capturing the behavior near the corner and the RI shape. Since the 9-cm case is a stable one, the magnitude of RI and mRI are lower than those in the 14-cm case. Low RI shows that there is no instability occurring.

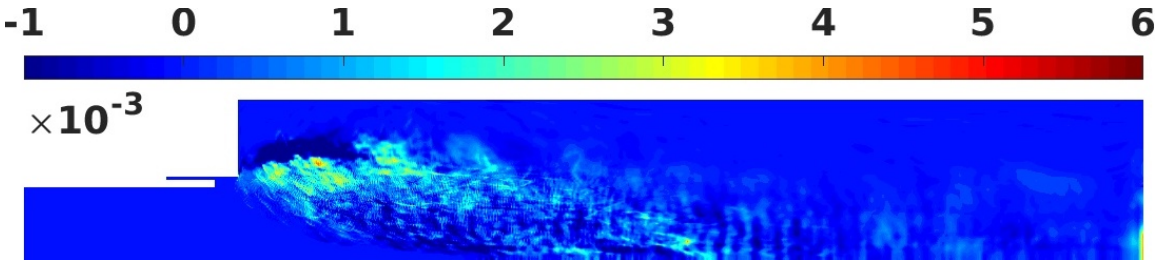

(a) Table-based CFD: mRI

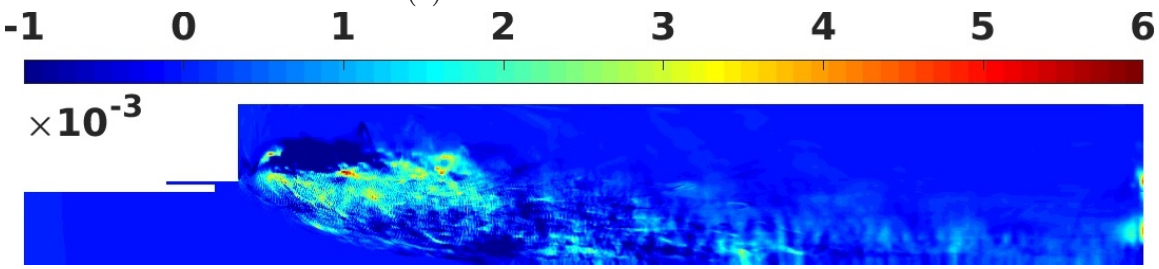

(b) NN_b-based CFD: mRI

Figure 4.38: 9-cm case: comparison ofmRI from the NN_b-based and the table-based simulations

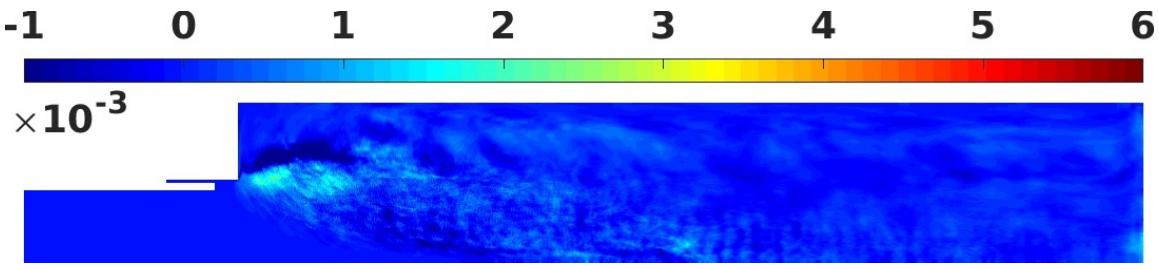

(a) Table-based CFD: RI

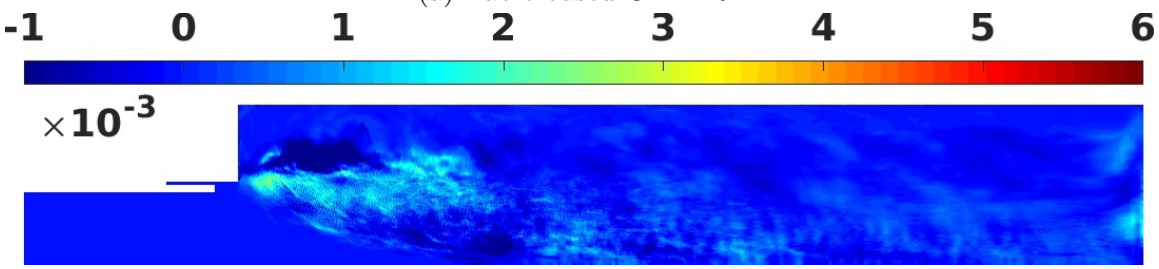

(b) NN_b-based CFD: RI

Figure 4.39: 9-cm case: comparison of RI afrom the NN_b-based and the table-based simulations

4.2.3 Computational Cost

The computational cost for the NN-based and table-based simulations are compared in Table 4.3. One millisecond (200 snapshots) of data is generated from the dynamic equilibrium test cases for each of the simulations. The required CPU time to generate each of the snapshots is calculated for each of the three simulations; the minimum, average, standard deviation, and the maximum of the required CPU time for generating each simulation time step are reported in Table 4.3. The table-based simulation is considered as the reference, and the relative values of these quantities to the reference are also reported for the NN_a and NN_b. The average CPU times per time step for the NN_a-based and the NN_b-based simulations are around 39.2 and 100.7 times the average CPU time per time step of the table-based simulation. The table-based simulation is essentially the same code that was developed and discussed in [22]. [22], reported a 0.28 core-hour per millisecond for the computational cost of an axisymmetric simulation with $6.26e4$ grid points (the current work uses $1.375e5$ grid points) based on a flamelet model for combustion of 27 species, while a similar

work, discussed in [25], reported 53 core-hour per millisecond for the computational cost of an axisymmetric simulation with $5.5e4$ grid points based on a general equation and mesh solver (GEMS) for combustion of 4 species. Also, one should note that the computational costs for the NN-based simulations reported here are based on a non-optimized code; there is a potential to reduce the NN-based simulation computational cost considerably by applying methods to parallelize and optimize the code. Yet, optimizing the computational cost was not in the scope of this work.

Table 4.3: CPU time per time step between two consecutive time samples statistics comparison among table-based, NN_a-based, and NN_b-based simulations for 14-cm dynamic equilibrium case

Computational Time Step		**Table**	NN_a	NN_b
min	***Absoulte***	*15.000*	*558.000*	*1444.000*
	Relative	1.000	37.200	96.267
mean	**Absoulte**	18.407	721.201	1841.935
	Relative	1.000	39.181	100.067
std	**Absoulte**	5.574	255.471	778.595
	Relative	1.000	45.832	139.681
max	**Absoulte**	53.000	1995.000	7072.000
	Relative	1.000	37.642	133.434

Although NN-based closure models increase the computational cost over a flamelet table model, they reduce the required memory significantly. The flamelet model requires around 1.2 GB of the hard disk memory, while NN_a and NN_b require around 144.2 kB and 376 kB, respectively, to be stored on our computer machine. We estimated that loading NN-based models into CFD causes the required RAM to increase less than 1 MB, while loading the table-based model into CFD increases the required RAM around 276 MB. The difference between the volume of data when it is stored on the hard disk vs. when it is loaded in the RAM is because of the data on hard disk is stored as text file, while it is loaded as numbers in computer RAM. The very low required memory by NN-based models paves the way for utilization of Graphic Processing Units (GPUs) and consequently high levels of parallelization, which can significantly reduce the computational cost. Particularly, in 2010,

[86] provided examples of 16 to 137 times speedup in fluid mechanics related problems when they are implemented on GPU.

4.3 Concluding Remarks

In this study, we developed two deep learning neural network sets with different levels of complexity to represent a flamelet model in turbulent combustion with unsteady pressure. The design of the networks was explained, including input-output and training set selection. The goal is to explore the capability of neural networks as a tool for combustion modeling. The two developed models (NN_a and NN_b) are first validated by testing on the flamelet table data as an offline test and then validated by being implemented in CFD simulations of different cases and compared with the table-based simulations. These simulations include dynamic equilibrium and transient simulations on an unstable rocket configuration (14-cm oxidizer CVRC), and transient simulation in a stable configuration (9-cm oxidizer CVRC). NN_b, which contains more layers than NN_a, has shown a better performance both in offline and online validation. In the offline test, the difference between their error is very small (up to 2%). NN_b wins over the NN_a model in the accuracy competition. However, its required computational cost is 2.5 times of that for NN_a for retrieving one set of outputs.

In the dynamic equilibrium case, the two NN-based models have similar performance according to measures such as overall relative error and fluctuation correlation. The NN_a-based simulation results were in agreement with the table-based simulation results. The one shortcoming observed, however, was the slight underestimation of mRI near the dump plane through the NN_a-based simulation.

In the transient case, the main shortcoming of the NN_a-based simulation is in predicting the pressure limit cycle amplitude or rms of pressure fluctuation. On average, only 75% of

the fluctuation energy is captured by the NN_a simulation; whereas, the NN_b simulation can capture the amplitude with great consistency, close to 100%. In the transient case, NN_b is the proper model as it is capable of faithfully reproducing the unstable acoustic behavior. The NN_b-based model was also implemented in a case with 9-cm oxidizer post, which was characterized as a stable configuration of CVRC. Although the mean pressure was accurately predicted in this test, the pressure fluctuations of the NN-based simulation did not follow those from the table-based simulation exactly. In the stable case, the dynamics are significantly governed by turbulent combustion rather than acoustic behavior. The significance of turbulence combustion causes the simulation to resemble more chaotic behavior in different quantities. Particularly, our analyses in all three simulations show that NN-based simulation provides more correlated results with the table-based simulation, when the acoustic phenomenon dominates the system over the turbulence.

The results show that although NN requires higher computational cost than a look-up table representation of a flamelet table, it requires much less memory. This feature provides the flexibility of using GPU to reduce the associated computational cost [86].

Chapter 5

Physics-aware NN Design Based on CFD Simulation Data

In this chapter, we look into NN-based closure models from a different aspect. The objective here is to use data from CFD simulations for training NN models to replace the flamelet tables in other CFD simulations. [1]

5.1 Neural-Network Based Closure Model For CVRC: Learning From CFD Simulation Data

The ultimate goal of using NN is to develop a fully data-driven model from experimental and numerical data. This goal can be achieved if a rich enough data set of training samples is provided that covers different regions of flame dynamics. Since each NN is essentially designed to learn the pattern among these samples, the richer the training data set is, the more comprehensive model can be developed. In this work, we use only the data that are

[1] The material of this chapter is adapted from [87], submitted to combustion and flame Journal

generated from a single injector configuration. However, in a multi-dimensional system like combustion, one configuration observes only a manifold or a subset and not the whole dynamic. The availability of comprehensive data is essential in developing data-driven models. However, comparing the NNs trained based on limited data helps to test the extent of the modeling power of NN and paves the way for developing further and more complicated methods. The process of the NN development in this chapter is depicted in Figure 5.1.

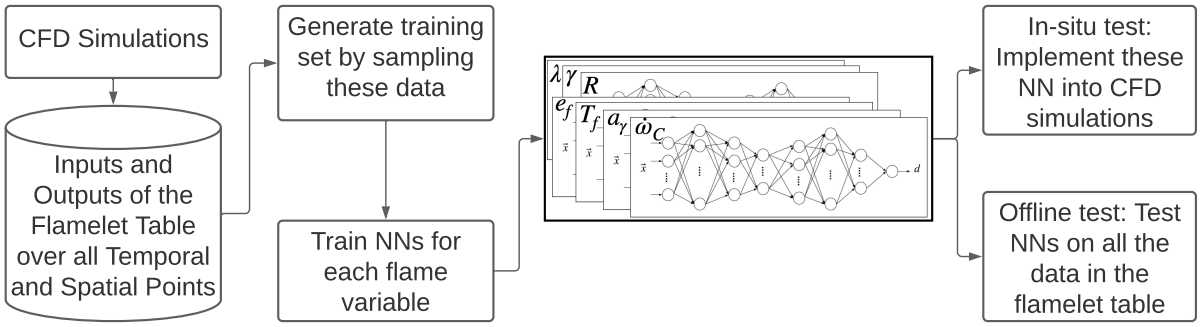

Figure 5.1: The NN development process

5.1.1 NN Development: Sample Selection

A challenge that is particularly associated with learning from large data sets (numerical and or experimental data) is the selection of a sufficiently representative training set that does not lead to a high computational cost for the training process. For example, a CFD simulation of spontaneous instability, in which the pressure signal grows from a relatively low pressure amplitude to a large amplitude limit cycle, requires simulation of 10 ms of the system to capture the whole dynamic. This simulation, the so-called transient case [66], is used mainly as the training set source. Sampling this simulation at 200 kHz leads to 2000 snapshots of the combustor. A snapshot of the combustor has around 137500 grid points in our axisymmetric set-up. Thus, the pool of data generated by such simulation has around 275 million points. Handling such a large data set and selecting the best training from these points is a challenging task.

In order to select the best training set at this stage, the framework of the flamelet table is utilized. In the table-based CFD set-up, the flame variables for a given input vector are calculated by linearly interpolating the values stored in the flamelet table. We then form the training set from the table values and corresponding inputs that have been called through the CFD simulation of each configuration. As mentioned above, by adding more simulations and experiments to the main pool of data, a richer set can be developed at the cost of more complex data management at the training stage. Here, we mainly use the transient case simulations of a combustor with a 14-cm oxidizer post, which is a highly unstable case. This data set leads to developing a relatively good model for every variable except for PVRR, due to lack of data in very high pressure regions. To remedy this situation, data from another simulation that is started after the occurrence of the instability, i.e. high limit cycles have set-in, the so-called dynamic equilibrium case is also included in the training set for PVRR. The flamelet table includes 10,342,800 data points. The observed points of the table from the transient case amount to 338283 points. Using only the transient case, significant regions of the table are not observed in the training set. Figure 5.2 shows the regions of the table that are observed in the training set as a function of each two elements of the input vector, which has four elements. The white regions in the figures show the part of the table that is not represented in the training samples. The colored graphs show the logarithm (base 10) of the concentration of samples in each region. In each graph for each of the two inputs shown, the number of observed points is the sum over the two other inputs that are not shown.

To have a more reliable model, it is important that our model meets the physics-related constraints of the system. The training set generated from sampling the CFD simulation data does not necessarily include the boundary points of the flamelet table, and these points define the flame dynamics of the sub-grid counterflow model. For example, for every pressure, turbulence level, and progress variable, the species mass fractions and temperature are known when the flow is purely oxidizer or purely fuel, which are indicated by $\widetilde{Z} = 0$ and $\widetilde{Z} = 1$.

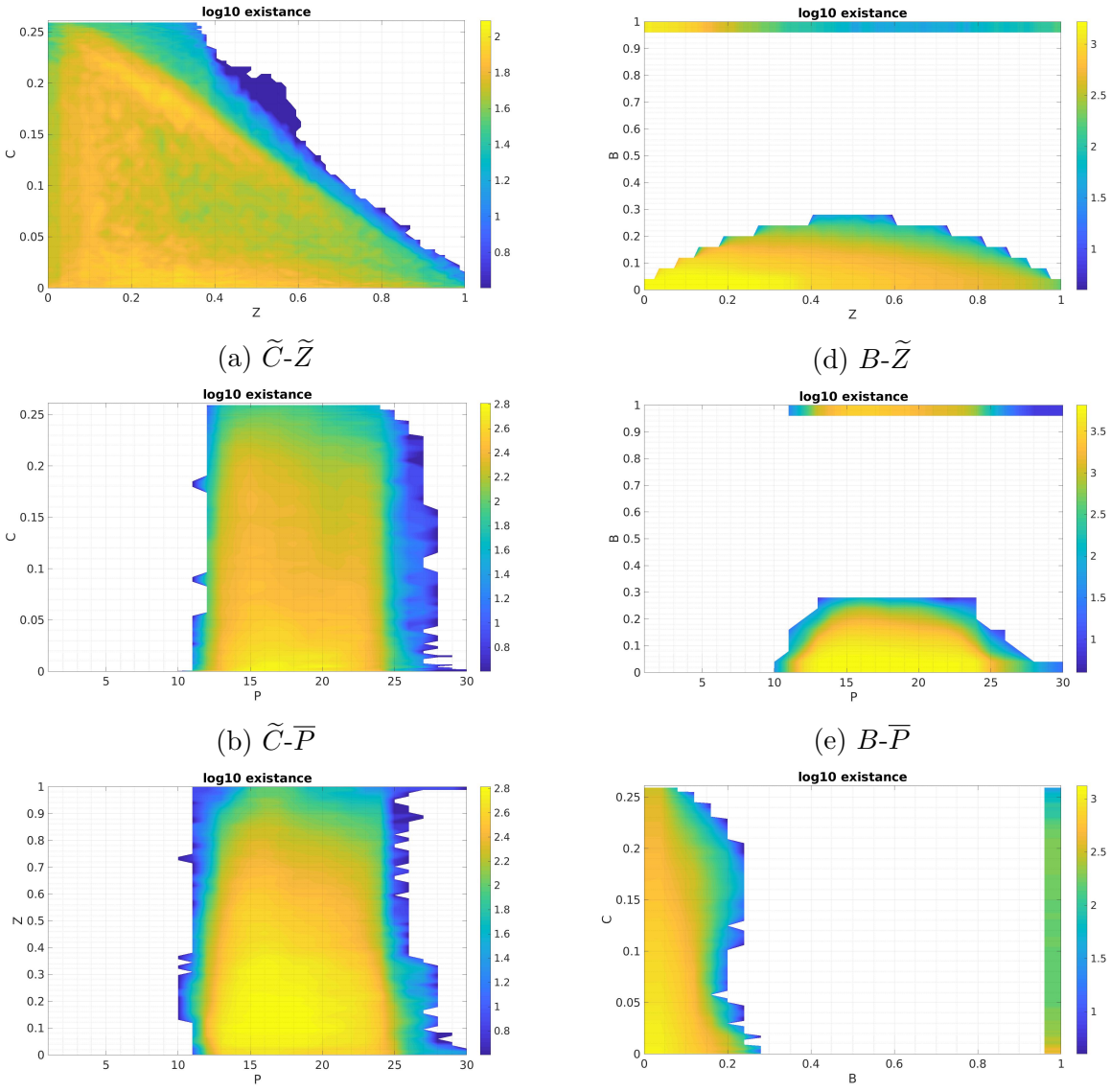

(a) $\widetilde{C}$-$\widetilde{Z}$ (d) B-$\widetilde{Z}$

(b) $\widetilde{C}$-$\overline{P}$ (e) B-$\overline{P}$

(c) $\overline{P}$-$\widetilde{Z}$ (f) $\widetilde{C}$-B

Figure 5.2: Coverage of the flamelet table by training set

Accordingly, the value of all other flamelet outputs is known at these two points, regardless of the availability of training data from these regions.

Another physical assumption that can help in the NN-based model development is the values of each variable when the progress variable is zero. At this point, there is no combustion, and the flamelet model is governed by the flow dynamics. Therefore, the training set can be reinforced by adding the parts of the table associated with points with $\widetilde{C} = 0$.

5.1.2 NN Development: Algorithm and Structure

The training set based on the transient CFD simulation is used to train the NNs for each output table variable. To this end, three main NN structures are proposed based on a trade-off between increasing accuracy and decreasing the computational cost in data retrieval. A NN with a lower number of neurons and layers but sufficiently small error is desired for each variable.

While the proposed structures are different for different variables, the training process is common. In all the NNs, the activation function in hidden layers is selected to be leaky rectified linear ($LReLU(x) = max(x, 0.001x)$ [79]), and in the output layer to be linear. The NN weights are initialized randomly by the Xavier initialization [83] algorithm and updated via the Adam update rule [77], used in the back-propagation algorithm. Mini-batch training mode is also used, as it is helpful to avoid local-minima in the training process and more efficiently handle large data sets. The issue of overfitting is observed even in simple regression problems, in which fitting a very high order polynomial leads to smaller fitting error but huge test error. To avoid overfitting and to improve the performance of the NN, we employed regularization during the training process.

The flamelet model assumes second-order ODEs for the species mass fractions and for the flame temperature. Other outputs of the flamelet model are essentially functions of species mass fractions and flame temperature. Thus, in developing NN-based models for those variables, the flame temperature is also considered as an input. Accordingly, we have managed to significantly improve the accuracy of our NN-based models for $\Phi_1 = [\widetilde{e}_f, \widetilde{R}, \widetilde{\lambda}, \widetilde{\gamma}, \widetilde{a}_\gamma]$. Including the flame temperature as an input along with the other flamelet inputs ($\Psi = [\widetilde{Z}, B, \widetilde{C}, \overline{P}]$) not only helps to improve the accuracy but also ensures that the flamelet outputs are consistent when utilized in a CFD simulation by maintaining correct physical dependencies

between different flame variables. A disadvantage of this approach is that the error in the model for $\widetilde{T_f}$ can propagate in other variables as well.

The NN designed for PVRR is the most expensive structure among all variables. Due to the very nonlinear dynamic of PVRR, finding an accurate NN model is a challenging task. Our study did not indicate a considerable improvement in coupling PVRR inputs with T_f. The large structure for PVRR is selected after testing many other smaller structures which failed to capture its dynamic. The size of each NN besides the training error and testing error for PVRR and other flame variables are provided in Table 5.1 and are further discussed in Sec. 5.2.

Table 5.1: Selected structure for each NN for the flame variables

	# of neurons in each layer	flop	training error(%)	testing error(%)
$\widetilde{T_f}$	4-15-10-15-1	375	0.59	4.83
$\widetilde{e_f}$	5-15-10-15-1	390	0.0566	0.57
$\widetilde{R}$	5-15-10-15-1	390	0.0526	0.65
$\widetilde{\lambda}$	5-15-10-15-1	390	0.21	3.57
$\widetilde{\gamma}$	5-15-10-15-1	390	0.0371	0.48
$\widetilde{a}_\gamma$	5-15-10-15-1	390	0.22	1.41
$\widetilde{\dot{\omega}_C}$	4-15-20-25-35-25-20-15-5-1	3490	1.49	32.86

In the third column of Table 5.1, the computational cost of generating one output from each of the proposed NNs is given in terms of flop. Implementing these NNs inside CFD costs around 5815 flop, which is the least NN-related computational cost that we could achieve among all of our several experiments, including our previous work [66]. As discussed in the literature, the computational cost issue related to the NN can be resolved by the utilization of GPU. However, in this work, CPU is used as the computational resource.

5.2 NN Performance Analysis

The designed NNs are validated through different levels of testing. The first test is conducted on the flamelet table itself. In the previous sections, the training performance of the NNs, as well as the test results on the flamelet table are discussed. The trained NN as described in Figure 5.1 are also implemented into CFD simulations. In addition to the dynamic equilibrium and the transient cases, another simulation exhibiting a triggered instability is analyzed. In this configuration, referred to as the triggering case, the wall thermal boundary condition is assumed to be isothermal at 1030 K, while in the other two cases, an adiabatic wall is considered. Nguyen et al., [23], extensively analyzed the triggering instability phenomenon with different excitation and also a different isothermal wall temperature. In this work, a set up with excitation through two periods of sinusoidal variation in mass flow rate is analyzed for the performance analysis of NN-based models.

5.2.1 Test on Flamelet Table

To analyze the performance of each NN, their outputs are compared with the corresponding outputs of the flamelet table, on the training set, and on the whole table. To compare the output sets the overall relative error (e_o) defined in Eq. (5.1) is used:

$$e_o = \frac{||\vec{d} - \vec{y}||_2}{||\vec{d}||_2} \tag{5.1}$$

Here, $\vec{d}$ represents the outputs of the truth model (flamelet table here), and $\vec{y}$ represents the outputs of the NN-based model. The training and testing errors are provided in Table 5.1, fourth and fifth columns. PVRR has the highest error in both cases. The variables in the ϕ_1 vector, which have flame temperature in their input set, are modeled with less than 0.25% in

training and 4% error in test error. The flame temperature is modeled with less than 0.6% in training and less than 5% in testing.

As discussed before, only parts of the flamelet library are included in the training set obtained from the CFD simulation (see Figure 5.2). The distribution of the input values collected is not uniform, and the performance of the NN in the training stage and consequently testing is skewed by these distributions. For example, the frequency of occurrence of inputs in the laminar region or regions with lower turbulence is higher than that of points with higher turbulence levels. Therefore, it is to be expected that the performance of NN in the laminar zone will be better than in the rest of the table.

In Figure 5.3, we also compare the outputs from the NNs (black crosses) for flame temperature, internal energy, gas constant, heat capacity ratio, its coefficient, and heat conductivity with the corresponding outputs from the flamelet table. Flame temperature is used as an extra input in the NN model for these variables (except itself). In each graph, a set of guidelines (dotted yellow line and dashed lines) are provided to measure the performance of the neural network in the training and testing stages. The dotted yellow line shows the 45-degree line, which is the loci of the desired data in a perfectly fitted model. The dashed guidelines reflect error bounds defined as a percentage of the maximum of the absolute value of each target variable, as shown in Figure 5.3.

Flame Temperature

As mentioned above, the flame temperature has a significant effect on the analysis of combustion. Therefore, a deeper analysis of the model's strengths and weaknesses could help in further improving the models. In the following, we compare the flamelet table data with the temperature calculated from both NN-based and the table-based models at different values of the parameter B. The effect of pressure on the errors in modeling flame temperature was

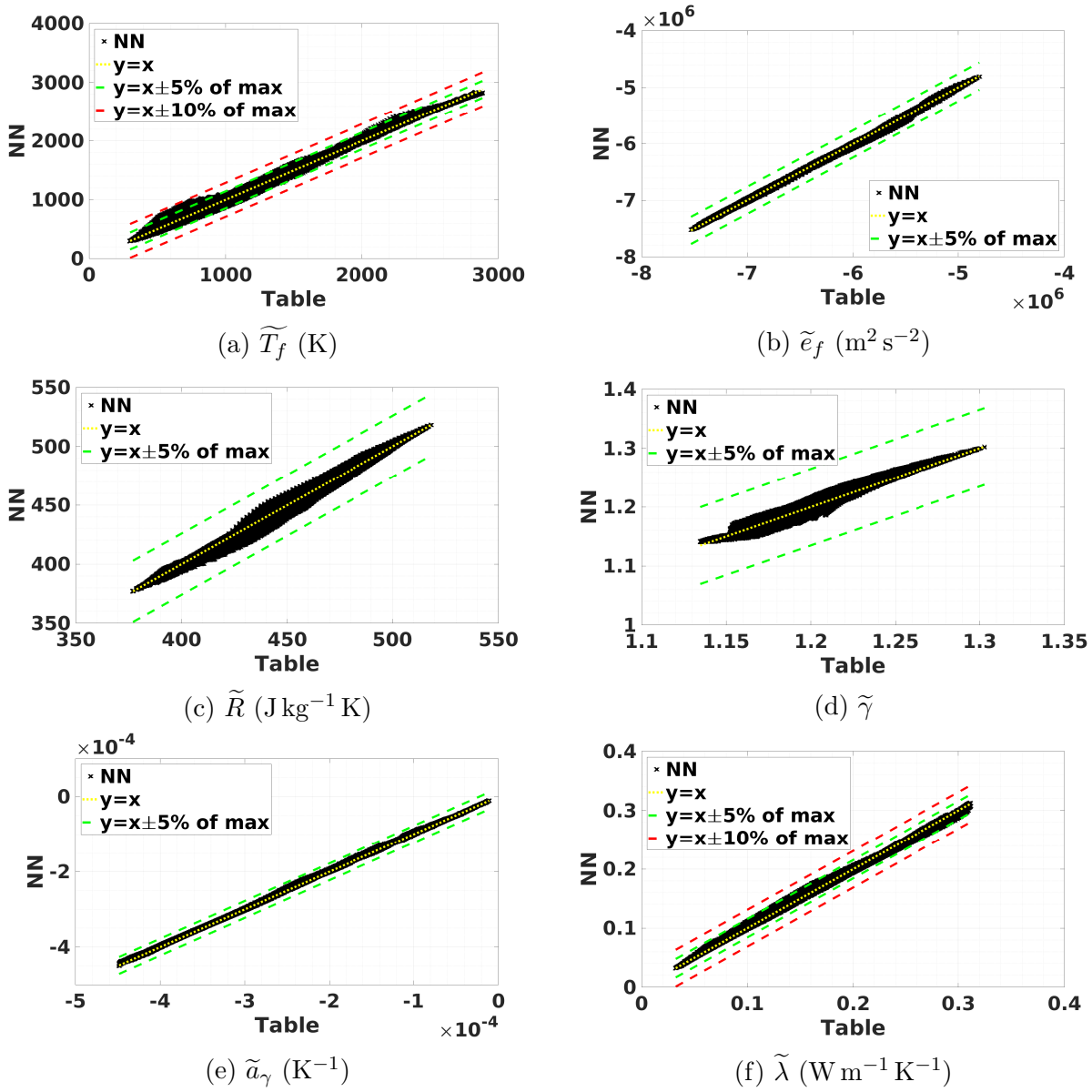

(a) $\widetilde{T_f}$ (K)

(b) $\widetilde{e}_f$ ($\mathrm{m^2\,s^{-2}}$)

(c) $\widetilde{R}$ ($\mathrm{J\,kg^{-1}\,K}$)

(d) $\widetilde{\gamma}$

(e) $\widetilde{a}_\gamma$ ($\mathrm{K^{-1}}$)

(f) $\widetilde{\lambda}$ ($\mathrm{W\,m^{-1}\,K^{-1}}$)

Figure 5.3: Comparison of NN-based models and the flamelet table data of internal energy and flame temperature

insignificant; therefore, we only show the flamelets at a relatively high pressure range, 20 atm in Figure 5.4. In each sub-figure, the flame temperature is plotted as a function of mixture fraction for different values of progress variable (solid black curves). When $\widetilde{C}$ increases, the maximum values of temperature increase, and curves converge together for higher $\widetilde{C}$ values. The dark blue curves show the counterpart of each flamelet solution from NN-based models. On each curve, points used in the training set are shown with red cross markers.

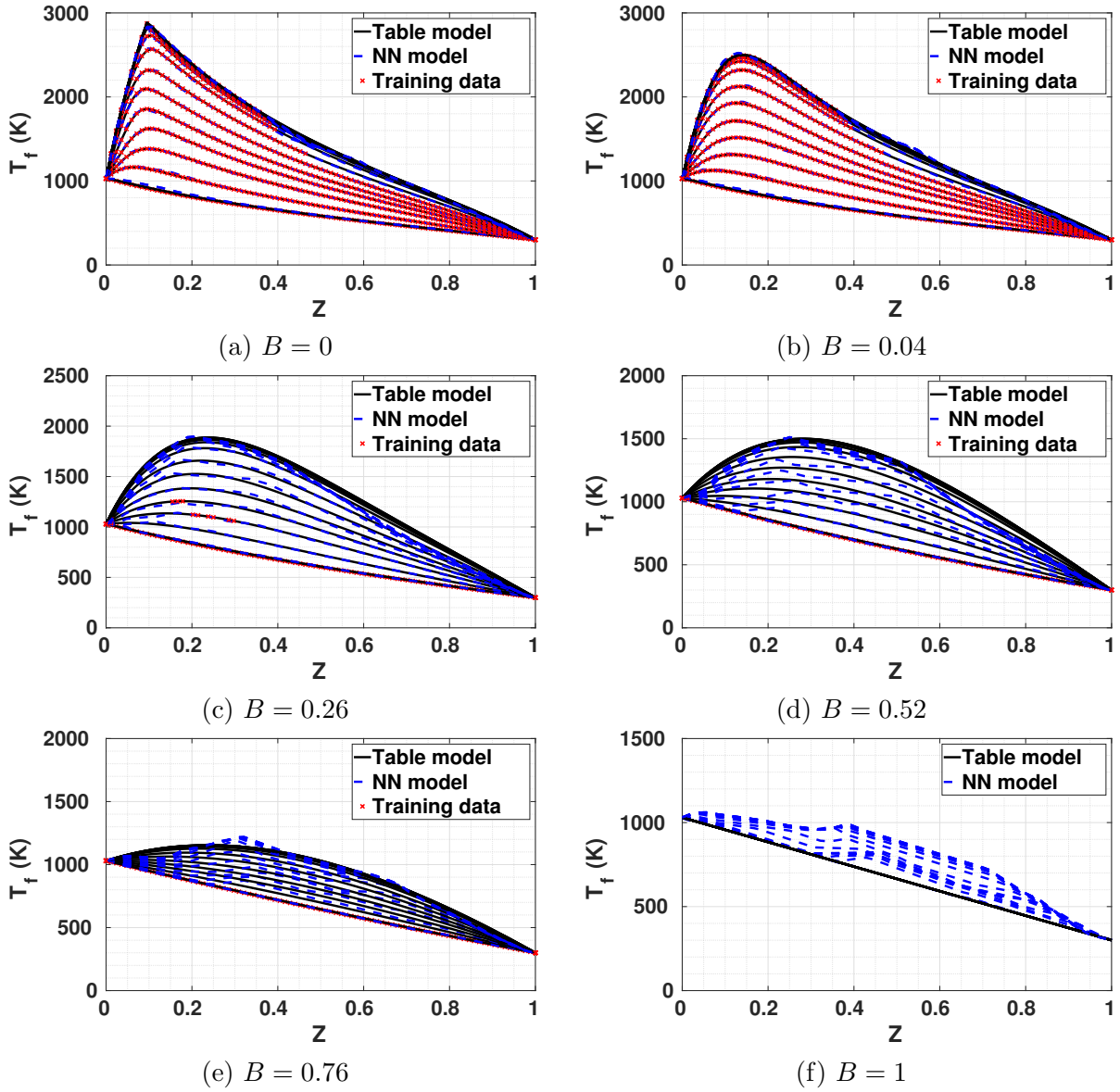

(a) $B = 0$ (b) $B = 0.04$

(c) $B = 0.26$ (d) $B = 0.52$

(e) $B = 0.76$ (f) $B = 1$

Figure 5.4: Comparison of $\widetilde{T_f}$ between NN-based and table-based flamelet models

The NN models for flame temperature are generated after reinforcing the training set with data from regions with high $\widetilde{Z}$ values. In those regions, because there is no combustion, empirical evidence shows that $\widetilde{T_f}$ depends linearly on $\widetilde{Z}$. Essentially, there is a threshold in $\widetilde{Z}$ value, which is a function of $\widetilde{C}$, B and $\overline{P}$, above which this linear dependency sets-in. To determine the threshold values, we linearly interpolate $\widetilde{T_f}$ values at specified $\widetilde{Z}$ points where linear behavior is observed in the original data set. This way of reinforcing the training set helps to account for lack of data in regions with high $\widetilde{Z}$ values. The CFD simulations

correspond to a fuel lean configuration, and therefore most of the data collected have lower $\widetilde{Z}$ values. The lack of training points with high $\widetilde{Z}$ values is correlated with deviations of NN-based models when $\widetilde{Z}$ is near to one.

In Figure 5.4a, the laminar flamelet model is shown. The availability of training data in the laminar zone is highest among different B values. It can be observed from Figure 5.4a that where there is no training data, the NN-based curves deviate from the table curve. By increasing the turbulence level (parameter B), the availability of training points on the curve reduces, and the deviation of the NN-based curves increases. The worst performance of these models can be observed in Figure 5.4f, which is the highest value parameter B in the flamelet model. Although there are very few training points available in the flamelet solutions on the plots with higher B values (Figure 5.4c to Figure 5.4f), the trends of the flamelet solutions are captured to a high extent. In all these plots, better performance can be observed in the lower mixture ratio side, where there are more data available.

Progress Variable Reaction Rate

PVRR is a significant output of the flamelet model as it represents the combustion energy driving the transport equation for the progress variable in the flamelet model. In this section, we investigate the performance of the NN-based model for PVRR. The magnitude of PVRR is drastically changed with pressure and, thus, it has multiple scales. This great range of magnitude affects the performance of the NN-based model. In the training process, we minimize the least squared error in absolute manner; therefore, data with larger magnitude dominates the learning process, and the design becomes more affected by those points. The NN-based estimation of PVRR is compared with its table-based values in Figure 5.5a. The black crosses show the test values. The testing points fall in the 5% guideline, only for PVRR with higher magnitudes. The points with smaller values, however, have a higher error range and fall in the 10% guidelines. In the analysis of combustion instability, the points associated

with higher energy dominate the physics; so, better performance for the NN-based model for points with higher magnitude works in our favor. This result was achieved by reinforcing the training set with data from the dynamic equilibrium simulation, in which more points with higher pressure are available.

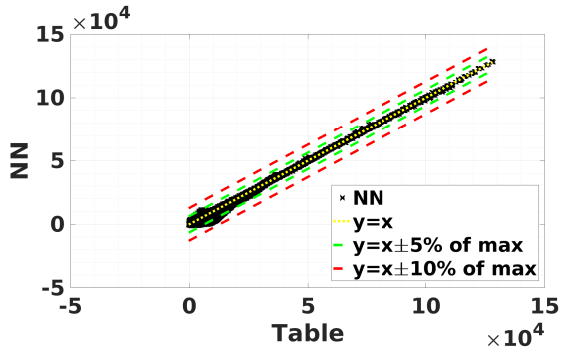

(a) $\widetilde{\dot{\omega}}_C$ (kg m^{-3} s^{-1})

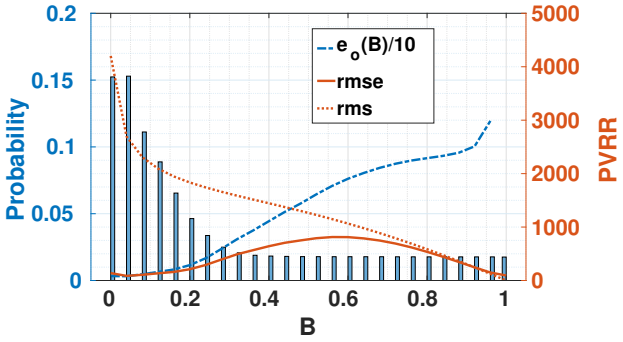

(b) rmse, rms and e_o as functions of B and B's histogram

Figure 5.5: PVRR NN performance analysis

In the following, we investigate the flamelet solutions for PVRR in more detail. PVRR is highly affected by pressure. There is no data available with pressure values lower than 10 atm, and as a result, the averaged relative error is higher for the lower pressure range. Parameter B is also affecting the NN-based model performance significantly. The rmse and rms of PVRR as functions of parameter B is provided in Figure 5.5b. The probability distribution of parameter B in the training set is also provided on the left axis of Figure 5.5b. Around 60% of the training set has a B value lower or equal to 0.2. The one-tenth scaled relative error as a function of B is also provided on the left axis in Figure 5.5b. For the laminar flame, where $B = 0$, the relative error is around 3%. Then it grows, as the probability distribution decreases in higher ranges of B values. The rms of PVRR also decreases with increasing the parameter B. The absolute error increases when the availability of data decreases and the distance of a point from B values with higher availability increases. When the rms becomes small, the rmse also decreases, while the relative error still goes higher.

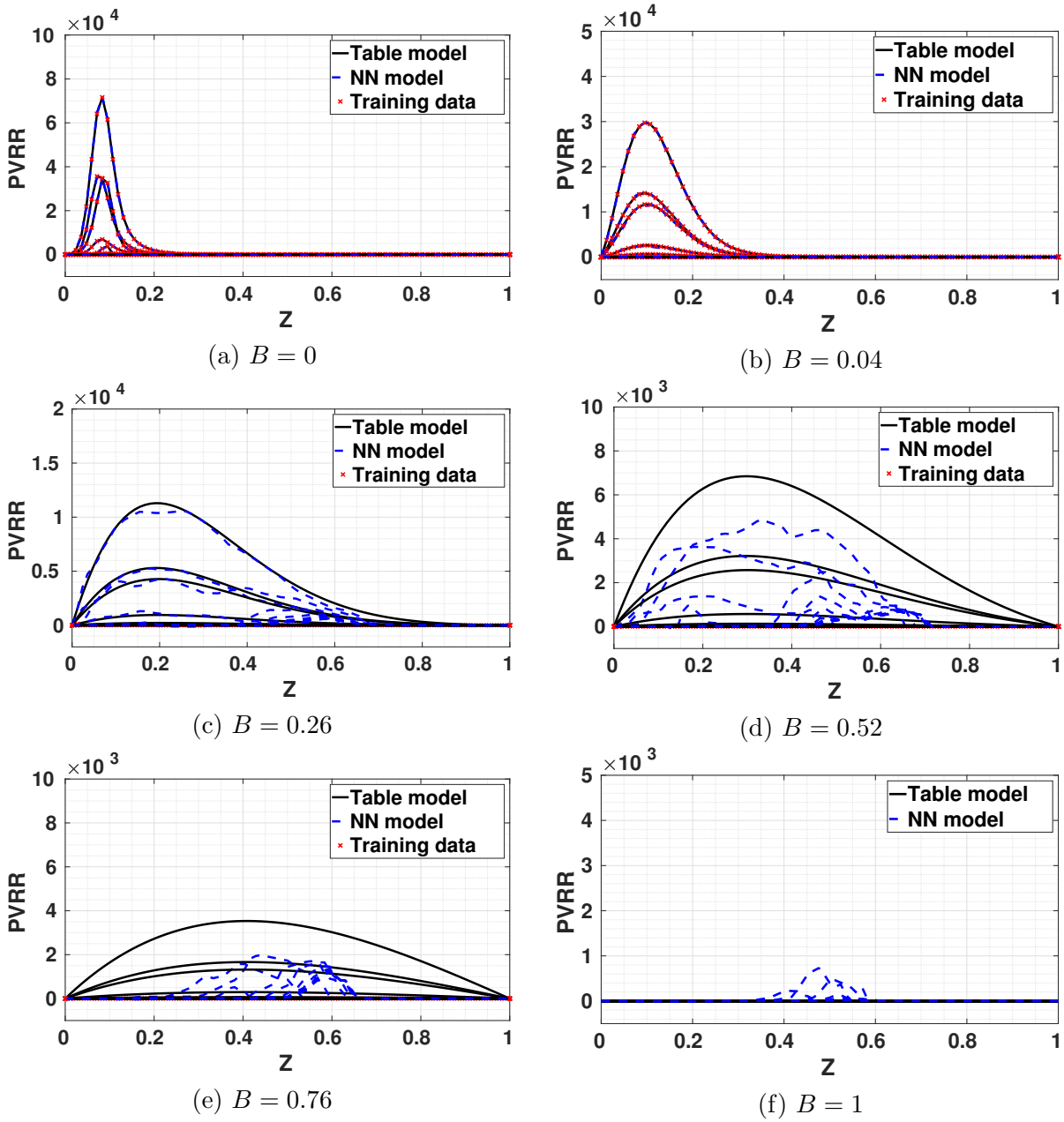

Figure 5.6: Comparison of PVRR between NN-based and table-based flamelet models

In Figure 5.6, we look into PVRR values of the flamelet table at 20 atm for different values of parameter B and progress variable.

Different flamelet solutions of PVRR are provided with the black curves at different $\widetilde{C}$ values in each plot. The behavior of PVRR changes drastically with the progress variable. Maximum values of PVRR occur at $\widetilde{C}$ values around 0.15. The solid dark blue line shows the

NN-based results. The training data are shown with a red cross when read from the flamelet table. For the laminar flame ($B = 0$), there is more data available, and the NN-based model follows the flamelet solutions particularly well for lower $\widetilde{Z}$ values, see Figure 5.6a. The NN-based model starts to deviate when $\widetilde{Z}$ goes to one, and there is not much data available due to fuel lean composition of the CFD-based data pool.

When $B = 0.04$, i.e. a low level of turbulence is considered in the analysis (Figure 5.6b), the maximum value of PVRR drops to half of what it was in the laminar flame. Again, the performance of the NN-based model degrades for higher $\widetilde{Z}$ values, due to lack of data. In Figure 5.6c through Figure 5.6f, by increasing the B values, the availability of training data decreases and performance degrades. The extrapolation maintained a decent level of accuracy even up to $B = 0.52$; yet, the results diverge more for higher B values. PVRR is the most challenging variable to model in the study of turbulent flame with unsteady pressure. As B increases in Figure 5.6c and Figure 5.6e, the performance of the NN-based model degrades.

Other Flamelet Outputs: Φ_1

In the following, the performance of the NNs developed for other flame variables that are collected in vector Φ_1 are analyzed. These variables have used flame temperature as an auxiliary input to the original inputs to the flamelet tables. The flamelet table for internal energy (Figure 5.7), thermal conductivity (Figure 5.8), heat capacity ratio (Figure 5.9) and its coefficient (Figure 5.10), and gas constant (Figure 5.11) are provided at 4 different B values. The laminar solution at $B = 0$ for all variables has the most training points, which are shown by red crosses. The NN-based flamelet model is shown via blue curves in each plot, while the table-based flamelet model is shown through black curves.

NN-based models show the best performance in modeling the laminar solutions. When the value of parameter B increases, i.e turbulence level increases, the performance degrades. This is consistent with the behavior of flame temperature and PVRR.

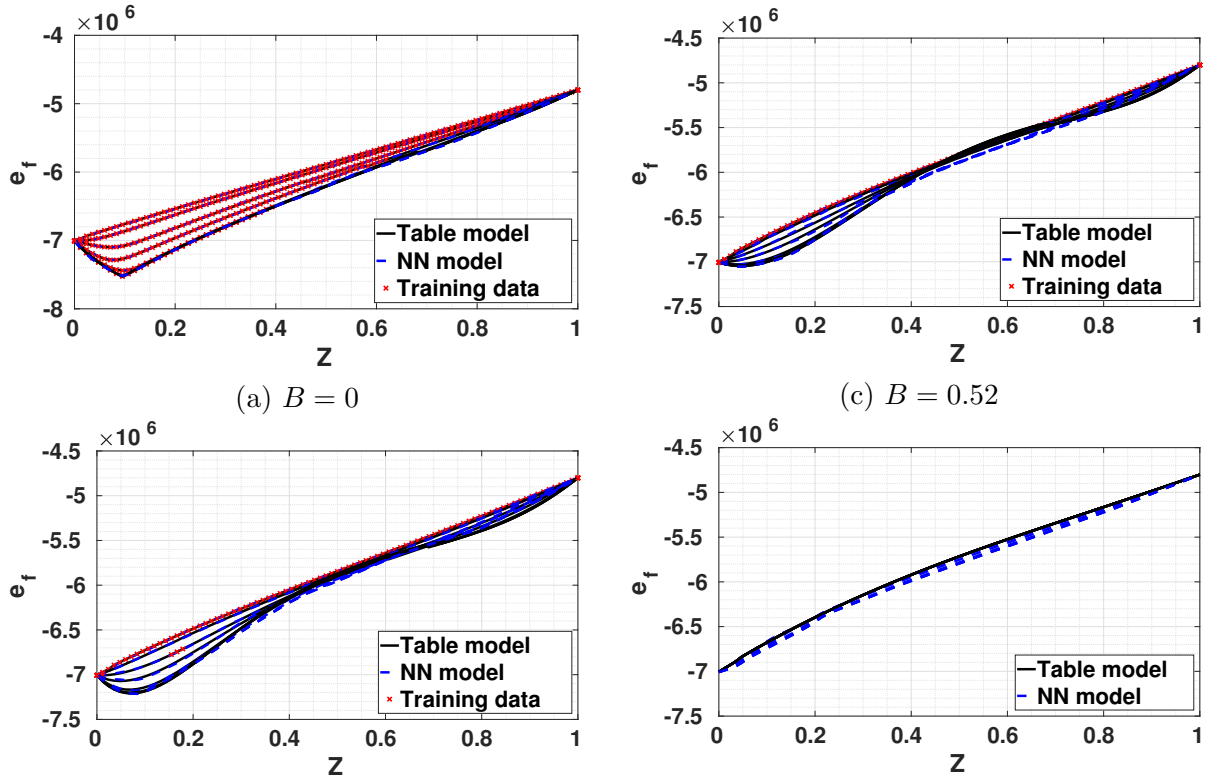

(a) $B = 0$ (c) $B = 0.52$

(b) $B = 0.26$ (d) $B = 1$

Figure 5.7: Comparison of $\widetilde{e_f}$ between NN-based and table-based flamelet models

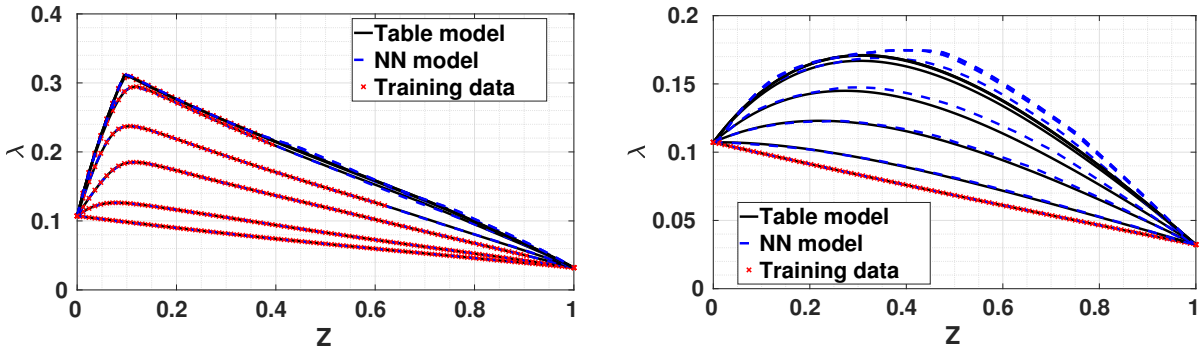

(a) $B = 0$

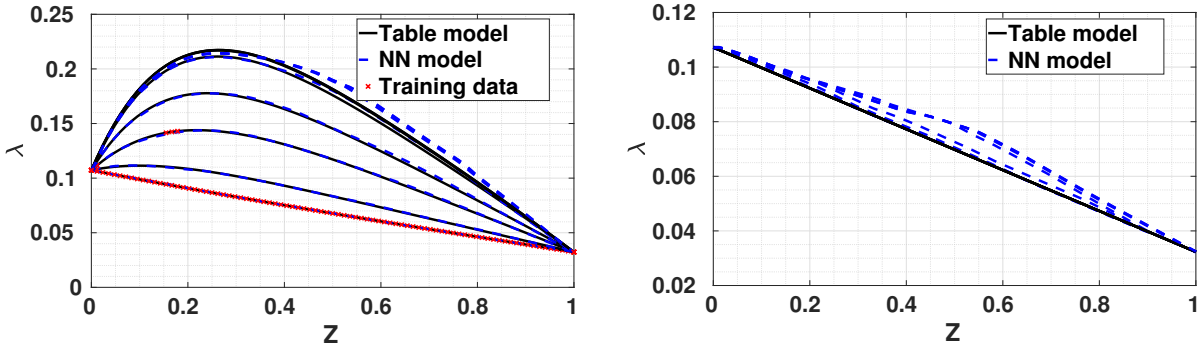

(b) $B = 0.26$

(c) $B = 0.52$

(d) $B = 1$

Figure 5.8: Comparison of $\widetilde{\lambda}$ between NN-based and table-based flamelet models

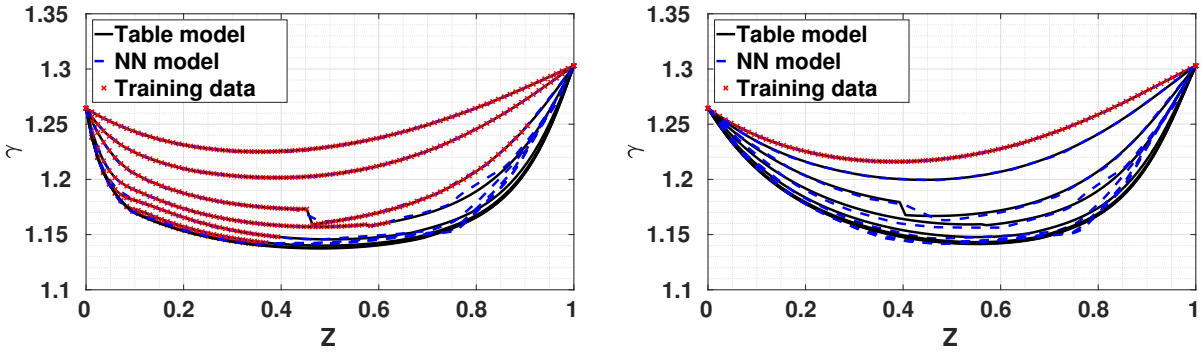

(a) $B = 0$

(c) $B = 0.52$

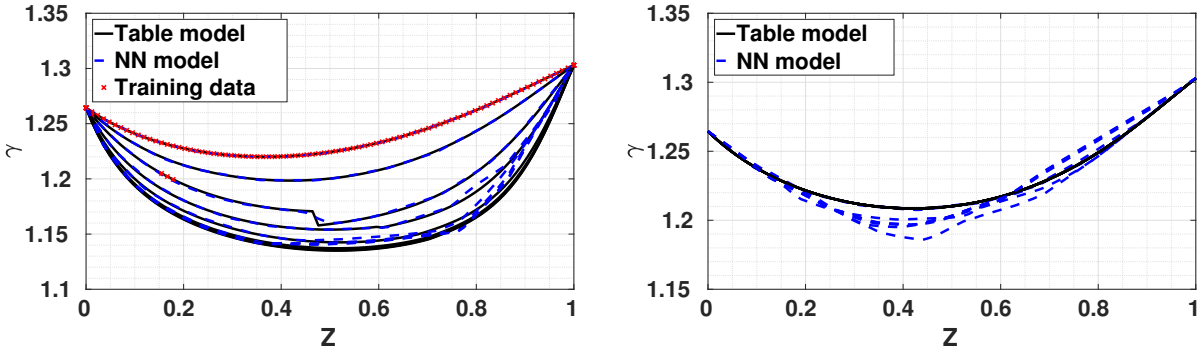

(b) $B = 0.26$

(d) $B = 1$

Figure 5.9: Comparison of $\widetilde{\gamma}$ between NN-based and table-based flamelet models

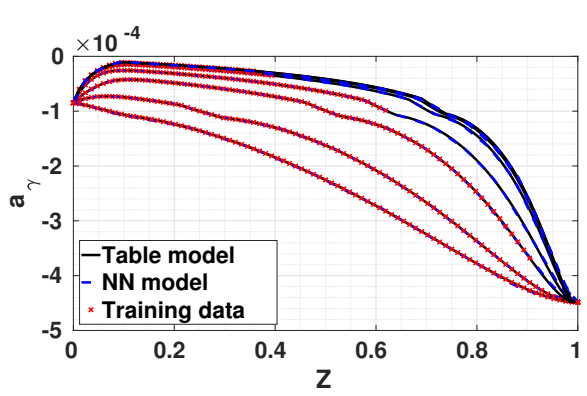

(a) $B = 0$

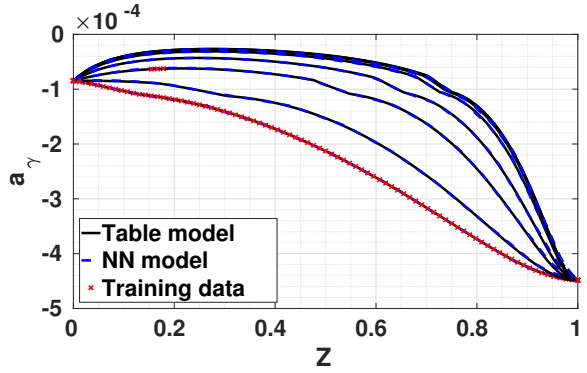

(b) $B = 0.26$

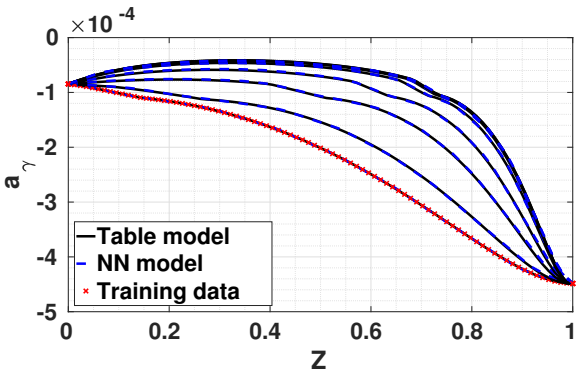

(c) $B = 0.52$

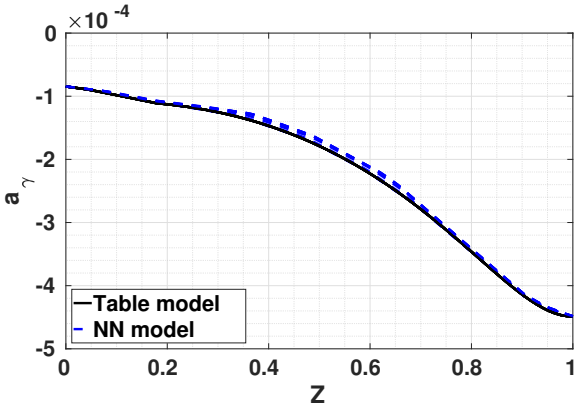

(d) $B = 1$

Figure 5.10: Comparison of $\widetilde{a}_\gamma$ between NN-based and table-based flamelet models

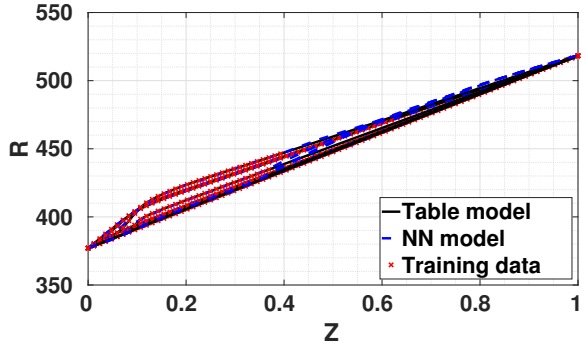

(a) $B = 0$

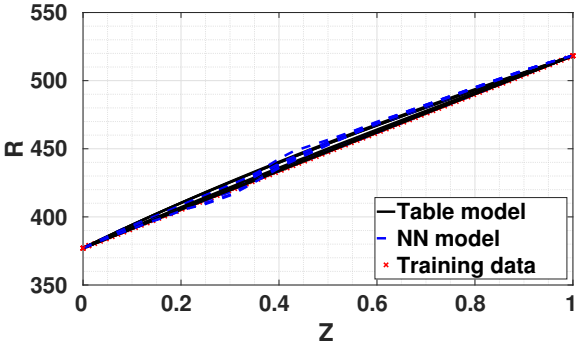

(c) $B = 0.52$

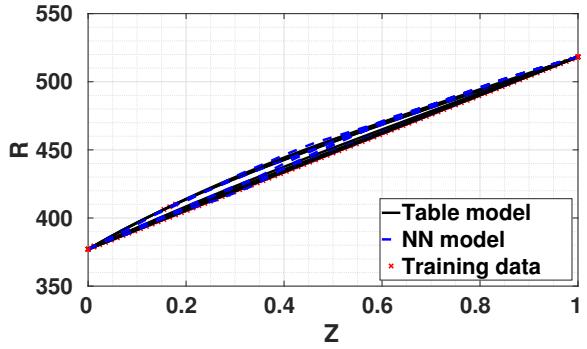

(b) $B = 0.26$

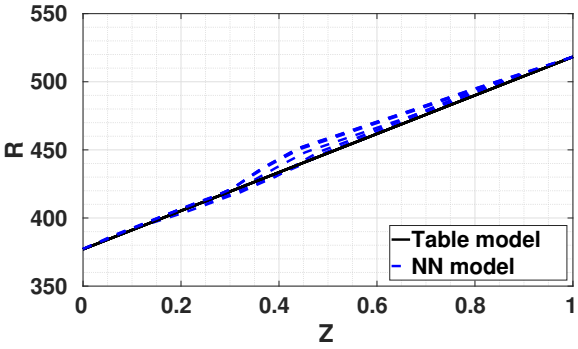

(d) $B = 1$

Figure 5.11: Comparison of $\widetilde{R}$ between NN-based and table-based flamelet models

Story of a Failure Leading to a Success

The great consistency of the introduced model is achieved by the physics-awareness concept introduced in this work. By being resourceful and adding proper points to the training set, we become successful in modeling the flame variables (except PVRR) with less than 5% error, with NN structures that have the least computational cost among our prior experiments. Adding the flame temperature to the inputs of variables in ϕ_1 not only helps to improve the accuracy of the models, it provides a high level of physical consistency between the outputs of the flamelet table.

To emphasize on the significance of this method, the results of the experiments that were built upon to reach this set of proposed models, are provided and discussed. Here, we focus on ϕ_1 variables and flame temperature. In that experiment, we tried to develop NNs that were computationally parsimonious, and we called them P-NN as parsimonious NN. The P-NNs have larger structures and larger overall relative error compared to those proposed here as physics-aware NNs (PA-NN). The relative errors and flop corresponded to P-NN are provided in Table 5.2.

Table 5.2: Summary of relative error and NN structure of P-NN

Variable	**structure**	**flops**	**training error**	**testing error**
$\widetilde{\gamma}$	4-10-15-20-10-20-15-10-5-1	1395	0.18%	2.46%
$\widetilde{a}_\gamma$	4-10-15-20-10-20-15-10-5-1	1395	2.45%	22.87%
$\widetilde{\lambda}$	4-10-15-20-10-20-15-10-5-1	1395	1.33%	9.31%
$\widetilde{R}$	4-15-20-5-20-15-4-1	924	0.29%	0.89%
$\widetilde{e}_f$	4-15-20-5-20-15-4-1	924	0.18%	0.90%
$\widetilde{T}_f$	4-15-20-5-20-15-4-1	924	1.23%	16.25%
$\widetilde{\dot{\omega}}_C$	4-10-15-20-35-20-15-10-5-1	3490	1.49%	36.72%

The results of these NN are compared with the new ones at $B = 0.08$ in Figure 5.12 to Figure 5.16. In the NNs associate to P-NN for $\widetilde{Z}$ close to 1, the NN-based flamelet solutions deviate from the table-based ones. Adding the value of the outputs at $\widetilde{Z} = 1$ helps the NN to learn the dynamic and catch the boundary condition of the diffusion flame.

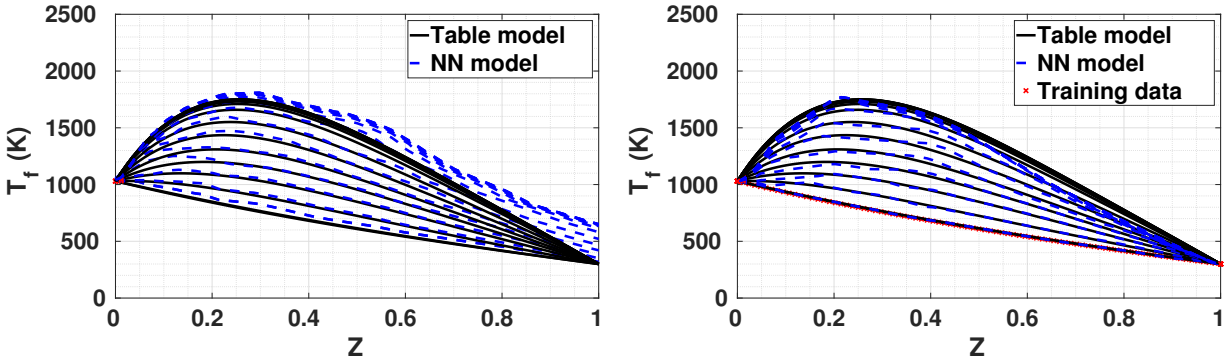

(a) P-NN (b) PA-NN

Figure 5.12: $\widetilde{T_f}$: comparison of NN and table between P-NN and PA-NN

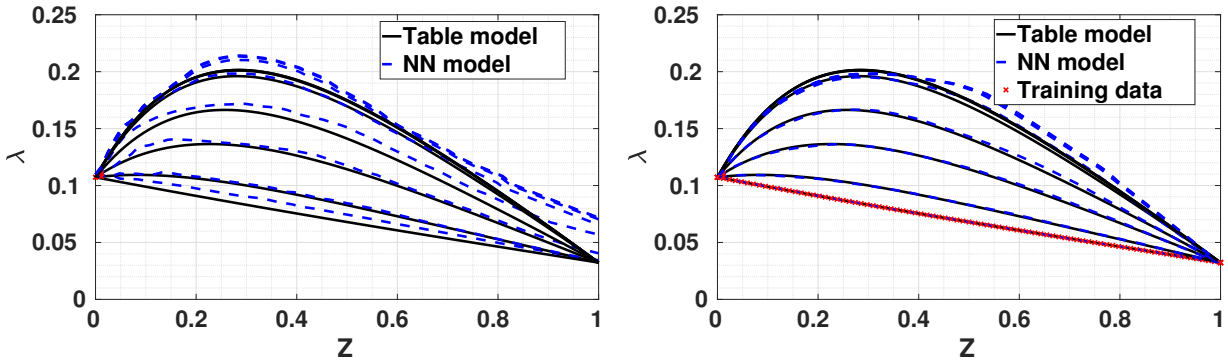

(a) P-NN (b) PA-NN

Figure 5.13: $\widetilde{\lambda}$: comparison of NN and table between P-NN and PA-NN

Changes from the P-NNs to the PA-NN occurred during several experiments and analyses. Adding the data points in the boundaries helped to improve the NN performance. Adding the values of the flame at $\widetilde{C} = 0$, which could be known from the flow dynamics, also helped the NNs. The curve in the bottom in Figure 5.12a is associated with $\widetilde{C} = 0$, the P-NN could not follow the curve in an exact manner as it was under the influence with the data in other curves having a downward curvature that the $\widetilde{C} = 0$ curve does not have. Adding those points to the training set helped the P-NN to obtain a more comprehensive picture of the flamelet model.

The added data to the training set helped a lot; however, there were still details about the flame dynamics that the NN could not see due to the lack of data in specific regions, such as

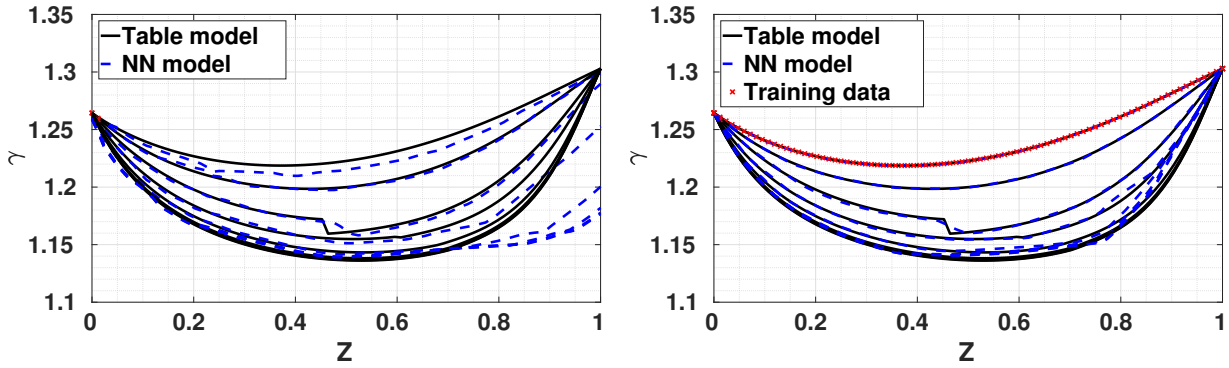

(a) P-NN (b) PA-NN

Figure 5.14: $\widetilde{\gamma}$: comparison of NN and table between P-NN and PA-NN

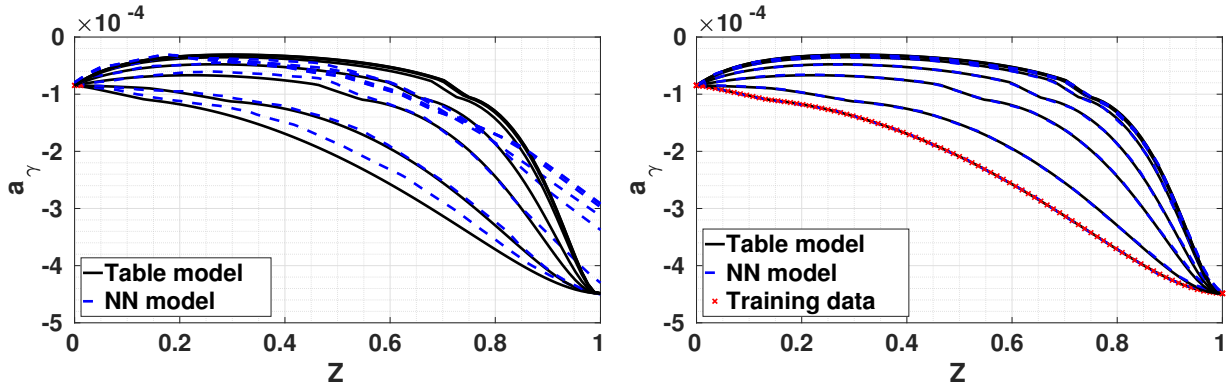

(a) P-NN (b) PA-NN

Figure 5.15: $\widetilde{a}_{\gamma}$: comparison of NN and table between P-NN and PA-NN

high $\widetilde{Z}$ values. The CFD results that were used as the source of training points are based on a fuel lean set-up. Therefore, the dynamic of higher $\widetilde{Z}$ points could not be followed by the NN as can be observed by the inconsistencies in Figure 5.14a. Adding flame temperature as an input to the NN helped the NN to follow the flamelet solutions even in high $\widetilde{Z}$ points.

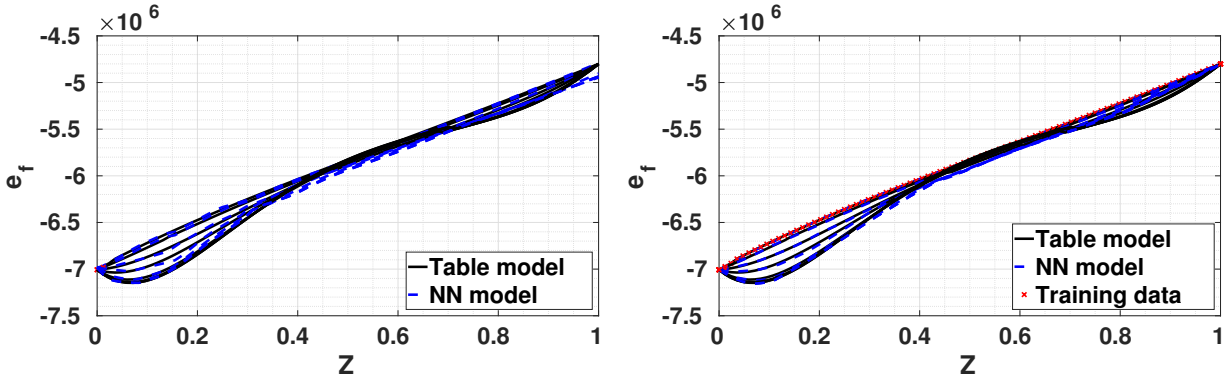

(a) P-NN (b) PA-NN

Figure 5.16: $\widetilde{e_f}$: comparison of NN and table between P-NN and PA-NN

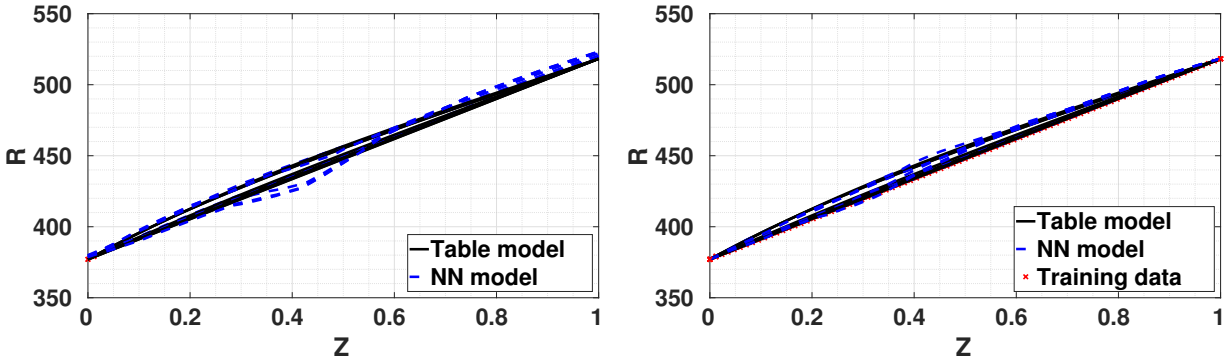

(a) P-NN (b) PA-NN

Figure 5.17: $\widetilde{R}$: comparison of NN and table between P-NN and PA-NN

5.2.2 In-Situ Test of NN-based Models in CFD

To test the NN-based models further, we implemented them into our CFD simulations by replacing the flamelet models. The configuration under study has a 14-cm oxidizer post length, which is characterized by a very high level of instability according to [22]. Two simulations describing the dynamic equilibrium and triggering cases are analyzed. The results of the NN-based simulations are compared with the table-based ones to validate our NN-based models. Since the NN models are trained on a set of data generated from a transient (TR) CFD simulation, as a first step, we implemented the model into the transient simulation. The pressure signal at two points in the oxidizer post and in the shear layers are compared for the NN-based and table-based simulations in Figure 5.18. The NN-based simulation is more accurate where the pressure signal reaches the high amplitude limit cycle, even though the amplitude of the limit cycle is higher than the amplitude in the transient case. The success of our NN-based model in this simulation is manifested by its ability to follow the pressure growth from a low pressure point to a high amplitude limit cycle. The NN-based models are implemented next in the dynamic equilibrium and triggering cases to expand our validation process.

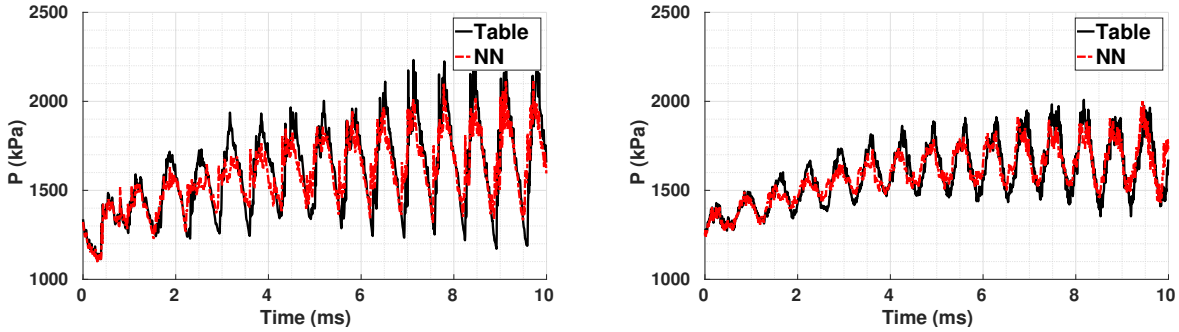

(a) Oxidizer post, $r = 0.5$ cm, $x = -10$ cm (b) Shear layer, $r = 1.13$ cm, $x = 8$ cm

Figure 5.18: TR: comparison of pressure time signals at representative points

Test on CFD: Dynamic Equilibrium

First, we analyze the results from the dynamic equilibrium (DE) scenario, in which the simulation starts from an initial condition in which instability has already set-in. In our analysis, we look at the overall relative error calculated at each spatial point by computing the norm of the difference of the pressure time waveforms from the NN- and table-based CFD simulations. This relative error spatial and numerical distribution are shown in Figure 5.19a and Figure 5.19b, respectively.

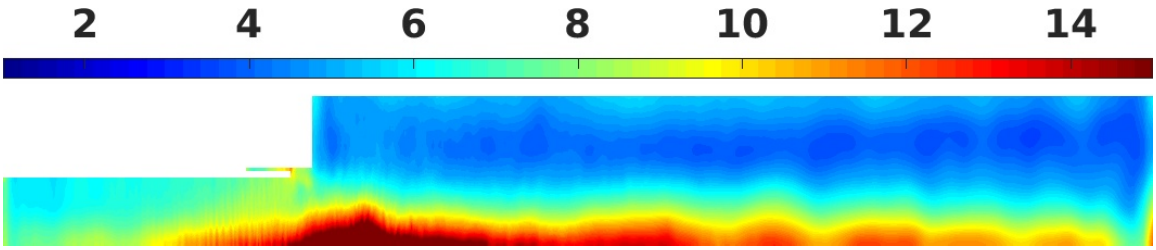

(a) Overall relative error (%)

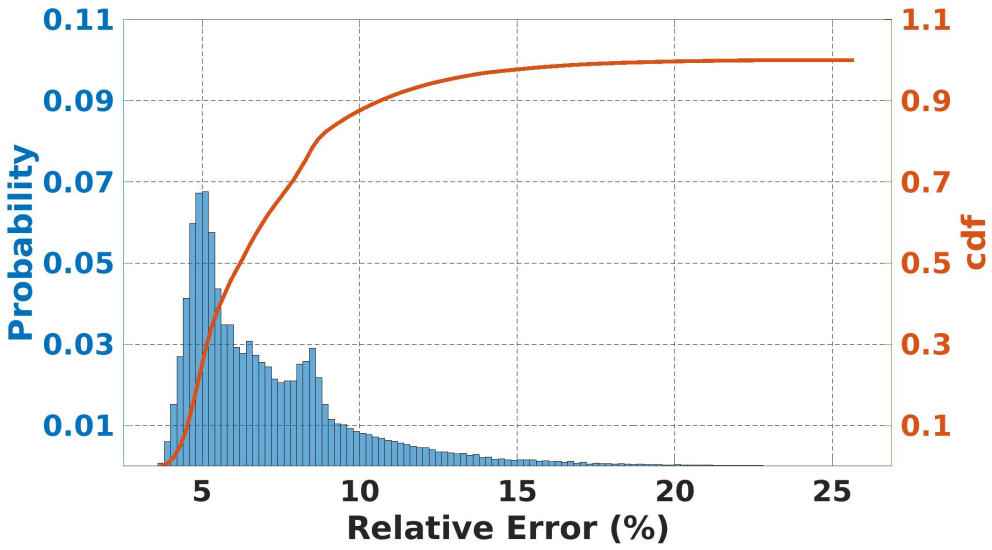

(b) Overall relative error (%) distribution

Figure 5.19: DE: distribution of relative error (%) between NN-base and table-based simulations

Subtracting the mean pressure from each signal, we can also look into the correlation of the fluctuation of the pressure signals between the NN-based simulation and table-based one. This correlation is calculated using Pearson's formula [88], and is provided in Figure 5.20a and Figure 5.20b showing the spatial and numerical distribution of the correlations, respectively.

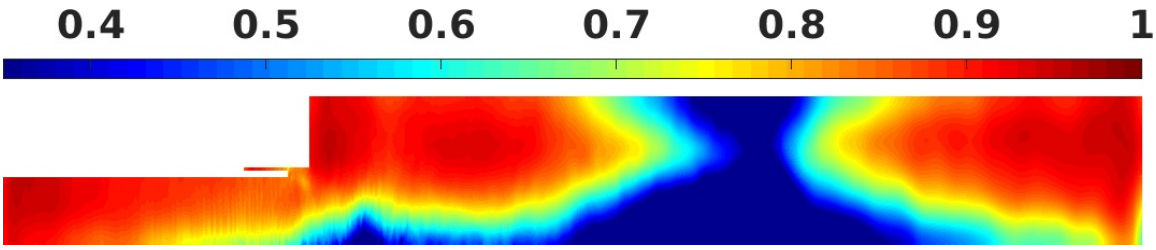

(a) Fluctuation correlation

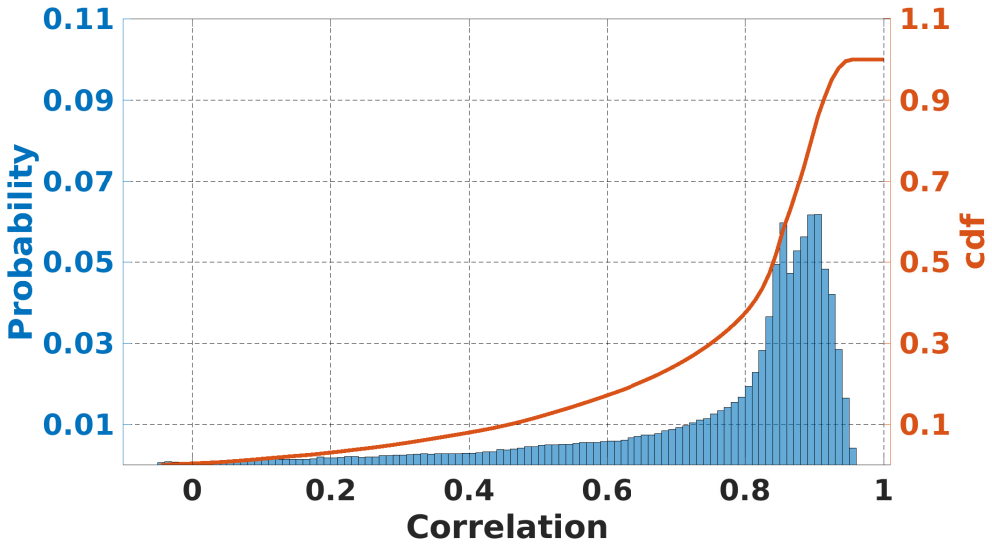

(b) Fluctuation correlation distribution

Figure 5.20: DE: distribution of pressure signal fluctuation correlation between NN-based and table-based simulations

Next, we look at the pressure time waveform and its FFT at two representative locations, one in the oxidizer post and another in the shear layer, see Figure 5.21. In both locations, there is a great consistency between the table-based and NN-based simulations.

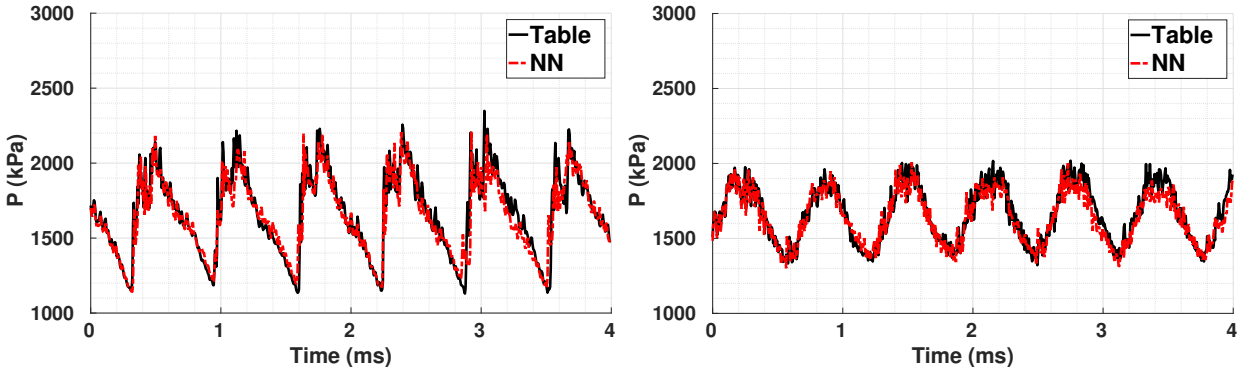

(a) Oxidizer post, $r = 0.5$ cm, $x = -10$ cm

(c) Shear layer, $r = 1.13$ cm, $x = 8$ cm

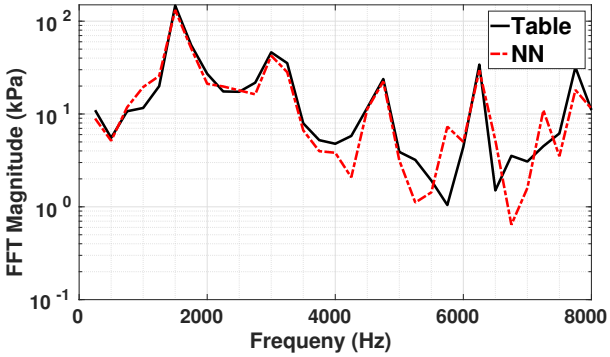

(b) Pressure FFT at $r = 0.5$ cm, $x = -10$ cm

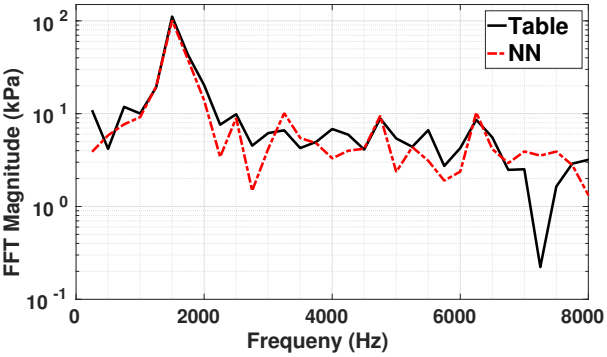

(d) Pressure FFT at $r = 1.13$ cm, $x = 8$ cm

Figure 5.21: DE: comparison of pressure time signals at representative points

The pressure longitudinal mode shapes at the centerline are plotted in Figure 5.22. They represent the modulus of the Fourier spectrum peaks of pressure signals at each grid point along the centerline. The phase of the first mode is also compared at each grid point for the NN-based and table-based simulations in Figure 5.22d. There is a great agreement in all of these graphs between NN-based and table-based simulations, with the exception of some inconsistencies in the vicinity of 20 cm location, which is a pressure node. The pressure waveform at the node can be considered as a noise signal, as the amplitude of the first harmonic is close to zero. The frequencies of the first and the second longitudinal modes across the combustor are around 1500 Hz and 3000 Hz, respectively.

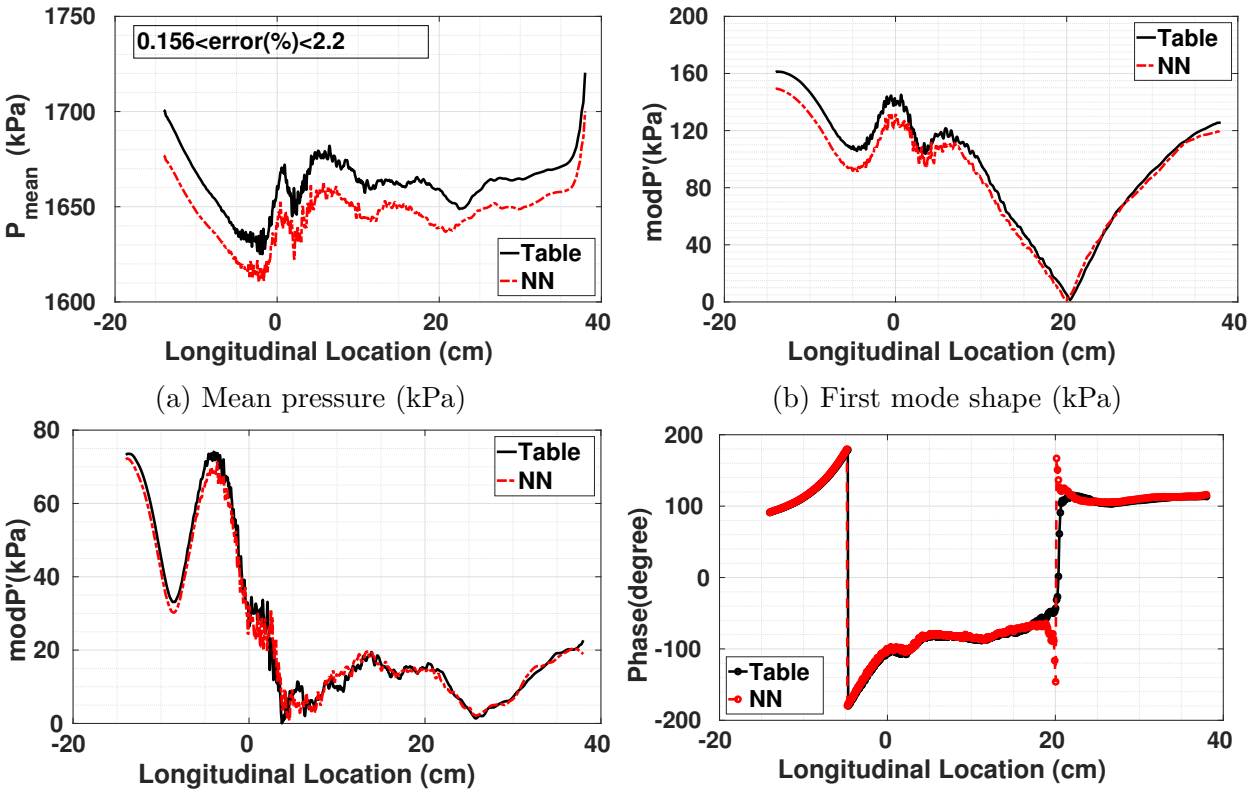

(a) Mean pressure (kPa)

(b) First mode shape (kPa)

(c) Second mode shape (kPa)

(d) Phase of first mode shape (kPa)

Figure 5.22: DE: comparison of pressure mean, the first mode and its phase, and the second mode shapes between NN-based and table-based simulations along the centerline

The signal power of pressure fluctuations across the grid points of the combustor are compared between the NN-based and table-based simulations, in Figure 5.23b and Figure 5.23a, respectively. The blue region in the combustor shows the vicinity of the pressure node where the oscillations have noisy behaviors. The main difference between the two simulations occurs in the middle of the oxidizer post, in which the NN-based simulation underestimates the rms. As shown in Figure 5.23c around 85% of the points in the NN-based simulation are underestimated by less than 10%. This is attributed to the inaccuracies in the PVRR model. In the oxidizer post, the PVRR should be zero or very close to zero, as there is no combustion occurring there. However, the training data was skewed toward higher values of PVRR, as they are important in the modeling of combustion instabilities. Generating an optimized training set for PVRR is one of the next steps of this work.

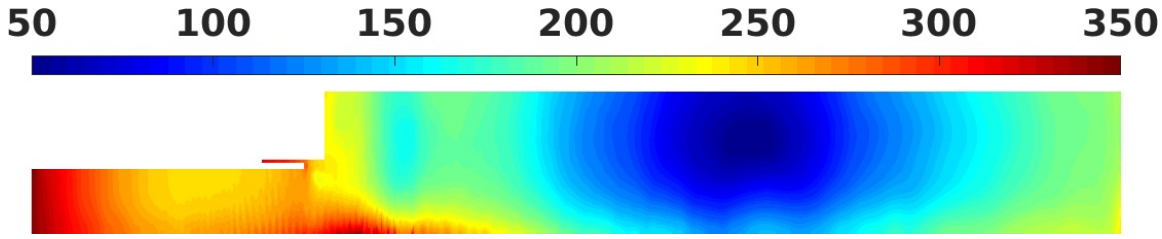

(a) Table: rms

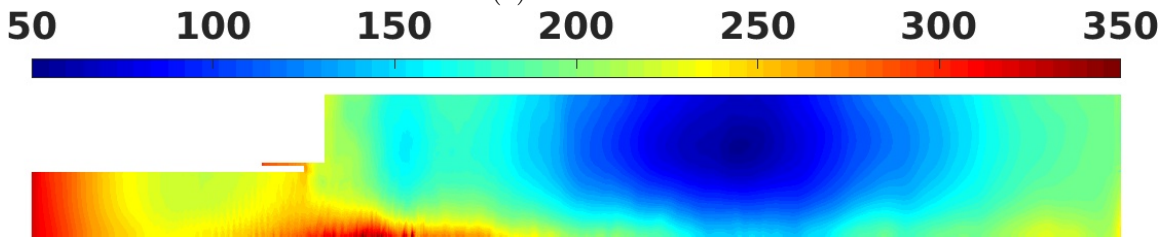

(b) NN: rms

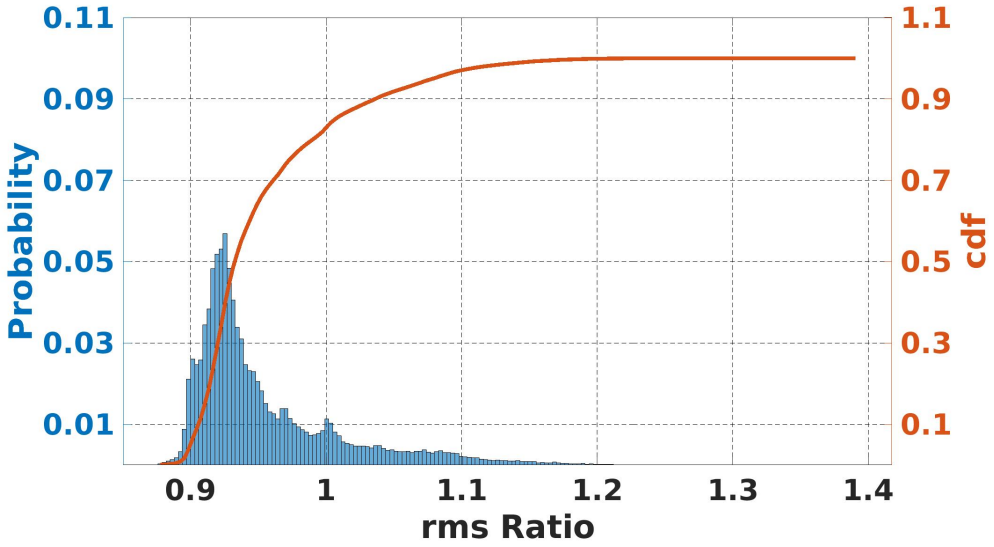

(c) Power ratio distribution

Figure 5.23: DE: the rms of pressure signal fluctuations are compared between the simulations based on NN (5.23b) and table(5.23a).

Furthermore, the modified Rayleigh index is compared between the NN-based and table-based simulations in Figure 5.24a and Figure 5.24b in a 2D manner, respectively. The comparison of radially averaged 1D mRI is provided in Figure 5.24c. The high positive values in the left upper corner of combustor shows the driving effect combustion on pressure instabilities and the two simulations are more consistent in the upper zone of combustor.

As it was discussed in [66], the behavior near the centerline is more complicated due to numerical considerations.

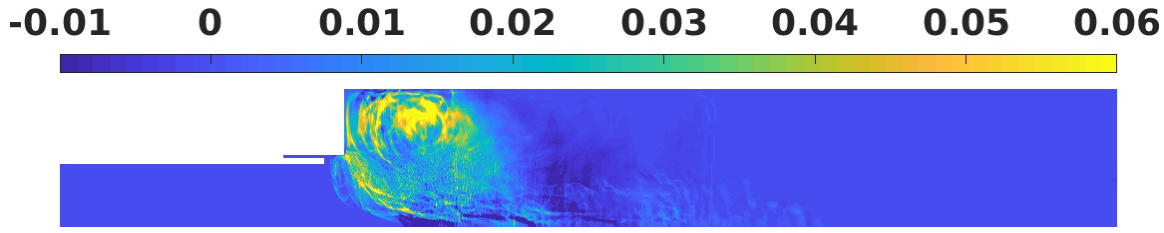

(a) Table: mRI

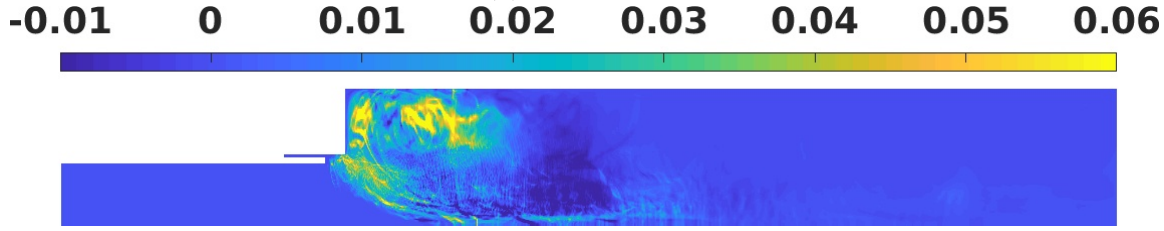

(b) NN: mRI

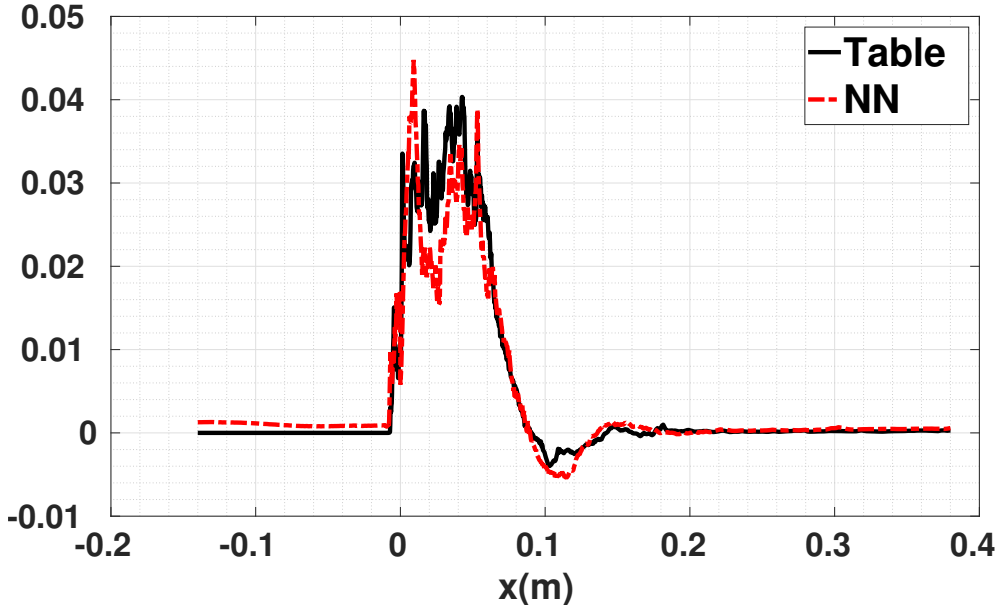

(c) Longitudinal distribution of mRI

Figure 5.24: DE: the mRI from the NN-based and the table-based simulations are compared

In Figure 5.25 to Figure 5.28, time-averaged values of temperature, density, PVRR, and axial velocity from the NN-based and the table-based simulations are compared. In all these variables, great consistency is observed between the two simulations. Mainly, PVRR shows

differences on the centerline, and axial velocity in the vicinity of pressure node. In both of these locations, noisy behavior is observed due to numerical and physical characteristics.

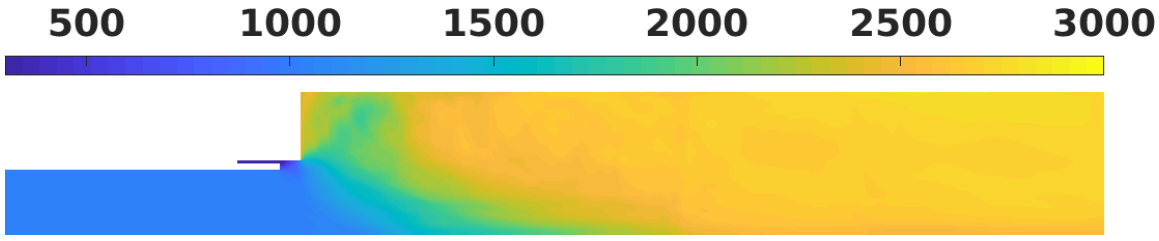

(a) $\widehat{T}$ (K), table

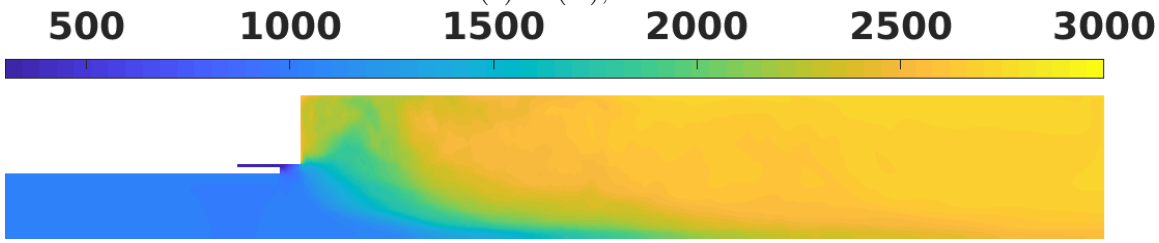

(b) $\widehat{T}$ (K), NN

Figure 5.25: DE: time-averaged values of flow temperature from the NN-based and the table-based simulations

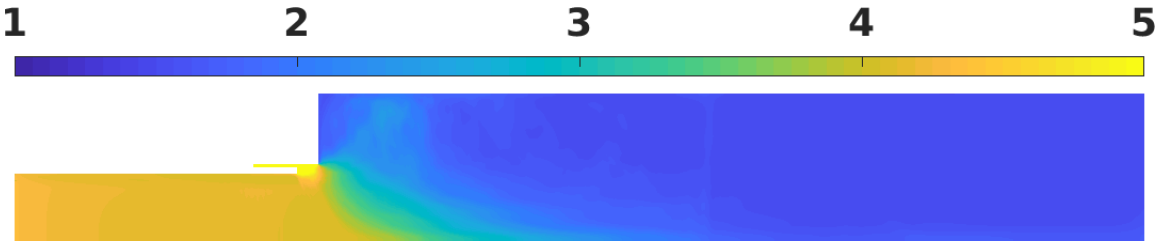

(a) $\bar{\rho}$ (kg m^{-3}), table

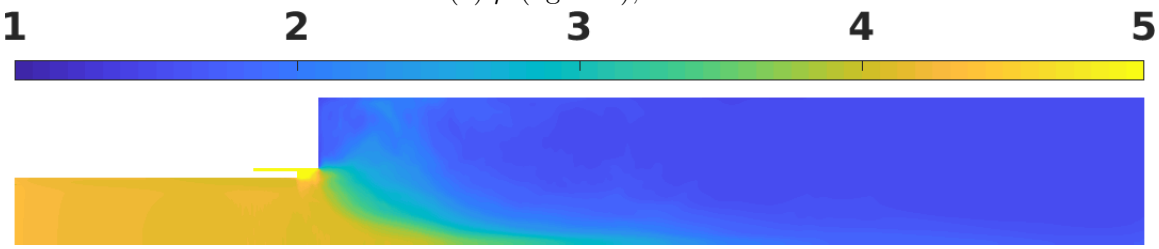

(b) $\bar{\rho}$ (kg m^{-3}), NN

Figure 5.26: DE: time-averaged values of density from the NN-based and the table-based simulations

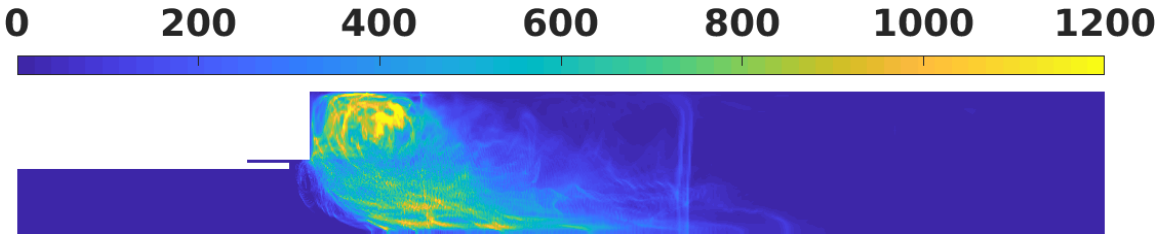

(a) $\widehat{\dot{\omega}}_C$ ($\mathrm{kg\,m^{-3}\,s^{-1}}$), table

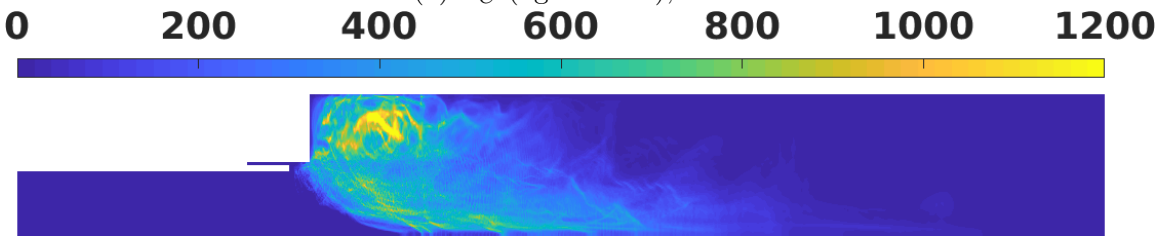

(b) $\widehat{\dot{\omega}}_C$ ($\mathrm{kg\,m^{-3}\,s^{-1}}$), NN

Figure 5.27: DE: time-averaged values of PVRR from the NN-based and the table-based simulations

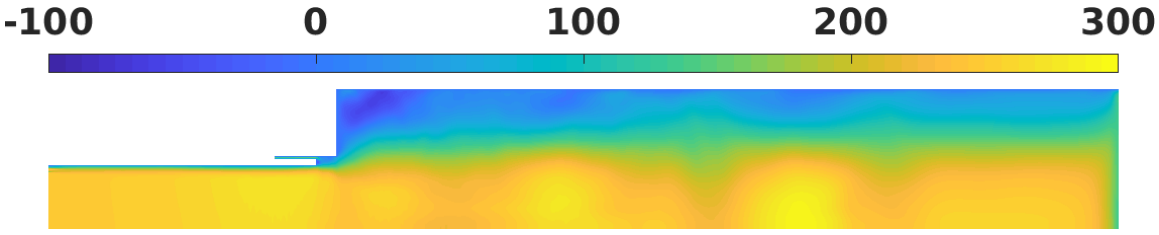

(a) $\widehat{U}$ ($\mathrm{m\,s^{-2}}$), table

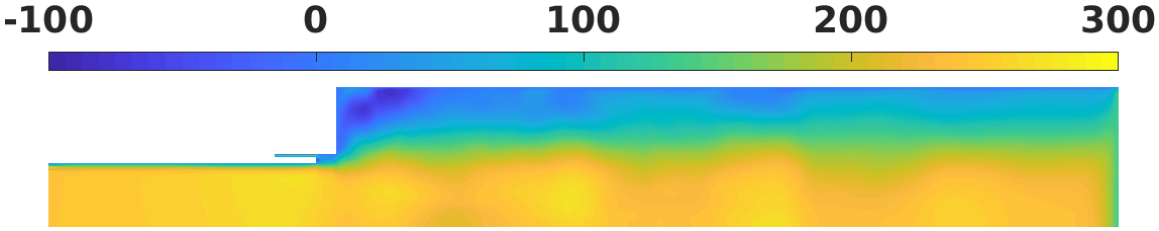

(b) $\widehat{U}$($\mathrm{m\,s^{-2}}$), NN

Figure 5.28: DE: time-averaged values of axial velocity from the NN-based and the table-based simulations

Test on CFD: Triggered Oscillation

In the triggering (TG) scenario, heat loss is introduced by imposing an isothermal boundary condition on the chamber wall, and a sine wave perturbation on the propellant mass flow rate is applied for two periods. The top wall is modeled to be isothermal at 1030 K.

The overall relative error was calculated for each spatial point by computing the norm of the difference of pressure time waveforms between NN and table-based simulations. The overall relative error is shown in Figure 5.29a. As shown in Figure 5.29b, Around 98% of the points are estimated with less than 8% error.

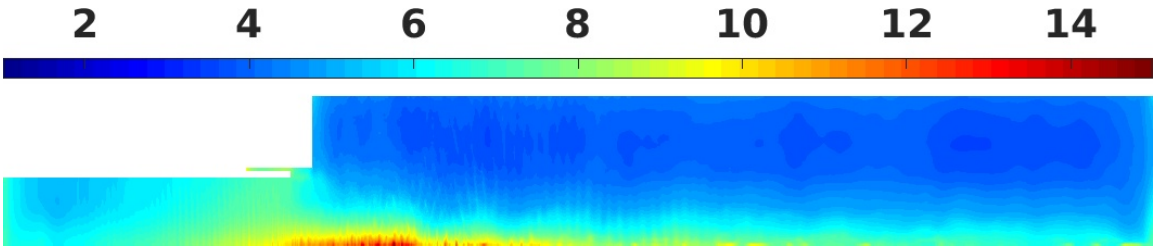

(a) Overall relative error (%)

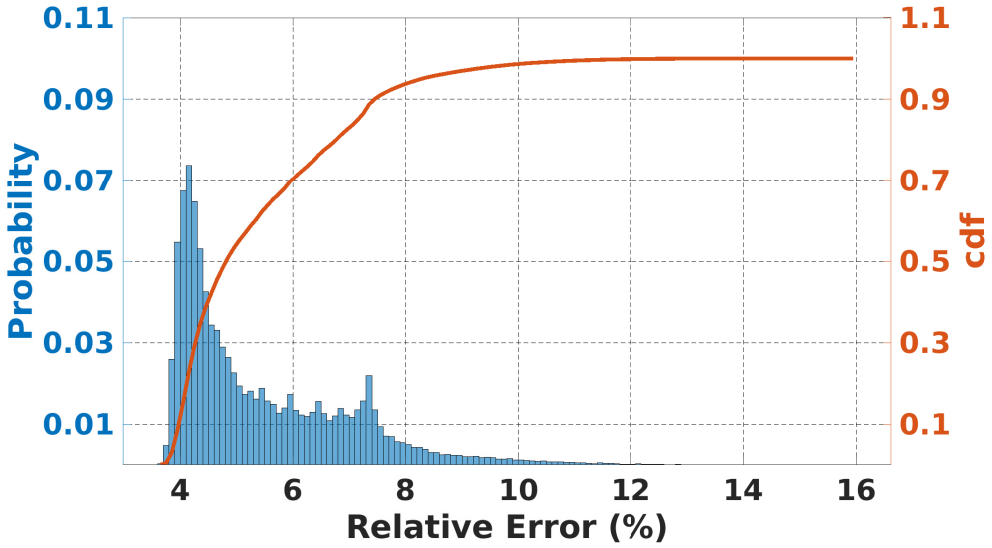

(b) Overall relative error (%) distribution

Figure 5.29: TG: distribution of relative error (%) between NN-based and table-based simulations

We can also look into the correlation of the fluctuation of the pressure signals between the NN-based and table-based simulations using the Pearson formula. The correlations are very high, except on the centerline in the vicinity of the pressure node, as seen in Figure 5.30a and Figure 5.30b showing the spatial and numerical distribution of the correlations, respectively.

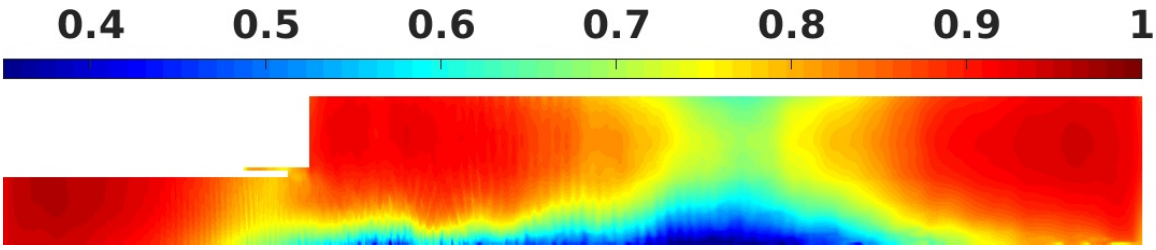

(a) NN Fluctuation correlation

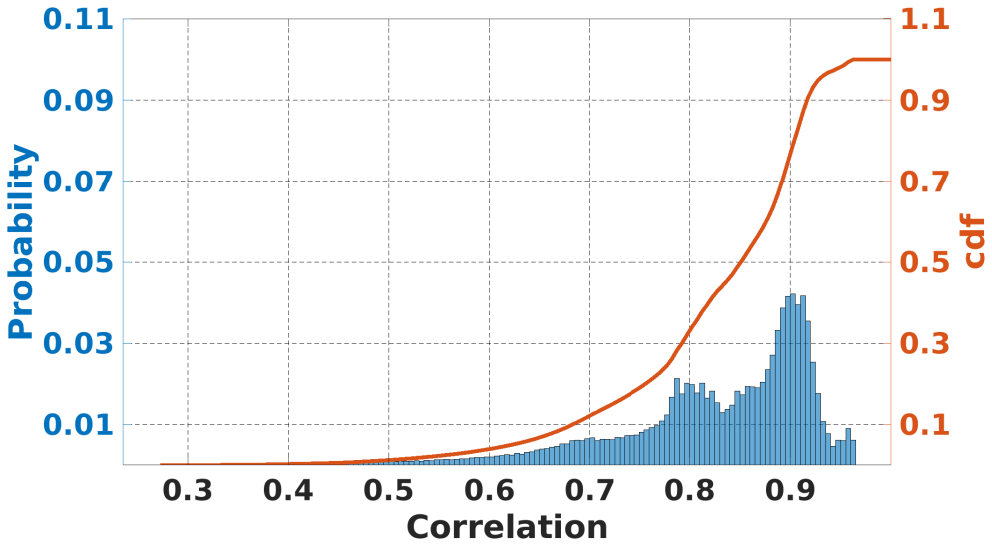

(b) Fluctuation correlation distribution

Figure 5.30: TG: distribution of pressure signal fluctuation correlation between NN-based and table-based simulations

Great consistency can be observed in the pressure signal and its FFT at the two representative locations (one in the oxidizer post and another in the shear layer), Figure 5.31. The pressure response to the perturbation in the mass flow rate can be observed in both simulations, with its effect on the response becoming damped after 2.5 ms. As shown in Figure 5.31b and Figure 5.31d, the FFT of pressure signals at both of these points from the NN-based simulation are in great agreement with the ones from the table-based simulation.

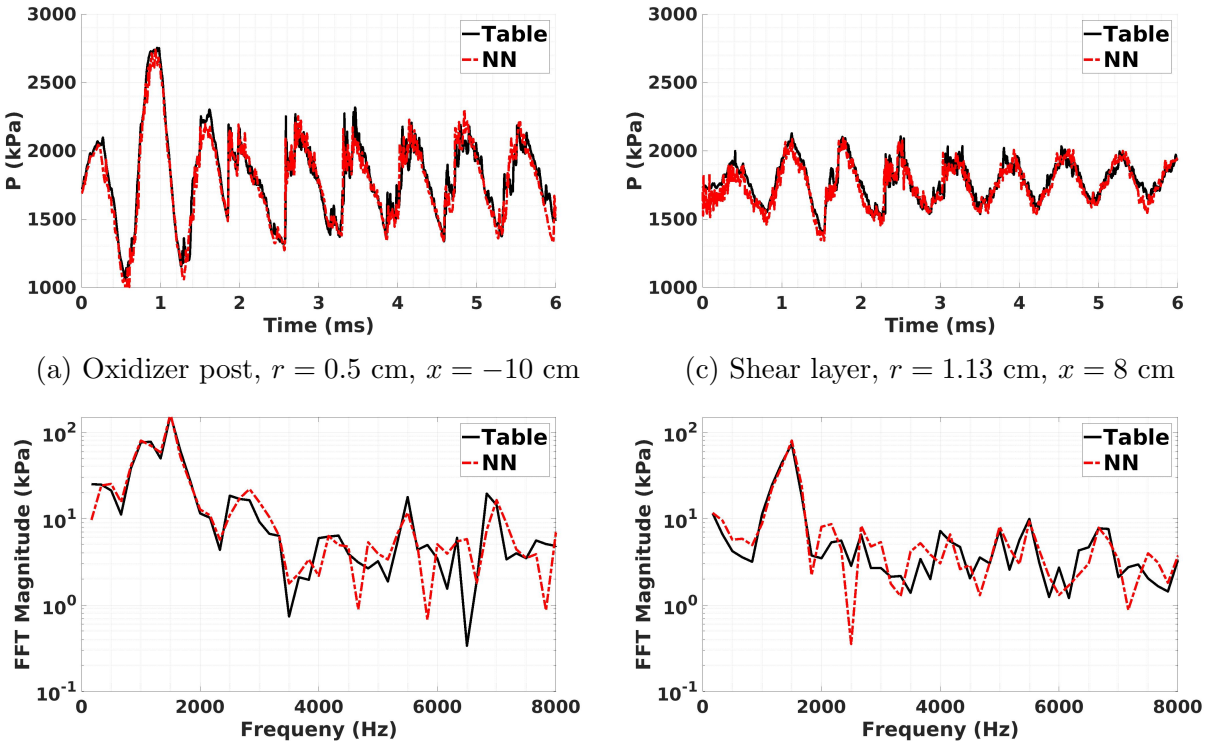

(a) Oxidizer post, $r = 0.5$ cm, $x = -10$ cm

(c) Shear layer, $r = 1.13$ cm, $x = 8$ cm

(b) Pressure FFT at $r = 0.5$ cm, $x = -10$ cm

(d) Pressure FFT at $r = 1.13$ cm, $x = 8$ cm

Figure 5.31: TG: comparison of pressure time signals at representative points

The mean pressure calculated from the NN-based simulation is within 2% of the table-based simulation. The amplitude of the first and second modes are highly consistent between the two simulations. Differences exist in the inlet of the oxidizer post and near the nozzle mostly in the second mode. The phase graph of the NN-based simulation matches the one for the table-based simulation, to a great extent. The frequencies of the first and the second longitudinal modes across the combustor are around 1500 Hz and 3000 Hz, respectively.

Similar to dynamic equilibrium scenario, the rms of pressure fluctuations across the grid points of the combustor are compared between the NN-based and table-based simulations in Figure 5.33b and Figure 5.33a, respectively. The two graphs from the two simulations are highly similar. Slight differences exist in the blue boundary in the combustion zone, indicating a slight overestimation of the pressure fluctuations in the NN-based simulation, as shown in Figure 5.33c.

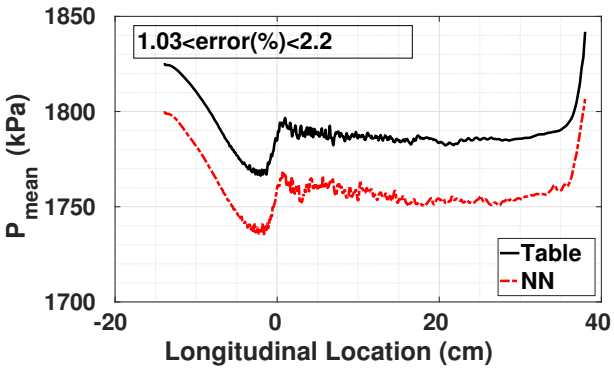

(a) Mean pressure (kPa)

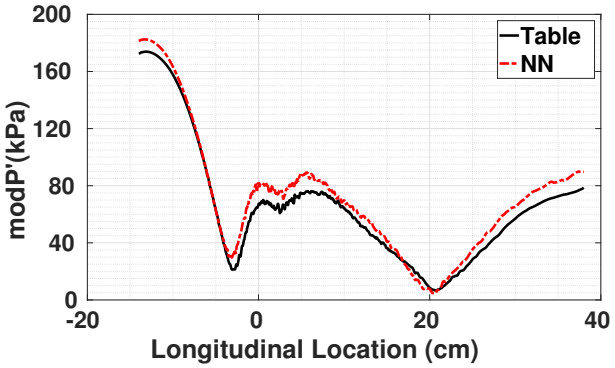

(b) First mode shape (kPa)

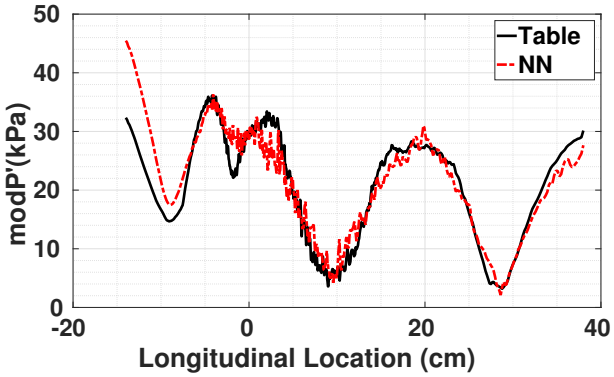

(c) Second mode shape (kPa)

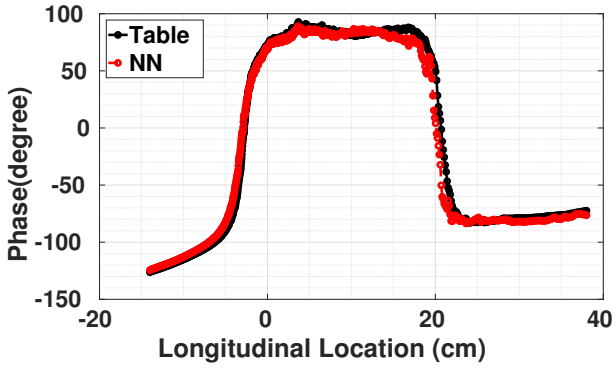

(d) Phase of first mode shape (kPa)

Figure 5.32: TG: comparison of pressure mean, the first mode and its phase, and the second mode shapes between NN-based and table-based simulations along the centerline

This overestimation can also be observed through the local 2D mRI quantity that is compared between the NN-based and table-based simulations in Figure 5.34a and Figure 5.34b, respectively. The mRI shown in Figure 5.34b indicates higher values leading to a higher instability level. The comparison of radially averaged 1D mRI is also provided in Figure 5.34c.

In Figure 5.35, the snapshots of density are compared at the three time points of 1, 2, and 3 ms. The graphs are highly consistent between the two simulations. The first row in the figure shows the table-based simulation and the second row shows the NN-based simulation. This consistency is also observed in the comparison of time snapshots of axial velocity in Figure 5.36, flow temperature in Figure 5.37, PVRR Figure 5.38, and mixture fraction in Figure 5.39.

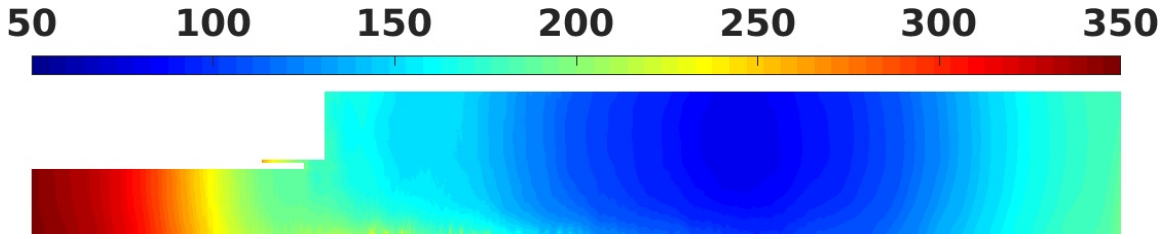

(a) Table: rms

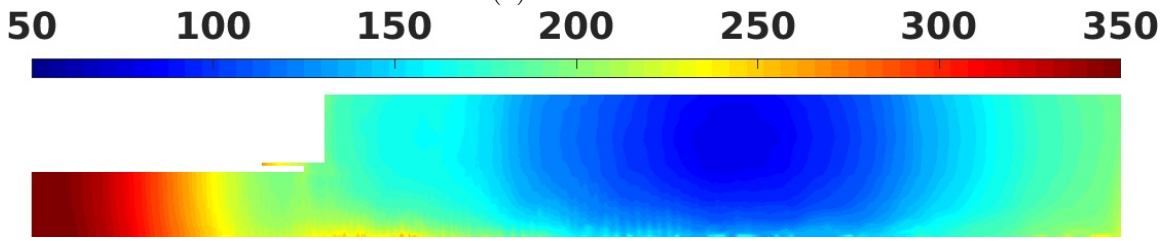

(b) NN: rms

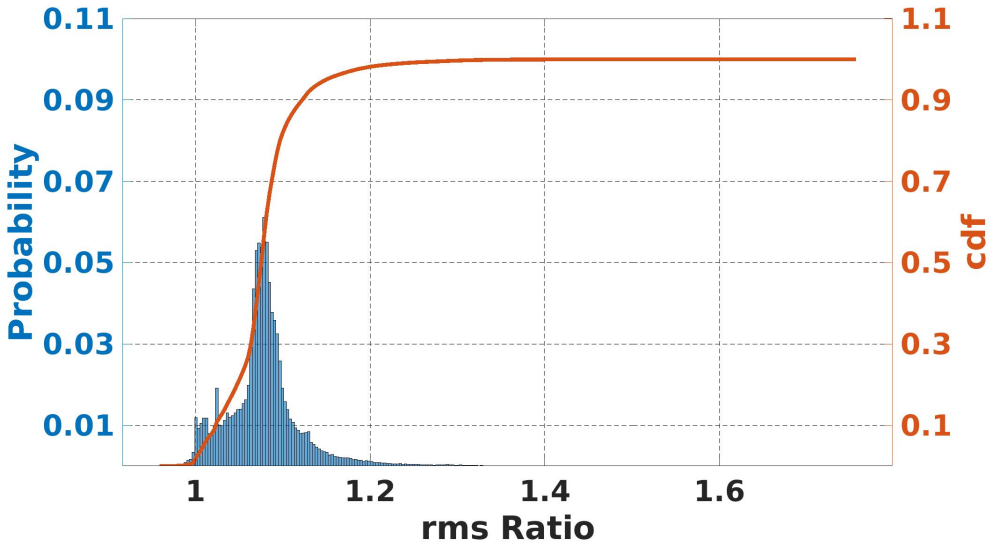

(c) Power ratio distribution

Figure 5.33: TG: the rms of pressure signal fluctuations are compared between the simulations based on NN (5.33b) and table(5.33a)

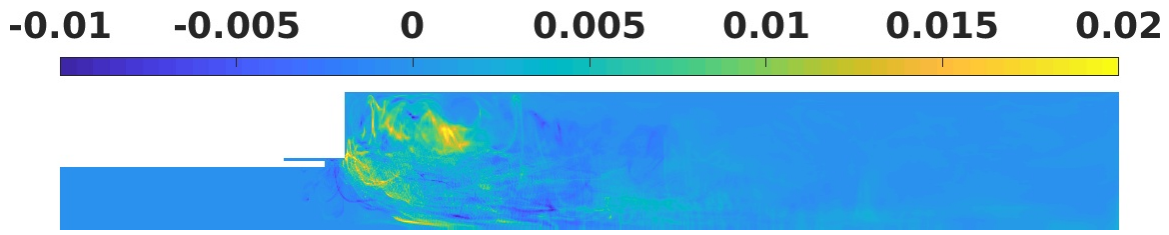

(a) Table: mRI

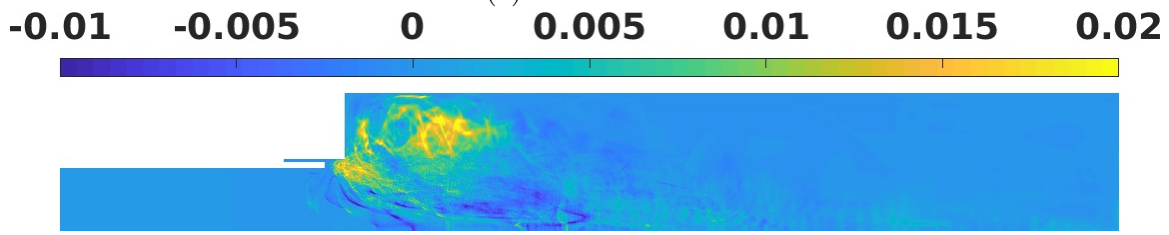

(b) NN: mRI

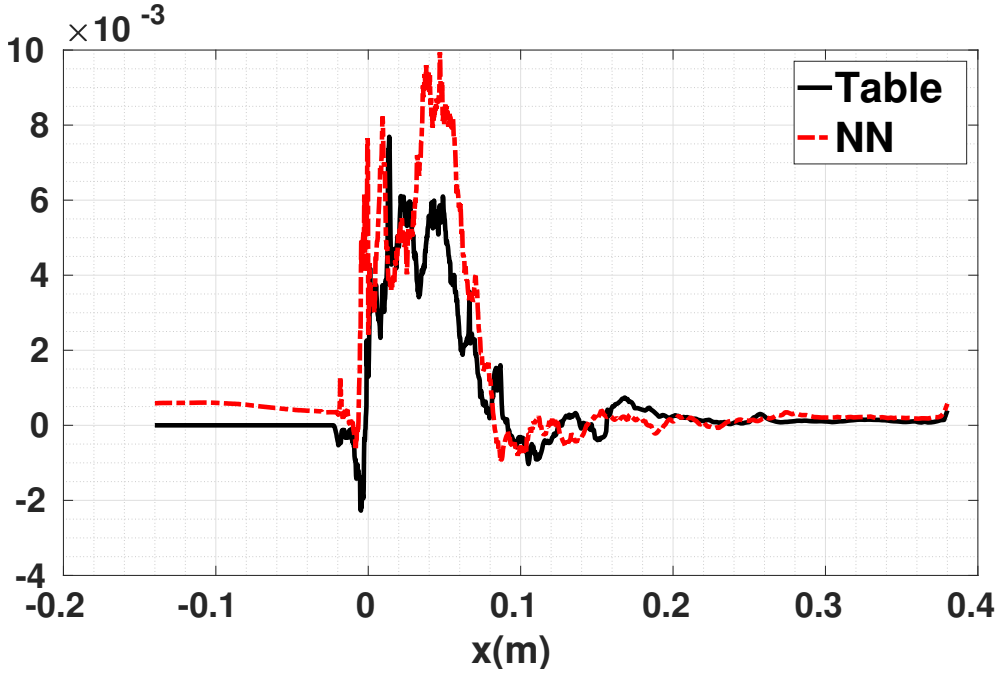

(c) Longitudinal distribution of mRI

Figure 5.34: TG: the mRI from the NN-based and the table-based simulations are compared

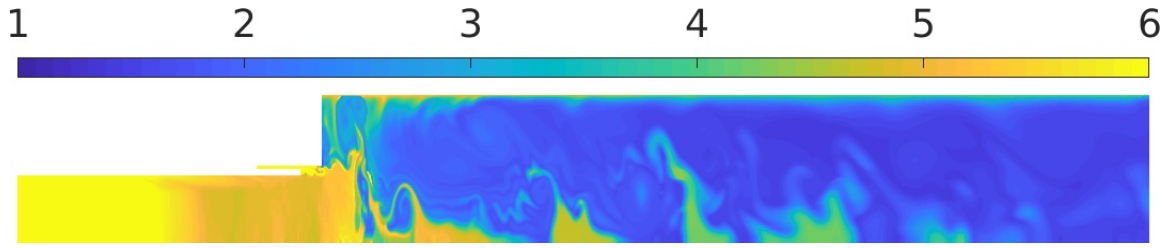

(a) $\overline{\rho}$ (kg m^{-3}), t_1, table

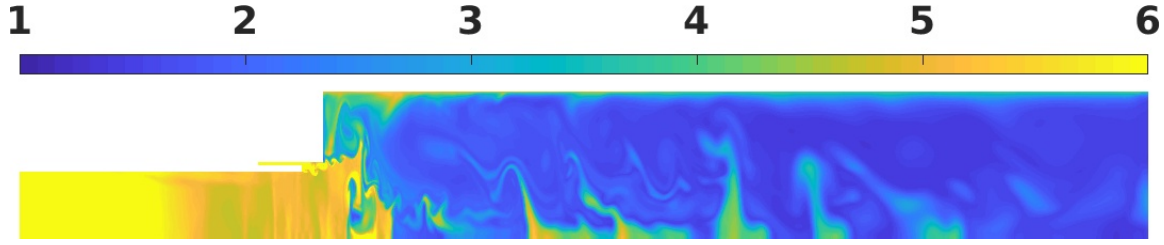

(b) $\overline{\rho}$ (kg m^{-3}), t_1, NN

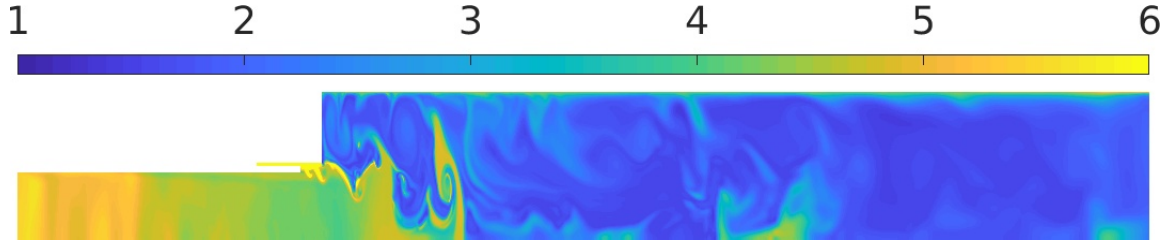

(c) $\overline{\rho}$ (kg m^{-3}), t_2, table

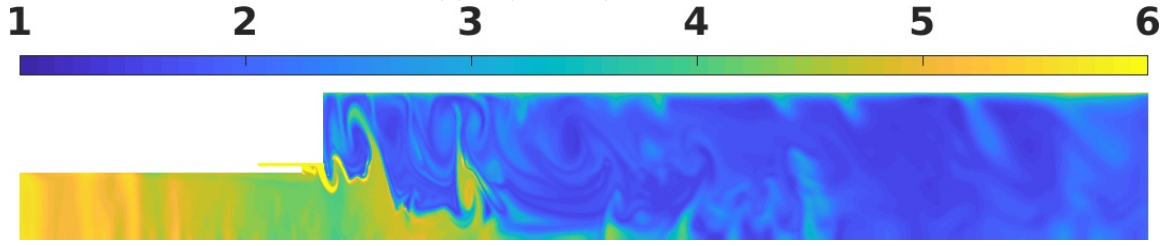

(d) $\overline{\rho}$ (kg m^{-3}), t_2, NN

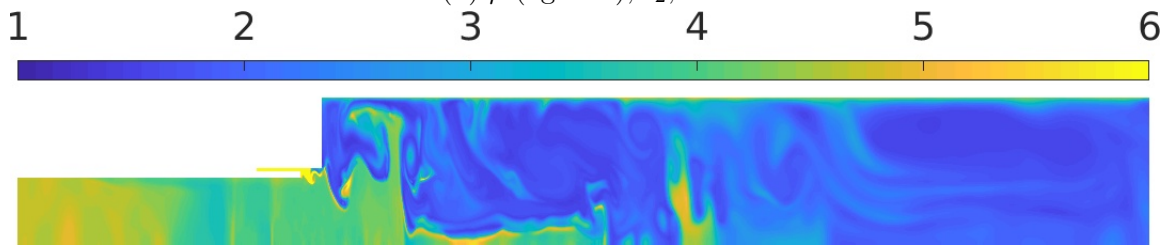

(e) $\overline{\rho}$ (kg m^{-3}), t_3, table

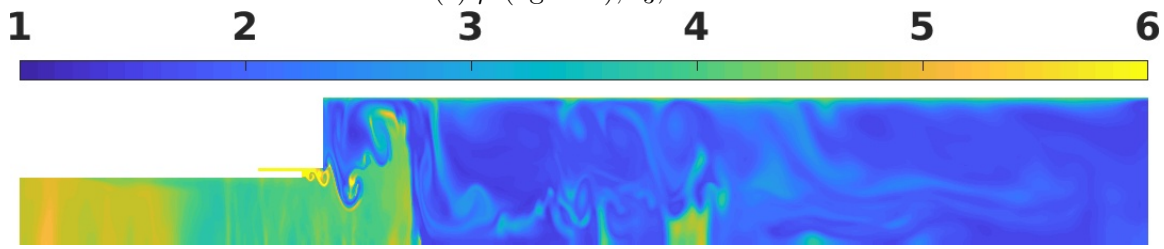

(f) $\overline{\rho}$ (kg m^{-3}), t_3, NN

Figure 5.35: TG: density

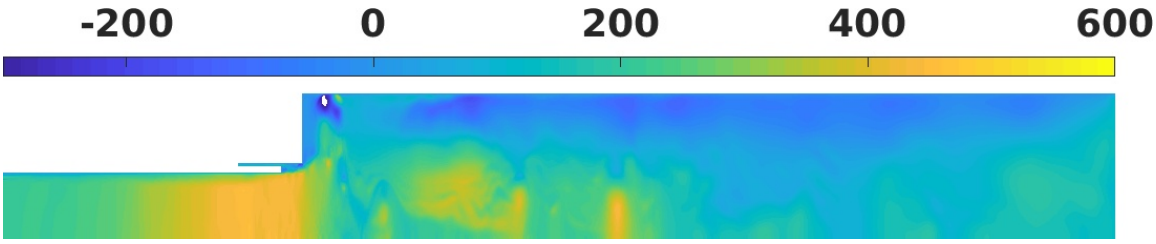

(a) $\widetilde{U}$ $(\mathrm{m\,s^{-1}})$, t_1, table

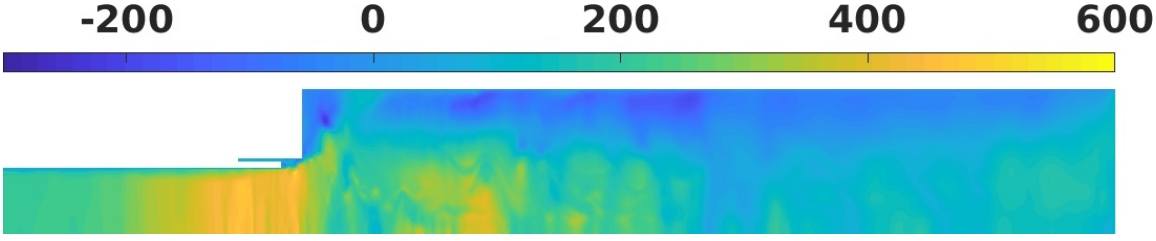

(b) $\widetilde{U}$ $(\mathrm{m\,s^{-1}})$, t_1, NN

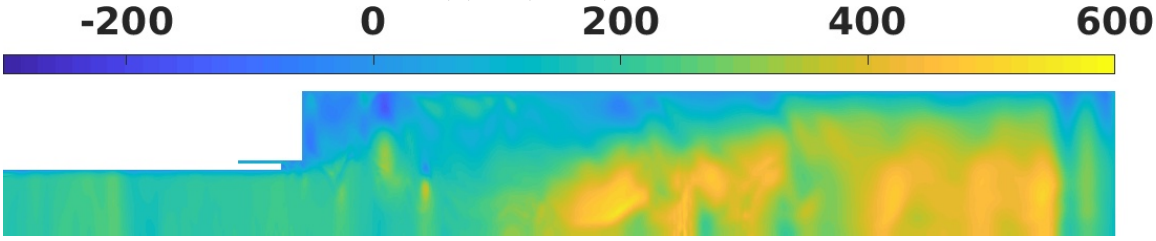

(c) $\widetilde{U}$ $(\mathrm{m\,s^{-1}})$, t_2, table

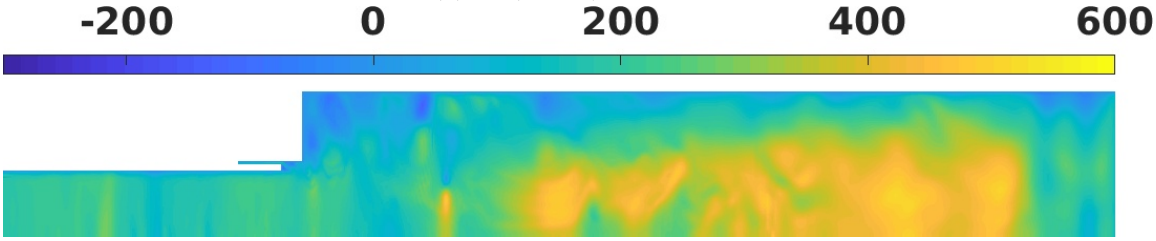

(d) $\widetilde{U}$ $(\mathrm{m\,s^{-1}})$, t_2, NN

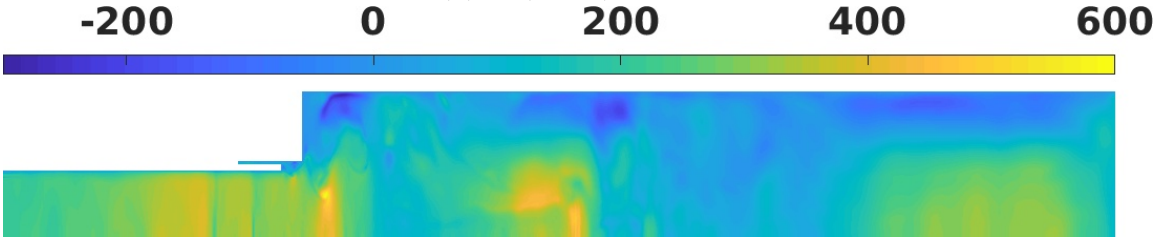

(e) $\widetilde{U}$ $(\mathrm{m\,s^{-1}})$, t_3, table

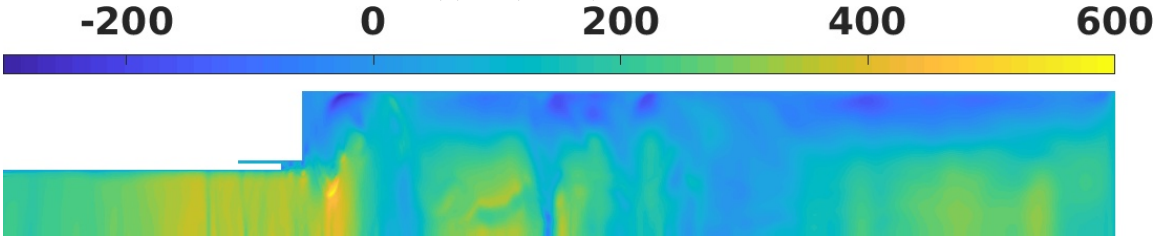

(f) $\widetilde{U}$ $(\mathrm{m\,s^{-1}})$, t_3, NN

Figure 5.36: TG: axial velocity

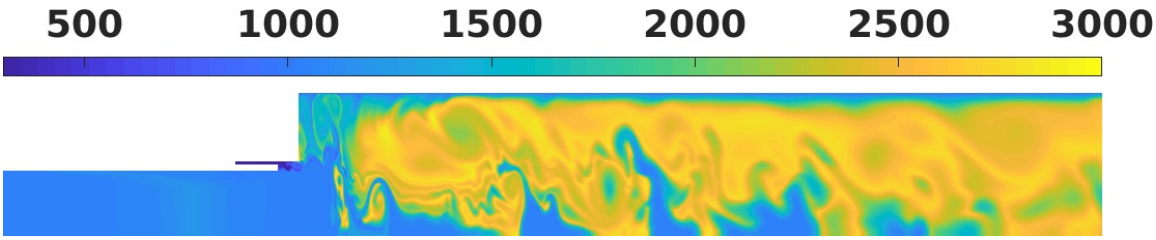

(a) $\widetilde{T}$ (K), t_1, table

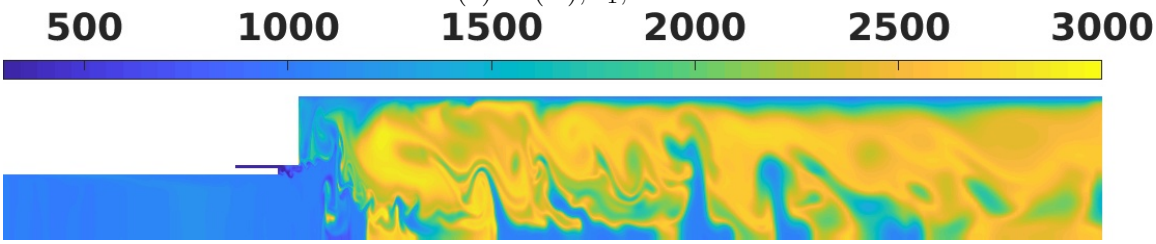

(b) $\widetilde{T}$ (K), t_1, NN

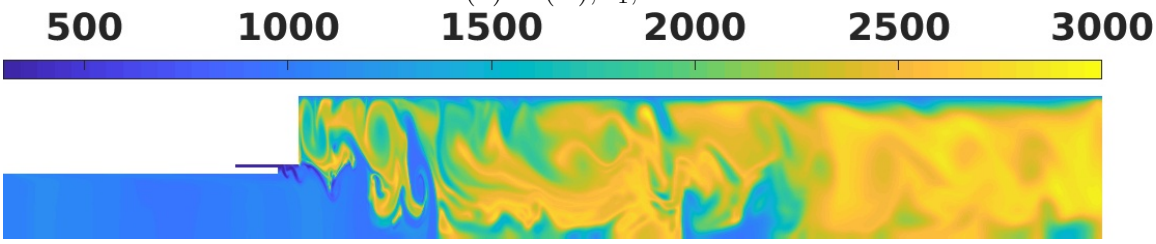

(c) $\widetilde{T}$ (K), t_2, table

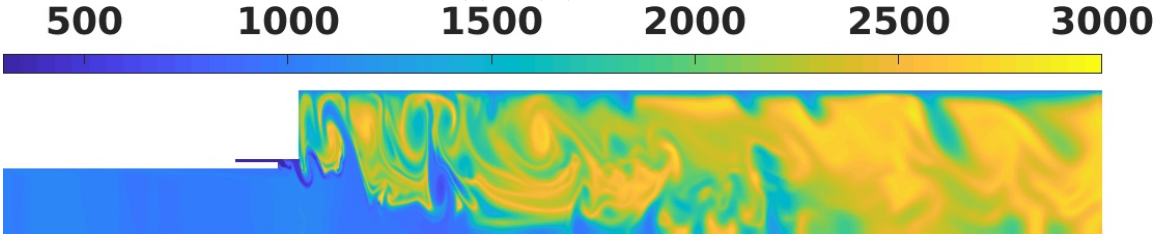

(d) $\widetilde{T}$ (K), t_2, NN

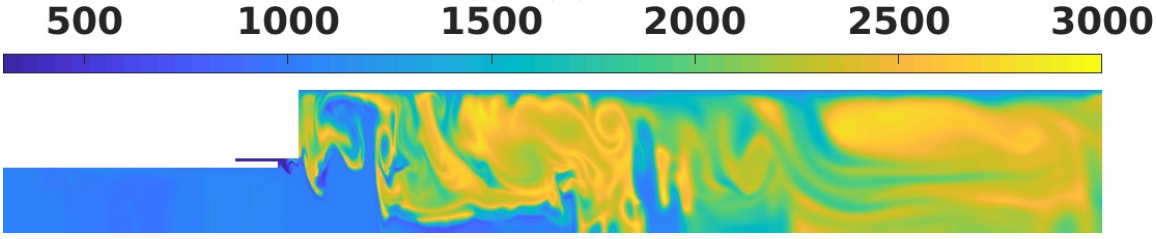

(e) $\widetilde{T}$ (K), t_3, table

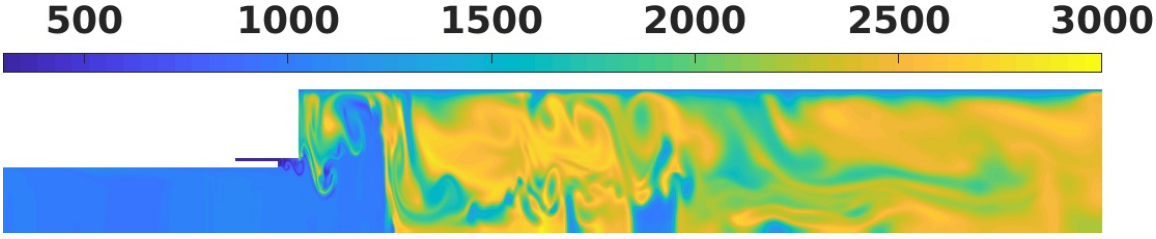

(f) $\widetilde{T}$ (K), t_3, NN

Figure 5.37: TG: temperature

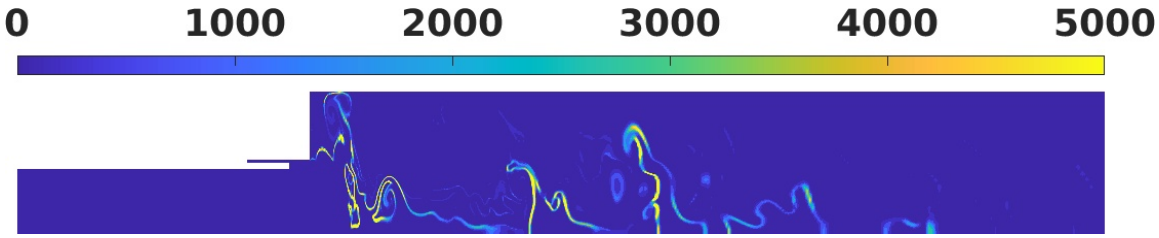

(a) $\widetilde{\omega}_C$ ($\mathrm{kg\,m^{-3}\,s^{-1}}$), t_1, table

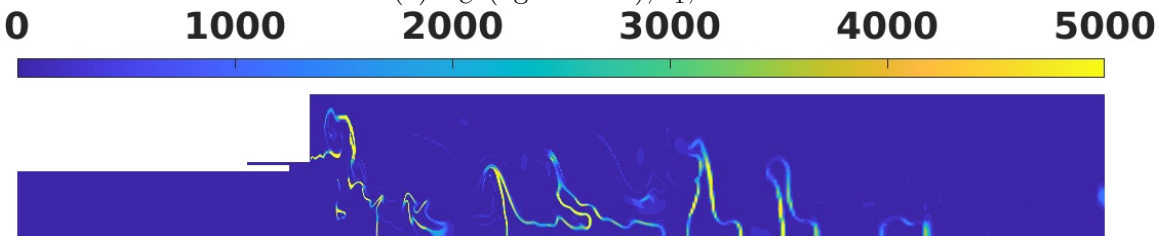

(b) $\widetilde{\omega}_C$ ($\mathrm{kg\,m^{-3}\,s^{-1}}$), t_1, NN

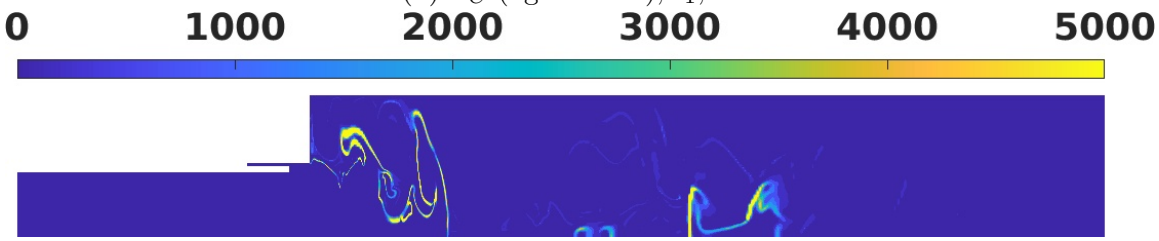

(c) $\widetilde{\omega}_C$ ($\mathrm{kg\,m^{-3}\,s^{-1}}$), t_2, table

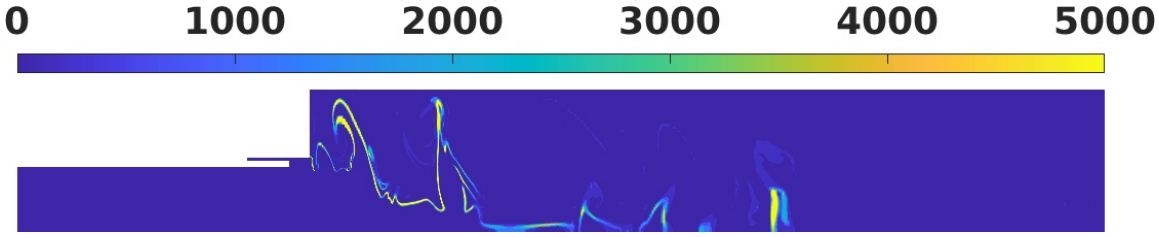

(d) $\widetilde{\omega}_C$ ($\mathrm{kg\,m^{-3}\,s^{-1}}$), t_2, NN

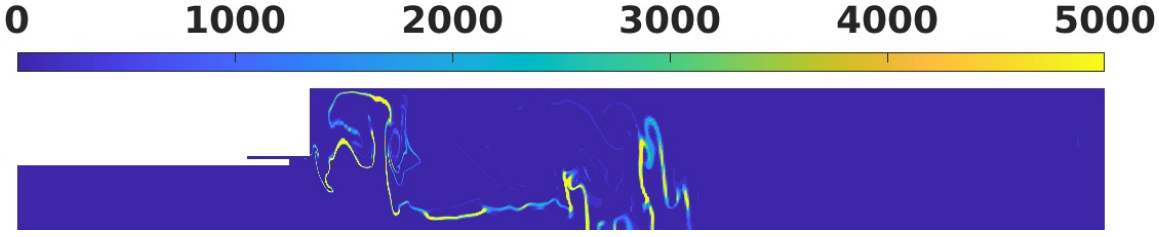

(e) $\widetilde{\omega}_C$ ($\mathrm{kg\,m^{-3}\,s^{-1}}$), t_3, table

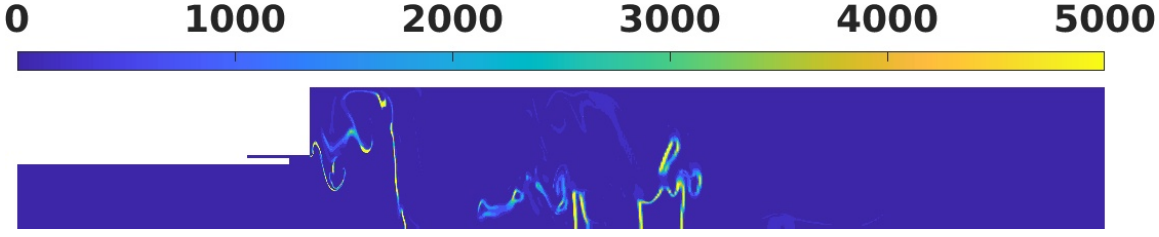

(f) $\widetilde{\omega}_C$ ($\mathrm{kg\,m^{-3}\,s^{-1}}$), t_3, NN

Figure 5.38: TG: PVRR

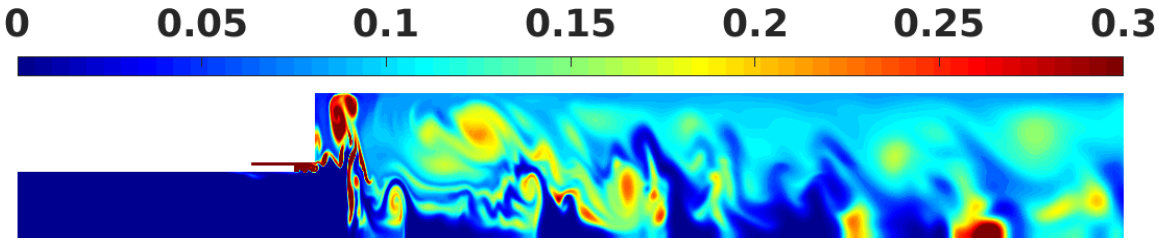

(a) $\widetilde{Z}$, t_1, table

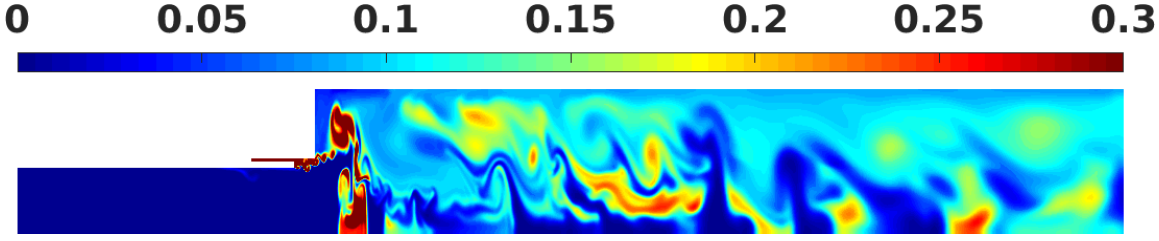

(b) $\widetilde{Z}$, t_1, NN

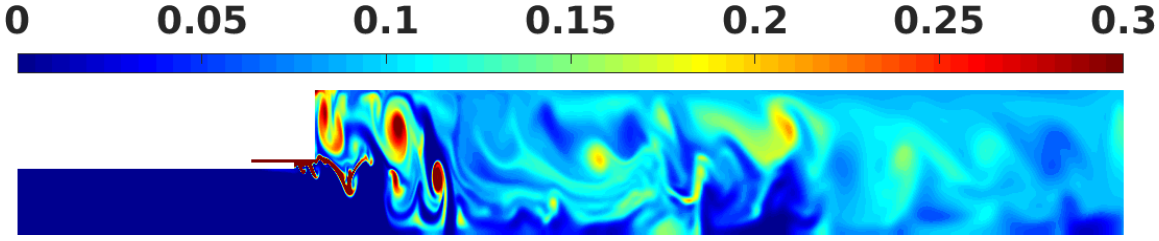

(c) $\widetilde{Z}$, t_2, table

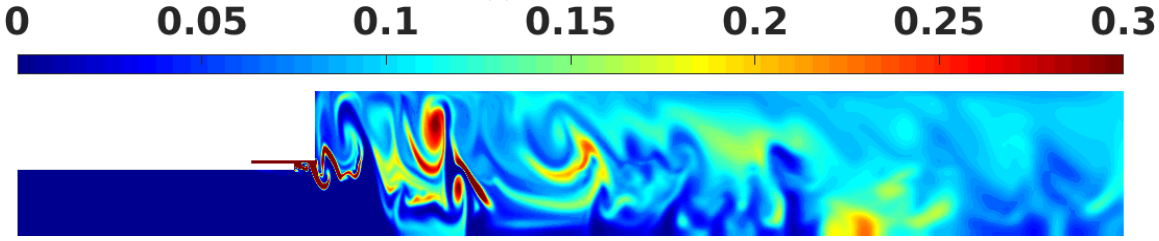

(d) $\widetilde{Z}$, t_2, NN

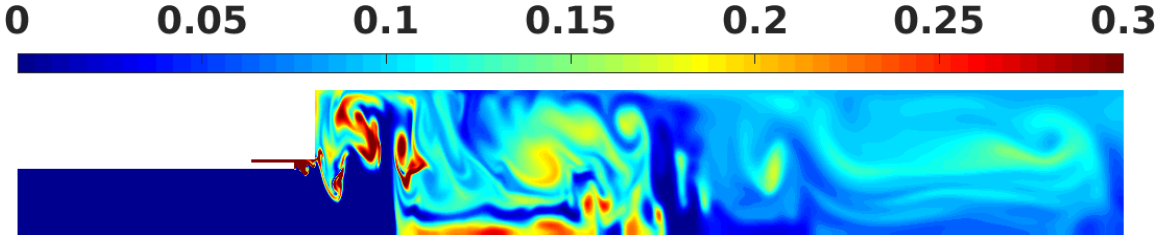

(e) $\widetilde{Z}$, t_3, table

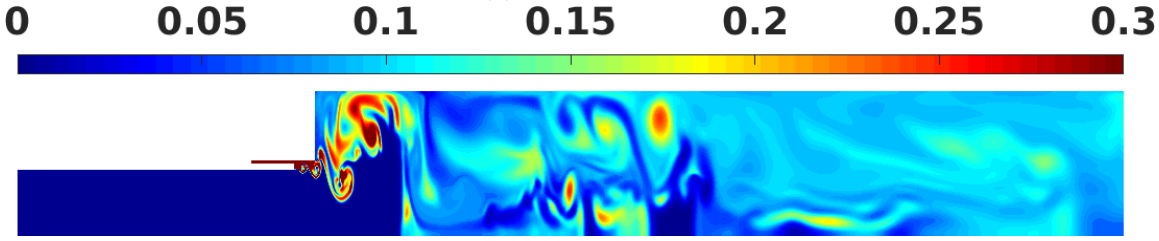

(f) $\widetilde{Z}$, t_3, NN

Figure 5.39: TG: mixture ratio

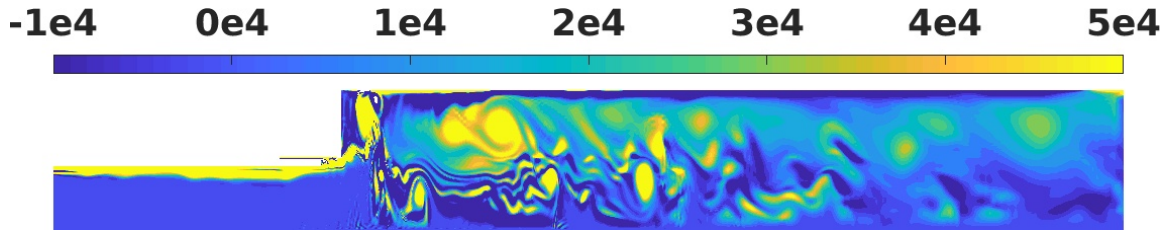

(a) $\widetilde{\Omega}$, t_1, table

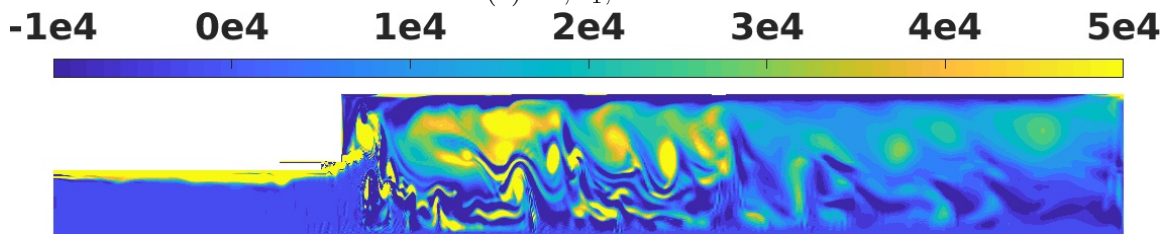

(b) $\widetilde{\Omega}$, t_1, NN

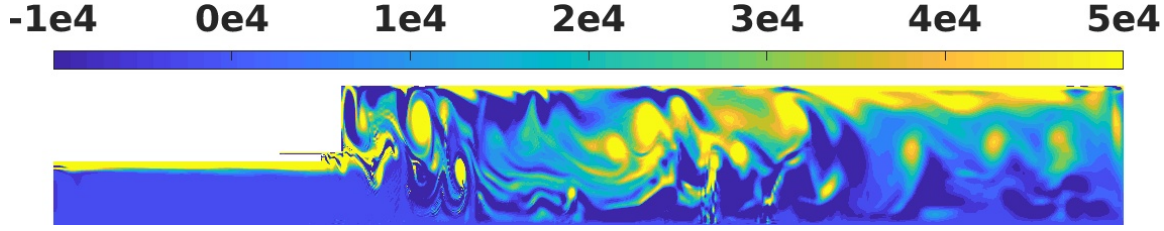

(c) $\widetilde{\Omega}$, t_2, table

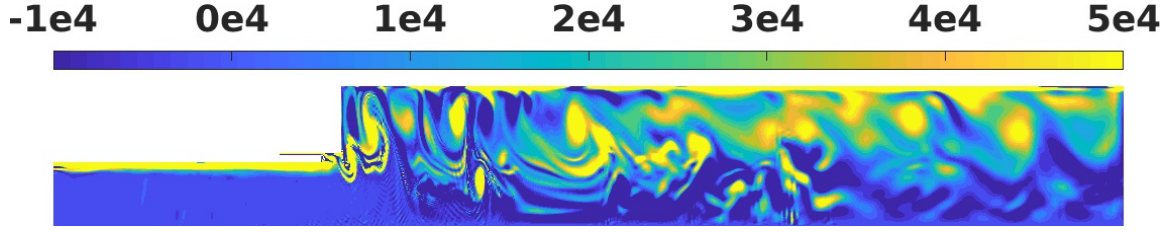

(d) $\widetilde{\Omega}$, t_2, NN

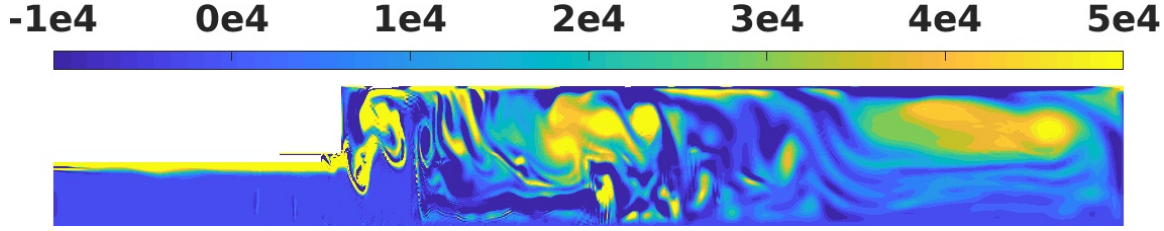

(e) $\widetilde{\Omega}$, t_3, table

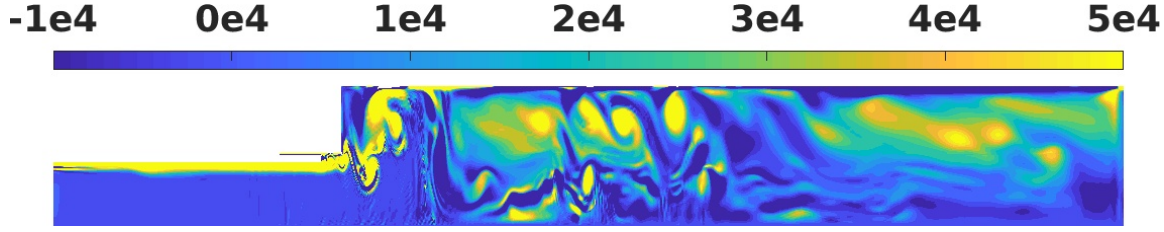

(f) $\widetilde{\Omega}$, t_3, NN

Figure 5.40: TG: vorticity

9-cm Case

In the two previous cases, we changed the thermal boundary condition and verified our NN-based models in two different dynamical configurations. To extend our verification process, in this section, we verify the models by implementing them into a 9-cm oxidizer post CFD simulation, as of a different geometrical configuration. In the previous two cases, the oxidizer post was set to be 14-cm, which demonstrates high levels of spontaneous instability [22]. In the 9-cm, the pressure oscillations grow to a limit cycle, which is much smaller than in the 14-cm case. Therefore, the 9-cm is considered to be stable. The e_o between the NN-based and table-based simulations and its distribution are shown in Figure 5.41a and Figure 5.41b.

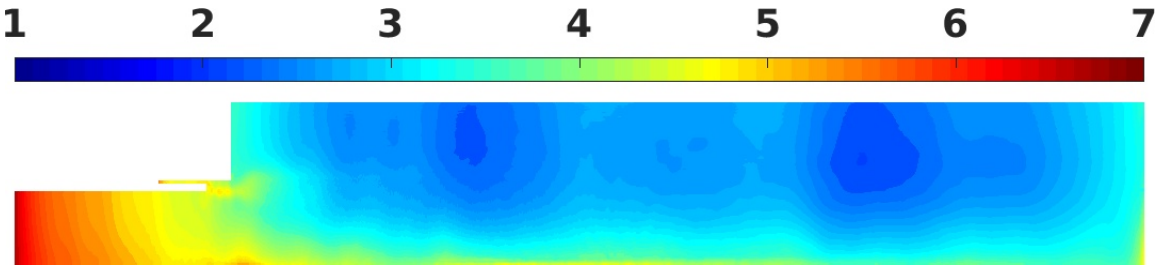

(a) Overall relative error (%)

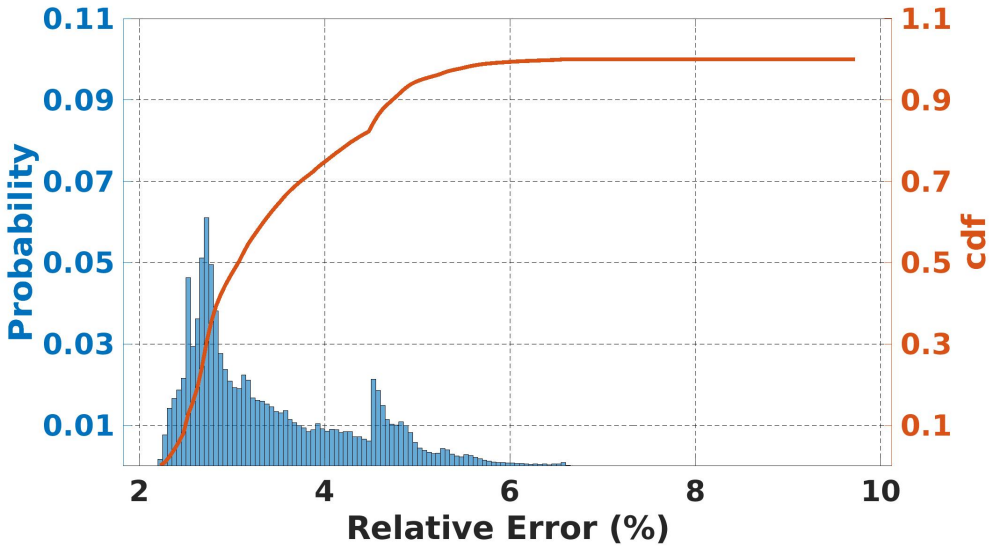

(b) Overall relative error (%) distribution

Figure 5.41: 9-cm case: distribution of relative error (%) between pressure signals calculated from the NN-based and the table-based simulations

The highest relative error occurs in the inlet of the oxidizer post, where there is no combustion occurring. As discussed before, the model for PVRR has deficiencies in estimating PVRR with low amplitude. This causes inconsistencies in the non-reacting zones. A similar issue was observed in our previous work, which was discussed in chapter 4.1 and [66]. The NN sets proposed in this part are designed to avoid this issue. The design is highly successful for all outputs except PVRR. In the future, the focus should be on a better model for PVRR in order to rectify the inconsistencies. The correlation of the fluctuations of the pressure signals from their mean value from the NN-based and table-based simulations is shown in Figure 5.42a, and in Figure 5.42b as distribution.

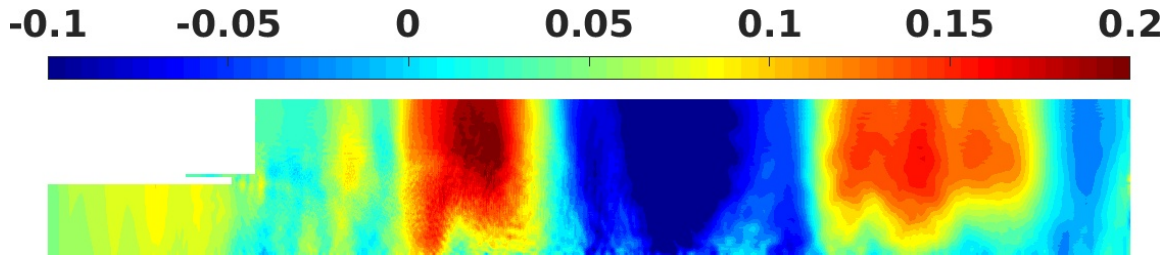

(a) Fluctuation correlations

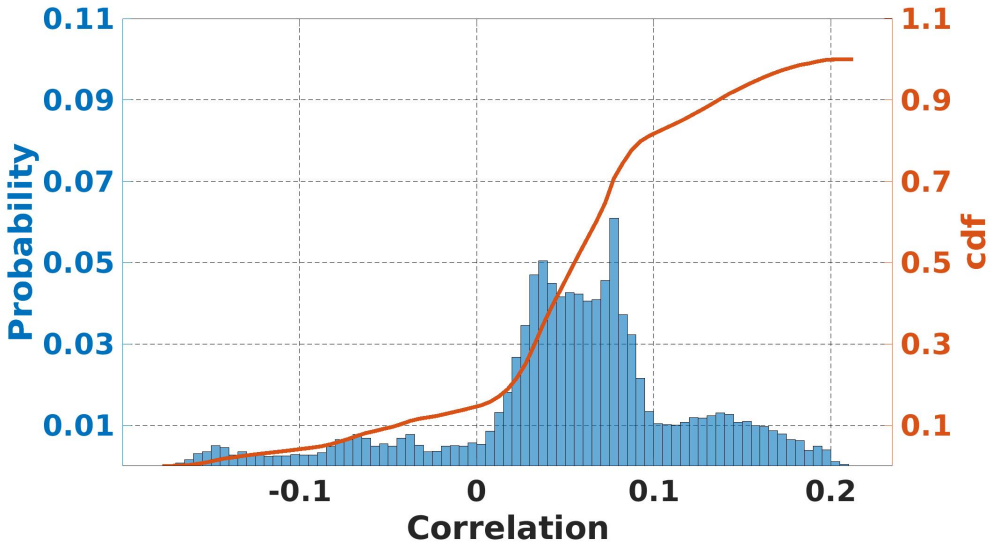

(b) Fluctuation correlation distribution

Figure 5.42: 9-cm case: fluctuation correlation between pressure signals calculated from the NN-based and the table-based simulations

The distribution of the ratio of pressure fluctuation rms in the NN-based simulation (Figure 5.43b) to that in the table-based one (Figure 5.43a) is shown in Figure 5.43c. The NN-based simulation mostly overestimates the rms values, and around 70% of the points have estimated between 100% to 110% of the rms from table-based simulation. The rms values in the 9-cm case are also lower than the ones in the 14-cm unstable case. The pressure rms values are higher at the inlet, and they become smaller throughout the combustor.

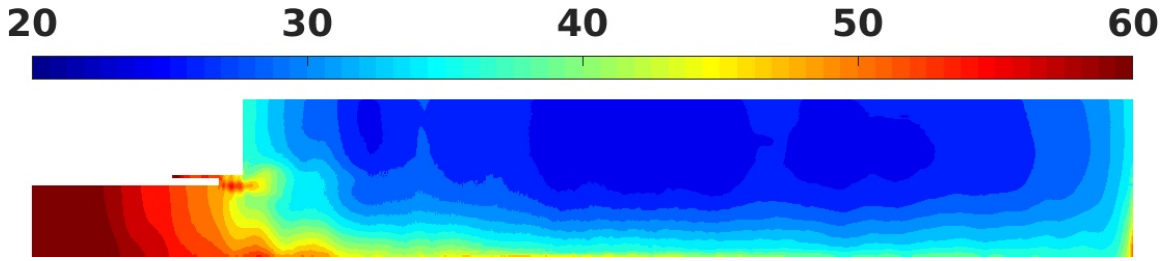

(a) Table-based pressure signal rms (kPa)

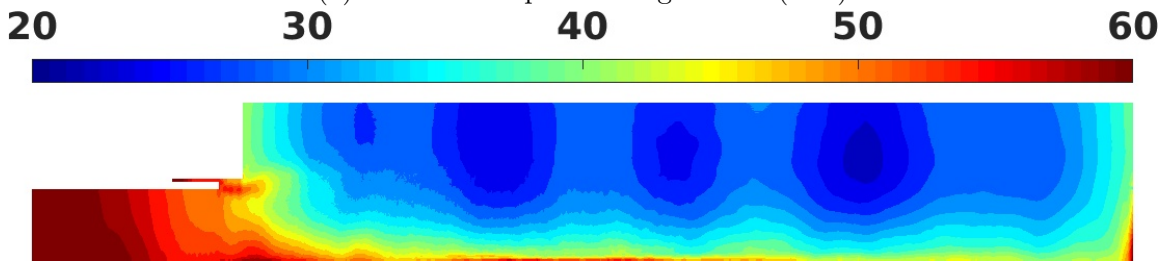

(b) NN-based pressure signal rms (kPa)

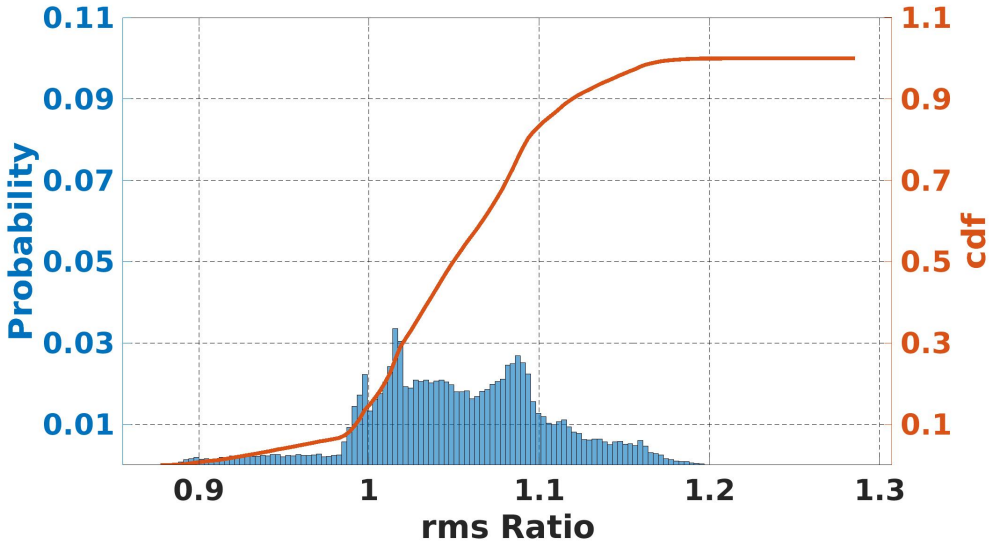

(c) rms ratio distribution

Figure 5.43: 9-cm case: the distribution of the ratio of the rms of the pressure signal from NN-based (5.43b) to the one from table-based (5.43a) simulations

Figure 5.44 compares the pressure signal and its FFT at two points, similar to the previous cases, one in shear layer and one in oxidizer post, calculated from the NN-based simulation with that from the table-based simulation. The point in the oxidizer post has a stronger second mode and larger oscillations in both the table-based and NN-based simulations. The noisy nature of the pressure waveform in this configuration can be seen in these figures. Although it is harder to generate a fully correlated signal, the modal frequencies and signal trends are similar between the NN-based and table-based simulations.

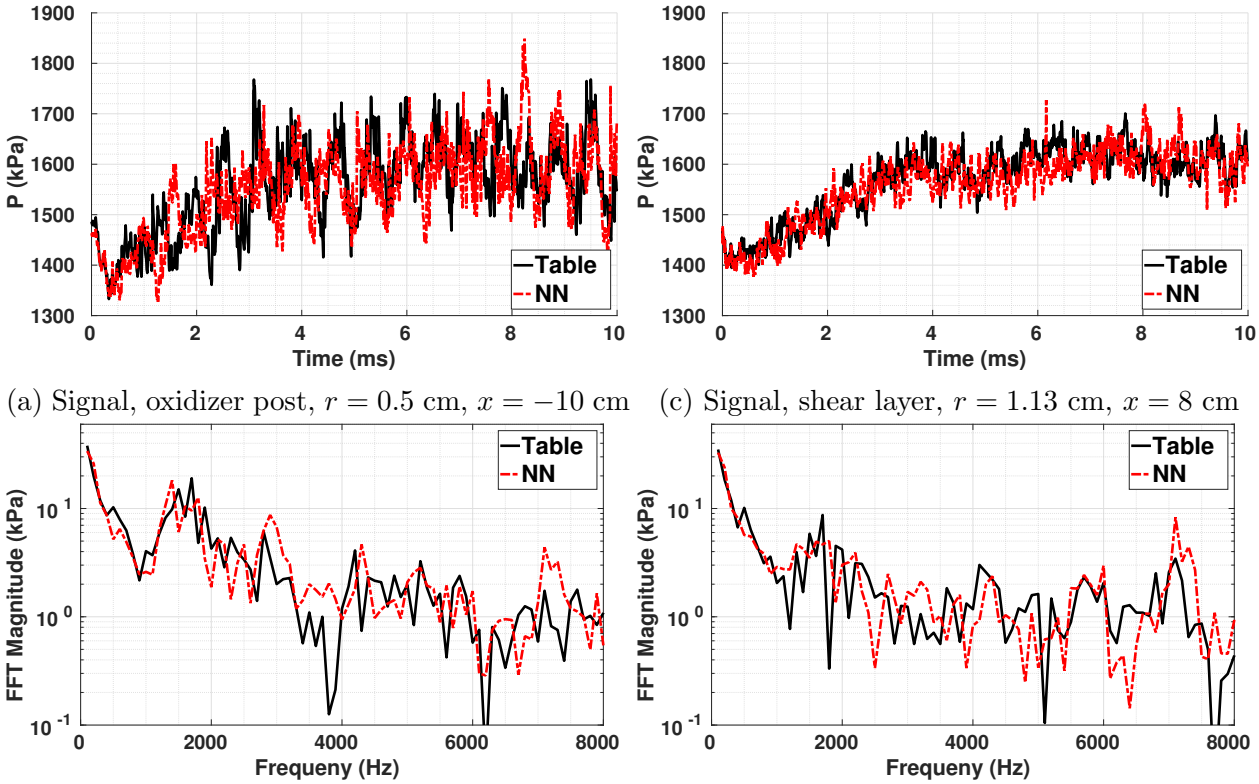

(a) Signal, oxidizer post, $r = 0.5$ cm, $x = -10$ cm

(c) Signal, shear layer, $r = 1.13$ cm, $x = 8$ cm

(b) Pressure FFT at $r = 0.5$ cm, $x = -10$ cm

(d) Pressure FFT at $r = 1.13$ cm, $x = 8$ cm

Figure 5.44: 9-cm case: comparison of pressure signals at two representative point and their FFT, between the NN-based and the table-based simulations

The pressure mode shape shows similar behavior in Figure 5.45 for the mean value and the first and the second mode shapes, where the modes are not predicted as well as the mean. The first and the second modes in the 9-cm case have relatively small magnitudes; also, the magnitude of the modes are approximately equally distributed, although the first mode has

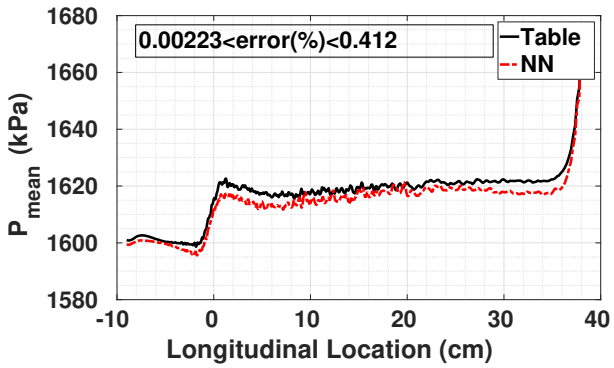

(a) Mean pressure (kPa)

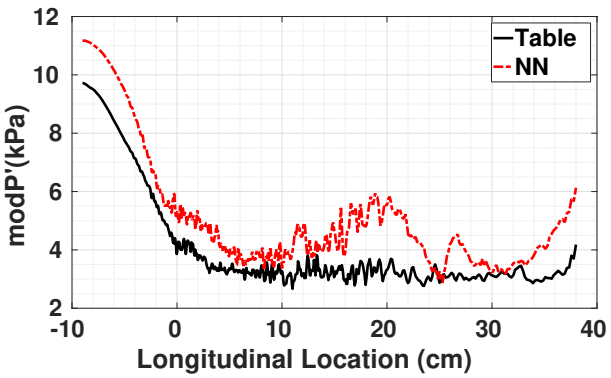

(b) First mode shape (kPa)

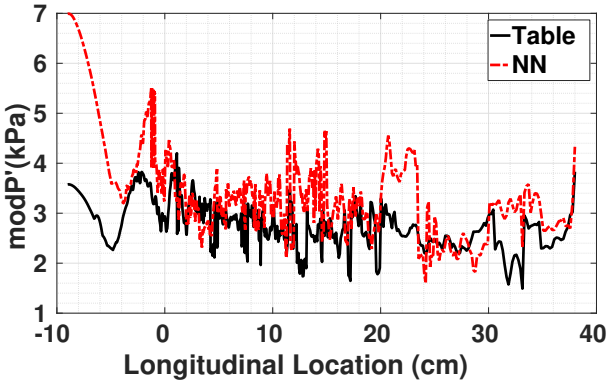

(c) Second mode shape (kPa)

Figure 5.45: 9-cm case: comparison of pressure mean and the first and second mode shape between NN-based and table-based simulations

a slightly larger magnitude. The modes have amplitude less than 1% of the mean pressure throughout the centerline.

The local mRI is compared for the two simulations in Figure 5.46. Comparing Figure 5.46a with Figure 5.46b shows that the NN-based simulation is very similar to the table-based one in capturing the behavior, particularly in the shear layer, of the mRI shape. Since the 9-cm case is a stable one, the magnitude of mRI are lower than those in the 14-cm case. Low mRI shows that there is no instability occurring.

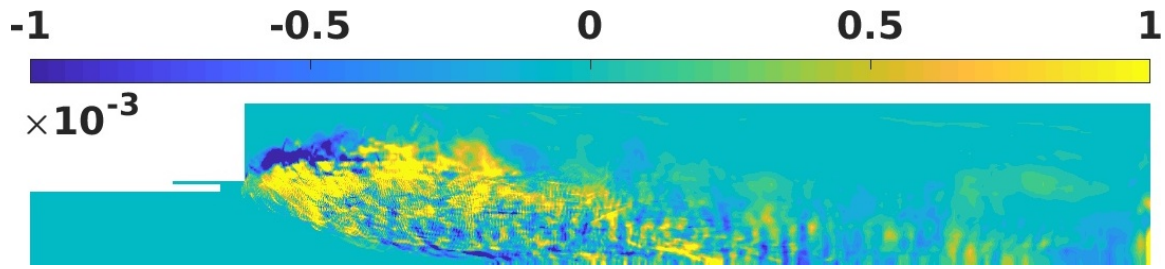

(a) Table-based CFD: mRI

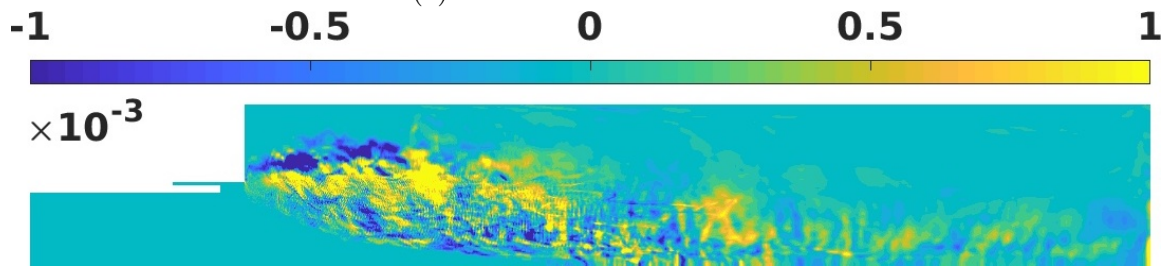

(b) NN-based CFD: mRI

Figure 5.46: 9-cm case: comparison of mRI from the NN-based and the table-based simulations

5.3 Concluding Remarks

Relatively low cost, NN models are proposed with less than 0.6% training error except for PVRR, for which a very deep and more computationally expensive NN model is required for accurate modeling. For PVRR, the training error turned to be around 1.5%, and the model fits great for high values of PVRR, which are crucial for modeling combustion instability. We exploited our knowledge of the physics of the problem in our favor to enhance the training data set. We achieve this by adding more points implied by the physical constraints to the training set. We also use the flame temperature which is an output of the flamelet model as an auxiliary input for the other outputs. This method helps to improve each model's accuracy and consistency between the model outputs.

These NN-based models are validated first by testing them on the whole flamelet table, and then by implementing them in CFD simulations of different unstable and stable configurations. The NN-based simulations are compared with the table-based ones in the highly unstable configuration with14-cm oxidizer post for the dynamic equilibrium and triggered

instability cases of the CVRC experiment. The models are also implemented into a transient CFD simulation, which is the source of the original training data set. The underlying physics here has chaotic dynamics. Particularly, the transient simulation shows large sensitivity to small errors in the flamelet models. In the two scenarios of dynamic equilibrium and triggering instability, great consistency is observed in different measures such as pressure, modified Rayleigh index, and temporal behavior of other quantities. The model showed some weaknesses in modeling regions where there is no combustion, i.e. the oxidizer post, due to the lack of sufficient training data collected through the CFD simulation.

The NN models are also implemented in a stable simulation with 9-cm oxidizer post, in which the observed pressure fluctuations resemble relatively small amplitude. These oscillations have a noisy behavior, and the NN-based simulation leads to similar statistical behavior, such as mRI, rather than regenerating exactly the same solution as the reference model.

Offline comparison of the NN models with the flamelet libraries confirms that the performance of the NN model is better in regions where more data is included in the training set. As the source simulation is a fuel lean setup, higher values of $\widetilde{Z}$ were lacking in the training set. Similarly, regions with higher turbulence levels of the table (high B values) have weaker performance because of the lack of data in the training set.

Chapter 6

Conclusions and Future Work

In this work, the capabilities of deep learning in modeling turbulent flame in the simulation of turbulent reacting flow with unsteady pressure in liquid propellant rocket engines are explored. Flamelet models provide a good stepping stone, as evidenced by the encouraging results shown in this work. The framework presented in this work can be applied to high-quality data from sources other than the flamelet table, such as high fidelity LES or even DNS, where the cost saving of using machine learning models can be highly advantageous.

The use of neural network closure of sub-grid flame model provides a great level flexibility and potential saving on computational cost. Regarding the flamelet model, neural networks require a significantly lower memory, which makes them perfect for being implemented on GPU. Whereas the large memory requirement of tabular methods causes them to be challenging for GPU implementation and parallel computing. Although the data retrieval from a NN model is more time costly than reading the data from a look-up table, the computational cost is still lower than using the chemical kinetics solver.

Here, two approaches for developing NN closure model for the flamelet model are presented. The main difference between the two approaches is the source of data used for the training

process in the NN development. The NNs proposed in the second approach are more optimal in terms of data retrieval computational cost. The NNs proposed in both approaches are tested on reconstructing the flamelet libraries. They are verified by being implemented in CFD simulations of CVRC test cases with different geometry and stability configurations.

In the first approach, the flamelet libraries are used as a source for training NN-based models. Around 5% of data in the flamelet table is sampled to generate the original training set. During the training process, NNs are tested on the flamelet table, and the data points with the highest relative errors are added back to the training set. The final training set included 15% of the flamelet table.

Two sets of NNs with different sizes are studied. One set has NNs with multiple outputs and smaller depths; yet, the other set of NNs are designed separately for each of the seven outputs of the flamelet table. In the most accurate case, separate NNs for each of the flame variables are designed and tested by comparing the NN output values with the corresponding values in the table. The gas constant, internal flame energy, and flame heat capacity ratio are estimated with 0.0506%, 0.0852%, and 0.0778% error, respectively. Flame temperature, thermal conductivity, and the coefficient of heat capacity ratio are estimated with 0.63%, 0.68%, and 0.86% error, respectively. The progress variable reaction rate is also estimated with a 3.59% error. The errors are calculated based on the mean square error over all points in the table.

These NNs are implemented into the transient and dynamic equilibrium scenarios of the 14-cm oxidizer post configuration of CVRC. They are also implemented in a 9-cm oxidizer post with a transient scenario. In the 9-cm oxidizer post, the dynamic of the system is governed significantly by turbulent combustion rather than acoustic behavior. The turbulence leads to a stochastic behavior in fluctuations for different quantities. Good agreement is observed between the NN-based simulations and the table-based ones.

In the second approach, NN-based models are proposed to represent the flamelet model outputs. The NN models are trained from data that are sampled from a CFD simulation of a transient scenario of a CVRC engine, in which pressure oscillations spontaneously reach to a high limit cycle from a low value. Then, the pressure oscillates with a constant amplitude reaching a dynamic equilibrium. The sample set is reinforced by adding data from physical constraints and considerations of the problem at hand, giving rise to a physics-aware NN-based model. The flame thermal properties such as temperature at boundaries of the mixture ratio are provided in the training data set. The flame quantities are also provided in the training set when there is no combustion, assuming they are calculated from the fluid mechanics' point of view. Another physics-based source of information introduced here to enhance the NN performance is the addition of the flame temperature (which is an output of the flamelet table) as an input for the other outputs of the flamelet table (except for PVRR). Our method contributed to developing much better models that obey the physical constraints of the problem. Further investigation on selecting the right set of input and data can help in achieving better models.

These NNs are also implemented into the transient and dynamic equilibrium scenarios of the 14-cm oxidizer post configuration of CVRC, which resemble spontaneous instability. The NNs are also implemented in a scenario with triggering instability of the 14-cm oxidizer post. The spontaneous instability is avoided in this configuration by the use of an isothermal wall boundary condition instead of an adiabatic one. Then, instability was triggered by perturbing mass flow rate by two periods of sinusoid waves. The 9-cm case is also tested as a representative of a different geometry. Good agreement is observed between the NN-based simulations and the table-based ones in all cases.

In both of these approaches, our data retrieval code for NN-based CFD is not optimized. The computational cost of NN-based simulation is much larger than that of the table-based one. Although our design in the second approach leads to a much cheaper computational

cost, it is still more expensive than the table-based one (about 7 times more). In the future, the computational cost of NN modeling should be revisited after parallelizing and optimizing the codes for a GPU implementation.

Along the same direction as our first approach, in the future, with new flamelet models, we propose moving directly to the flamelet calculations (possibly augmented by experimental data). Instead of learning from the table, we propose to learn from the algorithm that generates the table. This could help the accuracy of the flamelet model implementation because of the capability of NNs in nonlinear interpolations.

The ultimate goal of this work is to explore the possibilities of developing data-driven combustion models only from data generated from highly accurate numerical simulations or experiments. The significance is that each source of data observes only a subset of the actual model (which is assumed to be the flamelet library in this work). The information fusion power of NNs has been essentially tested in this work. Having a richer training set from multiple experiments allows having a more comprehensive NN model by providing better coverage of the actual dynamic behavior.

Bibliography

[1] Culick, F. E., and Yang, V., "Overview of Combustion Instabilities in Liquid-Propellant Rocket Engines," *Liquid Rocket Engine Combustion Instability*, Vol. 169, 1995, pp. 3–37.

[2] Oefelein, J. C., and Yang, V., "Comprehensive Review of Liquid Propellant Combustion Instabilities in F-1 Engines," *Journal of Propulsion and Power*, Vol. 9, No. 5, 1993, pp. 657–677.

[3] Crocco, L., and Cheng, S.-I., "High Frequency Combustion Instability in Rockets with Distributed Combustion," *Fourth Symposium (International) on Combustion*, Vol. 4, 1953, pp. 865–880.

[4] Crocco, L., and Cheng, S.-I., "Theory of Combustion Instability in Liquid propellant Rocket Motors," *Monograph 8*, AGARD, 1956.

[5] Garby, R., Selle, L., and Poinsot, T., *Analysis of the Impact of Heat Losses on an Unstable Model Rocket-engine Combustor Using Large-Eddy Simulation*, chapter and pages. https://doi.org/10.2514/6.2012-4085.

[6] Harrje, D., and Reardon, F., *Liquid Propellant Rocket Combustion Instability*, NASA, 1972.

[7] Barr, P., Keller, J., Bramlette, T., Westbrook, C., and Dec, J., "Pulse Combustor Modeling Demonstration of the Importance of Characteristic Times," *Combustion and Flame*, Vol. 82, No. 3, 1990, pp. 252 – 269. https://doi.org/10.1016/0010-2180(90)900029.

[8] Celik, I., Zhang, W., Spenik, J. L., and Morris, G. J., "One-Dimensional Modeling and Measurement of Pulsating Gas-Solid Flow in Tubes," *Combustion Science and Technology*, Vol. 94, No. 1-6, 1993, pp. 353–378. https://doi.org/10.1080/00102209308935319.

[9] Popov, P. P., Sideris, A., and Sirignano, W. A., "Stochastic Modelling of Transverse Wave Instability in a Liquid-Propellant Rocket Engine," *Journal of Fluid Mechanics*, Vol. 745, 2014, p. 6291. https://doi.org/10.1017/jfm.2014.96.

[10] Popov, P. P., Sirignano, W. A., and Sideris, A., "Propellant Injector Influence on Liquid-Propellant Rocket Engine Instability," *Journal of Propulsion and Power*, Vol. 31, No. 1, 2015, pp. 320–331. https://doi.org/10.2514/1.B35400.

[11] Saghafian, A., Terrapon, V. E., and Pitsch, H., "An Efficient Flamelet-based Combustion Model for Compressible Flows," *Combustion and Flame*, Vol. 162, No. 3, 2015, pp. 652 – 667. https://doi.org/10.1016/j.combustflame.2014.08.007.

[12] Srinivasan, S., Ranjan, R., and Menon, S., "Flame Dynamics During Combustion Instability in a High-Pressure, Shear-Coaxial Injector Combustor," *Flow, Turbulence and Combustion*, 2014, pp. 1–26. https://doi.org/10.1007/s10494-014-9569-x.

[13] Yu, Y. C., Koeglmeier, S. M., Sisco, J. C., and Anderson, W. E., "Combustion Instability of Gaseous Fuels in a Continuously Variable Resonance Chamber (CVRC)," *AIAA 2008-4657*, 2008, pp. 1–12.

[14] Yu, Y. C., O'Hara, L., Sisco, J. C., and Anderson, W. E., "Experimental Study of High-Frequency Combustion Instability in a Continuously Variable Resonance Combustor," *AIAA 2009-234*, 2009, pp. 1–12.

[15] Yu, Y. C., Sisco, J. C., Rosen, S., Madhav, A., and Anderson, W. E., "Spontaneous Longitudinal Combustion Instability in a Continously Variable Resonance Combustor," *Journal of Propulsion and Power*, Vol. 28, No. 5, 2012, pp. 876–887.

[16] Ghani, A., Poinsot, T., Gicquel, L., and Staffelbach, G., "LES of Longitudinal and Transverse Self-Excited Combustion Instabilities in a Bluff-Body Stabilized Turbulent Premixed Flame," *Combustion and Flame*, Vol. 162, No. 11, 2015, pp. 4075 – 4083. https://doi.org/10.1016/j.combustflame.2015.08.024.

[17] Garby, R., Selle, L., and Poinsot, T., "Large-Eddy Simulation of Combustion Instabilities in a Variable Length Combustor," *Comptes Rendus Mecanique*, Vol. 341, 2013, pp. 220–229.

[18] Harvazinski, M. E., Anderson, W. E., and Merkle, C. L., "Analysis of Self-Excited Combustion Instabilities Using Two- and Three Dimensional Simulations," *Journal of Propulsion and Power*, Vol. 29, No. 2, 2013, pp. 396–409. https://doi.org/10.2514/1.B34732.

[19] Spalart, P., Jou, W.-H., Strelets, M., and Allmaras, S., "Comments on the Feasibility of LES for Wings, and on a Hybrid RANS/LES Approach," 1st AFSOR Conference on Advances in DNS/LES, Greyden Press, 1997, pp. 137–147.

[20] *Turbulent Combustion*, Cambridge Monographs on Mechanics, ????

[21] Pierce, C. D., and Moin, P., "Progress-Variable Approach for Large-Eddy Simulation of Non-Premixed Turbulent Combustion," *Journal of Fluid Mechanics*, Vol. 504, 2004, p. 7397. https://doi.org/10.1017/S0022112004008213.

[22] Nguyen, T. M., Popov, P. P., and Sirignano, W. A., "Longitudinal Combustion Instability in a Rocket Engine with a Single Coaxial Injector," *Journal of Propulsion and Power*, 2017, pp. 1–20. https://doi.org/10.2514/1.B36516.

[23] Nguyen, T. M., and Sirignano, W. A., "Spontaneous and Triggered Longitudinal Combustion Instability in a Single-Injector Liquid-Rocket Combustor," *AIAA Journal*, Vol. 57, No. 12, 2019, pp. 5351–5364. https://doi.org/10.2514/1.J057743.

[24] Nguyen, T. M., and Sirignano, W. A., "The Impacts of Three Flamelet Burning Regimes in Nonlinear Combustion Dynamics," *Combustion and Flame*, Vol. 195, 2018, pp. 170 – 182. https://doi.org/10.1016/j.combustflame.2018.03.031, special Commemorative Issue: Professor Chung King (Ed) Law 70th Birthday.

[25] Harvazinski, M. E., "Modeling Self-excited Combustion Instabilities Using a Combination of Two- and Three-dimensional Simulations," Ph.D. thesis, Purdue University, 2012.

[26] Brunton, S. L., Noack, B. R., and Koumoutsakos, P., "Machine Learning for Fluid Mechanics," *Annual Review of Fluid Mechanics*, Vol. 52, No. 1, 2020, pp. 477–508. https://doi.org/10.1146/annurev-fluid-010719-060214.

[27] Duraisamy, K., Iaccarino, G., and Xiao, H., "Turbulence Modeling in the Age of Data," *Annual Review of Fluid Mechanics*, Vol. 51, No. 1, 2019, pp. 357–377. https://doi.org/10.1146/annurev-fluid-010518-040547.

[28] Faller, W. E., and Schreck, S. J., "Unsteady Fluid Mechanics Applications of Neural Networks," *Journal of Aircraft*, Vol. 34, No. 1, 1997, pp. 48–55. https://doi.org/10.2514/2.2134.

[29] Duraisamy, K., Zhang, Z. J., and Singh, A. P., "New Approaches in Turbulence and Transition Modeling Using Data-driven Techniques," *53rd AIAA Aerospace Sciences Meeting*, AIAA SciTech Forum, American Institute of Aeronautics and Astronautics, 2015. https://doi.org/10.2514/6.2015-1284.

[30] Ling, J., Kurzawski, A., and Templeton, J., "Reynolds Averaged Turbulence Modelling Using Deep Neural Networks with Embedded Invariance," *Journal of Fluid Mechanics*, Vol. 807, 2016, p. 155166. https://doi.org/10.1017/jfm.2016.615.

[31] Singh, A. P., Medida, S., and Duraisamy, K., "Machine-Learning-Augmented Predictive Modeling of Turbulent Separated Flows over Airfoils," *AIAA Journal*, Vol. 55, No. 7, 2017, pp. 2215–2227. https://doi.org/10.2514/1.J055595.

[32] Tracey, B. D., Duraisamy, K., and Alonso, J. J., "A Machine Learning Strategy to Assist Turbulence Model Development," *53rd AIAA Aerospace Sciences Meeting*, AIAA SciTech Forum, American Institute of Aeronautics and Astronautics, 2015. https://doi.org/10.2514/6.2015-1287.

[33] San, O., and Maulik, R., "Machine Learning Closures for Model Order Reduction of Thermal fluids," *Applied Mathematical Modelling*, Vol. 60, 2018, pp. 681 – 710. https://doi.org/10.1016/j.apm.2018.03.037.

[34] Ranade, R., Li, G., Li, S., and Echekki, T., "An Efficient Machine-Learning Approach for PDF Tabulation in Turbulent Combustion Closure," *Combustion Science and Technology*, Vol. 193, No. 7, 2021, pp. 1258–1277. https://doi.org/10.1080/00102202.2019.1686702.

[35] Kohonen, T., Hynninen, J., Kangas, J., and Laaksonen, J., "SOM PAK: The Self-organizing Map Program Package," 1970.

[36] Franke, L. L., Chatzopoulos, A. K., and Rigopoulos, S., "Tabulation of combustion chemistry via Artificial Neural Networks (ANNs): Methodology and application to LES-PDF simulation of Sydney flame L," *Combustion and Flame*, Vol. 185, 2017, pp. 245–260. https://doi.org/10.1016/j.combustflame.2017.07.014.

[37] Blasco, J., Fueyo, N., Dopazo, C., and Chen, J.-Y., "A Self-organizing-map Approach to Chemistry Representation in Combustion Applications," *Combustion Theory and Modelling*, Vol. 4, No. 1, 2000, pp. 61–76. https://doi.org/10.1088/1364-7830/4/1/304.

[38] Lei, S., "CFD Analysis/Optimization of Thermo-Acoustic Instabilities In Liquid Fueled Aero Stationary Gas Turbine Combustors," Ph.D. thesis, University of Manchester, 2010.

[39] Maries, A., Luciani, T., Pisciuneri, P. H., Nik, M. B., Yilmaz, S. L., Givi, P., and Marai, G. E., "A Clustering Method for Identifying Regions of Interest in Turbulent Combustion Tensor Fields," *Visualization and Processing of Higher Order Descriptors for Multi-Valued Data*, edited by I. Hotz and T. Schultz, Springer International Publishing, Cham, 2015, pp. 323–338.

[40] Nguyen, H.-T., Domingo, P., Vervisch, L., and Nguyen, P.-D., "Machine Learning for Integrating Combustion Chemistry in Numerical Simulations," *Energy and AI*, Vol. 5, 2021, p. 100082. https://doi.org/10.1016/j.egyai.2021.100082.

[41] MacQueen, J., *Some Methods for Classification and Analysis of Multivariate Observations*, 2014.

[42] Wan, K., Barnaud, C., Vervisch, L., and Domingo, P., "Chemistry Reduction Using Machine Learning Trained from Non-premixed Micro-mixing Modeling: Application to DNS of a Syngas Turbulent Oxy-flame With Side-wall Effects," *Combustion and Flame*, Vol. 220, 2020, pp. 119–129. https://doi.org/10.1016/j.combustflame.2020.06.008.

[43] Frouzakis, C., Kevrekidis, Y., Lee, J., Boulouchos, K., and Alonso, A., "Proper Orthogonal Decomposition of Direct Numerical Simulation Data: Data Reduction and Observer Construction," *Proceedings of the Combustion Institute*, Vol. 28, 2013, p. 7581. https://doi.org/10.1016/S0082-0784(00)80197-6.

[44] Isaac, B. J., Coussement, A., Gicquel, O., Smith, P. J., and Parente, A., "Reduced-order PCA Models for Chemical Reacting Flows," *Combustion and Flame*, Vol. 161, No. 11, 2014, pp. 2785–2800. https://doi.org/10.1016/j.combustflame.2014.05.011.

[45] Coussement, A., Isaac, B. J., Gicquel, O., and Parente, A., "Assessment of Different Chemistry Reduction Methods Based on Principal Component Analysis: Comparison of the MG-PCA and Score-PCA Approaches," *Combustion and Flame*, Vol. 168, 2016, pp. 83–97. https://doi.org/10.1016/j.combustflame.2016.03.021.

[46] Nunno, A. C., Perry, B. A., Macart, J. F., and Mueller, M. E., *Data-Driven Dimension Reduction in Turbulent Combustion: Utility and Limitations*, chapter and pages. https://doi.org/10.2514/6.2019-2010.

[47] Aversano, G., Bellemans, A., Li, Z., Coussement, A., Gicquel, O., and Parente, A., "Application of Reduced-Order Models Based on PCA and Kriging for the Development of Digital Twins of Reacting Flow Applications," *Computers and Chemical Engineering*, Vol. 121, 2019, pp. 422–441. https://doi.org/10.1016/j.compchemeng.2018.09.022.

[48] Alqahtani, S., and Echekki, T., "A Data-based Hybrid Model for Complex Fuel Chemistry Acceleration at High Temperatures," *Combustion and Flame*, Vol. 223, 2021, pp. 142–152. https://doi.org/10.1016/j.combustflame.2020.09.022.

[49] Mirgolbabaei, H., Echekki, T., and Smaoui, N., "A Nonlinear Principal Component Analysis Approach for Turbulent Combustion Composition Space," *International Journal of Hydrogen Energy*, Vol. 39, No. 9, 2014, pp. 4622–4633. https://doi.org/10.1016/j.ijhydene.2013.12.195.

[50] D'Alessio, G., Attili, A., Cuoci, A., Pitsch, H., and Parente, A., *Analysis of Turbulent Reacting Jets via Principal Component Analysis*, chapter and pages, pp. 233–251. https://doi.org/10.1007/978-3-030-44718-2_12.

[51] Christo, F., Masri, A., Nebot, E., and Turanyi, T., "Utilising Artificial Neural Network and Repro-modelling in Turbulent Combustion," *Proceedings of ICNN'95 - International Conference on Neural Networks*, Vol. 2, 1995, pp. 911–916 vol.2. https://doi.org/10.1109/ICNN.1995.487540.

[52] Christo, F., Masri, A., and Nebot, E., "Artificial Neural Network Implementation of Chemistry with PDF Simulation of H2/CO2 Flames," *Combustion and Flame*, Vol. 106, No. 4, 1996, pp. 406–427. https://doi.org/10.1016/0010-2180(95)00250-2.

[53] Christo, F., Masri, A., Nebot, E., and Pope, S., "An Integrated PDF/neural Network Approach for Simulating Turbulent Reacting Systems," *Symposium (International) on Combustion*, Vol. 26, No. 1, 1996, pp. 43–48. https://doi.org/10.1016/S0082-0784(96)80198-6.

[54] Blasco, J., Fueyo, N., Dopazo, C., and Ballester, J., "Modelling the Temporal Evolution of a Reduced Combustion Chemical System With an Artificial Neural Network," *Combustion and Flame*, Vol. 113, No. 1, 1998, pp. 38–52. https://doi.org/10.1016/S0010-2180(97)00211-3.

[55] Ding, T., Readshaw, T., Rigopoulos, S., and Jones, W., "Machine Learning Tabulation of Thermochemistry in Turbulent Combustion: An Approach Based on Hybrid

Flamelet/random Data and Multiple Multilayer Perceptrons," *Combustion and Flame*, Vol. 231, 2021, p. 111493. https://doi.org/10.1016/j.combustflame.2021.111493.

[56] Readshaw, T., Ding, T., Rigopoulos, S., and Jones, W. P., "Modeling of Turbulent Flames with the Large Eddy Simulation Probability Density Function (LESPDF) Approach, Stochastic Fields, and Artificial Neural Networks," *Physics of Fluids*, Vol. 33, No. 3, ????, p. 035154. https://doi.org/10.1063/5.0041122.

[57] Nikolaou, Z. M., Chrysostomou, C., Vervisch, L., and Cant, S., "Progress Variable Variance and Filtered Rate Modelling Using Convolutional Neural Networks and Flamelet Methods," *Flow, Turbulence and Combustion*, Vol. 103, No. 2, 2019, pp. 485–501.

[58] Lapeyre, C. J., Misdariis, A., Cazard, N., Veynante, D., and Poinsot, T., "Training Convolutional Neural Networks to Estimate Turbulent Sub-grid Scale Reaction Rates," *Combustion and Flame*, Vol. 203, 2019, pp. 255–264. https://doi.org/10.1016/j.combustflame.2019.02.019.

[59] Yellapantula, S., de Frahan, M. T. H., King, R., Day, M., and Grout, R., *Machine Learning of Combustion LES Models from Reacting Direct Numerical Simulation*, chapter and pages, pp. 273–292. https://doi.org/10.1007/978-3-030-44718-2_14.

[60] Yao, S., Wang, B., Kronenburg, A., and Stein, O., "Conditional Scalar Dissipation rate Modeling for Turbulent Spray Flames Using Artificial Neural Networks," *Proceedings of the Combustion Institute*, Vol. 38, No. 2, 2021, pp. 3371–3378. https://doi.org/10.1016/j.proci.2020.06.135.

[61] Yao, S., Wang, B., Kronenburg, A., and Stein, O. T., "Modeling of Sub-grid Conditional Mixing Statistics in Turbulent Sprays Using Machine Learning Methods," *Physics of Fluids*, Vol. 32, No. 11, 2020, p. 115124. https://doi.org/10.1063/5.0027524.

[62] Owoyele, O., Kundu, P., Ameen, M. M., Echekki, T., and Som, S., "Application of Deep Artificial Neural Networks to Multi-dimensional Flamelet Libraries and Spray Flames," *International Journal of Engine Research*, Vol. 21, No. 1, 2020, pp. 151–168. https://doi.org/10.1177/1468087419837770.

[63] Sen, B. A., Hawkes, E. R., and Menon, S., "Large Eddy Simulation of Extinction and Reignition with Artificial Neural Networks Based Chemical Kinetics," *Combustion and Flame*, Vol. 157, No. 3, 2010, pp. 566 – 578. https://doi.org/10.1016/j.combustflame.2009.11.006.

[64] Sen, B. A., and Menon, S., "Linear Eddy Mixing Based Tabulation and Artificial Neural Networks for Large Eddy Simulations of Turbulent Flames," *Combustion and Flame*, Vol. 157, No. 1, 2010, pp. 62 – 74. https://doi.org/10.1016/j.combustflame.2009.06.005.

[65] Ihme, M., Schmitt, C., and Pitsch, H., "Optimal Artificial Neural Networks and Tabulation Methods for Chemistry Representation in LES of a Bluff-Body Swirl-Stabilized Flame," *Proceedings of the Combustion Institute*, Vol. 32, No. 1, 2009, pp. 1527–1535. https://doi.org/10.1016/j.proci.2008.06.100.

[66] Shadram, Z., Nguyen, T. M., Sideris, A., and Sirignano, W. A., "Neural Network Flame Closure for a Turbulent Combustor with Unsteady Pressure," *AIAA Journal*, Vol. 59, No. 2, 2021, pp. 621–635. https://doi.org/10.2514/1.J059721.

[67] Zhang, J., Huang, H., Xia, Z., Ma, L., Duan, Y., Feng, Y., and Huang, J., "Artificial Neural Networks for Chemistry Representation in Numerical Simulation of the Flamelet-Based Models for Turbulent Combustion," *IEEE Access*, Vol. 8, 2020, pp. 80020–80029. https://doi.org/10.1109/ACCESS.2020.2990943.

[68] Shadram, Z., Nguyen, T. M., Sideris, A., and Sirignano, W. A., "A Neural Network-Based Flamelet Model for a Liquid Propellant Rocket Engine with Partially-Premixed Flame," WSSCI Technical Meeting, Combustion Institute, 2019.

[69] Shadram, Z., Nguyen, T. M., Sideris, A., and Sirignano, W. A., "Neural Network Closure Models for Estimating Flame Variables in a Liquid-Propellant Rocket Engine," *AIAA Scitech 2019 Forum*, AIAA SciTech Forum, American Institute of Aeronautics and Astronautics, 2019. https://doi.org/10.2514/6.2019-2008.

[70] Harvazinski, M. E., Huang, C., Sankaran, V., Feldman, T. W., Anderson, W. E., Merkle, C. L., and Talley, D. G., "Combustion Instability Mechanisms in Pressure-Coupled Gas-gas Coaxial Rocket Injector," *AIAA 2013-3990*, AIAA, 2013.

[71] Poinsot, T., and Veynannte, D., *Theoretical and Numerical Combustion*, 2nd ed., R. T. Edwards, 2005.

[72] Crocco, L., and Sirignano, W. A., "Effects of Transverse Velocity Components on the Nonlinear Behavior of Short Nozzles," *AIAA Journal*, Vol. 4, 1966, pp. 1428–1430.

[73] Lopez-Camara, C.-F., Jorda Juanos, A., and Sirignano, W. A., "Strain Rate and Pressure Effects on Multi-branched Counterflow Flames," *Combustion and Flame*, Vol. 221, 2020, pp. 256–269. https://doi.org/10.1016/j.combustflame.2020.07.041.

[74] Sirignano, W. A., "Combustion with Multiple Flames under High Strain Rates," *Combustion Science and Technology*, Vol. 0, No. 0, 2019, pp. 1–30. https://doi.org/10.1080/00102202.2019.1685507.

[75] Sirignano, W. A., "Counterflow and Wall Stagnation Flow with Three-dimensional Strain," *Physics of Fluids*, Vol. 31, No. 5, 2019, p. 053605. https://doi.org/10.1063/1.5096472.

[76] Sirignano, W. A., "Combustion with Multiple Flames under High Strain Rates," *Combustion Science and Technology*, Vol. 193, No. 7, 2021, pp. 1173–1202. https://doi.org/10.1080/00102202.2019.1685507.

[77] Murphy, K. P., *Machine Learning: a Probabilistic Perspective*, MIT Press, 2013.

[78] Rumelhart, D. E., Hinton, G. E., and Williams, R. J., "Learning Representations by Back-propagating Errors," *Nature*, Vol. 323, No. 6088, 1986, pp. 533–536. https://doi.org/10.1038/323533a0.

[79] Goodfellow, I., Bengio, Y., and Courville, A., *Deep Learning*, MIT Press, 2016.

[80] Ruder, S., "An overview of gradient descent optimization algorithms," *CoRR*, Vol. abs/1609.04747, 2016.

[81] Spall, J. C., *Introduction to Stochastic Search and Optimization*, chapter and pages. https://doi.org/10.1002/0471722138.

[82] Ruder, S., "An Overview of Gradient Descent Optimization Algorithms," *CoRR*, Vol. abs/1609.04747, 2016.

[83] Xavier, G., and Yoshua, B., "Understanding the Difficulty of Training Deep Feedforward Neural Networks," *Proceedings of the Thirteenth International Conference on Artificial Intelligence and Statistics*, Proceedings of Machine Learning Research, Vol. 9, Sardinia, Italy, 2010, pp. 249–256.

[84] Hinton, G., Srivastava, N., and Swersky, K., "Neural Networks for Machine Learning Lecture 6a Overview of Mini-Batch Gradient Descent," , 2012.

[85] Loader, C., *Local Regression and Likelihood*, Springer-Verlag New York, 1999.

[86] Nickolls, J., and Dally, W. J., "The GPU Computing Era," *IEEE Micro*, Vol. 30, No. 2, 2010, pp. 56–69.

[87] Shadram, Z., Nguyen, T. M., Sideris, A., and Sirignano, W. A., "Physics-Aware Neural Network Flame Closure for Combustion Instability Modeling in a Single-Injector Engine," , 2021.

[88] Kirch, W., *Pearson's Correlation Coefficient*, chapter and pages, pp. 1090–1091. https://doi.org/10.1007/978-1-4020-5614-7-2569.

[89] Nguyen, T. M., "Nonlinear Rocket-engine Longitudinal Combustion Instability," Ph.D. thesis, University of California, Irvine, 2018.

Appendix A

Numerical Framework for CVRC

Following Nguyen et al. ([22], [89]), the numerical framework is given as follows.

A.1 Governing Equations

For a multispecies mixture, the Favre-Averaged Navier-Stokes equations are written in conservative form following

$$\frac{\partial \bar{\rho}}{\partial t} + \frac{\partial \bar{\rho}\tilde{v}_j}{\partial x_j} = 0 \tag{A.1}$$

$$\frac{\partial \bar{\rho}\tilde{v}_i}{\partial t} + \frac{\partial \bar{\rho}\tilde{v}_i\tilde{v}_j}{\partial x_j} = -\frac{\partial \bar{p}}{\partial x_i} + \frac{\partial(\tau_{ij} + \tau_{ij}^R)}{\partial x_j} \tag{A.2}$$

$$\frac{\partial \bar{\rho}\tilde{E}}{\partial t} + \frac{\partial \tilde{v}_j(\bar{\rho}\tilde{E} + \bar{p})}{\partial x_j} = \frac{\partial}{\partial x_j}\left[\tilde{v}_i(\tau_{ij} + \tau_{ij}^R) + \left(\mu + \sigma_k \mu_t \frac{\partial k}{\partial x_j}\right)\right] + \frac{\partial}{\partial x_j}\left[\left(\frac{\lambda}{c_p} + \frac{\mu_t}{Pr_t}\right)\frac{\partial \tilde{h}}{\partial x_j}\right] \tag{A.3}$$

where $\bar{\rho}$ is the mean density, u_i is the velocity in the x_i direction. $\bar{p}$ is the mean pressure. μ and μ_t are the molecular and turbulent viscosity. λ and C_p are the heat conduction and constant specific heat coefficients. τ_{ij}, τ_{ij}^R are the molecular and turbulent viscous stress tensors, respectively:

$$\tau_{ij} = \mu\left(\frac{\partial \tilde{v}_i}{\partial x_j} + \frac{\partial \tilde{v}_j}{\partial x_i} - \frac{2}{3}\frac{\partial \tilde{v}_k}{\partial x_k}\delta_{ij}\right) \qquad \tau_{ij}^R = \mu_t\left(\frac{\partial \tilde{v}_i}{\partial x_j} + \frac{\partial \tilde{v}_j}{\partial x_i} - \frac{2}{3}\frac{\partial \tilde{v}_k}{\partial x_k}\delta_{ij}\right) \tag{A.4}$$

The total energy, $\tilde{E}$, has the form of

$$\tilde{E} = \frac{1}{2}\left(\sum_{j=1}^{n} \tilde{v}_j \tilde{v}_j\right) + k + \tilde{e} \tag{A.5}$$

where n is the number of dimensions. The first term on the right side is the mean flow kinetic energy. The second term is the turbulent kinetic energy, k. $\tilde{e}$ is the total thermal energy which includes the sensible and chemical energies. Enthalpy, $\tilde{h}$, is related to the total thermal energy as $\tilde{h} = \tilde{e} + \frac{\bar{p}}{\bar{\rho}}$. For high-pressure combustion, the ideal-gas law is assumed ($\bar{p} = \bar{\rho}RT$), where R is the specific gas constant. The turbulent Schmidt (Sc_t) and Prandtl (Pr_t) numbers are assumed to be constant at 0.9.

A.2 Turbulence Model

Here, turbulence is modeled using the Delayed Detached Eddy Simulation (DDES) approach. The formulation is based on the 2006 Wilcox $k-\omega$ model. The conservative form of the governing equations for the turbulent kinetic energy (k) and the turbulent dissipation rate (ω) are written as follows

$$\frac{\partial \bar{\rho}k}{\partial t} + \frac{\partial(\bar{\rho}\tilde{v}_j k)}{\partial x_j} = (\tau_{ij} + \tau_{ij}^R)\frac{\partial \tilde{v}_i}{\partial x_j} - \beta^* \bar{\rho}\omega k + \frac{\partial}{\partial x_j}\left[\left(\mu + \sigma_k \frac{\rho k}{\omega}\right)\frac{\partial k}{\partial x_j}\right] \tag{A.6}$$

$$\frac{\partial \bar{\rho}\omega}{\partial t} + \frac{\partial(\bar{\rho}\tilde{v_j}\omega)}{\partial x_j} = \frac{\gamma\omega}{k}(\tau_{ij} + \tau_{ij}^R)\frac{\partial \tilde{v_i}}{\partial x_j} - \beta\bar{\rho}\omega^2 + \frac{\partial}{\partial x_j}\left[\left(\mu + \sigma_\omega \frac{\bar{\rho}k}{\omega}\right)\frac{\partial \omega}{\partial x_j}\right] + \frac{\bar{\rho}\sigma_d}{\omega}\frac{\partial k}{\partial x_j}\frac{\partial \omega}{\partial x_j} \quad \text{(A.7)}$$

where $\beta^*, \beta, \sigma_k, \sigma_\omega, \sigma_d$ are modeling constants. The turbulent viscosity is calculated as $\mu_t = \frac{\bar{\rho}k}{\hat{\omega}}$, where $\hat{\omega}$ is the turbulent frequency corrected by the maximum of ω and the flow mean strain rate.

In DDES, the dissipation term in equation A.6 (second term on the right side) is modified to exclude any grid-realized contribution in the turbulent viscosity. This can be achieved using the mathematical definition:

$$\beta^*\rho\omega k = \rho k^{3/2}/L_T^* \quad \text{(A.8)}$$

where the corrected turbulent length scale is defined as

$$L_T^* = min(L_T, C_{DES}L_{GRID}) \quad \text{(A.9)}$$

where C_{DES} is a modeling constant, and L_T and L_{GRID} are the turbulent and grid length scales where $L_T = k^{1/2}/(\beta^*\omega)$ and $L_{GRID} = L_T - F_D(L_T - \Delta)$. Δ is the largest grid dimension for the cell. F_D is a blending function that eliminates the grid-size arbitrariness by determining the location of the cell away from the wall.

A.3 Combustion Model

Here, turbulence-flame interaction is modeled using the Compressible Flamelet Progress Variable (CFPV) approach [21, 22]. Presumed Probability Density Functions (PDFs) are used to relate the laminar flamelet solutions in the mixture fraction space to their Favre-

averaged/mean counterpart. β PDF is assumed for mixture fraction while Dirac δ PDF is assumed for both the progress variable and pressure. The Favre-averaged thermo-chemical quantities ($\tilde{\psi}_i$) at each pressure value are pre-processed as lookup libraries using the convolution:

$$\tilde{\psi}_i(\tilde{Z}, \widetilde{Z''^2}, \tilde{C}, \bar{p}) = \int_0^1 \int_0^1 \psi_i(Z, C)\beta(Z, Z''^2)\delta(C)dZdC \tag{A.10}$$

where Z is the mixture fraction, C is the progress variable.

During the CFD computation, the transport equations for the mean scalars $\tilde{Z}, \widetilde{Z^2}, \tilde{C}$ are solved. The mean mixture fraction squared ($\widetilde{Z^2}$) is related to the mean mixture fraction and the mean variance as: $\widetilde{Z^2} = \tilde{Z}^2 + \widetilde{Z''^2}$. With Lewis number equal to one, the transport equations for these scalars are given as

$$\frac{\partial \bar{\rho}\tilde{Z}}{\partial t} + \frac{\partial \bar{\rho}\tilde{v}_j\tilde{Z}}{\partial x_j} = \frac{\partial}{\partial x_j}\left[\left(\frac{\lambda}{c_p} + \frac{\mu_t}{Sc_t}\right)\frac{\partial \tilde{Z}}{\partial x_j}\right] \tag{A.11}$$

$$\frac{\partial \bar{\rho}\widetilde{Z^2}}{\partial t} + \frac{\partial \bar{\rho}\tilde{v}_j\widetilde{Z^2}}{\partial x_j} = \frac{\partial}{\partial x_j}\left[\left(\frac{\lambda}{c_p} + \frac{\mu_t}{Sc_t}\right)\frac{\partial \widetilde{Z^2}}{\partial x_j}\right] - \bar{\rho}C_x\omega(\widetilde{Z^2} - \tilde{Z}^2) \tag{A.12}$$

$$\frac{\partial \bar{\rho}\tilde{C}}{\partial t} + \frac{\partial \bar{\rho}\tilde{v}_j\tilde{C}}{\partial x_j} = \frac{\partial}{\partial x_j}\left[\left(\frac{\lambda}{c_p} + \frac{\mu_t}{Sc_t}\right)\frac{\partial \tilde{C}}{\partial x_j}\right] + \tilde{\dot{\omega}}_C \tag{A.13}$$

where C_x has a constant value of 2.0. Turbulence mixing and turbulence/flame interaction of the mean mixture fraction are modeled by solving equation (A.12), which implicitly describes the variance of the mean mixture fraction ($\widetilde{Z''}$).

At each time step, the local values of these scalars along with the pressure allow us to retrieve quickly properties such as local compositions, temperature, specific heat (c_p), enthalpy, and

thermal diffusivity using pre-tabulated flamelet libraries.

At the end of each time step, the local values of the Favre-averaged thermal energy ($\tilde{e}$) can differ from the thermal energy (e_f) computed from the turbulent flamelet transport equations (equations A.11-A.13). However, the local compositions are the same for both quantities. For a given $\tilde{e}$ value computed from the Navier-Stokes equations, an expansion around the thermal energy of the flamelet solutions has the form

$$\tilde{e} = e_f + \int_{T_f}^{\tilde{T}} c_v(T)dT = e_f + \int_{T_f}^{\tilde{T}} \frac{R_f}{\gamma(T)-1}dT \tag{A.14}$$

where the subscript "f" denotes the values of the flamelet solution. The specific heat ratio (γ) can be expressed as:

$$\gamma(\tilde{T}) = \gamma_f + a_\gamma(\tilde{T} - T_f) \tag{A.15}$$

where a_γ is the local linear expansion coefficient and tabulated during the pre-processing step as a flamelet library.

Integrating equation (A.14) and solving for $\tilde{T}$ we get

$$\tilde{T} = T_f + \frac{\gamma_f - 1}{a_\gamma}\left(\exp(a_\gamma(\tilde{e} - e_f)/R_f) - 1\right) \tag{A.16}$$

Equation (A.16), together with the ideal gas law, illustrate the nonlinear coupling between the flame and the acoustical field.

A.4 Numerical Scheme

As previously mentioned in the main text, the code is a structured, multi-block, finite difference compressible solver written in axisymmetric formulation. The advection and diffusion

terms are discretized using central differencing. Since either weak or strong shock waves have been observed in the CVRC, Jameson-Schmidt-Turkel (JST) 4th order numerical dissipation is added for stability and shock-capturing purposes. Time integration is performed using a low-storage 4-stage Runge-Kutta time integration scheme.

A.5 Solution Procedure

For clarification, a schematic of the solution procedure is also included. From known conditions at time n, the solution will be advanced to time n+1 As shown in Figure A.1, the code

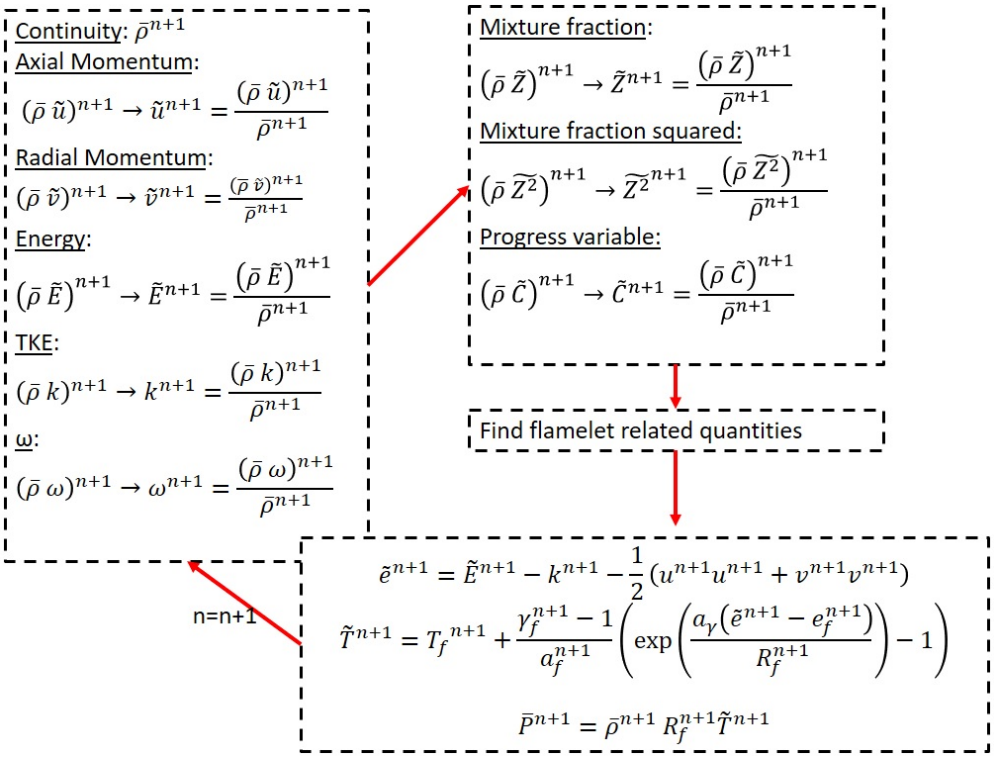

Figure A.1: Block presentation of the solution [89]

updates all of these conserved variables at the same time to ensure strong coupling. The step of finding all the flamelet related quantities can be summarized as follows. Each quantity such as $(T_f^{n+1}, e_f^{n+1}, a_f^{n+1}, R_f^{n+1})$ has its corresponding pre-tabulated flamelet libraries (four-dimensional arrays). At each grid point in the computational domain, using the values

of $\tilde{Z}^{n+1}, \widetilde{Z^2}^{n+1}, \tilde{C}^{n+1}, \bar{P}^n$, each quantity is computed from interpolation using its respective flamelet library.

A.6 Multiblock Domain

Figure A.2 provides a schematic of the CVRC configuration, which is divided to four sections. The figure shows the mesh distribution over the geometry. The mesh is more dense near the dump plane and in the shear layer. FP and FP1 section on the plot show the fuel post (injector) and the shear layer below that it. OP shows the oxidizer post, and CH is the above section of the combustor.

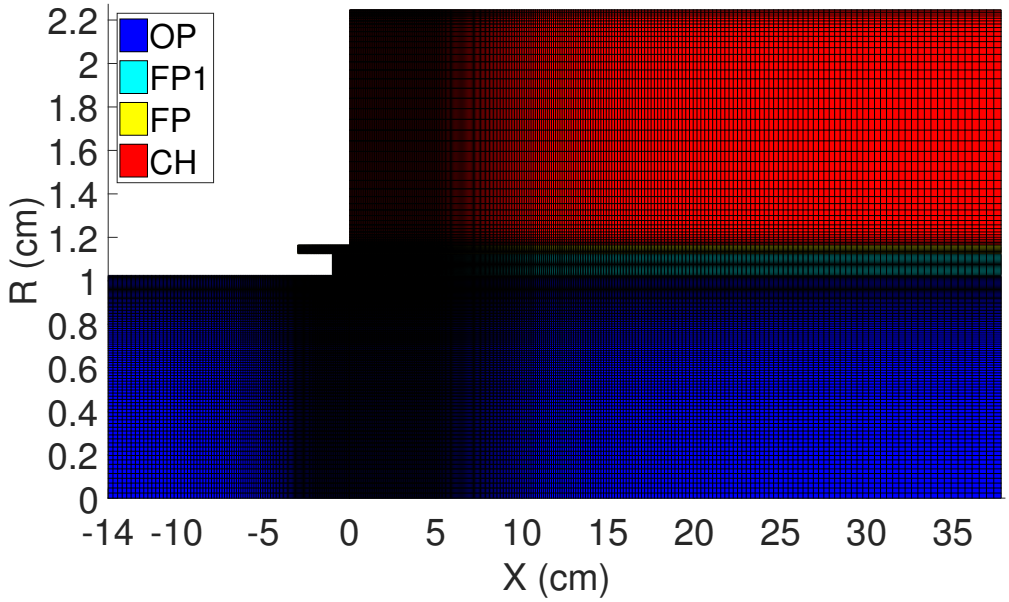

Figure A.2: Sectioning and the computational mesh. [89]